Technische Universität München
TUM School of Natural Sciences

Characterization of Edge Modes in Different Confinement Regimes of Fusion Plasmas

Joey Kalis

Vollständiger Abdruck der von der TUM School of Natural Sciences der Technischen Universität München zur Erlangung eines

Doktors der Naturwissenschaften (Dr. rer. nat.)

genehmigten Dissertation.

Vorsitz: Prof. Dr. Lorenzo Tancredi

Prüfende der Dissertation:

1 Priv.-Doz. Dr. Gregor Birkenmeier

2 Prof. Dr. Rudolf Neu

Die Dissertation wurde am 25.06.2024 bei der Technischen Universität München eingereicht und durch die TUM School of Natural Sciences am 23.09.2024 angenommen.

HELMHOLTZ
SPITZENFORSCHUNG FÜR
GROSSE HERAUSFORDERUNGE

MAX-PLANCK-INSTITUT
FÜR PLASMAPHYSIK

Characterization of Edge Modes in Different Confinement Regimes of Fusion Plasmas

PhD Thesis

by

Joey Kalis

25. June 2024

Technical University Munich

School of Natural Sciences

Supervisor: *Dr. habil. Gregor Birkenmeier*

HELMHOLTZ
SPITZENFORSCHUNG FÜR
GROSSE HERAUSFORDERUNGE

MAX-PLANCK-INSTITUT
FÜR PLASMAPHYSIK

Charakterisierung von Randmoden in verschiedenen Einschlussregimen eines Fusionsplasmas

Doktorarbeit

von

Joey Kalis

25. Juni 2024

Technische Universität München

School of Natural Sciences

Gutachter: Dr. habil. Gregor Birkenmeier

Contents

Zusammenfassung

Die kontrollierte Kernfusion nach dem Konzept des magnetischen Einschlusses in einem Tokamak ist ein vielversprechender Kandidat für die zukünftige Energieproduktion. Dabei werden frei bewegliche Elektronen und Ionen, also ein Plasma, durch Magnetfelder eingeschlossen und auf mehrere Millionen Grad Kelvin aufgeheizt, um den Kernfusionsprozess anzuregen. Diese hohen Temperaturen sind für die Wand des Plasmagefäßes untragbar, sodass sowohl die Temperatur als auch die Dichte des Plasmas zum Gefäßrand hin abnehmen müssen. Insbesondere in der so-genannten H-Mode treten am Plasmarand starke Dichte- und Temperaturgradienten auf, die wiederrum zu Plasmarandinstabilitäten führen. Von besonderer Bedeutung sind die Typ-I randlokalisierten Moden (ELMs), die bei hinreichend großen Druckgradienten an der so genannten Peeling-Ballooning-Grenze auftreten und genügend Energie vom Plasmazentrum auf die Wand übertragen, um zukünftige, große Fusionsreaktoren zu beschädigen. Glücklicherweise ist es gelungen, durch geeignete Wahl der Plasmaparameter, wie z.B. der geometrischen Form des Plasmas, H-Moden-artige Regime ohne Typ-I ELMs zu erzeugen: die ELM-freien Regime. Die ELM-freien Szenarien werden von Randmoden begleitet, die durch Randinstabilitäten verursacht werden. Diese Randmoden sind der Grund für die Abwesenheit der Typ-I ELMs, wenn sie ausreichend hohen Transport verursachen und somit die Randprofile abflachen, sodass die Peeling-Ballooning-Grenze nicht erreicht wird. Um die beobachteten Moden einer Randinstabilität zuzuordnen, sind ihre poloidale Größe und Geschwindigkeit im Plasmabezugssystem Schlüsselgrößen. Diese werden experimentell mit der thermischen Heliumstrahldiagnostik bestimmt, die die Lichtintensität von angeregten, lokal injizierten He-Teilchen misst.

Die vorliegende Arbeit untersucht die Dynamik am Plasmarand, insbesondere der Randmoden, in den folgenden ELM-freien Regimen: enhanced D_α high confinement mode (EDA H-mode), quasi-continuous exhaust regime (QCE), intermediate phase (I-phase) und improved energy confinement mode (I-mode). Es wird festgellt, dass die quasi-kohärente Mode (QCM) in EDA H-mode und QCE-Szenarien eine elektromagnetische Ballooning-Mode ist. Darüber hinaus ist die Precursor-Mode in der I-phase eine (Micro-)Tearing-Mode ((M-)TM) oder eine kinetische Peeling-Ballooning-Mode (KPBM). Die schwach kohärente Mode (WCM) in der I-mode ist driftwellenartig, d.h. eine Driftwelle, eine Trapped-Electron-Mode, eine MTM oder KPBM.

Abstract

Controlled nuclear fusion using the magnetic confinement concept of the tokamak is a promising candidate for future energy production. In this approach, freely moving electrons and ions, i.e. a plasma, are confined by superimposed magnetic fields and heated to several million degrees Kelvin using various heating methods to drive the nuclear fusion process. These high temperatures and energetic particles are intolerable for the wall of the plasma vessel, so both the temperature and the density of the plasma must necessarily decrease toward the vessel, in the plasma edge. Especially in the so-called high confinement regime (H-mode), strong density and temperature gradients occur at the plasma edge, which in turn lead to plasma edge instabilities. Particularly important are the so-called type-I edge localized modes (ELMs), which appear at sufficiently large pressure gradients at the so-called peeling-ballooning limit and transfer sufficient energy from the plasma center to the wall to damage future large fusion reactors. Fortunately, by a suitable choice of plasma parameters, such as the geometrical shape of the plasma, it has been possible to create H-mode-like regimes without type-I ELMs: the ELM-free regimes. Instead, the ELM-free scenarios are accompanied by so-called edge modes caused by edge instabilities. These edge modes are the reason for the absence of the type-I ELMs, if they cause sufficient transport and thus flatten the edge profiles so that the peeling-ballooning limit is not reached. To assign the experimentally observed modes to an edge instability, the poloidal size of the mode and its poloidal velocity in the plasma frame are key quantities. These are determined experimentally with the thermal helium beam diagnostic, which measures the light intensity of excited, locally injected He particles.

The present work investigates the edge dynamics and in particular the edge modes in the following ELM-free regimes: enhanced D_α high confinement mode (EDA H-mode), quasi-continuous exhaust regime (QCE), intermediate phase (I-phase) and improved energy confinement mode (I-mode). It is found that the quasi-coherent mode (QCM) in EDA H-mode and QCE scenarios is an electromagnetic ballooning mode. Furthermore, the precursor mode in the I-phase seems to be a (micro-)tearing mode or a kinetic peeling-ballooning mode, and the weakly coherent mode (WCM) in the I-mode is drift-wave-like, i.e. a drift wave, a trapped electron mode, a micro-tearing mode or a kinetic peeling ballooning mode.

1 Introduction

"The scientist is not responsible for the laws of nature. It is his job to find out how these laws operate. It is the scientist's job to find the ways in which these laws can serve the human will. However, it is not the scientist's job to determine whether a hydrogen bomb should be constructed, whether it should be used, or how it should be used." [1] Edward Teller, often referred to as the 'father of the hydrogen bomb', said these words to explain what a scientist's job is and is not. In other words, although the hydrogen bomb [2] (like the atomic bomb [3]) itself, was a devastating and world-changing discovery, the physics behind it and its research into nuclear fusion cannot be ignored. These sparked the idea that it is possible to release energy on Earth through the process of nuclear fusion. Although they began for nuclear weapon-oriented reasons, the whole effort of uncontrolled energy release paved the way for controlled nuclear fusion as we know it today. And indeed, controlled thermonuclear fusion is a promising option for energy production in addition to alternative energy sources such as wind, solar, hydro, geothermal and biofuels [4]. As energy consumption per person on Earth continues to increase [5], it is inevitable that multiple sources of energy will be sought to replace exhaustible sources such as coal or oil in the long term. In science, it is usually proven that nature itself is the best guide when it comes to finding new methods in the most efficient way. And this is where nuclear fusion comes in, as it is the most energy releasing process found in the observable universe. This is not to say that nuclear fusion is the only true solution, but it is always wisest to think broadly and promote multiple possibilities. In this thesis, we will delve deeper and deeper into the matter of nuclear fusion on Earth, and in order to better internalize the overall picture of the work, we will first introduce the nuclear fusion process and then discuss at a possible solution on Earth.

1.1 Introduction to Nuclear Fusion

The basic process of nuclear fusion is based on the same principle as nuclear fission, i.e. the binding energy in nucleons gets released. The binding energy per nucleon is drawn against the number of nucleons A in Fig. 1.1a. For heavy nuclei (high A), fission is used to generate energy, while for light nuclei (low A) fusion leads to energy release.

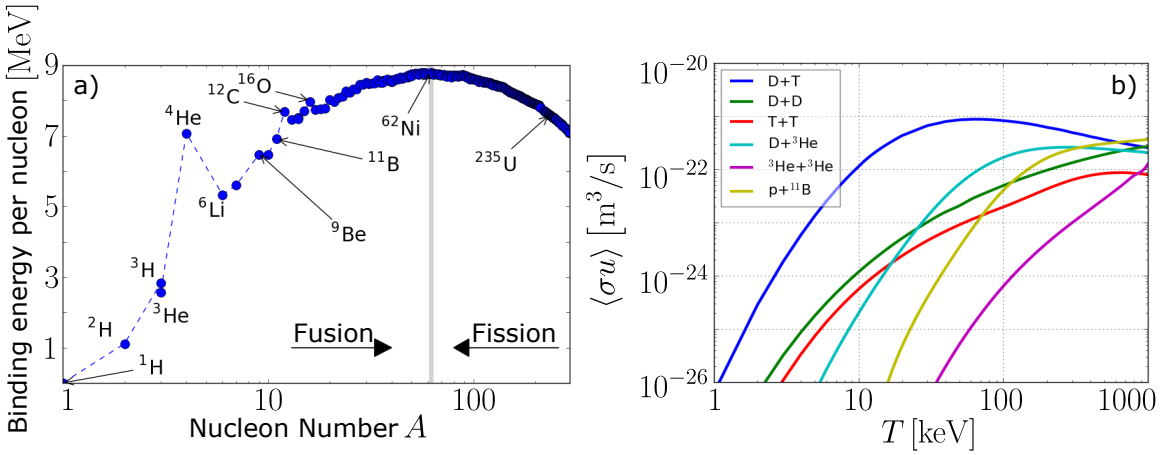

Figure 1.1: Binding Energy and Reaction Parameter
(a) The binding energy per nucleon increases up to the maximum around ^{62}Ni. To the left of this maximum, fusion of two light nuclei yields energy due to the mass defect. At higher mass numbers A, the curve decreases and fission of heavier nuclei lead to the release of energy. (b) The reaction parameter $\langle \sigma u \rangle$ for different fusion processes changes with temperature. Deuterium-tritium (D+T) has the highest reaction rate. Figs. adapted from Ref. [6].

Nuclear fusion is a natural, long time step in stellar evolution after large masses of hydrogen have clumped together and high temperatures T have been created by the release of gravitational energy [7]. At these high temperatures[1], we find hydrogen and other atoms in the state of a plasma, in which the ions and electrons are no longer bound and can move freely. In stars, the plasma is held together by the strong effect of gravity, and the fusion of atomic particles occurs when the ions overcome their electromagnetic repulsion - the Coulomb barrier - with the tunnel effect [8] playing a key role. Furthermore, in stellar objects, a total of four protons fuse to form a helium particle ($\alpha-$particle) in sum, whereby this can occur at low temperatures via the so-called pp-chain or, for $T > 1\,\mathrm{keV}$, catalytically via the Bethe-Weizsäcker cycle [9]. In order to estimate the efficiency of nuclear fusion as such, we need a high fusion rate of the ion species a and b per unit volume and time, given as [10]

$$R_{\mathrm{ab}} = n_{\mathrm{a}} n_{\mathrm{b}} \langle \sigma u \rangle \,, \tag{1.1}$$

corresponding to the probability that fusion will occur. We see in Eq. 1.1 that the fusion rate depends both on the density of the two species n_{a} and n_{b} and on the reaction parameter $\langle \sigma u \rangle$, which consists of the cross section of the reaction σ and relative velocity of the particles u. $\langle \sigma u \rangle$ varies for different fusion reactions (or fusion material) and reaches its maximum at different temperatures (or energy) depending on

[1] In plasma physics, the temperature is usually expressed in electronvolts (eV), for which 1 eV corresponds to 11 605 K, and the conversion is simply given by Boltzmann's constant k_{B}.

the used fusion material, shown in Fig. 1.1b. It can be shown that the proton reaction mentioned above gives far too low values and that fusion takes place on a time scale of at least 10^{10} years, far too long for our purposes [11]. So we cannot directly imitate nature.

Instead, the reaction of deuterium, a hydrogen nucleus with one neutron, and tritium, a hydrogen nucleus with two neutrons, i.e. [12]

$$^2\mathrm{H} + {}^3\mathrm{H} = {}^2\mathrm{D} + {}^3\mathrm{T} \longrightarrow {}^4\mathrm{He}\,(3.5\,\mathrm{MeV}) + n\,(14.1\,\mathrm{MeV}) \tag{1.2}$$

has proven to be the most promising candidate and features the highest reaction parameter (blue line in Fig. 1.1b). The fusion power released by this reaction is [13]

$$P_{\mathrm{fus}} = \frac{1}{4} n^2 \langle \sigma u \rangle_{\mathrm{DT}} E_{\mathrm{fus}} \propto p^2 V_{\mathrm{pl}} \tag{1.3}$$

and depends on the pressure p, which is the product of the density n and the temperature T in the plasma[2], i.e. $p = nT$, and the plasma volume V_{pl}. Accordingly, we should aim for high densities and temperatures and large plasma volumes, but we will take a closer look at the individual parameters and their physical limitations in Sec. 2.1.

It should be noted that radioactive tritium occurs naturally in exhaustible quantities on Earth and would have to be bred from lithium [14]. Deuterium, on the other hand, can be found on Earth in almost inexhaustible quantities from water, making it a useful experimental material. Therefore, most fusion experiments are conducted in deuterium (green line in Fig. 1.1b), but also in hydrogen or helium plasmas, which have a lower energy gain, but do not have the problem of resource depletion. But how is it possible to achieve nuclear fusion on Earth and how do we confine the plasma?

Unlike stellar plasmas, which are confined by strong gravity as described above, there are generally two basic methods for confining plasma in the laboratory. The first is inertial confinement fusion (ICF) [15], in which DT pellets are bombarded with a high-power laser or heavy ion beams to achieve extremely high temperatures for a short time. However, the material diverges and fusion occurs only on the time scale when the material is still in range, exploiting the inertia of the material, hence the name ICF. This confinement mechanism is in some sense similar to that of natural fusion, since natural fusion in stars is determined by the heavy mass and inertial fusion by the inertial mass of the particles, which are known to be the same [16]. Of particular note is the record shot from the national ignition facility (NIF) in 2021, which demonstrated the highest power conversion ever achieved (more on the power conversion later) [17]. The second and more important method for the present work is magnetic confinement

[2]The ideal gas law is actually written as $p = nk_{\mathrm{B}}T$, where k_{B} is the Boltzmann constant, which will be dropped as we proceed.

fusion (MCF). As the name suggests, magnetic fields are used to confine the freely moving charged particles in the plasma. MCF is further divided into two concepts: the stellarator, for which the reader should refer to Refs. [12, 18, 19], and the tokamak, whose concept and geometry we will discuss in more detail. This follows from the fact that all experiments and simulations in this thesis have been performed on the ASDEX Upgrade tokamak. The future fusion reactor ITER [20], whose goal is to create a plasma that produces net energy for the first time, is also a tokamak. In addition, DEMO [21], which is the successor project to ITER, could also be a tokamak, although this has not yet been decided.

1.2 The Tokamak

The tokamak, which is an acronym for 'Toroidalnaya Kamera i Magnitnaya Katushka' (toroidal chamber and magnetic coil) and has been developed in the Soviet Union, is the most widely used and advanced design for solving the challenge of nuclear fusion [22]. A schematic structure of a tokamak is shown in Fig. 1.2 and it typically has a donut-like shape. In general, the construct consists of a toroidal vacuum chamber and two magnetic fields B that together give rise to screwed field lines. The toroidal coordinate ϕ is the coordinate along the long circumference of the torus and the toroidal magnetic field B_t is generated externally by coils. The poloidal coordinate θ can be seen in a cross section in the $xy-$plane and corresponds to the coordinate along the short circumference of the tours. The poloidal magnetic field B_pol is induced by a plasma current I_p running in the toroidal direction. Due to the excellent electrical conductivity of a plasma, low voltages are sufficient to generate currents in the MA range, which heat the plasma ohmically. Nonetheless, $B_\mathrm{t} > B_\mathrm{pol}$ holds. In addition to the angular coordinates, the small (r) and the large radius (R) are important in the tokamak geometry. The different types of tokamaks are characterized in particular by their major R_maj and minor plasma radius a_min, as well as by their ratio, the so-called inverse aspect ratio $\varepsilon = a_\mathrm{min}/R_\mathrm{maj}$.

Due to the toroidal axisymmetry of the tokamak, most of the properties and dynamics in the tokamak can be described in the poloidal cross section as shown in Fig. 1.3a, corresponding to a 2D plane for a given fixed toroidal angle. This plane is given by the cylindrical coordinates R and z, where we can introduce other necessary geometric quantities that we will often encounter in this thesis.

As the temperature and density needs to decrease toward the chamber wall, a pressure gradient ∇p is created that is orthogonal to the magnetic field lines. We will see later (Sec. 3.1) that in equilibrium this pressure gradient is given by the current

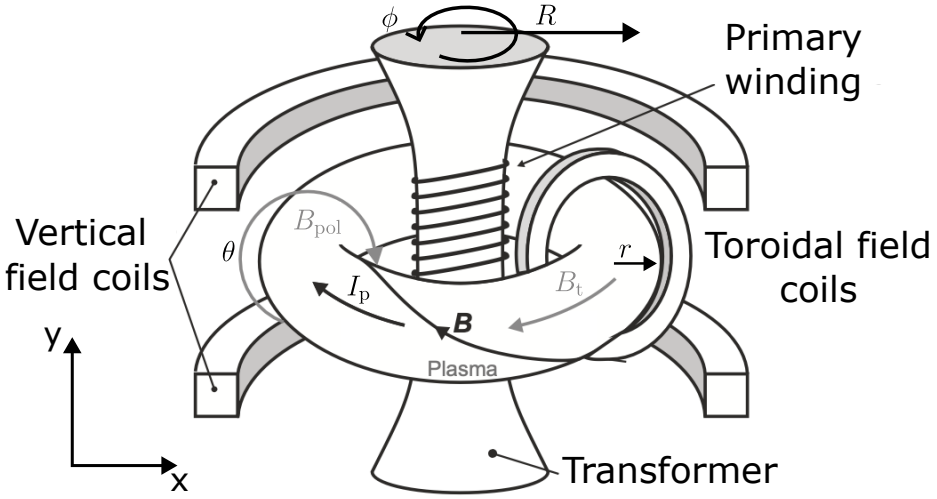

Figure 1.2: Sketch of a Tokamak
The tokamak schematically consists of the superposition of a toroidal (ϕ) magnetic field B_{t}, generated by the toroidal field coils, and a poloidal (θ) magnetic field B_{pol} to form a total magnetic field B. The latter is induced by the plasma current I_{p} generated in the transformer. The radial coordinate of the donut-shaped plasma is determined by the large radius R and the small radius r. Fig. adapted from Ref. [12].

density $\boldsymbol{j}$ and the total magnetic field $\boldsymbol{B}$ as follows [23, 24]:

$$\nabla p = \boldsymbol{j} \times \boldsymbol{B}. \tag{1.4}$$

It follows that the pressure along a magnetic field line is constant, and by introducing the magnetic flux ψ, we observe isobaric concentric magnetic flux surfaces (dashed lines in Fig. 1.3a). These are nested, with the innermost one on the so-called magnetic axis ψ_{a} representing the highest pressure, but decreasing with increasing r. The flux surfaces are closed up to $r = a_{\mathrm{min}}$ (for which the vertical field coils are important), so the last closed flux surface (LCFS) plays a superordinate role and is called the separatrix (ψ_{sep}). The entire area up to the separatrix is called the confined region, and the one beyond that with open field lines is called the scrape-off layer (SOL). To assign a coordinate to these regions, we introduce the normalized poloidal magnetic flux coordinate, i.e.

$$\rho_{\mathrm{pol}} = \sqrt{\frac{\psi - \psi_{\mathrm{a}}}{\psi_{\mathrm{sep}} - \psi_{\mathrm{a}}}} = \sqrt{\psi_{\mathrm{N}}}, \tag{1.5}$$

which denotes the confined region for values between $0 < \rho_{\mathrm{pol}} < 1$, the separatrix for $\rho_{\mathrm{pol}} = 1$ and the SOL for values $\rho_{\mathrm{pol}} > 1$. Sometimes the normalized magnetic flux ψ_{N} is used instead of ρ_{pol}, which are related by the square root as shown in Eq. 1.5. It is interesting to see how temperature and density change with respect to ρ_{pol}, and we

see in Fig. 1.3b and c that these two quantities decrease significantly. The distinction between the red and blue lines in Fig. 1.3b and c will be discussed below. In addition, we see that the separatrix has an X-point at which the field lines (and thus the particles and heat) are directed into the lower region of the configuration, the so-called divertor. Measurements at the divertor can in particular indicate how much particles or heat are being transferred and whether this is acceptable, which we will discuss in more detail in Sec. 2.1. It is also possible to adjust the shape of the plasma as required by the experiment. To describe the geometry of the plasma, the elongation [12]

$$\kappa_{\mathrm{geo}} = \frac{b}{a_{\mathrm{min}}}, \tag{1.6}$$

where b is half of the vertical distance between the highest and lowest point of the

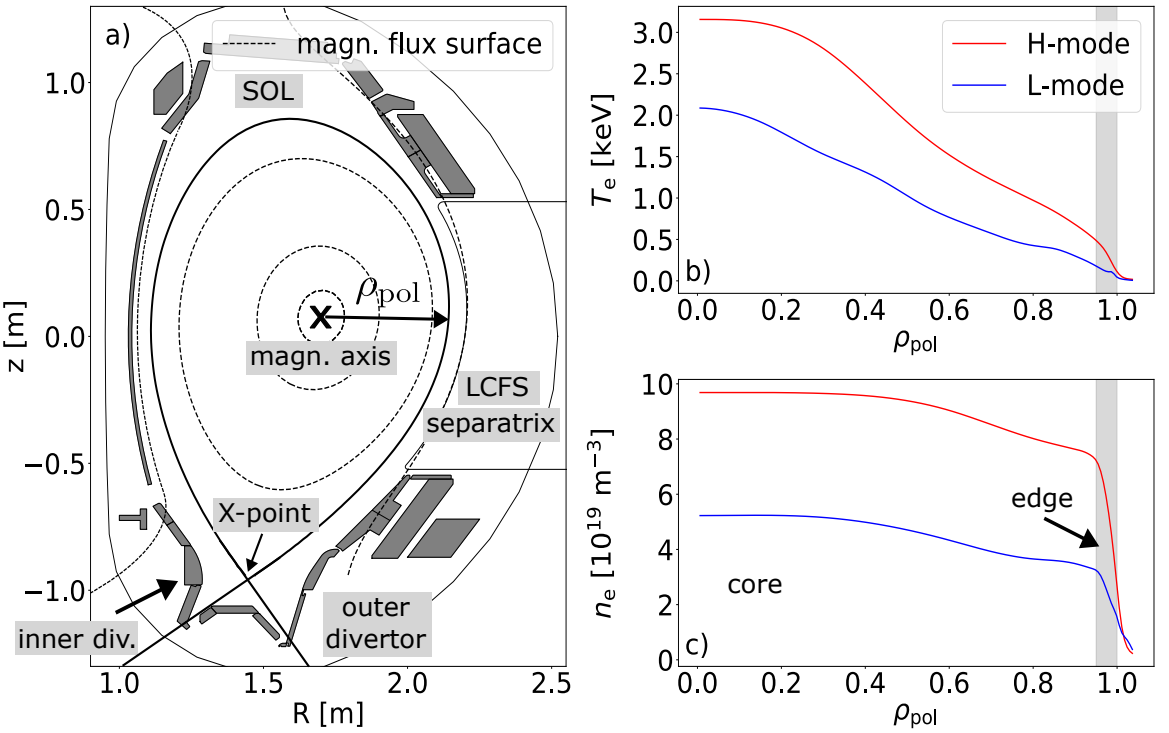

Figure 1.3: Poloidal Cross Section and Profiles for L- and H-Mode
(a) From the poloidal cross section of the tokamak plasma (discharge #39510, t = 3.8 s) the geometric quantities of the plasma are shown. The coordinate ρ_{pol} can be derived from the magnetic flux surfaces (dashed) where the same pressure prevails. The last closed flux surface (LCFS) is called the separatrix, has an X-point and leads the field lines into the divertor. Outside the separatrix is the scrape-off layer (SOL). The electron temperature T_e (b) and density n_e (c) decrease along ρ_{pol}, with the high confinement mode (H-mode, red, #36300 and t = [3.6 s, 3.7 s]) generally having higher T_e and n_e than the low confinement mode (L-mode, blue, #34918 and t = [3.0 s, 3.1 s]). The edge of the plasma is highlighted in gray and is the region where steep gradients occur.

LCFS, and the triangularity [25]

$$\delta = \frac{2R_{\text{geo}} - R_{\text{u}} - R_{\text{l}}}{2a_{\text{min}}} \tag{1.7}$$

are used. R_{geo} is the radial position of the midpoint within the LCFS along the magnetic axis, and R_{u} and R_{l} are the radial positions of the highest and lowest (i.e. X-point) vertical point of the LCFS, respectively.

Furthermore, the plasma in tokamaks lasts a few seconds, and we speak of single discharges, which are displayed as *#number* and whose time development we will analyze in the next section.

A long time sufficiently high temperatures and densities could not be achieved and the confinement was too low, which is why this regime is called the low-confinement mode (L-mode). However, experiments have shown that with sufficiently high induced heating power, the plasma changes its behavior and a better, higher confinement is possible, and the regime is called the high-confinement mode (H-mode) [26]. The H-mode has typically a two times better thermal insulation than the L-mode and, thus, fusion temperatures and densities can be much easier achieved in H-mode. Therefore, the H-mode is considered to be an attractive plasmas regime for a fusion reactor. The difference between L- and H-mode and its issues will be explained in more detail in the next section.

1.3 High Confinement Mode Without Type-I Edge Localized Modes

Time traces of the most important plasma quantities to describe a discharge are shown for a typical L-mode in Fig. 1.4 as the red line and a typical H-mode as the blue line.

First, the applied power P_{aux} is shown in Fig. 1.4a and we can see that the H-mode requires significantly higher heating power. Next, we see the line-integrated density at the plasma core $\overline{n}_{\text{e}}^{\text{core}}$ in Fig. 1.4b, which is measured by interferometry [27]. The H-mode is characterized by much higher density values. Similarly, the energy stored in the plasma W_{MHD} from Fig. 1.4c is calculated as the product of density, temperature and the plasma volume. If we know the behavior of the density, W_{MHD} gives us information about the temperature, which is significantly higher in the H-mode. Finally, the divertor current I_{div} is presented in Fig. 1.4d, which gives information about how many particles and energy arrive at the divertor [28], as described in Sec. 2.1, the less particles and heat is transferred to divertor tiles the better. We see that I_{div} in the L-mode fluctuates around zero. The H-mode, on the other hand, shows strong spikes in I_{div}, indicating that particles and heat are transferred to the divertor

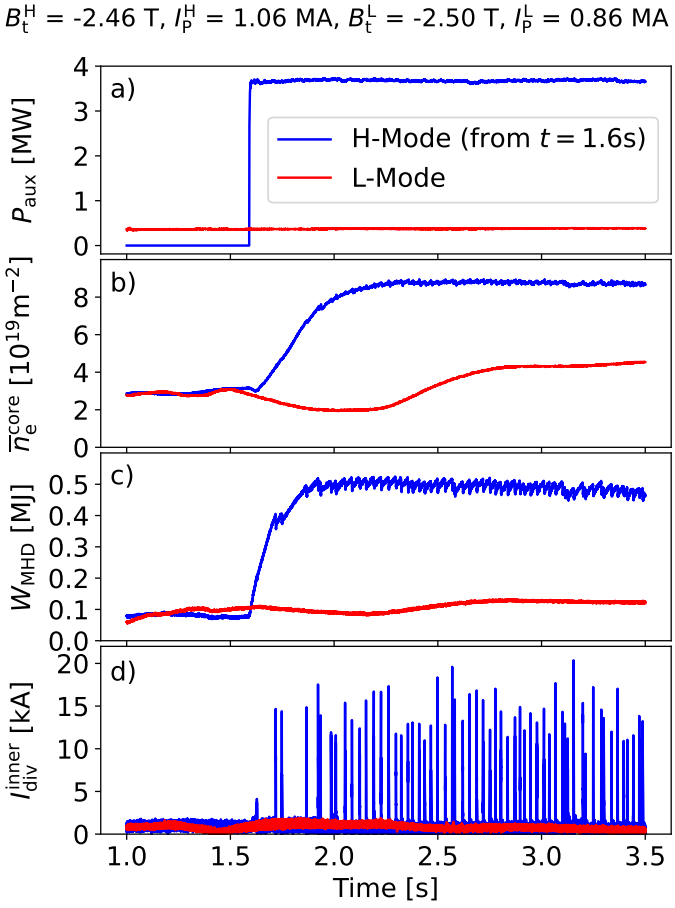

Figure 1.4: Time Series of Typical L- and H-Mode Discharges
The time evolution of the power of the auxiliary heating P_{aux} a), the line-integrated electron density in the plasma core $\overline{n}_e^{core}$ b), the energy stored in the plasma W_{MHD} c), and the current at the inner divertor I_{div}^{inner} d) of a classical L-mode (#34918 in red) and an H-mode (#36300 in blue) are shown. The H-mode becomes established after about $t = 1.6$ s, and at the same time strong bursts in the divertor current appear, indicating type-I edge localized modes (ELMs).

in a regular manner with an almost constant frequency. The bursts are very large and are caused by an instability that occurs in the 'classical' H-mode, the so-called type-I edge localized modes (ELMs). Therefore, this kind of H-mode is also called ELMy H-mode.

In general, instabilities occur when large gradients are involved [12], which can be clearly seen at the plasma edge in the H-mode (see Fig. 1.3b, c). It has been shown that type-I ELMs transfer about $5 - 10\%$ of the energy stored in the plasma to the divertor and plasma facing components (PFCs) [29], which is unacceptable in future large fusion devices such as ITER and can damage the divertor or the PFCs. So we are at a crossroad where we want to ensure the enhanced energy and particle confinement of the H-mode, but need to avoid the type-I ELMs. Fortunately, there are already

anticipated solutions for this endeavor: the so-called type-I edge localized mode free regimes. We will see that phases without type-I ELMs are always accompanied by the appearance of a more or less coherent oscillation at the plasma edge, a so-called edge mode. These edge modes are caused by edge instabilities. Therefore, it is reasonable to assume that these edge modes might be the cause of the ELM freedom. And it is precisely the task of this work to investigate these edge modes in various plasma regimes and to check whether these really ensure that the type-I ELMs do not appear.

1.4 Structure of the Thesis and Key Questions

As described above, we want to investigate plasma scenarios without type-I edge localized modes (ELMs) and study the edge modes occurring there as precisely as possible in order to identify their underlying instability. Only then we can use theoretical models and simulations to determine whether these regimes also occur in reactor plasmas.

However, before we will examine concrete scenarios without type-I ELMs, we will first clarify in Chapter 2 *what requirements have to be met for a future reactor scenario and then present four promising ELM-free regimes in detail and discuss if they are reactor relevant.* The types of edge instabilities, *how they can provide the absence of ELMs*, and *what measurable quantities we need to be able to assign the experimental edge fluctuations to the theoretically described instabilities* are presented in Chapter 3. Chapter 4 shows the experimental setup, the crucial diagnostics with a focus on the thermal helium beam spectroscopy, and the data analysis tools and clarifies the question *whether and to what extent we can reliably analyze edge modes by means of this diagnostic.* In Chapters 5, 6 and 7 we then present and discuss the experimental results on the edge fluctuations, with the aim of determining *whether they can be attributed to an underlying instability from Chapter 3, and whether the edge modes can really cause the absence of type-I ELMs.* Chapter 5 deals with the quasi-coherent mode in enhanced D_α high confinement modes (EDA H-mode) and quasi-continuous exhaust plasmas (QCE), Chapter 6 with the precursor mode in the I-phase scenario, and Chapter 7 summarizes the results on the weakly coherent mode in the improved energy confinement mode (I-mode). Finally, Chapter 8 summarizes all the questions and tasks just posed and gives an outlook on possible future research questions.

2 Type-I Edge Localized Mode Free Regimes and Reactor Relevance

Before discussing the possible reactor-relevant confinement regimes, it is first necessary to clarify which parameters and which characteristics a plasma regime must fulfill in order to be called 'reactor-relevant'. This is followed by a phenomenological description of the ELM-free regimes using discharges on ASDEX Upgrade (AUG). Finally, there will be an evaluation of the scenarios presented with regard to reactor relevance and the variables presented in Sec. 2.1 will be compared with the target values for the DEMO reactor.

2.1 Requirements for Reactor Scenarios

As already stated in the beginning of this work, the first long-term goal of the fusion research community is to achieve a positive power balance in a future fusion reactor. The condition for this endeavor is to sustain fusion-relevant plasma conditions only through $\alpha-$particle heating, that originate from the fusion process, portrayed in Eq. 1.2. The fusion reaction shows that in addition to the neutron, which is not affected by the magnetic fields, a charged helium nucleus ($\alpha-$particle) is created, which is immediately decelerated in the plasma, heating the plasma. Thus, the plasma continues to heat itself and maintain the temperature, which is also known as $\alpha-$particle heating [12]. The point, at which this positive energy balance is achieved, is called ignition and is described by the Lawson criterion [30], using the triple product as the characterizing quantity, i.e.

$$n_\mathrm{e} T_\mathrm{e} \tau_\mathrm{E} \gtrsim 3 \cdot 10^{21}\,\mathrm{keV\,s\,m^{-3}}, \tag{2.1}$$

where n_e is the electron density, T_e is the electron temperature and τ_E is the energy confinement time. For this equation, the approximation $T_\mathrm{e} \approx T_\mathrm{i}$ with T_i as the ion temperature has been used. The distinction between electrons and ions, especially their temperatures T_e and T_i, respectively, is an important topic. However, in a large future reactor, the approximation $T_\mathrm{e} \approx T_\mathrm{i}$ is justified because τ_E should be sufficiently large [31] to allow electrons and ions to thermally equilibrate.

In order to reach these high temperatures and reduce the requirements of Eq. 2.1, external auxiliary heating power P_{aux} is required. One option is neutral beam injection (NBI) [32], with which - as the name suggests - high-energetic neutral particles are injected into the plasma and ionized by collisions with the plasma particles. As a result, these particles are also bound to the magnetic field and heat the plasma by collisional deceleration. This also drives the rotation of the plasma, which can lead to new phenomena, as we will see in Sec. 2.2. The second method is to heat the plasma by radiating high-frequency waves with a frequency close to the cyclotron frequency of the ions (ion cyclotron resonance heating, ICRH) [33] or electrons (ECRH) [34] to take advantage of the resonance phenomenon.

The fusion gain Q is therefore defined as

$$Q = \frac{P_{\text{fus}}}{P_{\text{aux}}}, \tag{2.2}$$

quantifying how the plasma performs in terms of fusion power production for a given input power. Intuitively, one would expect that a value of $Q \geq 1$ would be sufficient to show that fusion works in principle. However, there are requirements for the $Q-$factor for economic viability, whereby the general rule is: the higher the Q, the better. A value of $Q = 22$ is considered to be required that a nuclear fusion reactor produces power [35]. To date, the highest Q experimentally achieved in magnetic confinement fusion is $Q = 0.67$ at the Joint European Torus (JET) facility [36] and ITER should show $Q = 10$ [20].

At the plasma control level, it is possible to adjust various parameters such as the shape of the plasma, the heating methods, the heating power, the amount of gas pumped into the vessel and many more. By a suitable choice of these control parameters, certain (dimensionless) physical parameters, which will be presented below, should be achieved. These desired physical parameters can be achieved by different approaches, which are categorized as plasma scenarios or regimes.

In the following, important parameters and conditions are introduced for the evaluation of various plasma scenarios with regard to their reactor relevance. All of the parameters are dimensionless in order to enable extrapolations to future experiments like ITER [37] and DEMO [38].

Energy Confinement $H_{98\text{y}2}$

The energy confinement is characterized by the energy confinement time $\tau_{\text{E}} = W_{\text{pl}}/P_{\text{loss}}$, representing the typical time it takes to lose the plasma energy content W_{pl} through the power loss P_{loss}. The power loss is usually described by the heating power, since, in equilibrium, the total power loss is balanced by the input heating power. The

normalized quantity

$$H_{98y2} = \frac{\tau_E}{\tau_{E,IPB98(y,2)}} \tag{2.3}$$

compares the experimental confinement times τ_E with the empirical scaling $\tau_{E,IPB98(y,2)}$, derived from a multi-machine database. The empirical scaling is given by [39]

$$\tau_{E,IPB98(y,2)} = 0.0562 I_p^{0.93} B_t^{0.15} P_{loss}^{-0.69} \overline{n}_e^{-0.41} m_i^{0.19} R_{maj}^{1.97} \varepsilon^{0.58} \kappa_{geo}^{0.78}, \tag{2.4}$$

where I_p is the plasma current in MA, B_t is the toroidal magnetic field strength in T, $\overline{n}_e$ is the line-averaged electron density in $10^{19}\mathrm{m}^{-3}$, m_i is the average ion mass in u, R_{maj} is the major radius in m, $\varepsilon = a_{min}/R_{maj}$ is the inverse aspect ratio with a_{min} as the minor radius and κ_{geo} is the elongation.

For a reactor scenario, a value of $H_{98y2} \geq 1$ is desirable, although it has proven difficult to obtain values much higher than one, as the highest value measured was $H_{98y2} \approx 1.7$ in a stationary plasma [40].

Plasma β_N

Apart from the confinement time, as discussed, the two factors of the triple product (see Eq. 2.1) can be combined to the electron pressure, as $p_e = n_e k_B T_e$. To obtain a dimensionless quantity, the electron pressure is usually normalized to the magnetic field pressure, containing the toroidal and poloidal magnetic field strengths, i.e. $B = B_t + B_{pol}$, and is defined as

$$\beta = \frac{p_e}{B^2/(2\mu_0)} \tag{2.5}$$

with μ_0 as the vacuum permeability. The plasma β is a crucial factor as it provides information about the stability of a plasma. Typically, β needs to stay below the Troyon limit [41] for a stable plasma, which has been discovered via ideal magnetohydrodynamic (MHD) numerical studies and depends on several factors, e.g. the plasma shape. We will deal with the corresponding dimensionless restriction of the Troyon-normalized beta, i.e.

$$\beta_N = 100 \frac{\beta}{I_p/(a_{min} B_t)} \leq 3. \tag{2.6}$$

Despite this limitation, the plasma beta should be as high as possible, as this automatically leads to a high triple product. For example, EU-DEMO aims for $\beta_N = 2.6$ [42].

Safety Factor q_{95}

Another quantity, displaying the stability of a plasma against current-driven instabilities (Sec. 3.1.3 and 3.2.6) is the safety factor q. Generally, q is defined as

$$q = \frac{\text{number of toroidal orbits}}{\text{number of poloidal orbits}} \text{ of one magnetic field line.} \tag{2.7}$$

Using the cylindrical approximation, the safety factor can be represented as

$$q \approx \frac{rB_\mathrm{t}}{RB_\mathrm{pol}}. \tag{2.8}$$

The safety factor varies along the radial axis, since it depends on the outer (R) and inner radial position (r). When approaching the separatrix, q diverges, which is why the safety factor is typically evaluated at $\rho_\mathrm{pol} = 0.95$ and is named q_{95}. The Kruskal-Shafranov limit [43, 44] indicates an upper limit for the plasma current I_p. Above this maximum value, a disruption occurs. This is an event in which the entire current gets lost on a very short timescale, exerting a strong force on the fusion device, which must be strictly avoided. Due to the fact that the poloidal magnetic field is proportional to the plasma current I_p at the plasma edge, i.e. $q_{95} \propto B_\mathrm{t}/I_\mathrm{p}$, the demand in I_p leads to a restriction in q_{95}. To avoid an increased likelihood of disruptions or other plasma instabilities, the common requirement is: $q_{95} \geq 3$. However, q should not be too large because for this I_p must be very small, which in turn results in a shorter confinement time (see Eq. 2.4). Therefore, values close to the limit are desired.

Greenwald Fraction f_GW

In order to approach the criterion in Eq. 2.1, one can increase the density n_e, but unfortunately, a disruption and radiation collapse will occur, if the line-averaged edge density $\overline{n}_\mathrm{e}$ exceeds a certain value: the Greenwald density n_GW, named after its discoverer [45]. n_GW was empirically determined by the analysis of a huge data set at various tokamaks and is given by a simple expression, just depending on I_p and the poloidal plasma cross section area. The normalized Greenwald fraction, including the experimentally achieved densities, should fulfill the following condition for a reactor-relevant scenario:

$$f_\mathrm{GW} = \frac{\overline{n}_\mathrm{e}}{n_\mathrm{GW}} = \frac{\overline{n}_\mathrm{e}}{I_\mathrm{p}/\left(\pi a_\mathrm{min}^2\right)} \leq 1. \tag{2.9}$$

However, in order to keep the triple product high, we should operate close to this limit.

Pedestal Top Collisionality $\nu^{\star}_{\mathrm{ped}}$

In addition to the density, the temperature T_{e} can also be increased to enhance the triple product (Eq. 2.1). The dimensionless parameter that describes T_{e} is the collisionality $\nu^{\star}$, since it has a strong dependence on T_{e}. $\nu^{\star}$ has its origin in the neoclassical theory: Due to the magnetic mirror effect [12] and a decreasing magnetic field towards the outer side of the torus - resulting in a gradient in the magnetic field strength ∇B - a part of the particles is trapped and moves on banana-shaped orbits in the poloidal plane. The collisionality $\nu^{\star}$ is defined as the number of collisions a particle experiences in the time it takes to complete one banana orbit. Additionally, it quantifies the importance of collisions, and thus the importance of neoclassical transport mechanisms [46]. In this work, the following definition for the electron collisionality is used [47]

$$\nu^{\star}_{\mathrm{e}} = 6.923 \cdot 10^{-18} \frac{q_{95} R_{\mathrm{maj}} n_{\mathrm{e}} Z_{\mathrm{eff}} \ln \Lambda}{T_{\mathrm{e}}^{2} \varepsilon^{3/2}}, \tag{2.10}$$

where $Z_{\mathrm{eff}} = \sum_i n_{\mathrm{i}} Z_{\mathrm{i}}^2 / n_{\mathrm{e}}$ is the effective ion charge for all ion densities n_{i} and charges Z_{i}, and $\ln \Lambda = 31.3 - \ln\left(\sqrt{n_{\mathrm{e}}}/T_{\mathrm{e}}\right)$ is the Coulomb logarithm, also depending on n_{e} and T_{e}. Both, n_{e} and T_{e} are varying strongly along the radial axis, but we aim for a low $\nu^{\star}_{\mathrm{e}}$ in the plasma core, i.e. high T_{e}, which results in a low collisionality at the pedestal top area (at $\rho_{\mathrm{pol}} \approx 0.95$). Thus, we determine the collisionality in this region, and use $\nu^{\star}_{\mathrm{ped}} \leq 0.1$ as an approximate criterion [48].

Detachment

In addition, there are steady-state heat fluxes entering the divertor that are too strong for the divertor tiles to withstand long enough. Thus, additional dissipation channels must be created to reduce the energy and momentum of the plasma near the divertor. At an electron temperature below $T_{\mathrm{e}} < 1\,\mathrm{eV}$, recombination processes between electrons and ions become possible again and the plasma is completely decoupled from the divertor. This is called complete detachment [12]. Divertor detachment leads also to reduced ion particle flux and plasma temperature in the divertor region [49, 50]. It is only possible if the plasma density in the scrape-off layer (SOL) and the impurity radiation loss is sufficiently high.

H-Mode Power Fraction f_{LH}

As described in Sec. 1.3 the transition between L- and H-mode was achieved by exceeding a certain threshold of input power in the fusion system. This L-H power threshold has been determined by means of a multi-machine data base and resulted in the scaling

law [51]

$$P_{\mathrm{LH}} = 0.049 \overline{n}_{\mathrm{e}}^{0.72} B_{\mathrm{t}}^{0.8} S^{0.94}, \tag{2.11}$$

where S is the plasma surface, which approximately scales as $S \propto R_{\mathrm{maj}}$. The power crossing the separatrix P_{sep} should be at least as large as the L-H power threshold, i.e. $P_{\mathrm{sep}} \geq P_{\mathrm{LH}}$ to ensure that the plasma stays in H-mode despite potential radiation losses P_{rad} [52]. The power crossing the separatrix is defined as $P_{\mathrm{sep}} = P_{\mathrm{Ohm}} + P_{\mathrm{aux}} - P_{\mathrm{rad,c}} - dW_{\mathrm{pl}}/dt$, in which all the auxiliary heating powers P_{aux}, the Ohmic power P_{Ohm} and the core (inside separatrix) radiation power $P_{\mathrm{rad,c}}$ are included. The parameter, rating how close we are to the H-mode is given by

$$f_{\mathrm{LH}} = \frac{P_{\mathrm{sep}}}{P_{\mathrm{LH}}}. \tag{2.12}$$

A value of $f_{\mathrm{LH}} > 1$ means that we are above the H-mode power threshold.

It is therefore desirable to operate with margin above P_{LH}, although care must be taken not to put too much power into the system, otherwise the divertor will overheat. This interplay leads to a compromise, which was chosen to be $f_{\mathrm{LH}} \approx 1.2$ [31].

Other Remarks

There are other parameters to evaluate the performance of specific plasma scenarios. For instance, it is required that the effective ion charge Z_{eff} should be as low as possible, as it is proportional to the radiation losses due to Bremsstrahlung in the plasma [53]. Another aspect is the usage of the heating mechanism. As it was stated in the beginning that the plasma in a reactor will mainly be heated by $\alpha-$particles. Therefore, it is advisable to imitate this kind of heating, which is dominantly heating electrons, and to not put too much torque, e.g. via NBI heating, into the system.

2.2 Confinement Regimes Without Type-I Edge Localized Modes

Some of the desired properties just mentioned are fulfilled by the classical ELMy H-mode introduced in Sec. 1.3, but this scenario is accompanied by type-I edge localized modes (ELMs), which is an exclusion criterion for operation on the future fusion reactor. Hence, it is necessary to operate future fusion reactors in the high-confinement mode (H-mode) without evoking type-I edge localized modes (ELMs). Currently, there are two favoured possibilities to avoid ELMs in H-mode, i.e. by the usage of

i) active ELM control techniques in order to mitigate or suppress ELMs [54], or

ii) natural type-I ELM-free operation scenarios.

The first case is achieved by using e.g. resonant magnetic perturbation coils (RMPs) [55]. As their name suggests, the RMPs perturb the magnetic field at the plasma edge, in order to obtain either ELM mitigation, i.e. smaller, but more frequent ELMs or complete ELM suppression.

In the scope of this thesis, we will focus on the second case, i.e. natural ELM-free plasma regimes. The term 'ELM-free' means type-I ELM-free, other ELM-like instabilities are generally tolerated. Type-II ELMs are encountered in Sec. 2.2.2 and are often referred to as grassy ELMs and cause an acceptable heat load on the divertor plates. Type-III ELMs have even smaller amplitudes and will be discussed in more detail in Chapter 6.

Meanwhile, there are several natural ELM-free regimes, which are established in various international fusion experiments and there are numerous review papers like Ref. [48]. Table 2.1 summarizes the ELM-free scenarios regarding their operational access condition and present edge fluctuations. By comparing Table 2.1 with the criteria from Sec. 2.1, we see that the quiescient high confinement mode (QH-mode) does not seem to be relevant for a fusion reactor as it typically needs high rotation and counter-injected neutral beam heating, which both is difficult to be realized in a fusion reactor. As mentioned above, RMPs are not part of this work and the negative triangularity discharges (NT) have not yet been included in the subsequent analyses. The X-point radiator regime (XPR) will be discussed briefly at the end of this chapter, but it does not appear to have any edge fluctuation so far. Thus, the first four ELM-free regimes of Table 2.1 are of the utmost importance in the context of this thesis.

Table 2.1: Summary of ELM-free Regimes

All type-I ELM-free plasma scenarios are shown with their access condition, corresponding edge fluctuation and references.

Scenario	Access Condition	Edge Fluctuation	References
EDA H-mode	high shaping	QCM	[56, 57]
QCE	high shaping	small ELMs + QCM	[58–60]
I-phase	LH-transition	LCO + Precursor	[61–63]
I-mode	unfavorable ∇B	WCM	[64, 65]
XPR	seeding	?	[66, 67]
QH-mode	high rotation	EHO	[68, 69]
Negative δ	$\delta < 0$	No fluctuation	[70]
RMP	$n = 2$ MP	3D	[71]

The following section contains a phenomenological description of the enhanced D_α high confinement (EDA H-mode), quasi-continuous exhaust regime (QCE), the intermediate phase (I-phase) between L- and H-mode and the improved energy confinement

mode (I-mode) using discharges on ASDEX Upgrade (AUG). A detailed description of the present edge fluctuations in each scenarios can be found in Chapter 5 for the EDA H-mode and QCE, Chapter 6 for the I-phase and in Chapter 7 for the I-mode.

2.2.1 Enhanced D_α High Confinement Mode (EDA H-Mode)

The enhanced D_α high confinement mode, abbreviated as EDA H-mode in the following, is a natural ELM-free H-mode-like regime first discovered in Alcator C-mod in 1998 [56]. It was first achieved by using ion cyclotron resonance heating (ICRH) only. Greenwald *et al.* named the scenario due to its characteristic amount of D_α radiation produced in these kind of discharges. A notable accomplishment in an EDA H-mode was the achievement of a world-record volume-averaged core plasma pressure ever [72]. After the successful operation of the EDA H-mode in Alcator C-Mod, other fusion experiments like DIII-D [73, 74] and the Experimental Advanced Superconducting Tokamak (EAST) [75] were able to implement this regime. DIII-D used neutral beam injection as their main core heating. EAST used lower hybrid wave (LHW) heating [76]. In 2018, it was possible to reproduce this scenario in ASDEX Upgrade (AUG). At first only with electron cyclotron heating (ECRH) heated plasmas [57], it is now accessible under various circumstances. Typically, high fueling is used for this scenario, and it is characterized by high collisionality and features safety factors of $q_{95} \geq 3$. EDA H-modes can be operated in various magnetic field strengths of $1.8\,\mathrm{T} \leq B_\mathrm{t} \leq 7.8\,\mathrm{T}$ and are independent of the used heating mechanism, as it was possible to produce purely Ohmic ones [77] without any torque. Operationally, the EDA H-mode is achieved in favorable ∇B drift direction at high triangularity ($\delta \geq 0.3$) and elongation ($\kappa_\mathrm{geo} \geq 1.65$). The operation close to double null allows a broader input power window for the regime, showing the importance of the plasma shaping. Though, if the edge ∇p_e becomes sufficiently large, small or even type-I ELMs will return.

Time traces of various quantities for a typical EDA H-mode in AUG are shown in Fig. 2.1. The plasma starts in the L-mode and is heated with a gradually increasing ECRH (Fig. 2.1a). At $t = 3.3\,\mathrm{s}$ the plasma stored energy, W_MHD, and the line-integrated density in the core and edge $\overline{n}_\mathrm{e}$ rise rapidly (Fig. 2.1b), marking the transition to the H-mode. A good confinement, $H_\mathrm{98y2} \approx 1$, emphasizing the H-mode behavior, a Greenwald fraction of $f_\mathrm{GW} \approx 0.8$ and a Troyon-normalized plasma pressure of $0.8 \leq \beta_\mathrm{N} \leq 1.5$ can be seen (Fig. 2.1c). Additionally, the H-mode power fraction shows values of $0.5 \leq f_\mathrm{LH} \leq 0.9$. Despite the H-mode properties of the discharge, the shunt current signals in the inner and outer divertor do not exhibit major events (Fig. 2.1d), thus type-I ELMs are absent. Simultaneously, one single and coherent fluctuation with a frequency f_QCM, evolving between 15 kHz and 24 kHz, is present in the spectrogram (Fig. 2.1e) of the thermal helium beam data (cf. Sec. 4.2), measuring fluctuations in

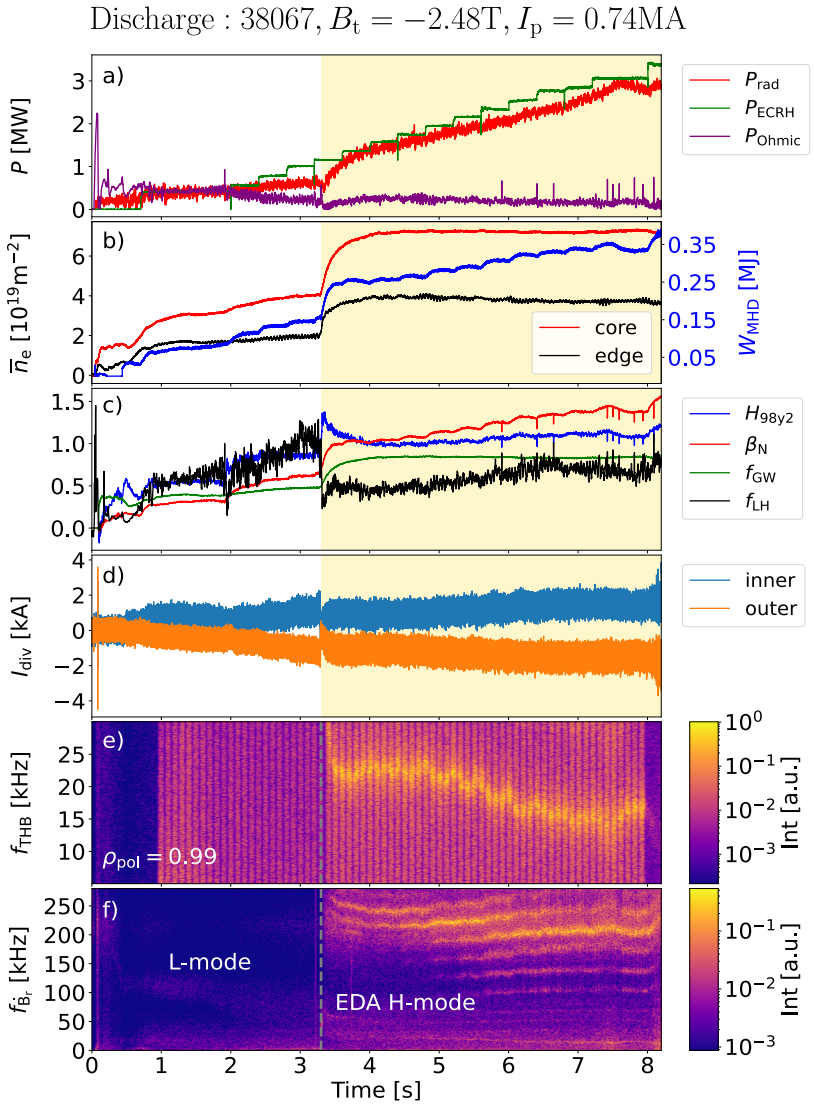

Figure 2.1: Time Traces of an EDA H-mode Discharge
The golden background in a)-d) indicates the EDA H-mode phase. ECR heating, radiated and Ohmic power a), line averaged electron density and plasma energy content b) as well as the dimensionless quantities H_{98y2}, β_N, f_{GW} and f_{LH} c) are shown. No major events are visible in the divertor shunt currents d), but simultaneously the quasi-coherent mode appears in the measurements of the thermal helium beam e) and other higher harmonic modes appear in the radial component of the magnetic signal f).

$\tilde{T}_e$ and $\tilde{n}_e$ at the plasma edge (in this case at $\rho_{pol} = 0.99$). This fluctuation is called the quasi-coherent mode, abbreviated as QCM hereinafter, which is the most characteristic feature of EDA H-mode discharges [57, 77–80]. As will be shown in Sec. 5.1, the QCM is also visible in the signal of magnetic pick-up coils, measuring radial magnetic field fluctuations $\dot{B}_r$ (see Sec. 4.3). In addition, higher harmonic modes (HHMs) can be observed in the magnetic coils during the EDA H-mode [81].

2.2.2 Quasi-Continuous Exhaust (QCE)

The quasi-continuous exhaust regime (QCE), former known as the small ELM or type-II ELM regime, has been established across many fusion devices like AUG [59, 60, 82], TCV [83], JET [58], DIII-D [84], EAST [85] and JT60-U [86]. The scenario is type-I ELM free and features safety factors around $q_{95} = 3$, low pedestal top collisionality and no high-Z impurity accumulation. Typically, QCE discharges show enhanced rotation and an outward impurity convection.

As its former name already suggests, the characteristic of the QCE is the appearance of reduced ELM energy losses, small ELM amplitudes and a higher ELM frequency, i.e. type-II ELMs, compared to type-I ELMs. At AUG it has been determined that a high separatrix density $n_{\mathrm{e,sep}}$ is a necessity in order obtain small ELMs and not evoke type-I ELMs [87]. The high $n_{\mathrm{e,sep}}$ is characteristic for QCE discharges and is achieved by a high fueling rate. Moreover, the higher $n_{\mathrm{e,sep}}$ correlates with a significantly higher power fall-off length λ_{q} compared to e.g. EDA H-modes [88]. λ_{q} corresponds to the width of the heat flux channel that is directly connected to the divertor target plates [89]. Operationally, a similar plasma shape as for the EDA H-modes (see Sec. 2.2.1), i.e. high triangularity ($\delta \geq 0.3$) and elongation ($\kappa_{\mathrm{geo}} \geq 1.65$), is another requirement for this kind of discharges. Generally, QCE discharges are similar to EDA H-modes in AUG, except for the fact that a higher $n_{\mathrm{e,sep}}$ is achieved and many small ELMs are present. Furthermore, in the QCE scenario, filaments [90] are discharged continuously and without interruption, which is why the term 'continuous exhaust' is used. A detailed description of the differences between EDA H-modes and QCE discharges is presented in Sec. 5.6.

In Fig. 2.2 the time evolution of a QCE discharge in AUG is displayed. The discharge is operated via NBI and ICRH heating (Fig. 2.2a) and enters the H-mode at around $t = 1.8\,\mathrm{s}$. One can clearly see the increase in W_{MHD} and $\overline{n}_{\mathrm{e}}$ (core and edge) in Fig. 2.2b. Moreover, the dimensionless quantities $H_{98\mathrm{y2}} \approx 0.9$, $1.0 \leq \beta_{\mathrm{N}} \leq 1.8$, $f_{\mathrm{GW}} \approx 0.6$ and $f_{\mathrm{LH}} \approx 1.1$ in Fig. 2.2c are in a similar range to those for the EDA H-mode in Sec. 2.2.1. In the beginning of the QCE interval, type-I ELMs can be seen, but after approximately $t = 2.6\,\mathrm{s}$ only small divertor currents can be measured, indicating the appearance of small ELMs (Fig. 2.2d). Again, we observe simultaneously to the absence of the type-I ELMs, a single fluctuation in the thermal helium beam signal (see Sec. 4.2) at a frequency of around $f_{\mathrm{QCM}} = 35\,\mathrm{kHz}{-}68\,\mathrm{kHz}$ (Fig. 2.2e). It will be shown in Chapter 5 that this fluctuation is as well the quasi-coherent mode (QCM). In the magnetic signal (see Sec. 4.3) no higher harmonic modes (HHMs) are visible (Fig. 2.2f). Solely, the QCM is visible in the magnetic signal, albeit barely.

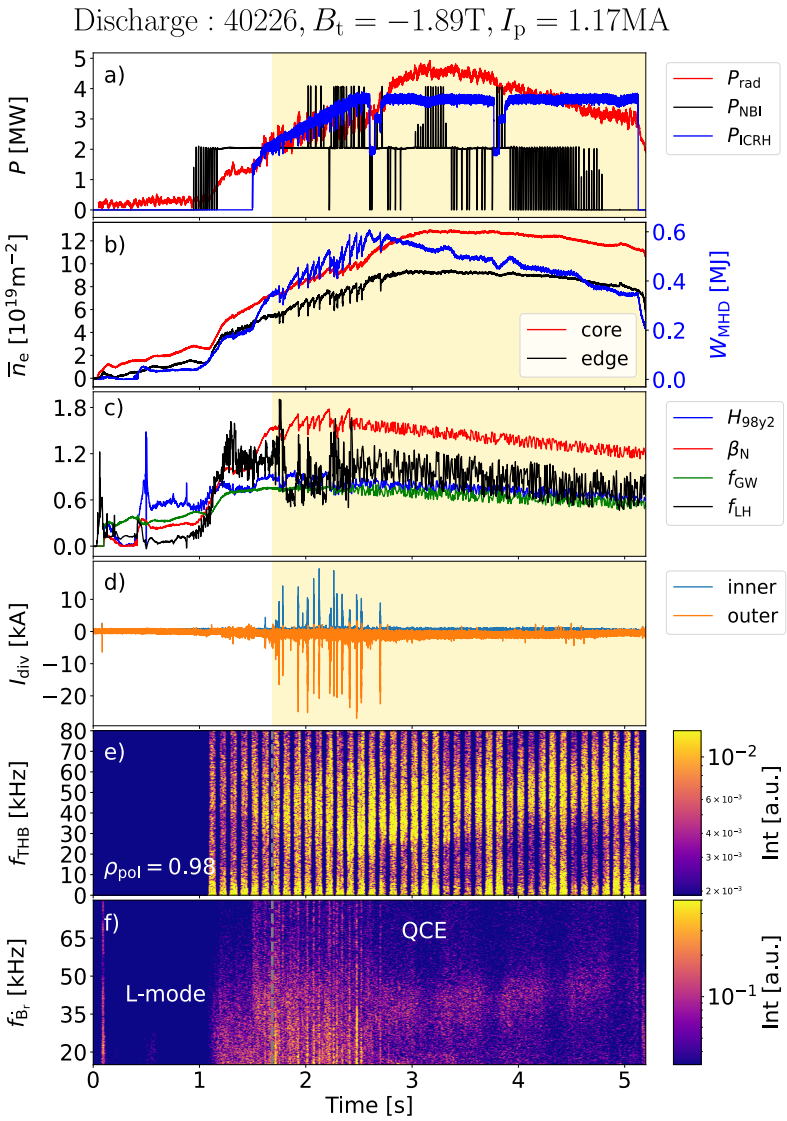

Figure 2.2: Time Evolution of a QCE Discharge

The golden background in a)-d) indicates the QCE. Heating and radiated power a), line averaged electron density and plasma energy content b) as well as the dimensionless plasma quantities H_{98y2}, β_N, f_{GW} and f_{LH} c) are shown. When entering the H-mode phase, type-I ELMs are visible in the divertor current signal, but disappear after $t = 2.6$ s d). Simultaneously, the QCM appears in the thermal helium beam e) and in the magnetic signal f).

2.2.3 Intermediate Phase (I-Phase)

Between the L-mode and fully developed H-mode or vice versa, there is another ELM-free intermediate confinement regime, called I-phase, which can also be operated stationary.

The I-phase is observed at many machines as AUG [63, 91], DIII-D [92], COMPASS [93] and EAST [94]. At JET the I-phase is called M-mode [62], but it has been elab-

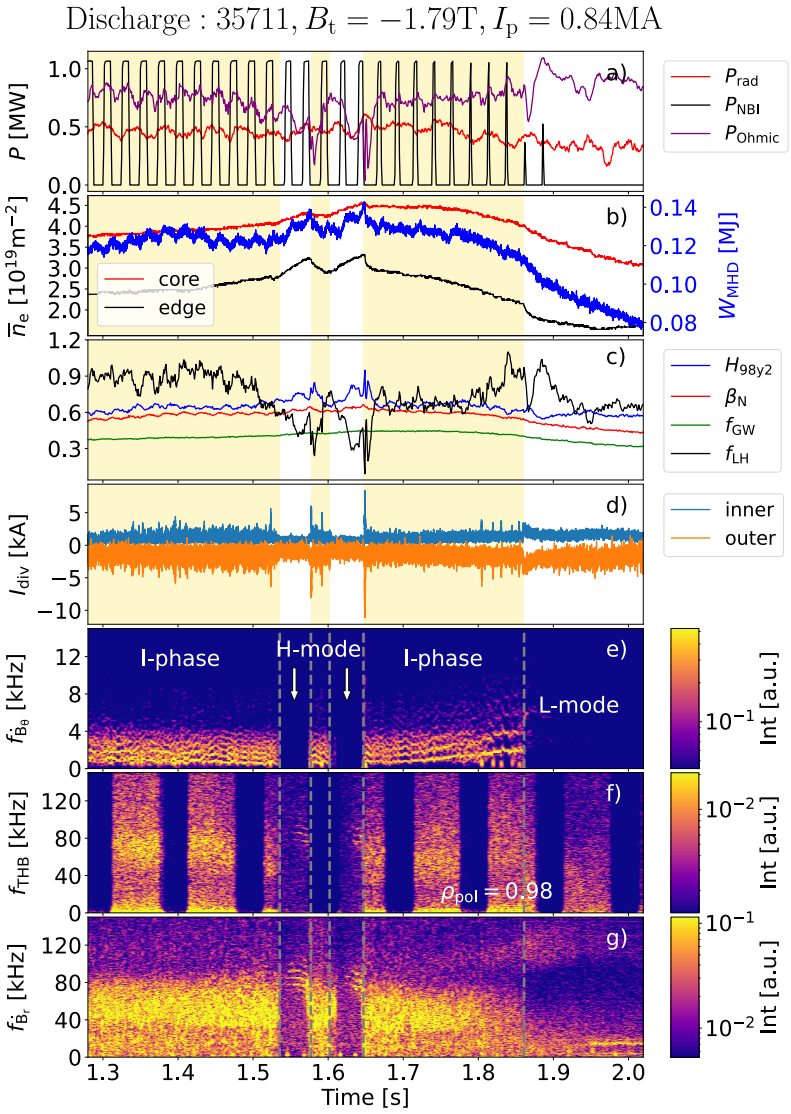

Figure 2.3: Time Traces of an I-Phase Discharge

The golden background in a)-d) indicates the I-phase. Heating, radiated and Ohmic power a), line averaged electron density and plasma energy content b) as well as the dimensionless plasma quantities H_{98y2}, β_N, f_{GW} and f_{LH} c) are shown. The divertor current signals do not exhibit large events d), but simultaneously the limit cycle oscillations appear in the spectrogram of the poloidal magnetic field coils e), as well as the precursor mode in the thermal helium beam f) and radial magnetic coils g).

orated that both scenarios are the same [95]. The I-phase features improved particle and energy confinement compared to the L-mode, but not as pronounced as in the fully developed H-mode regimes like the ELMy H-modes (see Sec. 1.3).

Fig. 2.3 shows a typical I-phase discharge in AUG, in which a transition happens from I-phase to H-mode (I-H) at $t = 1.53$ s and $t = 1.61$ s, H-I at $t = 1.58$ s and $t = 1.64$ s and I-L (I-phase to L-mode) at $t = 1.85$ s. The plasma is heated only with NBI and Ohmic power (Fig. 2.3a). Moreover, the transitions to H-mode or

L-mode are visible in W_{MHD} and core and edge $\overline{n}_{\mathrm{e}}$, presented in Fig. 2.3b. During the I-phase the dimensionless parameters, illustrated in Fig. 2.3c, exhibit values of $0.6 \leq H_{98\mathrm{y2}} \leq 0.7$, $\beta_{\mathrm{N}} \approx 0.55$, $f_{\mathrm{GW}} \approx 0.4$ and $0.6 \leq f_{\mathrm{LH}} \leq 1.0$. The divertor currents show some kind of small ELM behavior during the I-phase (Fig. 2.3d) compared to the L-mode or the (completely ELM-free) H-mode. Only just before the transition to the H-mode or vice versa, a large ELM appears. The most characteristic property of I-phases are the harmonic low frequent fluctuations with frequencies of $f_{\mathrm{LCO}} \leq 5\,\mathrm{kHz}$ (for AUG), which can be observed in the magnetic field coils (cf. Sec. 4.3), measuring deviations of the poloidal magnetic field $\dot{B}_{\theta}$ (Fig. 2.3e) and many other diagnostics. These fluctuations are called limit cycle oscillations (LCOs) [63, 96]. Besides the LCOs, another fluctuation, the so-called 'precursor' mode with $f_{\mathrm{pre}} \approx 70\,\mathrm{kHz}$ is visible in the thermal helium beam (see Sec. 4.2) and in the $\dot{B}_{\mathrm{r}}$ magnetic coils (see Sec. 4.3), shown in Fig. 2.3f and g.

2.2.4 Improved Energy Confinement (I-Mode)

First observed in unfavorable ∇B configuration, i.e. in a configuration with the ion ∇B drift pointing towards the active X-point, the improved energy confinement mode (I-mode) was discovered at ASDEX Upgrade and Alcator C-mod in the late 1990s [97, 98] for all different kind of heating mechanisms and is generally type-I ELM-free. In unfavorable ∇B configurations, a higher power input is necessary to access the H-mode compared to the favorable configuration. Meanwhile, the regime is established at various fusion machines like DIII-D [99] and EAST [100]. The establishment in different machines and hence, different wall materials, indicates that the I-mode can be achieved independent from the used wall material of the tokamak. This type of regime is characterized by L-mode-like particle transport, i.e. n_{e} is as low as in L-modes, and H-mode-like energy confinement, i.e. T_{e} profiles show the same high pedestal top values as in H-modes. Furthermore, good impurity transport properties, thus no impurity accumulation, and the possibility for detachment of the inner divertor [101] in N-seeded plasmas characterize the I-mode.

Fig. 2.4 demonstrates a typical I-mode discharge in AUG. The I-mode is heated via gradually increasing steps of ECRH (Fig. 2.4a). At the second ECRH step ($t = 2.8\,\mathrm{s}$), the plasma enters the I-mode. It is observable that the line integrated densities (edge and core) do not change, but the plasma energy content W_{MHD} does (Fig. 2.4b). This underlines the unique characteristic of enhanced energy, but L-mode-like particle confinement. Hence, $H_{98\mathrm{y2}}$ as well as β_{N} are increased in the I-mode, but the Greenwald fraction remains constant at $f_{\mathrm{GW}} \approx 0.25$. In the discharge shown, the H-mode power fraction increases continuously during the I-mode period with values of $1.2 \leq f_{\mathrm{LH}} \leq 2.4$, shown in Fig. 2.4c. It should be emphasized that the L-H power threshold from

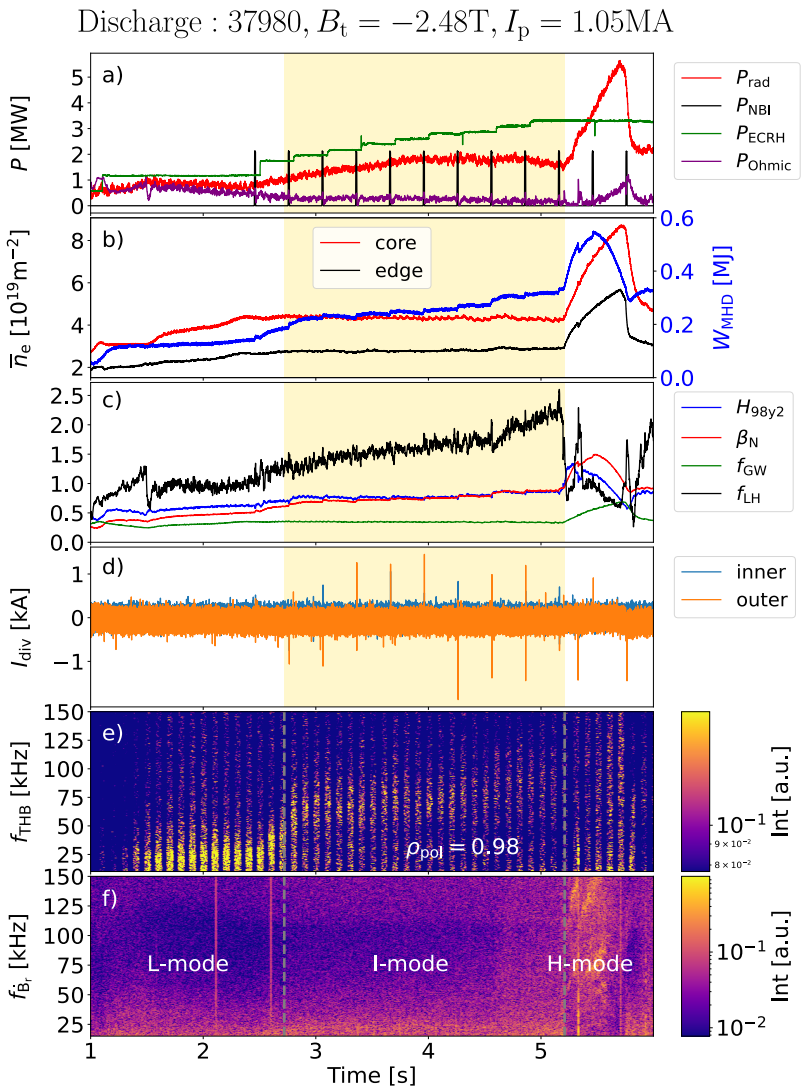

Figure 2.4: Time Traces of an I-Mode Discharge

The golden background in a)-d) indicates the I-mode. Heating, radiated and Ohmic power a), line averaged electron density and plasma energy content b) as well as the dimensionless plasma quantities H_{98y2}, β_N, f_{GW} and f_{LH} c) are shown. No type-I ELMs are detected in the divertor current signals d), but during the I-mode (and before) the weakly coherent mode appears in the signals of the thermal helium beam e). No mode or other activity is visible in the magnetic spectrogram f).

the definition of the H-mode power fraction in Eq. 2.11 applies only to favorable configurations. In general, in unfavorable configuration, which is a prerequisite for the I-mode, the transition from L- to I-mode as well as from I- to H-mode is achieved at higher powers [102]. Accordingly, f_{LH} is not meaningful here and is shown only for the sake of completeness. The divertor signal in Fig. 2.4d shows isolated small peaks, but no type-I ELMs are detected. The thermal helium beam signal (see Sec. 4.2) in Fig. 2.4e measures repeatedly a single fluctuation with $f_{WCM} \approx 70$ kHz during the ELM-free

phase. This fluctuation is called the weakly coherent mode (WCM) [64], named after its broad appearance in the frequency spectrum. It is notable, that the WCM seems to be present even before entering the I-mode, i.e. in the L-mode [103]. The magnetic signal (Sec. 4.3) in Fig. 2.4f does not contain a coherent mode during the I-mode.

2.3 Reactor Relevance of ELM-free Regimes

After having introduced the four plasma regimes relevant for this thesis by means of example discharges at AUG, we will asses their reactor relevance in the following. Tab. 2.2 compares the four presented regimes and the X-point radiator (XPR) regime with the baseline scenario for the future DEMO reactor (DEMO BL). The data was taken from Ref. [48] and references inside, except for the I-phase, XPR and the values of f_{LH}, which have been evaluated for a subset of AUG discharges. The aim is to develop a plasma scenario, that gets as close as possible to the desired DEMO BL parameters (see Sec. 2.1).

First, the EDA H-mode is compatible with almost all requirements for a DEMO scenario. The only value that is far from the desired target value is the pedestal top collisionality $\nu^{\star}_{\mathrm{ped}}$, i.e. the desired temperature at the pedestal top or plasma core seems to be too low. A key factor for a future scenario is the possibility of operating the EDA H-mode close to the L-H transition, i.e. $f_{\mathrm{LH}} \sim 1.2$. Additionally, the access condition is basic, since the plasma only needs to exhibit sufficiently high triangularity and elongation. Together with its low Z_{eff}, the possibility to achieve divertor detachment and no dependence on any specific heating mechanism, the EDA-H mode is a strong candidate for the operation in ITER or DEMO.

The same access condition, i.e. the specific shaping of the plasma, holds for the quasi-continuous exhaust regime. This scenario also fulfills nearly all the conditions from Tab. 2.2 to become a potential DEMO scenario. The desired collisionality $\nu^{\star}_{\mathrm{ped}}$ for DEMO is also not achieved, but it is significantly lower than that for the EDA H-mode. On the other hand, QCE is usually operated well above the L-H transition, i.e. $f_{\mathrm{LH}} \geq 1.4$, enhancing the power heat load on the plasma-facing materials (see Sec. 2.1). Moreover, the separatrix conditions of the QCE regime are strongly compatible with the ones predicted for ITER and DEMO, making it as well a strong scenario candidate for those reactors.

The I-phase requires the operation between the L- and fully developed H-mode, which can be seen from Tab. 2.2 as the H-mode power fraction is around $f_{\mathrm{LH}} \sim 1.0$. A full comparison between the parameters obtained in the I-phase and the desired DEMO BL values indicates that this regime only satisfies the requirement for the safety factors q_{95}, f_{LH} and detachment. Thus, at first sight, the role of the I-phase

does not appear to be important for future reactors. However, it will be considered as possible reactor relevant due to the following context. As mentioned in Sec. 2.1, there is a need to reduce the power-heat load on the divertor plates, or more generally on the plasma-facing components. One way to achieve this is to inject low-Z or medium-Z impurities into the plasma, called seeding. These convert most of the power flux into radiation. For a burning plasma in DEMO, an extremely high radiation fraction ($P_{\mathrm{rad}}/P_{\mathrm{heat}}$) of 95% can be expected [104]. In the JET tokamak, attempts have been made to achieve this high radiation output using Ne and N_2 seeding in high-density H-modes. Radiation fractions of up to 75% were reached. Surprisingly, they ended up in an ELM-free steady-state and stable I-phase [105, 106]. This leaves open the possibility that DEMO will (unintentionally) operate in the I-phase regime, indicating its importance.

The I-mode is the only regime fulfilling the conditions for the collisionality. Additionally, the circumstance that the I-mode is operated in unfavorable ∇B configuration leads to a higher power demand to enter the H-mode. Generally the L-I power threshold only has a weak dependence on B_{t} [102, 107] compared to the L-H power threshold (see Eq. 2.11), widening the existence window of the I-mode at high B_{t}. On the other hand, the L-I power threshold in unfavorable configuration is reached at higher powers than the usual L-H transition in the favorable one, making it a challenge for ITER and DEMO. The operation at reversed field is not straightforward in general in ITER. Moreover, other disadvantages can be seen from Tab. 2.2. The L-mode-like densities in I-modes lead to small Greenwald fractions f_{GW} and $H_{98\mathrm{y}2}$. So far, it was experimentally only possible to detach the inner divertor, which leads ultimately to unacceptable high power loads on the outer divertor tiles. Once the previous obstacles have been solved, the I-mode could become reactor relevant [107].

The regime with an X-point radiator (XPR) is achieved by strong impurity seeding to obtain deep divertor detachment. Most of the radiation concentrates then in a small region at the X-point or even further inside the confined region. A major advantage is that the position of the X-point radiator can be actively controlled. Additionally, if the XPR is moved to a certain height above the X-point, type-I ELMs get fully suppressed. This regime has been developed at AUG and has already been observed at TCV [66]. The XPR regime is a strong candidate as an operation scenario in the future due to its high compatibility to the DEMO BL scenario (see Tab. 2.2). The simple reason, why this scenario is not further considered in this thesis, is that no marginal fluctuation at the plasma edge has been observed so far.

Having discussed the relevance of the ELM-free operation scenarios regarding the requirements for a future fusion reactor, presented in Sec. 2.1, it is evaluated in the following whether these scenarios can actually occur in such a device. As already

Table 2.2: ELM-free Regimes Compared to EU-DEMO Baseline Scenario
The type-I ELM-free regimes presented in Sec. 2.2 are summarized in terms of the dimensionless parameters that play a major role in their reactor relevance (Sec. 2.1). The DEMO baseline (BL) scenario [48] shows the desired values.

Quantities	EDA H-mode	QCE	I-phase	I-mode	XPR	DEMO BL
$\nu^{\star}_{\mathrm{ped}}$	2–10	0.8–6	0.8–14	0.1–2	0.5–5	0.1
β_{N}	0.3–1.6	0.5–2	0.4–0.9	0.2–1.3	1–1.3	1.2
$H_{98\mathrm{y2}}$	0.9–1.3	0.6–1.3	0.6–0.9	0.6–0.7	0.7–1.0	1.1–1.4
q_{95}	≥ 3	≥ 3	≥ 3.5	≥ 2.5	≥ 3.7	4
f_{LH}	0.5–1.2	0.9–2.0	0.6–1.2	1.2–2.7	0.9–5.0	1.2
f_{GW}	0.3–1.0	0.3–1.0	0.3–0.7	0.05–0.6	0.7–0.8	0.9
Detached	yes	yes	yes	inner div.	yes	yes

mentioned in Sec. 2.1, the most fundamental prerequisite is the absence of type-I ELMs. The questions that arise are: what is the reason for the absence of ELMs in these scenarios and what do the scenarios have in common? The answer to this question seems to be obvious based on the example discharges in Figs. 2.1 to 2.4: during the phases with absence of ELMs, a fluctuation is present at the plasma edge. Hereby we hypothesize that the edge fluctuation (hereafter referred to as edge mode) is a necessary condition for ensuring the absence of type-I ELMs. However, before we can make any predictions about the occurrence of the edge modes in the respective scenario, it is necessary to reveal the underlying nature of the corresponding fluctuation. To do this, we must first of all understand what types of modes, or instabilities, can exist in a plasma and especially at the plasma edge. This theory of instability determination is described in the next chapter.

3 Theory of Plasma Edge Instabilities

As described in Chapter 2 natural type-I edge localized mode (ELM) free regimes are associated with edge fluctuations, which we call those edge modes. In order to be able to make extrapolations and predictions about ELM-free regimes, it is necessary to investigate the nature of these edge modes, which are caused by certain plasma instabilities. Therefore, as a first step, we need to understand what kind of instabilities can occur at the plasma edge. Much attention will be paid to the experimental determination and particularity of each instability in order to characterize the different edge modes introduced in Chapter 2. To do this, it is necessary to introduce determining properties of modes, which we will encounter repeatedly in the following. These are described in Fig. 3.1, which shows a characteristic illustration of an edge mode in the poloidal cross section of a tokamak.

The poloidal structure size of the mode is quantified by its poloidal wavelength, i.e.

$$\lambda_\theta = \frac{2\pi}{|k_\theta|}, \tag{3.1}$$

where k_θ is the poloidal wavenumber. Another possibility to characterize the poloidal size of the mode is the poloidal mode number m_{mode}, which represents the number of its maxima (or minima) along the poloidal circumference. The toroidal mode number n_{mode} is not shown here, but is the toroidal analogue of m_{mode} and thus, describes the number of maxima of the mode in toroidal direction. One of the most commonly measured mode property is the frequency ω, which is related to the mode velocity $\boldsymbol{v} = (v_{\mathrm{r}}, v_\theta, v_\phi)^T$ and the corresponding wavenumber $\boldsymbol{k}$ as $\omega = \boldsymbol{v} \cdot \boldsymbol{k}$. Hence, k_θ usually features a sign, indicating the propagation direction of the mode, which is a crucial and determining quantity. It should be noted, however, that the propagation direction and the associated phase velocity in the co-moving plasma frame v_{ph} is determining. Here, it has to be taken into consideration that the plasma itself rotates with a background velocity $v^{\mathrm{bg}}_{\mathrm{E\times B}}$, so that the apparent velocity v_{lab} as it is measured with diagnostics in the laboratory frame, is the sum of the phase velocity and the background velocity, i.e. $v_{\mathrm{lab}} = v_{\mathrm{ph}} + v^{\mathrm{bg}}_{\mathrm{E\times B}}$. Similarly, the radial wavenumber $k_{\mathrm{r}} = 2\pi/\lambda_{\mathrm{r}}$ provides information about the radial expansion of the mode (λ_{r}), but more on this later.

Additionally, it will be shown later that the radial turbulent transport caused by

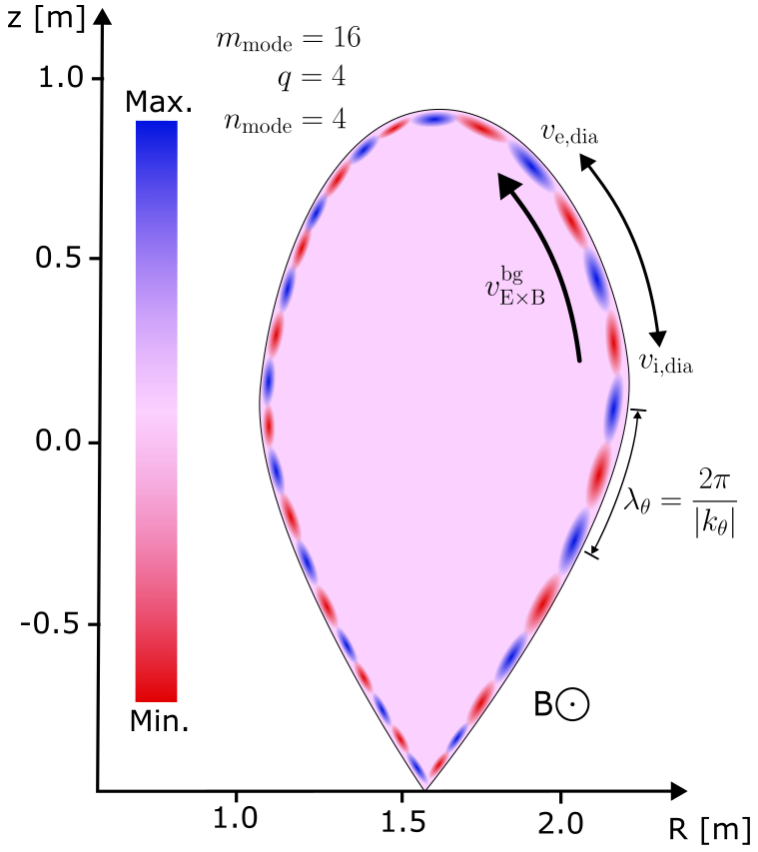

Figure 3.1: Poloidal Cross Section and Mode Properties
The main mode characteristics are displayed in the poloidal plane. The artificial mode is active just inside the separatrix and has 16 maxima (blue) and minima (red), so that $m_{\mathrm{mode}} = 16$. *Using Eq. 3.15, the toroidal mode number can be calculated as* $n_{\mathrm{mode}} = 4$ *from known safety factor* $q = 4$. *Its poloidal size* λ_θ *is given by the distance between two maxima/minima and is represented by the poloidal wavenumber* k_θ. *The whole plasma rotates through the* $E \times B$ *background velocity* $v^{\mathrm{bg}}_{\mathrm{E\times B}}$ *in the electron diamagnetic direction and the magnetic field points into the poloidal plane.*

the mode is important for the absence of ELMs. The transport that is subject to edge modes is called anomalous and can only be fully described using turbulence theory. Turbulence is ubiquitous and has occupied great scientists for a long time[1]. There are several models that attempt to describe the plasma edge turbulence, such as the Drift-Alfvén (DALF) [28, 109] and the gyrofluid electromagnetic model (GEM) [28]. We will return to the former in Sec. 5.3. In this chapter, however, we only discuss the drive of turbulent transport: the linear instabilities, and will not go into the statistical methods of turbulence theory. The reader is therefore referred to Refs. [28, 110, 111]. Fortunately, a connection between the plasma frame propagation of the mode and its transport can be made. This circumstance will be discussed in detail in Sec. 3.3.2 due

[1] 'When I meet God, I will ask him two questions: why relativity? And why turbulence? I already believe He has an answer to the first question.' - assigned to Werner Heisenberg [108].

to its novelty and consequences.

Some instabilities are described using the theory of magnetohydrodynamics (MHD) and are called MHD instabilities, which we will discuss in the first section and is based on Ref. [24]. Those that do not fall into this category are called microinstabilities and are subject to gyrofluid or kinetic theory. These are presented in the second section. Additionally, the ELM cycle is introduced to show how edge modes can lead to the absence of type-I ELMs. In a final step, all instabilities will be summarized.

3.1 Magnetohydrodynamic Instabilities

The theory of single-fluid magnetohydrodynamics (MHD) assumes that we can treat the plasma as a continuum, similar to the approach in hydrodynamics. This requires the particle orbit of an ion, the ion Larmor radius, with charge q to be smaller than the typical system size L, i.e.

$$\rho_{\mathrm{L,i}} = \frac{\sqrt{m_{\mathrm{i}} T_{\mathrm{i}}}}{qB} \underbrace{=}_{T_{\mathrm{e}}=T_{\mathrm{i}}} \frac{\sqrt{m_{\mathrm{i}} T_{\mathrm{e}}}}{qB} = \rho_{\mathrm{s}} \ll L, \tag{3.2}$$

where ρ_{s} is the hybrid gyroradius. For edge modes, the normalized quantity $k_\theta \rho_{\mathrm{s}}$ is typically used for this criterion, where k_θ is the poloidal wavenumber, defined in Eq. 3.1. As a rule of thumb, it is usually assumed that phenomena with $k_\theta \rho_{\mathrm{s}} < 0.01$ obey the MHD theory, and $k_\theta \rho_{\mathrm{s}} \geq 0.1$ are subject to microinstabilities. However, especially in the transition region, small-scale effects such as finite Larmor radius (FLR) effects are also important, but will be considered separately later. In addition, the particle distribution function $f_\alpha(\boldsymbol{x}, \boldsymbol{v}, t)$ must be Maxwellian or at least close to it. This condition can be checked mathematically in the form of the mean free path length λ_{mfp} [24], i.e.

$$\lambda_{\mathrm{mfp}} \sim \frac{T_{\mathrm{e}}^2}{n_{\mathrm{e}}} \ll L. \tag{3.3}$$

For a tokamak plasma this condition is typically fulfilled perpendicular to the magnetic field, but it is violated parallel to it.

The derivation of the single-fluid MHD equations leads via the production of moments of the kinetic equation [12] to the following set of equations:

$$\frac{\partial \rho_{\mathrm{m}}}{\partial t} + \nabla \cdot (\rho_{\mathrm{m}} \boldsymbol{v}) = 0, \tag{3.4}$$

$$\rho_{\mathrm{m}} \left(\frac{\partial \boldsymbol{v}}{\partial t} + (\boldsymbol{v} \cdot \nabla) \boldsymbol{v} \right) = -\nabla \overleftrightarrow{P} + \boldsymbol{j} \times \boldsymbol{B}, \tag{3.5}$$

$$\boldsymbol{E} + \boldsymbol{v} \times \boldsymbol{B} = \frac{1}{\sigma} \boldsymbol{j} + \frac{1}{en} (\boldsymbol{j} \times \boldsymbol{B} - \nabla p_{\mathrm{e}}) - \frac{m_{\mathrm{e}}}{e^2 n} \frac{\partial \boldsymbol{j}}{\partial t}. \tag{3.6}$$

Eq. 3.4 presents the continuity equation with the mass density $\rho_\mathrm{m} = mn$, and the center-of-mass velocity $\boldsymbol{v}$. The second equation 3.5 represents the force balance, including the pressure tensor $\overleftrightarrow{P}$, which is usually isotropic, so that only the diagonal elements of it are non-zero, yielding the well-known relationship between pressure p, temperature T and density n, i.e. $\mathrm{tr}\left(\overleftrightarrow{P}\right) = p = nT$. Additionally, the current density $\boldsymbol{j}$ and the magnetic field $\boldsymbol{B}$ occur. Eq. 3.6 is the generalized Ohm's law with elementary charge e and introduces the electric field $\boldsymbol{E}$ and the conductivity σ. Together with the four Maxwell equations and the adiabatic closure assumption

$$\frac{d}{dt}\left(\frac{p}{\rho_\mathrm{m}^{\gamma_\alpha}}\right) = 0, \tag{3.7}$$

where γ_α is the adiabatic coefficient, a closed system of equations is achieved. Moreover, it is often possible to consider the hot plasma as an outstanding electrical conductor ($\sigma \to \infty$), especially when typical MHD instabilities exist for a shorter time period τ_MHD than the typical current diffusion timescale, characterized by the system size L and temperature T, i.e. if

$$\tau_\mathrm{MHD} \ll L^2 \mu_0 \sigma \sim L^2 T^{3/2}, \tag{3.8}$$

where μ_0 is the magnetic permeability. It can be shown that this consideration and Eq. 3.2 reduce Eq. 3.6 to [24]

$$\boldsymbol{E} + \boldsymbol{v} \times \boldsymbol{B} = 0, \tag{3.9}$$

and is known as the ideal MHD theory.

One of the most important results of the ideal MHD equations is the mathematical description of the equilibrium of the tokamak plasma, represented by the Grad-Shafranov equation [112]. Here, $\boldsymbol{j}$, $\boldsymbol{B}$ and ∇p must be arranged in such a way that a force-free situation is created, i.e. the time derivative of an equilibrated quantity vanishes. However, it is necessary to check whether a system in equilibrium is stable or unstable against small deviations. Fig. 3.2 shows a mechanical analogue of different initial situations, which can be described as linear stable or unstable. As it can be seen, it is important whether the potential W is able to compensate a small deviation from the equilibrium or not, or mathematically:

$$\delta W < 0 \quad \text{the system is unstable,} \tag{3.10}$$

$$\delta W > 0 \quad \text{the system is stable.} \tag{3.11}$$

We therefore introduce a small displacement $\boldsymbol{\xi}(\boldsymbol{x}, t)$, with which we express the velocity as $\boldsymbol{v} = \underbrace{\boldsymbol{v_0}}_{=0} + d\boldsymbol{\xi}/dt$.

If we now insert the displacement into the force balance of the MHD equations to first order (Eq. 3.5), we obtain the following:

$$\rho_{\mathrm{m},0}\frac{\partial^2\boldsymbol{\xi}}{\partial t^2} = \hat{\boldsymbol{F}}\boldsymbol{\xi} \xrightarrow{\boldsymbol{\xi}(\boldsymbol{x},t)=\boldsymbol{\xi_0}(\boldsymbol{x})\exp(-i\gamma t)} -\gamma^2\rho_{\mathrm{m},0}\boldsymbol{\xi} = \hat{\boldsymbol{F}}\boldsymbol{\xi}. \tag{3.12}$$

$\hat{\boldsymbol{F}}$ is the force operator. On the right hand side a temporal Fourier ansatz to the displacement has been carried out and leads to an eigenvalue equation. It can be shown that γ determines whether the solutions of $\boldsymbol{\xi}$ are purely oscillatory and stable ($\gamma^2 > 0$), or exponentially growing or decaying and unstable ($\gamma^2 < 0$).

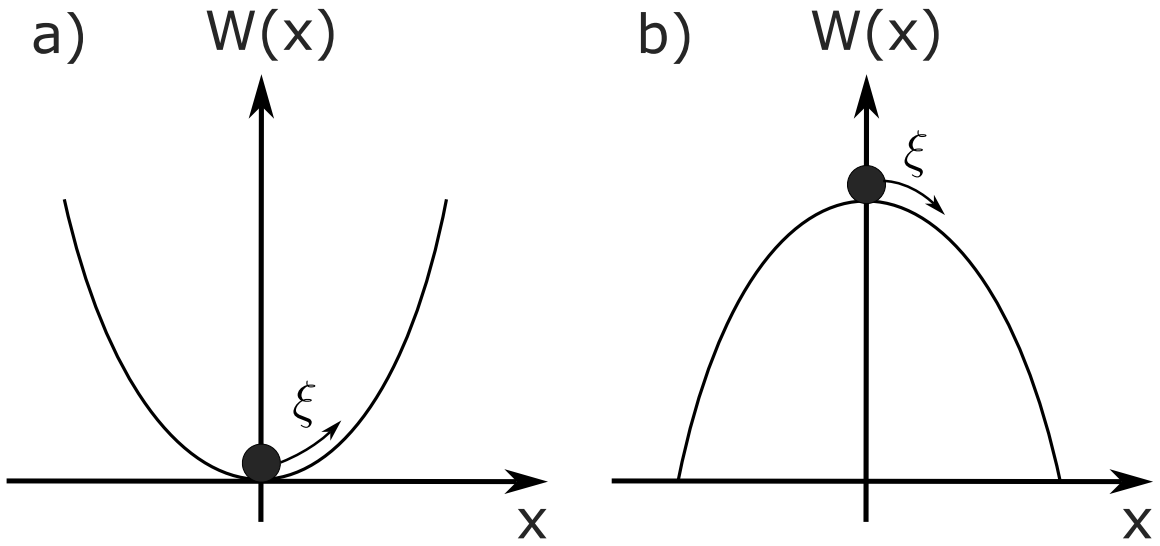

Figure 3.2: Mechanical Linear Stability
For a minimum ($\delta W > 0$), the ball (black sphere) will return to its initial position, when it is slightly moved by ξ and the system is linearly stable a). Otherwise ($\delta W < 0$), the system is unstable b).

As claimed above in Eqs. 3.10 and 3.11, we consider the potential of the system as the decisive criterion regarding stability, which is called the energy principle and can be related to the force operator as follows

$$\delta W\left(\boldsymbol{\xi}^\star, \boldsymbol{\xi}\right) = -\frac{1}{2}\int \boldsymbol{\xi}^\star \hat{\boldsymbol{F}}\boldsymbol{\xi}. \tag{3.13}$$

Here, $\boldsymbol{\xi}^\star$ is the complex conjugate of $\boldsymbol{\xi}$ and δW corresponds to the work done by the system against the force, created by $\boldsymbol{\xi}$. δW usually consists of a vacuum contribution δW_{V}, a surface part δW_{S} and the fluid/plasma contribution δW_{F}. Though, we will ignore the vacuum and surface part in the following due to the fact that we are mainly

interested in the plasma edge modes. The fluid part can be derived to

$$\delta W_{\mathrm{F}} = \frac{1}{2}\int_{\mathrm{F}} \Bigg\{ \overbrace{\frac{\left|\boldsymbol{B}_{\mathbf{1},\perp}\right|^2}{2\mu_0}}^{(1)} + \overbrace{\left(\frac{\left|\boldsymbol{B}_{\mathbf{0},\perp}\right|^2}{2\mu_0}\left|\nabla\cdot\boldsymbol{\xi}_\perp + 2\boldsymbol{\xi}_\perp\cdot\boldsymbol{\kappa}\right|^2\right)}^{(2)} + \overbrace{\gamma_\alpha p_0\left|\nabla\cdot\boldsymbol{\xi}\right|^2}^{(3)} \\ \underbrace{-2\left(\boldsymbol{\xi}_\perp\cdot\nabla p_0\right)\left(\boldsymbol{\kappa}\cdot\boldsymbol{\xi}_\perp^\star\right)}_{(4)} \underbrace{-\frac{j_{0,\parallel}}{\left|\boldsymbol{B_0}\right|}\left(\boldsymbol{\xi}_\perp^\star\times\boldsymbol{B_0}\right)\cdot\boldsymbol{B_1}}_{(5)} \Bigg\}\, dV, \tag{3.14}$$

where $\boldsymbol{\kappa} = \boldsymbol{b}\cdot\nabla\boldsymbol{b}$ with $\boldsymbol{b} = \boldsymbol{B_0}/\left|\boldsymbol{B_0}\right|$ is the curvature vector, $\boldsymbol{B_1} = \nabla\times(\boldsymbol{\xi}\times\boldsymbol{B_0})$ and $\perp$ and $\parallel$ denote the vector components perpendicular and parallel to the magnetic field $\boldsymbol{B_0}$. Ref. [24] calls Eq. 3.14 the intuitive form of the fluid energy part as "it allows to characterize the different stabilizing and destabilizing contributions by their physics nature". And indeed, terms (1) - (5) can be used individually to determine stability. Terms (1) to (3) are all positive and contribute to the stability according to Eq. 3.11. Terms (1) and (2) describe the contributions from shear and compressional Alfvén waves respectively, and (3) represents sound waves. This leaves terms (4) and (5), both of which can become negative and contribute to destabilization and thus to the creation of instabilities at the plasma edge. These MHD modes are called ballooning (4) and peeling modes (5).

If we extend the energy principle to the tokamak [24], we can show that these instabilities are most likely to occur where the periodicity of these instabilities coincides with that of the field lines. We can describe this mathematically with the safety factor, presented in Sec. 2.1

$$q = \frac{m_{\mathrm{mode}}}{n_{\mathrm{mode}}}, \tag{3.15}$$

where m_{mode} and n_{mode} are the poloidal and toroidal mode numbers (Fig. 3.1).

3.1.1 Ideal Ballooning Mode

Pressure-driven modes are generally subject to the mechanism of the interchange instability (IC) [12]. Generally speaking, the interchange instability is the MHD analogue of the Rayleigh-Taylor (RT) instability [113], known from hydrodynamics. The RT instability appears when a higher density fluid lies above a lower dense one in a gravitational potential. The difference in a tokamak plasma is that magnetic curvature or the diamagnetic drift in an inhomogeneous magnetic field is responsible for the IC. We can see the first case directly from term (4) in Eq. 3.14: if $\nabla p_0\cdot\boldsymbol{\kappa} < 0$, i.e. ∇p_0 and $\boldsymbol{\kappa}$ are anti parallel, the system is stable, and vice versa.

Particularly, the IC is shown schematically in Fig. 3.3 for the case of the low-field side (LFS) of a tokamak, which is explained in the following. Assume that the plasma is

subject to a sinusoidal density perturbation $\tilde{n}_\mathrm{e}$. Initially, the ion and electron densities are equal due to quasi-neutrality, shown in Fig. 3.3a, but the inhomogeneous magnetic field in a tokamak leads to a ∇B-drift [12], i.e.

$$\boldsymbol{v}_{\nabla B} \sim -\frac{\nabla B \times \boldsymbol{B}}{qB^3} \tag{3.16}$$

causes the ions to move upwards and the electrons downwards. In our case, more ions would move from the high (n_1) to the low density region (n_2) than the other way around. This results in an excess of ions at the phase boundary between n_1 and n_2, which creates an electric field $\boldsymbol{E}$ in the $y-$direction. The resulting electric field gives rise to an $E \times B$ drift pointing in $x-$direction ($\hat{\boldsymbol{x}}$), i.e.

$$\boldsymbol{v}_\mathrm{ExB} = \frac{\boldsymbol{E} \times \boldsymbol{B}}{B^2} = \frac{E}{B}\hat{\boldsymbol{x}} \tag{3.17}$$

which amplifies the initial density perturbation at the respective points as shown in Fig. 3.3b. The whole process can also be done with the diamagnetic drift, i.e.

$$\boldsymbol{v}_\mathrm{dia} = -\frac{\nabla p \times \boldsymbol{B}}{qnB^2}. \tag{3.18}$$

This drift is along the phase boundary and not $\hat{\boldsymbol{y}}$. Moreover, the direction of the ion motion is called ion diamagnetic direction (IDD), and that of the the electrons is called electron diamagnetic direction (EDD).

Of course, the opposite is true for the high-field side (HFS) since ∇p and $\boldsymbol{\kappa}$ are parallel there: the $E \times B$ drift weakens the perturbation and the drifts contribute to stabilisation. This is why we denote the curvature as favorable at the HFS and unfavorable at the LFS. In order to evaluate the energy principle in Eq. 3.14, we need to balance term (4) along a field line. Accordingly, there are stabilizing and destabilizing influences (favorable and unfavorable curvature). Overall, the interchange instability only occurs if we allow poloidal asymmetric modes, i.e. a higher amplitude of deformation on the LFS than on the HFS is needed. As a result, the plasma is strongly deformed on the unfavorable side and ballooned regions are formed. This is why these modes are known as ballooning modes.

Ballooning modes that can be described by ideal MHD theory are called ideal ballooning modes (IBM). As ballooning modes are ∇p-driven the stability of ideal ballooning modes is characterized by the normalized pressure gradient

$$\alpha_\mathrm{MHD} = q^2 R_\mathrm{maj} \frac{\beta}{\lambda_\mathrm{pe}}, \tag{3.19}$$

where the plasma β is defined in Eq. 2.5 and $\lambda_\mathrm{pe} = -p_\mathrm{e}/\nabla p_\mathrm{e}$ is the typical perpendicular

gradient length. When a certain value of α_{MHD} is exceeded, the so-called critical ideal MHD limit α_{c}, the plasma gets unstable to IBMs. According to Refs. [114, 115] α_{c} depends only on the geometrical properties of the plasma, i.e.

$$\alpha_{\mathrm{c}} = \kappa_{\mathrm{geo}}^{1.2}\,(1 + 1.5\delta) \tag{3.20}$$

with the elongation κ_{geo} and triangularity δ.

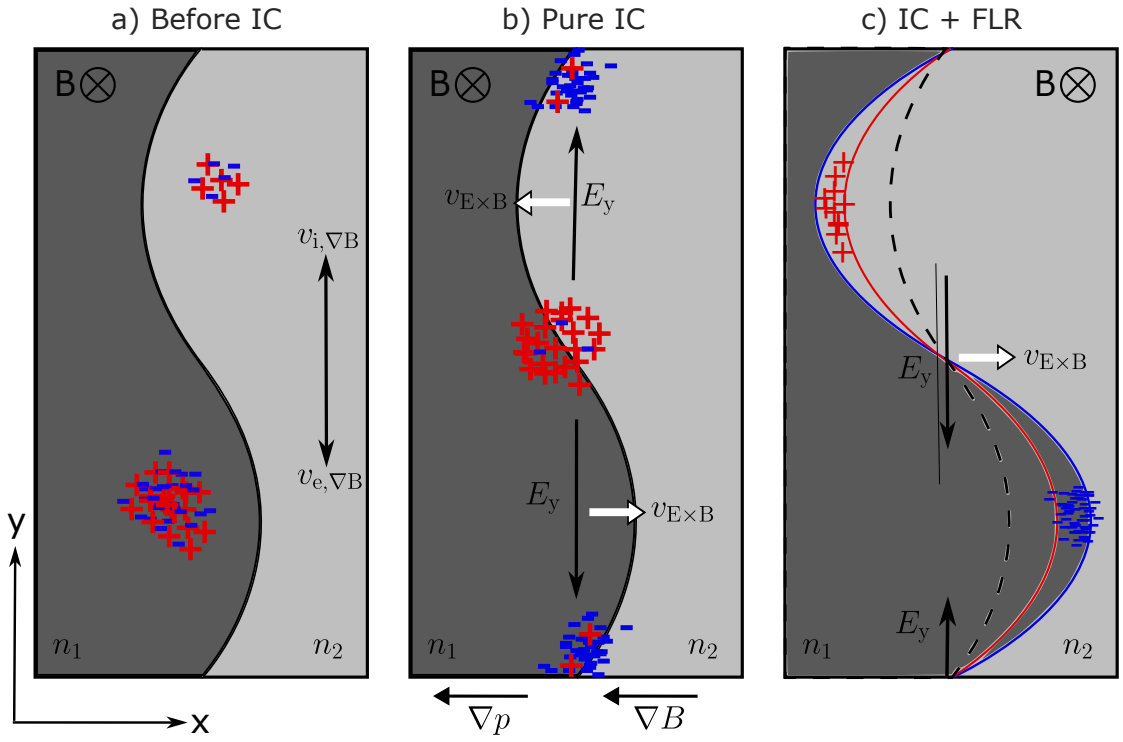

Figure 3.3: Interchange Mechanism and FLR Effects at the LFS
a) The sinusoidal density perturbation divides the plasma at the low-field side (LFS) of the torus into a region of higher (n_1) and a region of lower density (n_2). b) Due to the ∇B-drift, the ions (+) from the n_1 region migrate in the $y-$ direction upwards and the electrons (-) in the opposite direction. This leads to a charge separation, $E-$field formation and hence an increase in perturbation due to the resulting $E \times B$ drift. This is the interchange mechanism. c) Taking into account the small scale finite Larmor radius effects (FLR), there is a shift in the density boundary, which is now different for electrons (blue line) and ions (red line). Hence, an accumulation of electrons is established at the n_1 front and a deficit at n_2. This results in a shifted $E \times B$ drift, yielding an upward movement of the mode. Fig. adapted from Ref. [12].

From Fig. 3.3b it becomes clear that the density fluctuation $\tilde{n}_{\mathrm{e}}$ is in phase with the $E \times B$ drift. Usually, the cross-phase $\alpha_{\mathrm{n_e},\phi}$ between density and electric potential fluctuations $\tilde{\phi}$ is of interest, which we will see in Sec. 3.3.2. The corresponding electric field is determined by the electric potential, i.e. $E_{\mathrm{y}} = -\partial_{\mathrm{y}}\phi$. Fig. 3.3b displays

that $\tilde{n}_\mathrm{e}$ and $\tilde{\phi}$ are anti-correlated for the pure interchange case, i.e. $\alpha_{\mathrm{n_e},\phi} = \pi/2$. The interchange mechanism is described mathematically in Appendix A. There it is shown that the ideal ballooning mode without considering any kinetic effects does not propagate in the plasma frame and is a pure growing mode.

Further, IBMs have poloidal sizes of $k_\theta \rho_\mathrm{s} \lesssim 0.1$ and cause maximum transport [116]. It should be mentioned that in theory and in simulations the wavenumber in $y-$direction (k_y) or orthogonal to the magnetic field ($k_\perp$) is mostly used. However, we will encounter poloidal wavenumbers experimentally, which we will assume to be the same, i.e. $k_\mathrm{y} \sim k_\perp \sim k_\theta$. Though, it is important to consider that high-n MHD modes can have poloidal wavelengths of the order of the Larmor radius. By comparing this circumstance with Eq. 3.2, it seems necessary to apply kinetic corrections, in particular finite Larmor radius (FLR) effects, to the ideal MHD theory. A complete mathematical derivation of this correction can be found in Appendix A, but we will describe the consequences of the FLR effects by means of Fig. 3.3. First, the $E \times B$ drift has to be corrected for the contribution of a non-vanishing $k_\theta \rho_\mathrm{L}$. This gives [12]

$$v_\mathrm{E\times B}^\mathrm{FLR} = v_\mathrm{E\times B}\left(1 - \left(\frac{k_\theta \rho_\mathrm{L}}{2}\right)^2\right), \tag{3.21}$$

where $\rho_\mathrm{L} \propto m_\mathrm{part}$ is the Larmor radius, depending on the particle mass m_part. It can be directly seen from the definition of the Larmor radius (Eq. 3.2) and Eq. 3.21 that the $E \times B$ drift is now different for electrons and ions. Starting from the pure IC case in Fig. 3.3b, the higher $v_\mathrm{E\times B}^\mathrm{FLR,e}$ for the electrons leads to an excess of electrons at the high density front, where the perturbation amplitude is maximum (bottom half of the panel) and a deficiency of electrons at the low density front, where the perturbation amplitude is minimum (upper half of the panel). An electric field and $E \times B$ drift shifted relative to the pure IC case is formed as shown in Fig. 3.3c, which can be interpreted as an upward movement of the mode, i.e. the IBM propagates now in ion diamagnetic direction (IDD) with $v_\mathrm{ph} \approx v_\mathrm{i,dia}$ in the plasma frame. Further, the cross-phase between density and potential is now $\alpha_{\mathrm{n_e},\phi} = \pi$ and the radial transport is reduced. In reality, the FLR effects will have a reducing influence on the IBM and therefore the velocity will be lower. Thus, it can be shown mathematically that IBMs propagate with $v_\mathrm{ph} = 0.5 v_\mathrm{i,dia}$ in the ion diamagnetic direction, when taking FLR effects into account [117] (see Appendix A).

3.1.2 Resistive Ballooning Mode

If ideal MHD does not apply due to finite resistivity, i.e. $\eta = \sigma^{-1} > 0$, Eq. 3.6 has to be used. Analytically, this is too complex to handle (e.g. in Ref. [118]), but numerically

it can be shown that under resistive treatment a mode appears at the plasma edge: the resistive ballooning mode (RBM). The RBM is the resistive counterpart of the IBM and has similar poloidal wavenumbers $k_\theta \rho_\mathrm{s} \leq 0.1$ [116]. RBMs do also not propagate in the pure interchange case and cause maximum radial transport. Just as in the IBM case, however, a numerical inclusion of FLR effects leads to a propagation in the ion diamagnetic direction in the plasma frame. For RBMs the velocity is slightly higher than in the ideal case, since their velocity was found to be $v_\mathrm{ph} \geq 0.5 v_\mathrm{i,dia}$ [118]. Thus, the caused transport is reduced even more due to FLR effects than for IBMs.

The existence of RBMs plays an important role with respect to the turbulence at the plasma edge [119]. The parameter describing the stability of RBMs is the diamagnetic parameter, defined as [120]

$$\alpha_\mathrm{d} = \frac{1}{2\pi q R_\mathrm{maj}} \sqrt{\frac{m_\mathrm{i} c_\mathrm{s,i} R_\mathrm{maj}}{0.51 m_\mathrm{e} \nu_\mathrm{ei}}} \frac{R_\mathrm{maj}^{1/4}}{\lambda_\mathrm{p_e}^{1/4}}. \tag{3.22}$$

$c_\mathrm{s,i} = \sqrt{T_\mathrm{e}/m_\mathrm{i}}$ is the ion sound speed, ν_ei is the collision frequency between electrons and ions and $\lambda_\mathrm{p_e} = -p_\mathrm{e}/\nabla p_\mathrm{e}$. If the criterion $\alpha_\mathrm{d} > 1$ is fulfilled, the plasma is stable against (electrostatic) RBMs [121]. However, it is unclear to what extent the variation of the pressure gradient length $\lambda_\mathrm{p_e}$ has been taken into account in the work of Rogers, Drake and Zeiler [120], which is why the so-called turbulence parameter α_T can also be used [122], i.e.

$$\alpha_\mathrm{T} = \frac{1}{\pi^2} \frac{R_\mathrm{maj}^{1/2}}{\lambda_\mathrm{p_e}^{1/2}} \frac{1}{\alpha_\mathrm{d}^2} \approx 2.28 \cdot 10^{-19} R_\mathrm{maj} q^2 n_\mathrm{e} Z_\mathrm{eff} \ln \Lambda / T_\mathrm{e}^2. \tag{3.23}$$

This parameter is closely related to the collisionality, that we defined in Eq. 2.10.

3.1.3 Ideal Peeling Mode

From Eq. 3.14 we see that term (5) depends directly on the current density $j_{0,\parallel}$ parallel to $\boldsymbol{B}$. This indicates that $j_{0,\parallel}$ is the destabilizing factor for this instability, its so-called drive. The resulting modes are called ideal peeling modes (IPM) [123] and occur if $j_{0,\parallel}$ becomes too large. The responsible current $j_{0,\parallel}$ for IPMs includes the so-called bootstrap current j_BS, depending on the pressure gradient ∇p_e and the poloidal magnetic field field B_pol [24], i.e.

$$j_\mathrm{BS} \sim \frac{\nabla p_\mathrm{e}}{B_\mathrm{pol}}. \tag{3.24}$$

The bootstrap current is a neoclassical phenomenon (see Sec. 2.1) and plays an important role at low collisionality, i.e. $\nu_\mathrm{ped}^\star \leq 1$ (Eq. 2.10). From the dependence of j_BS on ∇p_e (or α_MHD from Eq. 3.19), a stability condition similar to that for IBMs from

Sec. 3.1.1 can be derived. The plasma is stable against IPMs if

$$\alpha_{\mathrm{MHD}} \frac{r}{R} \left(1 - \frac{1}{q^2}\right) > R \cdot q \cdot s \frac{j_{0,\parallel}}{B_{\mathrm{t}}} \tag{3.25}$$

is fulfilled. The term on the left represents the so-called Mercier contribution [124] and $s = (r/q)\partial_{\mathrm{r}} q$ is the normalized magnetic shear. Eq. 3.25 thus shows a linear relationship between $j_{0,\parallel}$ and α_{MHD}, which is illustrated in Fig. 3.7b. This relation will be discussed further in Sec. 3.3.1.

Overall, IPMs are closely related to external kink modes, which get their name from the fact that they cause the plasma to kink due to too high current, leading to reduced total energy in the system. By analogy, one can imagine a towel that kinks when twisted too much, except that the current takes on the role of the twisting. However, unlike the kink modes, there is a major difference in that there is no limitation toroidal and poloidal mode number for the peeling modes. Nevertheless, IPMs are very large toroidally and poloidally, i.e. $k_\theta \rho_{\mathrm{s}} \ll 0.1$ [28]. They are highly localized radially and affect a small radial area [125]. IPMs do not propagate in the plasma frame just like IBMs (without FLR effects) and cause enormous transport, especially when coupled to IBMs, as it will be shown in Sec. 3.3.1. IPMs and IBMs can be generally distinguished by their corresponding stability limit.

With global gyrokinetic simulation codes, a kinetic analog to the coupled peeling-ballooning mode has been found: the so-called kinetic peeling-ballooning mode (KPBM) [126]. It is sensitive to the safety factor q (Sec. 2.1), i.e. KPBMs require steep $q-$ profiles. In addition, higher collisions affect the frequency of the KPBM and reduce it. The poloidal size of the mode is found to be in the intermediate range between typical MHD and micro-instabilities (Sec. 3.2). KPBMs propagate in the electron diamagnetic direction in the plasma frame and are related to the peeling-ballooning modes and the kinetic ballooning mode (see Sec. 3.2.5). Moreover, KPBMs get more unstable in the electromagnetic regime, i.e. they tend to appear at higher plasma β (Eq. 2.5).

3.2 Plasma Micro-Instabilities

As described above, MHD theory can only be applied if Eqs. 3.2 and 3.3 are satisfied. However, there are many edge instabilities that do not fulfill these. In particular, Eq. 3.2 is often violated, since the following instabilities give rise to modes of the poloidal size of the order of the mixed Larmor radius ρ_{s} or even smaller. Due to their small structure size, they are called microinstabilities and are described by kinetic or gyrofluid theory. The starting point for explaining these modes is the kinetic equation, which cannot be solved analytically for real systems and is therefore not discussed

further here. However, gyrokinetic or gyrofluid simulation codes are typically used to analyze the properties of the resulting modes. In addition, some mechanisms causing the instabilities are largely understood and is described below for individual modes, with a strong emphasis on the drift wave mechanism. The following subsections base on Refs. [28, 127–130].

3.2.1 Electron Drift Wave

Besides the aforementioned interchange mechanism (IC) in Sec. 3.1.1, the drift wave (DW) mechanism is the most important one, in order to describe plasma edge instabilities, as these two are always present and compete with each other. The latter and the DW-IC competition will be discussed in detail in this section, based on Ref. [28].

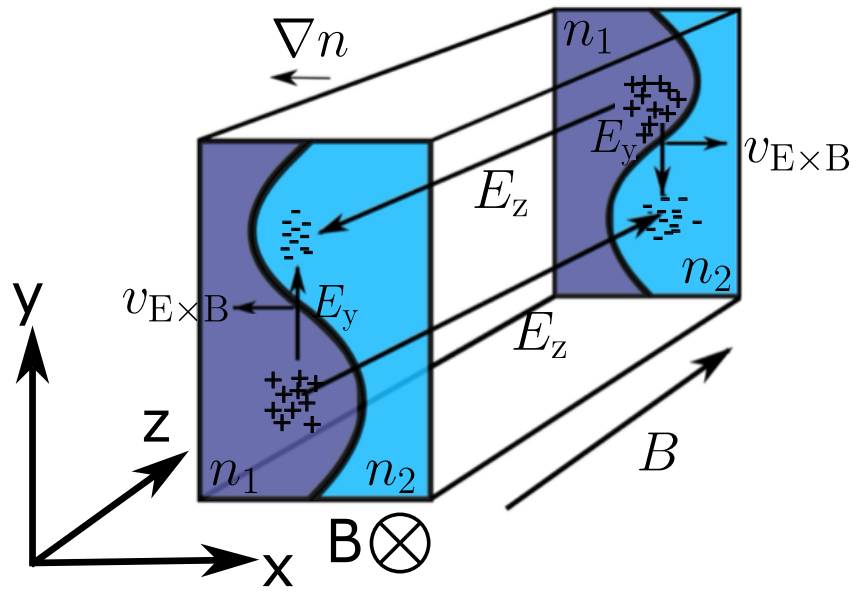

Figure 3.4: Drift Wave Mechanism
The mechanism is explained in the text: most important is the existence of a density perturbation ($n_1 > n_2$) parallel to the magnetic field lines (in the $z-$direction), which leads to parallel (E_z) and orthogonal (E_y) electric fields. The corresponding $E \times B$ drift causes the mode to propagate downwards (EDD). Fig. adapted from Ref. [28].

The basic requirement for the DW is that the perturbation not only occurs orthogonal but also along the magnetic field line, i.e. that a non-vanishing parallel wavenumber occurs $k_\parallel \neq 0$. To understand the mechanism, we follow Fig. 3.4. The parallel density perturbation creates a parallel pressure gradient, here in $z-$direction. According to Eq. 3.5, this leads to a motion of the plasma particles, which try to compensate $\partial_z p$. Consequently, the particles move with their corresponding sound velocity, which is

depending on the species, i.e.

$$c_{\mathrm{s,e}} = \sqrt{\frac{T_\mathrm{e}}{m_\mathrm{e}}} \quad \text{for electrons and} \quad c_{\mathrm{s,i}} = \sqrt{\frac{T_\mathrm{i}}{m_\mathrm{i}}} \quad \text{for ions.} \tag{3.26}$$

Hence, electrons compensate the perturbation quicker due to their lower mass. In general, electrons dominate the parallel dynamics. This compensation results in a charge separation and thus an electric field E_z in the $z-$direction, as shown in Fig. 3.4. Though, E_z counteracts the parallel electron motion u_z until equilibrium ($d_\mathrm{t} u_\mathrm{z} = 0$) is reached. By using Eq. 3.5 and ideal Ohm's law from Eq. 3.9 (we ignore resistivity for the moment), the following equation of motion is obtained:

$$-\frac{\partial p_\mathrm{e}}{\partial z} - neE_\mathrm{z} = 0 \tag{3.27}$$

As described above, the electric field is determined by the electric potential, i.e. $E_\mathrm{z} = -\partial_\mathrm{z}\phi$. p and ϕ are perturbed, so that we employ again a wave ansatz to the perturbation of the pressure, i.e. $p_\mathrm{e} = p_0 + \tilde{p}_\mathrm{e} \exp\left(i\left(k_\parallel z - \omega t\right)\right)$ and correspondingly for the potential. Furthermore, fluctuations in T_e are ignored, so that the pressure fluctuations are expressed as density fluctuations, i.e. $\tilde{p}_\mathrm{e} = T_\mathrm{e}\tilde{n}_\mathrm{e}$. Inserting all discussed terms in Eq. 3.27 in the first order yields

$$-ik_\parallel T_\mathrm{e}\tilde{n}_\mathrm{e} + ik_\parallel n_0 e\tilde{\phi} = 0 \Longleftrightarrow \frac{\tilde{n}_\mathrm{e}}{n_0} = \frac{e\tilde{\phi}}{T_\mathrm{e}}. \tag{3.28}$$

This is the so-called Boltzmann relation or Boltzmann response and describes the case, where potential perturbations can directly compensate for density perturbations or shorter: potential and density fluctuations are in phase, i.e. their cross-phase vanishes $\alpha_{\mathrm{n_e},\phi} = 0$. When Eq. 3.28 is fulfilled, the electrons are called adiabatic. For example, this is not the case for interchange instabilities (see Sec. 3.1.1).

Besides the parallel, there is also a perpendicular density perturbation in Fig. 3.4, i.e. a density gradient pointing in negative $x-$direction $\partial_\mathrm{x} n$. The charge separation in parallel direction described above induces a charge separation and thus an electric field in $y-$direction E_y. Positive charges accumulate in the high-density regions (n_1) and the negative ones in the low-density area (n_2). The resulting $E \times B$-drift points along the $x-$coordinate, i.e. $\tilde{v}_{\mathrm{E\times B}} = -\tilde{E}_\mathrm{y}/B_0$, and leads to a shift of the perturbation in the (negative) $y-$direction. This is equivalent to a propagation of the perturbation, which is why this phenomenon is called a drift wave (DW). It should be emphasized that the drift wave as described here with an adiabatic electron response is stable, i.e. a propagating wave with no increase of the perturbation amplitude. Only if additional effects take place, which are able to modify the Boltzmann relation (Eq. 3.28), the

DW can become unstable as described below.

In general, it are the ions that dominate the perpendicular dynamics. To establish the dispersion relation for a stable DW, the contributions of all the fluctuations, acting on the ions, in all three spatial dimensions are required. In $x-$direction, there is the $E\times B$-drift as just described and a density gradient, including the whole background density. Influences on the ion motion in the $z-$direction are described by the aforementioned parallel electric field, i.e. $eE_\mathrm{z} = m_\mathrm{i}\partial_\mathrm{t} v_\mathrm{i,z}$ and in the $y-$direction a polarisation drift of the form $\tilde{v}_\mathrm{pol} \propto \dot{\tilde{E}}_\mathrm{y} = (-i\omega)(-ik_\mathrm{y}\tilde{\phi})$ appears. With all these contributions and the application of the continuity equation 3.4 to the first order, the following expression is obtained

$$\frac{\partial \tilde{n}_\mathrm{i}}{\partial t} \underbrace{-\frac{1}{B_0}\frac{\partial \tilde{\phi}}{\partial y}}_{\tilde{v}_\mathrm{E\times B,x}} \frac{\partial n_0}{\partial x} + n_0 \underbrace{\frac{m_\mathrm{i}}{eB_0^2}\omega k_\mathrm{y}\frac{\partial \tilde{\phi}}{\partial y}}_{\partial_\mathrm{y}\tilde{v}_\mathrm{pol}} + n_0 \underbrace{\frac{ek_\parallel}{\omega m_\mathrm{i}}\frac{\partial \tilde{\phi}}{\partial z}}_{\partial_\mathrm{z}\tilde{v}_\mathrm{i,z}} = 0. \tag{3.29}$$

By applying the wave ansatz mentioned above and rearranging the equation, we get

$$\frac{\tilde{n}_\mathrm{i}}{n_0}\omega = \frac{e\tilde{\phi}}{T_\mathrm{e}}\left(\frac{T_\mathrm{e}}{e\lambda_{n_\mathrm{e}}B_0}k_\mathrm{y} - k_\mathrm{y}^2\rho_\mathrm{s}^2\omega + \frac{k_\parallel^2 c_\mathrm{s,i}^2}{\omega}\right), \tag{3.30}$$

where $\lambda_{n_\mathrm{e}} = -n_0/\partial_\mathrm{x} n_0$. In a final step, quasi-neutrality ($\tilde{n}_\mathrm{i} = \tilde{n}_\mathrm{e}$), the Boltzmann response (Eq. 3.28) and the assumption that $k_\parallel$ is comparatively small leads to the dispersion relation of the stable drift wave

$$\omega = \frac{\frac{T_\mathrm{e}}{e\lambda_{n_\mathrm{e}}B_0}k_\mathrm{y}}{1+k_\mathrm{y}^2\rho_\mathrm{s}^2} = \frac{v_\mathrm{e,dia}k_\mathrm{y}}{1+k_\mathrm{y}^2\rho_\mathrm{s}^2}, \tag{3.31}$$

where the electron diamagnetic velocity $v_\mathrm{e,dia}$ without the temperature gradient is included. Hence, the drift wave propagates in electron diamagnetic direction with $v_\mathrm{ph} = v_\mathrm{e,dia}/\left(1+k_\mathrm{y}^2\rho_\mathrm{s}^2\right)$. Typical poloidal wavenumbers of a DW are in the range of $k_\theta\rho_\mathrm{s} = 0.05-1$ [131, 132].

Crucial to the calculations above is the fact that the electrons can immediately compensate for potential perturbations (Boltzmann response in Eq. 3.28). If this is not the case and the motion of the electrons is hampered, either by increasing collisions ν or magnetic induction, a phase shift between $\tilde{n}_\mathrm{e}$ and $\tilde{\phi}$ occurs, i.e. $\alpha_{n_\mathrm{e},\phi} \neq 0$. The resulting phase can then be integrated into Eq. 3.28 by a so-called $i\delta^\star-$model, as follows [12]:

$$\frac{\tilde{n}_\mathrm{e}}{n_0} = \frac{e\tilde{\phi}}{T_\mathrm{e}}e^{-i\delta^\star} \approx \frac{e\tilde{\phi}}{T_\mathrm{e}}\left(1-i\delta^\star\right). \tag{3.32}$$

Here $\delta^\star$ is assumed to be a small real number representing a phase between density and potential. It simply follows that the dispersion relation of the DW (Eq. 3.31) is

extended by the $i\delta^\star$ term, yielding

$$\omega = \frac{v_{\mathrm{e,dia}} k_\mathrm{y}}{1 + k_\mathrm{y}^2 \rho_\mathrm{s}^2 - i\delta^\star} \approx \frac{v_{\mathrm{e,dia}} k_\mathrm{y}}{1 + k_\mathrm{y}^2 \rho_\mathrm{s}^2} + i \frac{v_{\mathrm{e,dia}} k_\mathrm{y}}{\left(1 + k_\mathrm{y}^2 \rho_\mathrm{s}^2\right)^2} \delta^\star. \tag{3.33}$$

In the last step, it was used that $|\delta^\star| \ll 1$, which might not be fulfilled in all real physical systems. Similarly to the terms in Eq. 3.12, the real part describes the frequency of the mode ω and the imaginary part gives the growth rate γ. If $\delta^\star > 0$, the perturbation grows, i.e. it gets unstable. In the following, we discuss possible reasons for a non-vanishing $\delta^\star$. First, we set up the equations of motion, but this time with a friction term in the parallel electron motion, caused by a finite electron-ion collision frequency ν_ei. The total electron velocity in $z-$direction, can then be calculated via [28]

$$-iT_\mathrm{e} k_\parallel \tilde{n}_\mathrm{e} + in_0 e k_\parallel \tilde{\phi} - n_0 m_\mathrm{e} \nu_\mathrm{ei} \tilde{v}_{\mathrm{e},\parallel} = 0 \Longleftrightarrow \tilde{v}_{\mathrm{e},\parallel} = \frac{ik_\parallel T_\mathrm{e}}{m_\mathrm{e}\nu_\mathrm{ei}} \left(\frac{e\tilde{\phi}}{T_\mathrm{e}} - \frac{\tilde{n}_\mathrm{e}}{n_0} \right). \tag{3.34}$$

Using the continuity equation 3.4 to first order and neglecting the polarization drift, i.e.

$$\frac{\partial \tilde{n}_\mathrm{e}}{\partial t} - \frac{1}{B_0} \frac{\partial \tilde{\phi}}{\partial y} \frac{\partial n_0}{\partial x} + n_0 \frac{\partial \tilde{v}_{\mathrm{e},\parallel}}{\partial z} = 0, \tag{3.35}$$

yields a relationship between $\tilde{n}_\mathrm{e}$ and $\tilde{\phi}$:

$$\frac{\tilde{n}_\mathrm{e}}{n_0} = \frac{e\tilde{\phi}}{T_\mathrm{e}} \left(\frac{v_{\mathrm{e,dia}} k_\mathrm{y} + ik_\parallel^2 T_\mathrm{e}/(m_\mathrm{e}\nu_\mathrm{ei})}{v_\mathrm{ph} k_\mathrm{y} + ik_\parallel^2 T_\mathrm{e}/(m_\mathrm{e}\nu_\mathrm{ei})} \right). \tag{3.36}$$

Making the denominator real and assuming that $k_\parallel^2 T_\mathrm{e}/(m_\mathrm{e}\nu_\mathrm{ei}) \gg v_\mathrm{ph} k_\mathrm{y}$, yields

$$\frac{\tilde{n}_\mathrm{e}}{n_0} = \frac{e\tilde{\phi}}{T_\mathrm{e}} \left(1 - i \frac{m_\mathrm{e}\nu_\mathrm{ei}}{T_\mathrm{e}} \frac{k_\mathrm{y}}{k_\parallel^2} \left(v_{\mathrm{e,dia}} - v_\mathrm{ph} \right) \right). \tag{3.37}$$

By comparison with equation 3.32, we observe

$$\begin{aligned} \delta^\star &= \frac{m_\mathrm{e}\nu_\mathrm{ei}}{T_\mathrm{e}} \frac{k_\mathrm{y}}{k_\parallel^2} \left(v_{\mathrm{e,dia}} - v_\mathrm{ph} \right) \overbrace{=}^{2.10} \frac{\nu_\mathrm{ped}^\star \varepsilon^{3/2} \sqrt{m_\mathrm{e}/T_\mathrm{e}}}{q_{95} R_\mathrm{maj}} \frac{k_\mathrm{y}}{k_\parallel^2} \left(v_{\mathrm{e,dia}} - v_\mathrm{ph} \right) \\ &\underbrace{=}_{3.26} \frac{\nu_\mathrm{ped}^\star \varepsilon^{3/2}}{c_{\mathrm{s,e}} q_{95} R_\mathrm{maj}} \frac{k_\mathrm{y}}{k_\parallel^2} \left(v_{\mathrm{e,dia}} - v_\mathrm{ph} \right) \approx \nu_\mathrm{ped}^\star \varepsilon^{3/2} q_{95} R_\mathrm{maj} \frac{\omega_{\mathrm{e,dia}} - \omega_\mathrm{ph}}{c_{\mathrm{s,e}}} \\ &\approx 30 \alpha_\mathrm{T} \left(\omega_{\mathrm{e,dia}}^\star - \omega_\mathrm{ph}^\star \right). \end{aligned} \tag{3.38}$$

In these calculations, we assume that $k_\parallel \approx 1/(q_{95} R_\mathrm{maj})$ and $30\alpha_\mathrm{T} \approx \nu_\mathrm{ped}^\star \varepsilon^{3/2} q_{95}$, where α_T (Eq. 3.23) is the turbulence parameter [122], introduced in Sec. 3.1.2. Additionally,

the frequency is related to the velocity and the wavenumber as $\omega = \boldsymbol{k}\cdot\boldsymbol{v}$ (Eq. 3.48) and the dimensionless frequency $\omega^\star = \omega R_{\mathrm{maj}}/c_{\mathrm{s,e}}$ is used. From Eq. 3.33 we know that for a small $\delta^\star$ the same frequency as for the aforementioned stable DW case is obtained. The resulting $\delta^\star$ from Eq. 3.38 provides the growth rate γ into which we insert the normalized frequency of the mode, i.e.

$$\gamma = \frac{\omega^\star_{\mathrm{e,dia}}}{\left(1+k_{\mathrm{y}}^2\rho_{\mathrm{s}}^2\right)^2} 30\alpha_{\mathrm{T}} \left(\omega^\star_{\mathrm{e,dia}} - \frac{\omega^\star_{\mathrm{e,dia}}}{1+k_{\mathrm{y}}^2\rho_{\mathrm{s}}^2}\right) = 30\alpha_{\mathrm{T}} \left(\omega^\star_{\mathrm{e,dia}}\right)^2 \underbrace{\frac{k_{\mathrm{y}}^2\rho_{\mathrm{s}}^2}{\left(1+k_{\mathrm{y}}^2\rho_{\mathrm{s}}^2\right)^3}}_{f(k_{\mathrm{y}}\rho_{\mathrm{s}})}. \tag{3.39}$$

In most cases we are interested in the most unstable mode, i.e. the one where γ reaches a maximum with respect to $k_{\mathrm{y}}\rho_{\mathrm{s}}$. Therefore, we need to find the maximum of $f\left(k_{\mathrm{y}}\rho_{\mathrm{s}}\right)$. Simple differential calculus yields a maximum for $k_{\mathrm{y}}\rho_{\mathrm{s}} = 1/\sqrt{2}$. The corresponding $\delta^\star$ becomes:

$$\delta^\star_{\mathrm{max}} = 30\alpha_{\mathrm{T}}\omega^\star_{\mathrm{e,dia}} \left.\frac{k_{\mathrm{y}}^2\rho_{\mathrm{s}}^2}{1+k_{\mathrm{y}}^2\rho_{\mathrm{s}}^2}\right|_{k_{\mathrm{y}}\rho_{\mathrm{s}}=1/\sqrt{2}} = 10\alpha_{\mathrm{T}}\cdot\omega^\star_{\mathrm{e,dia}}. \tag{3.40}$$

From Eqs. 3.32, 3.33 and 3.40, it is visible that a higher α_{T} leads to a larger growth rate γ of the instability and that α_{T} seems to play a role in the cross-phase between $\tilde{n}_{\mathrm{e}}$ and $\tilde{\phi}$. We hypothesize: the DW gets more unstable with increasing α_{T} [116] and its cross-phase deviates from zero, similar to the IC case, for which $\alpha_{\mathrm{n_e},\phi} = \pi/2$ (without FLR effects). That is why Ref. [122] calls α_{T} the turbulence parameter, since it determines if the plasma is more prone to DW ($\alpha_{\mathrm{T}} \ll 1$) or IC instabilities ($\alpha_{\mathrm{T}} \to 1$). The second factor from Eq. 3.38 indicates that the frequency (velocity) of the mode in the plasma frame can be related to $\alpha_{\mathrm{n_e},\phi}$ as well. This will be discussed in detail in Sec. 3.3.2.

3.2.2 Ion Temperature Gradient Mode

It was described in Sec. 3.1.1 that the interchange mechanism (IC) can cause a pressure-driven instability, which was identified in the context of the presented MHD formalism as a ballooning mode. The driving ∇p at the plasma edge, was there introduced as a density perturbation in Fig. 3.3 implicitly assuming a constant temperature. Similarly, the same interchange mechanism can also be explained by ∇T taking on the role of ∇n. To study the role of temperature and density, ∇p is expressed as a function of the gradient lengths of density $\lambda_{\mathrm{n_e}} = -n_{\mathrm{e}}/\nabla n_{\mathrm{e}}$ and temperature $\lambda_{\mathrm{T_e}} = -T_{\mathrm{e}}/\nabla T_{\mathrm{e}}$,

$\lambda_{\mathrm{T_i}} = -T_\mathrm{i}/\nabla T_\mathrm{i}$, respectively as follows

$$\begin{aligned}\nabla p = \nabla\left((T_\mathrm{i}+T_\mathrm{e})n_\mathrm{e}\right) &= T_\mathrm{i}\nabla n_\mathrm{e}\left(\frac{n_\mathrm{e}\nabla T_\mathrm{i}}{T_\mathrm{i}\nabla n_\mathrm{e}}+1\right)+T_\mathrm{e}\nabla n_\mathrm{e}\left(\frac{n_\mathrm{e}\nabla T_\mathrm{e}}{T_\mathrm{e}\nabla n_\mathrm{e}}+1\right)\\ &= T_\mathrm{i}\nabla n_\mathrm{e}\left(\underbrace{\frac{\lambda_{\mathrm{n_e}}}{\lambda_{\mathrm{T_i}}}}_{\eta_\mathrm{i}}+1\right)+T_\mathrm{e}\nabla n_\mathrm{e}\left(\underbrace{\frac{\lambda_{\mathrm{n_e}}}{\lambda_{\mathrm{T_e}}}}_{\eta_\mathrm{e}}+1\right).\end{aligned} \tag{3.41}$$

It can be directly seen from Eq. 3.41 that both ∇T_i and ∇T_e play an important role. The ion temperature gradient drives the so-called ion temperature gradient mode (ITG). The part that includes the electron temperature will be neglected for the moment, as this leads to electron temperature gradient modes, which will be briefly discussed in the following section. In particular, the factor η_i is decisive for the formation of ITGs, which is why this mode is often referred to as $\eta_\mathrm{i}-$mode. In particular, η_i shows the competition between ∇T_i, which destabilizes the mode and ∇n_e, stabilizing the ITGs.

ITGs occur mainly in the plasma core and outer core, but can also be found in the edge region [128]. Although, ITGs have been introduced above with the IC mechanism, it is interesting to note that the underlying mechanism for their formation can be different in the core and edge region. Originally, ITGs have been found to have poloidal wavenumbers of $k_\theta\rho_\mathrm{s} \sim 0.1$, which can also be seen in Fig 3.5, but at the plasma edge, however, ITG-like structures are more IC-like and are larger, i.e. $k_\theta\rho_\mathrm{s} \gtrsim 0.01$ [128]. ITGs propagate in the ion diamagnetic direction [133]. Moreover, ITGs exist mainly in low-β magnetized plasmas (see Fig. 3.6), because electromagnetic (EM) effects have a stabilizing effect on those [134]. Their EM counterpart is the kinetic ballooning mode (KBM), which will be discussed in Sec. 3.2.5. ITGs are responsible for the enormous ion heat transport and are associated with so-called stiff transport [135]. This means that the caused transport is kept small below a critical gradient of the ion temperature $\nabla T_\mathrm{i,c}$, and only when this is exceeded, the transport increases explosively. Furthermore, the ITG instability is in competition with trapped electron modes (TEM), which will be discussed in Sec. 3.2.4.

3.2.3 Electron Temperature Gradient Mode

Electron temperature gradient modes (ETGs) are characterized by the ∇T_e term in Eq. 3.41, so η_e is important for them, which is why they are also called $\eta_\mathrm{e}-$modes. ETGs are the smallest scale edge modes observed so far, having poloidal sizes of the order of $k_\theta\rho_\mathrm{s} > 0.7$ [128], but can also exhibit values of $k_\theta\rho_\mathrm{s} > 10$ [136], which is shown in Fig. 3.5. Additionally, ETG modes have a larger growth rate than ITGs or trapped electron

modes (TEMs). ETGs propagate in electron diamagnetic direction. According to the gyro-Bohm scaling, the electron heat transport caused by ETGs should be a factor $\sqrt{m_\mathrm{e}/m_\mathrm{i}}$ smaller than the ion heat transport caused by ITGs, but this is not consistent with observations [129]. One reason for the large electron heat transport of ETGs is the generation of streamers, i.e. radially elongated flows transferring particles and heat in the far SOL, thus increasing the electron heat transport [137]. Interestingly, ETGs seem to cause radial outward ($\eta_\mathrm{i} \lesssim 1$) and inward ($\eta_\mathrm{i} \gtrsim 1$) particle transport [128], depending on η_i from Eq. 3.41, which is not the drive of the mode. This fact yields the following mechanism: if the ETG generates outward particle flux ($\eta_\mathrm{i} \lesssim 1$), the density profile will flatten, i.e. $\lambda_{\mathrm{n_e}}$ rises, and hence η_i increases until inward particle flux is generated. In an ETG dominated edge plasma, a value of $\eta_\mathrm{i} \sim 1$ close to the turning point is expected.

3.2.4 Trapped Electron Mode

Not only passing particles, but also trapped ones can contribute to instabilities at the plasma edge. As presented in Sec. 2.1 the trapped particles move on so-called banana orbits and this phenomenon is important for plasmas with low collisionality (see Eq. 2.10). Similarly to the DW mechanism, we need to consider a parallel and perpendicular perturbation to the magnetic field lines. At first, trapped particles hamper the response of the electrons to the parallel pressure gradient as shown in Sec. 3.2.1. Even more important is the toroidal precession of the banana orbits due to the $\nabla B \times B_\mathrm{pol}-$drift, causing ions and electrons to move in different directions. This movement results in a charge separation, similarly to the constellation of the interchange instability case (Sec. 3.1.1) applied to the trapped particles. At high perturbation frequencies, i.e. $\omega_\mathrm{TEM} > k_\parallel c_\mathrm{s,i}$, the response of the ions deviates from the Boltzmann response (Eq. 3.28) and passing electrons counteract the charge separation. Hence, the so-called trapped electron mode (TEM) arises [28].

Similar to ITGs, the TEM requires a critical gradient, but for ∇T_e, which also induces stiff transport. In general, the TEM has a similar poloidal size as the ITG (see Fig. 3.5), but propagates in electron diamagnetic direction in the plasma frame. A crucial point of TEM dominated plasmas is that they are prone to impurity accumulation. In low density plasmas and if the plasma is TEM dominated, impurities from the far SOL will get into the plasma core and the radiation would be too high for the plasma to persist [28]. Electromagnetic effects also have a stabilizing effect on TEMs [134].

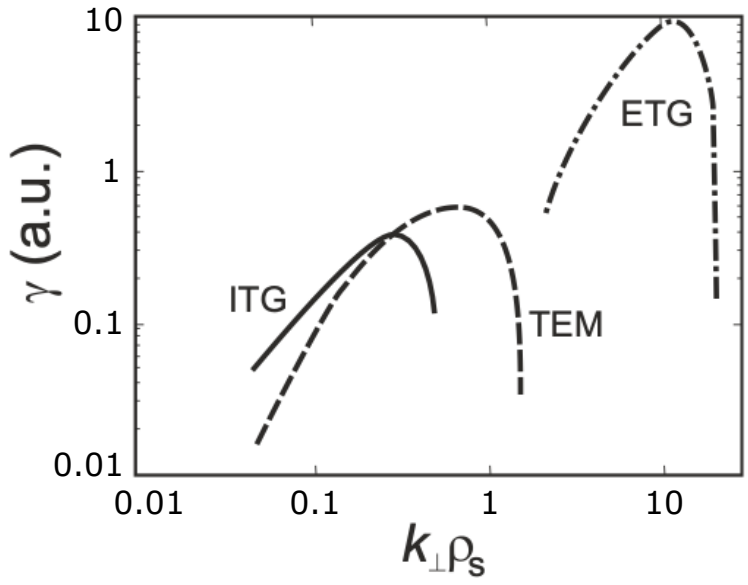

Figure 3.5: Growth Rate and Wavenumber of ITG, ETG and TEM
This is a result of analyses using the gyrokinetic simulation code GENE [138]. It can be seen that ion temperature gradient modes (ITGs) and trapped electron modes (TEMs) have both a similar normalized perpendicular structure size $k_\perp \rho_s$ and a similar growth rate γ. They differ mainly in their direction of motion. Electron temperature gradient modes (ETGs) are significantly smaller, as mentioned in Sec. 3.2.3, but have a more explosive growth rate. Fig. taken from Ref. [12].

3.2.5 Kinetic Ballooning Mode

Although kinetic ballooning modes (KBM) are called ballooning modes, they cannot be described by the MHD theory (Sec. 3.1) and require the consideration of kinetic effects. However, their stability can be analyzed by means of the MHD infinite-n ballooning modes [139]. The name of the KBM is derived from the fact that - similar to ideal ballooning modes (Sec. 3.1.1) - KBMs only occur when a critical value of normalized pressure gradient (Eqs. 3.19, 3.20) is reached. This critical value α_c^{KBM} is always lower than that of the IBMs, i.e.

$$\alpha_c^{\mathrm{KBM}} = \frac{\alpha_c}{1+\varepsilon}, \tag{3.42}$$

where $\varepsilon = a_{\mathrm{min}}/R_{\mathrm{maj}} < 1$ is the inverse aspect ratio. This means that KBMs always appear before the plasma becomes unstable to IBMs, which will be important for the ELM-cycle in Sec. 3.3.1.

A characteristic property of KBMs is that they are driven by ∇T_i. KBMs have poloidal dimensions that are slightly smaller than those of typical ballooning modes from Sec. 3.1.1 and 3.1.2, i.e. $k_\theta \rho_s \sim 0.1$ and propagate in ion diamagnetic direction [140]. They cause large transport. A lot of these points are also valid for ITGs (Sec. 3.2.2) except for the fact that KBMs are destabilized by electromagnetic effects [141],

i.e. they only appear at high β (Eq. 2.5), shown in Fig. 3.6. Thus, KBMs are often seen as an electromagnetic counterpart of the ITG mode. Particularly, there is a smooth transition from the ITG to the KBM dominated regime. Further, simulations have also found some kind of hybrid mode of KBM/ITG [142].

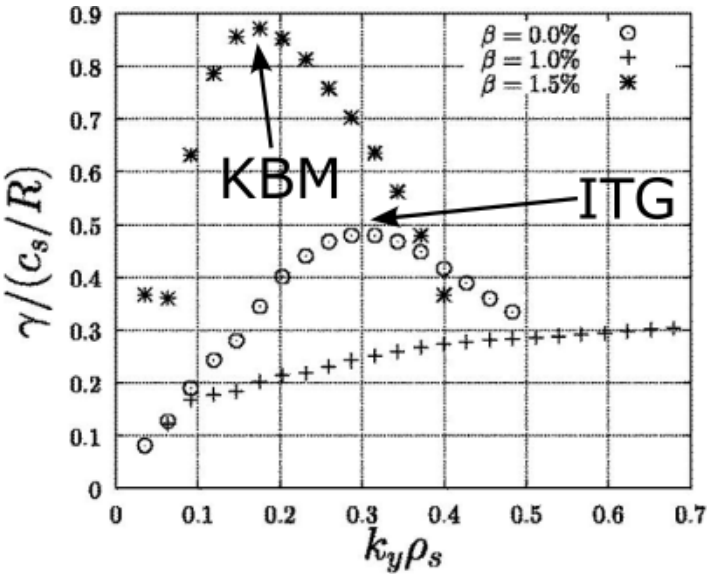

Figure 3.6: Electromagnetic Transition from ITGs to KBMs
In the electrostatic case ($\beta = 0$), an instability appears which has its maximum growth rate γ at a normalised orthogonal wave number of $k_y\rho_s = 0.3$ ($\odot$): the ion temperature gradient mode (ITG). If we increase β, the ITG growth rate is reduced ($+$). However, if we increase β even further ($*$), a strong instability appears at a lower wavenumber: the kinetic ballooning mode (KBM). Fig. taken from Ref. [140].

Additionally, in the dispersion relation of KBMs the term containing $k_\parallel$ becomes important. For instance, we have neglected this term in the dispersion relation for the drift wave in Eq. 3.30. However, this part describes the coupling of the mode with sound waves. If electromagnetic effects are included, a coupling with Alfvén waves (see Sec. 3.1) can be shown, leading to the phenomenon of magnetic flutter, indicating strong electromagnetic transport in the direction perpendicular to the magnetic field lines. This is called Alfvénic coupling and is a characteristic feature of KBMs [28].

3.2.6 Micro-Tearing Mode

Tearing modes are internal kink modes with poloidal mode numbers of $m_{\text{mode}} > 1$ [12]. Internal means that the last closed flux surface is not deformed. These types of internal kink modes are only possible if resistivity is included. Generally, tearing modes can lead to disruptions, which must be avoided in a future fusion reactor (see Sec. 2.1). In a fusion plasma, neoclassical tearing modes (NTM) are particularly important and are driven by the bootstrap current, similar to the IPMs discussed in

Sec. 3.1.3. They are called neoclassical because the bootstrap current is a neoclassical phenomenon. This means that a perturbation in ∇p leads to a perturbation in the bootstrap current, which in turn leads to the formation of separate confinement regions due to magnetic reconnection [143], so-called magnetic islands. Magnetic islands cause enhanced transport, as they magnetically connect radial regions which are otherwise not for the undisturbed flux surface. Thus they lead to a flattening of the pressure and temperature profile. The current perturbation and hence the island size increases.

On a smaller scale, there are so-called micro-tearing modes (MTM). These become important in the high β case [144], which usually occurs for H-modes - similar to KBMs (Sec. 3.2.5). However, gyrokinetic simulations have shown that MTMs are found in the pedestal top region and KBMs appear further outwards [145]. The dispersion relation of MTMs can be calculated analytically as [146]

$$\omega_{\mathrm{MTM}} = \left(\frac{T_{\mathrm{e}}}{e\lambda_{\mathrm{n_e}} B_{\mathrm{t}}} + \frac{5}{4} \frac{\nabla T_{\mathrm{e}}}{e B_{\mathrm{t}}} \right) k_{\mathrm{y}} \approx \frac{\nabla p_{\mathrm{e}}}{e n_{\mathrm{e}} B_{\mathrm{t}}} k_{\mathrm{y}} = v_{\mathrm{e,dia}} k_{\mathrm{y}}, \tag{3.43}$$

where we set the factor 5/4 to one. It is visible that the velocity of the MTM is close to that of the electron diamagnetic velocity $v_{\mathrm{e,dia}}$, but here also the temperature gradient is included, as opposed to Eq. 3.31. This fact in turn explains the DW-character of MTMs. MTMs are driven by ∇T_{e} and therefore, propagate in electron diamagnetic direction. Their poloidal wavenumber is similar to that of KBMs [127]. The bending of magnetic field lines has a stabilising influence on MTMs. In addition, MTMs require a critical electron temperature gradient.

3.3 Characterization of Edge Instabilities

The motivation for this chapter is to clarify how edge modes, found in ELM-free scenarios from Chapter 2 contribute to the absence of type-I ELMs in reality. To do this, we first need to understand the underlying instability of ELMs and how an ELM cycle works. Based on this it becomes clear that the edge modes must suppress the ELM crash by sufficiently induced transport. The transport caused by modes in general is then described mathematically and linked to their velocity in the plasma frame. In a final step, the presented candidates for edge fluctuations in ELM-free regimes are summarized together with characterizing physical quantities.

3.3.1 Edge-Localized Modes

The appearance of type-I ELMs in the classical ELMy H-mode and the fact that they eject typically $5 - 10\%$ [29] of the plasma stored energy into the far SOL towards

plasma-facing materials has already been discussed phenomenologically in Sec. 1.3. A characteristic feature of the H-mode is the formation of an edge transport barrier (ETB), giving rise to the so-called pedestal, which is characterized by a steep gradient in the pressure profile. As shown in Sec. 3.1.1, the normalized pressure gradient α_{MHD} (Eq. 3.19) can only rise to a critical value α_{c} (Eq. 3.20) before the plasma gets unstable with respect to ideal ballooning modes (IBMs). Additionally, as shown in Fig. 3.7a that the current also increases very strongly close to the separatrix. This edge current is mainly driven by the bootstrap current j_{BS}, which is directly related to ∇p_{e} (see Eq. 3.24). A steep current profile in turn yields the formation of ideal peeling modes (IPMs), discussed in Sec. 3.1.3. In general, these two instabilities couple together, which is why the plasma is referred to as peeling-ballooning (P-B) unstable [147]. The P-B theory will be explained as follows with the help of Fig. 3.7b: ∇p or α_{MHD} continues to rise until the IBM limit is reached. Then, ballooning transport occurs and α_{MHD} is slightly reduced, but the temperature at the plasma edge is still rising continuously for a short time, causing a sharp increase in the current density ($j_{0,\parallel}^{\mathrm{norm}}$). The plasma becomes P-B unstable and a strong transport event, i.e. the ELM crash, causes a flattening of the profiles. The process starts all over again.

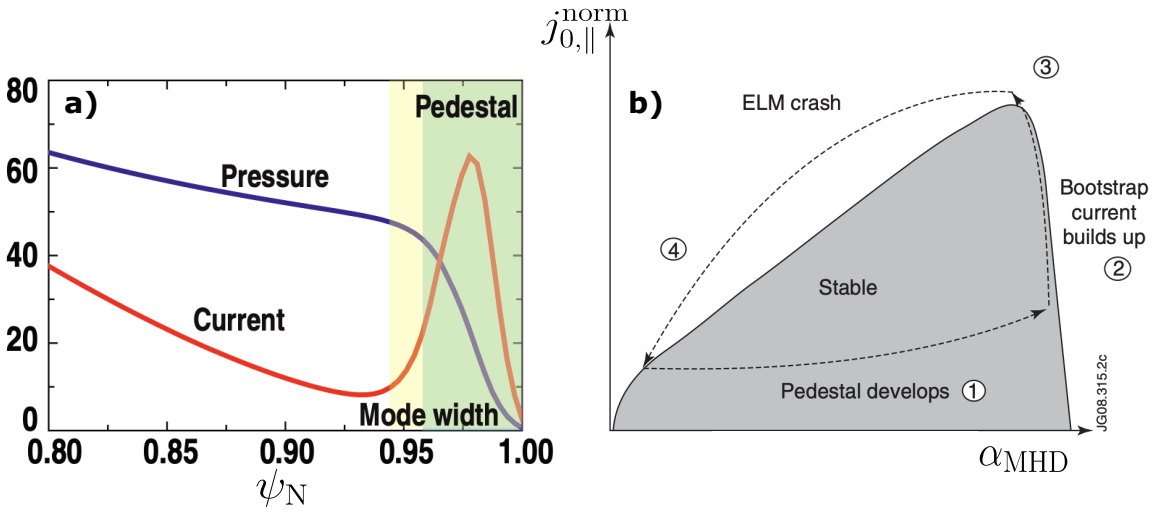

Figure 3.7: Profiles in ELMy H-mode and P-B Theory
a) Typical pressure and current edge profiles of an ELMy H-mode discharge depending on the normalised radius ψ_{N} (see Eq. 1.5). The pedestal is characterized by the green area and the radial expansion of the peeling-ballooning (P-B) mode by the yellowish area, covering the whole pedestal. b) Using the normalised pressure gradient α_{MHD} and the edge current density $j_{0,\parallel}^{\mathrm{norm}}$, the build-up process of the P-B mode at the plasma edge in the tokamak is shown schematically. Fig. a) taken from Ref. [148] and Fig. b) from Ref. [24].

However, it is fundamentally important to note that P-B modes are not as localized as usually assumed: they are subject to finite-n (toroidal mode number) effects and

their radial extent can occupy the entire width of the ETB [149]. The ELM-cycle will be described in the following using the more accurate EPED model [148]. This model is widely accepted nowadays. It attempts to express the P-B constraint by the pedestal height, defined as the electron pressure at the pedestal top $p_{\mathrm{ped}}^{\mathrm{P-B}}$, as a function of the pedestal width Δ_{ped}. It was found that the P-B constraint scales roughly as

$$p_{\mathrm{ped}}^{\mathrm{P-B}} \sim \Delta_{\mathrm{ped}}^{3/4}. \tag{3.44}$$

The second important component of the EPED model is the fact that before the plasma becomes IBM unstable, it will normally become unstable with respect to kinetic ballooning modes (KBM) as described in Sec. 3.2.5. According to Eq. 3.42 the critical pressure limit for KBMs is usually lower than that for IBMs. KBMs cause strong heat and particle transport, so intuitively the P-B constraint should occur while the plasma edge is KBM unstable. However, numerically it has been found that the pedestal width in the KBM case is related to the pedestal height as follows:

$$\Delta_{\mathrm{ped}} = \sqrt{p_{\mathrm{ped}}^{\mathrm{KBM}}} G\left(\nu_{\mathrm{ped}}^{\star}, \varepsilon, \dots\right), \tag{3.45}$$

where G is a function of various dimensionless parameters. Though, G is only weakly varying for standard $\varepsilon \sim 1/3$ tokamaks and has values in the range $G = 0.07 - 0.1$.

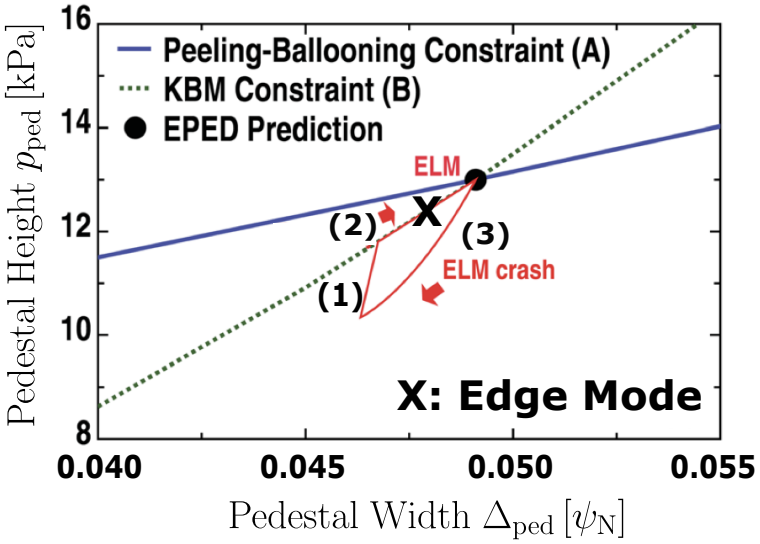

Figure 3.8: EPED Model and Role of Edge Modes
*Schematic presentation of the ELM cycle (red) based on the EPED model. The process is described in detail in the text. The edge mode (**X**) seems to stagnate the recovery phase (2) of the ELM cycle so that the ELM does not occur. Fig. adapted from Ref. [149].*

The KBM and the P-B constraint are displayed in a $\Delta_{\mathrm{ped}} - p_{\mathrm{ped}}$−diagram, depicted in Fig. 3.8, with which the ELM-cycle can be understood as follows: After an ELM

crash, the pressure increases (1) until it comes close to the KBM constraint (green dotted line). Now, Δ_{ped} increases and the pedestal height follows the KBM constraint (2). This remains until the KBM and the P-B constraint (blue line) intersect. Now the ELM gets triggered and the pedestal height and width are rapidly reduced (3). The process starts from the beginning and is called ELM-cycle.

And it is in this cycle that the edge modes, as they appear in ELM-free regimes come into play and interrupts it before the P-B constraint is reached. We now make the following hypothesis: The edge modes influence phase (2) in such a manner, that the pedestal width cannot expand any further and the cycle remains in the recovery phase, symbolized by the black X in Fig. 3.8. This happens mainly because the mode causes sufficient radial transport at the edge to prevent the pedestal height from increasing, which in turn causes the pedestal width to stagnate. The role of the transport caused by edge modes is therefore of utmost importance, which is why the following section is dedicated to this topic.

3.3.2 Linking Mode Transport and Propagation

The radial transport caused by a present edge mode is important to be determined in order to understand the absence of ELMs as described above, but it is generally a parameter that is difficult to access experimentally and can only be determined in very specific plasma scenarios using selected diagnostics, e.g. Langmuir probes [150]. In the following, we will describe the mode transport and then develop an approximation that allows us to estimate the transport by a measurable quantity: the poloidal mode propagation velocity in the plasma frame v_{ph}.

Transport

For the turbulent mode transport induced, only the part of the advection, i.e. the radial particle flow, is generally required [12]

$$\Gamma_{\mathrm{r}} = \Re(\tilde{n}_{\mathrm{e}}\tilde{v}_{\mathrm{r}}^{\star}), \tag{3.46}$$

where $\tilde{v}_{\mathrm{r}}^{\star}$ is the complex conjugate[2] of radial velocity fluctuations and we only need the real part of the expression $\Re(\dots)$. There are two types of transport, both of which can occur simultaneously: electromagnetic and electrostatic. The electromagnetic transport occurs at high plasma β and the instability causes fluctuations in the radial magnetic field $\tilde{B}_{\mathrm{r}}$. However, the electrostatic transport is for the moment more important

[2]The complex representation is only necessary if $\tilde{n}_{\mathrm{e}}$ and $\tilde{v}_{\mathrm{r}}$ are Fourier transformed. Otherwise, one can use the real time series.

for us, since most of the edge modes we will analyze feature a weak electromagnetic signature, and so the electrostatic transport is supposed to be dominant.

Electrostatic turbulent transport is caused by the $E \times B$ drifts resulting from the polarization of pressure perturbations, which are described in detail for both the interchange (Sec. 3.1.1) and drift wave mechanism (Sec. 3.2.1). As described in Eq. 3.46, it is therefore an interplay between density $\tilde{n}_\mathrm{e}$ and E-field fluctuations, or the underlying potential $\tilde{\phi}$. It was already discussed in Sec. 3.2.1 that it is important to consider the circumstance that $\tilde{n}_\mathrm{e}$ and $\tilde{\phi}$ do not have to be phase-locked to each other, so we include a finite phase of both variables, i.e. $\delta_\mathrm{n} \neq 0 \neq \delta_\phi$. Hence, we assume $\tilde{n}_\mathrm{e} = |\tilde{n}_\mathrm{e}| \exp\left[i\left(\boldsymbol{kr} - \omega t + \delta_\mathrm{n}\right)\right]$ for the density and the corresponding wave ansatz for the potential. This yields the following expression:

$$\Gamma_\mathrm{r} = \Re(\tilde{n}_\mathrm{e}\tilde{v}_\mathrm{r}^\star) = \Re\left(|\tilde{n}_\mathrm{e}|\, e^{i\delta_\mathrm{n}} \cdot \frac{ik_\mathrm{y}\left|\tilde{\phi}\right|}{B_\mathrm{t}} e^{-i\delta_\phi}\right) = \frac{k_\mathrm{y}}{B_\mathrm{t}} |\tilde{n}_\mathrm{e}| \left|\tilde{\phi}\right| \sin \underbrace{(\alpha_{\mathrm{n_e},\phi})}_{\delta_\mathrm{n}-\delta_\phi}. \tag{3.47}$$

It can therefore be seen that the transport caused by the mode depends not only on the strength of the respective fluctuations $|\tilde{n}_\mathrm{e}|$ and $\left|\tilde{\phi}\right|$, but also in particular on their cross-phase $\alpha_{\mathrm{n_e},\phi}$. If density and potential are in phase ($\alpha_{\mathrm{n_e},\phi} = 0$), the mode does not cause any transport (stable DW, see Sec. 3.2.1); if they are anti-correlated ($\alpha_{\mathrm{n_e},\phi} = \pi/2$), the mode causes maximum transport (IC, see Sec. 3.1.1).

Mode Propagation and its Relation to the Cross-Phase

If the poloidal structure size in terms of k_θ and the frequency ω are known, the velocity in poloidal direction can be calculated as

$$v_\mathrm{mode} = \frac{\omega}{k_\theta}. \tag{3.48}$$

Here we assumed that $k_\parallel$, k_r and v_r are really small at the plasma edge in general and only the poloidal component contributes to ω. It was mentioned in the introduction that the phase velocity of the mode in the co-moving plasma frame v_ph is of particular importance in order to identify the edge modes. ω can usually be measured by diagnostics from the 'outside', i.e. the diagnostic is not following the propagation of the mode. Here, we are in the so-called laboratory frame and the velocity is called v_lab. However, the plasma as a whole also rotates poloidally with the $E \times B$ background velocity $v_\mathrm{E\times B}^\mathrm{bg}$, which will be denoted as $v_\mathrm{E\times B}$ in the following. The radial electric field E_r induces the $E \times B$ drift [151], which reads according to the poloidal component of the force balance

$$v_\mathrm{E\times B} = \frac{E_\mathrm{r}}{B_\mathrm{t}} = \frac{\nabla p_\mathrm{i}}{e n_\mathrm{i} B_\mathrm{t} Z_\mathrm{i}} - v_\mathrm{pol} + v_\mathrm{t}\frac{B_\mathrm{pol}}{B_\mathrm{t}}, \tag{3.49}$$

where Z_i is the ion charge number, $p_\mathrm{i} \approx p_\mathrm{e}$ is the ion pressure and v_pol and v_t are the poloidal and toroidal rotation velocities, respectively. It is visible, that ion temperature and density data is needed here. In order to obtain the intrinsic mode velocity, the $E \times B$ velocity must be subtracted from the measured lab velocity,

$$v_\mathrm{ph} = v_\mathrm{lab} - v_\mathrm{E\times B}. \tag{3.50}$$

In order to derive a relation between the mode propagation and the cross-phase between density and potential fluctuations, we consider a perturbation of the density and the $E \times B$ background velocity, where the equilibrium velocity vanishes, i.e. $v_\mathrm{ExB,0} = 0\,\mathrm{km\,s^{-1}}$, hence:

$$n = n_0 + \overbrace{|\tilde{n}|\, e^{i\left(k_\theta r - \omega_\mathrm{ph} t + \delta_\mathrm{n}\right)}}^{\tilde{n}}, \tag{3.51}$$

$$v_\mathrm{ExB} = \frac{-\nabla\tilde{\phi}}{B_\mathrm{t}} = \frac{i k_\theta \left|\tilde{\phi}\right| e^{i\left(k_\theta r - \omega_\mathrm{ph} t + \delta_\phi\right)}}{B_\mathrm{t}}. \tag{3.52}$$

The continuity equation 3.4 to first order leads to the following calculation [152]:

$$\begin{aligned}
-i\omega_\mathrm{ph}\,|\tilde{n}|\, e^{i\left(k_\theta r - \omega_\mathrm{ph} t + \delta_\mathrm{n}\right)} &= \frac{i k_\theta \left|\tilde{\phi}\right| e^{i\left(k_\theta r - \omega_\mathrm{ph} t + \delta_\phi\right)}}{B_\mathrm{t}} \nabla n_0 \\
\xRightarrow{\text{Eq. 3.48}}\; k_\theta v_\mathrm{ph} &= -\frac{k_\theta \left|\tilde{\phi}\right| \nabla n_0}{|\tilde{n}|\, B_\mathrm{t}} e^{i\left(\delta_\phi - \delta_\mathrm{n}\right)} \\
\xRightarrow{\text{real part}}\; v_\mathrm{ph} &= \underbrace{-\frac{\left|\tilde{\phi}\right| \nabla n_0}{|\tilde{n}|\, B_\mathrm{t}}}_{>0} \cos\left(\alpha_{\mathrm{n_e},\phi}\right).
\end{aligned} \tag{3.53}$$

The pre-factor is positive, because ∇n_0 is always negative at the plasma edge. This results in a similar relation to that above for the transport, where the cross-phase $\alpha_{\mathrm{n_e},\phi}$ also appears, but here via the cosine. If density and potential fluctuations are in phase, i.e. $\alpha_{\mathrm{n_e},\phi} = 0$, the Boltzmann relation from Eq. 3.28 holds, i.e. $-\left|\tilde{\phi}\right| \nabla n_0 / \left(|\tilde{n}|\, B_\mathrm{t}\right) = v_\mathrm{e,dia}$ and hence, $v_\mathrm{ph} = v_\mathrm{e,dia}$. This is the drift wave case from Sec. 3.2.1. However, if $\alpha_{\mathrm{n_e},\phi} = \pi/2$, as in the interchange case, the mode would not propagate in the plasma frame. Further, for cross-phases above $\alpha_{\mathrm{n_e},\phi} > \pi/2$, the cosine in Eq. 3.53 would take on negative values and the mode would propagate in the ion diamagnetic direction, reaching a maximum velocity at $\alpha_{\mathrm{n_e},\phi} = \pi$. In a final step, the relations 3.47 and 3.53 will be combined and discussed.

Relation Between Transport and Phase Velocity

The equation describing the turbulent mode transport (Eq. 3.47) and the one describing the phase velocity in the plasma frame (Eq. 3.53) can be combined. To do this, we rearrange Eq. 3.53 to get the cross-phase $\alpha_{\mathrm{n_e},\phi}$, insert it into Eq. 3.47 and use the trigonometric theorem $\sin(\arccos x) = \sqrt{1-x^2}$, and get

$$\Gamma_\mathrm{r} = \frac{k_\mathrm{y}}{B_\mathrm{t}} \left|\tilde{n}_\mathrm{e}\right| \left|\tilde{\phi}\right| \sqrt{1 - \left| \frac{v_\mathrm{ph}}{\left|\tilde{\phi}\right| \nabla n_0 / (\left|\tilde{n}_\mathrm{e}\right| B_\mathrm{t})} \right|^2}. \tag{3.54}$$

Eq. 3.54 suggests that all modes with a velocity of $v_\mathrm{ph} = v_\mathrm{e,dia}$ (drift-wave) do not cause radial transport. In this case, the Boltzmann relation (Eq. 3.28) can be used to convert the denominator to the electron diamagnetic velocity $v_\mathrm{e,dia}$. In all other cases, the Boltzmann relation cannot be used. However, Γ_r increases for decreasing phase velocity v_ph, reaching a maximum for $v_\mathrm{ph} = 0\,\mathrm{km\,s^{-1}}$ (interchange) for otherwise constant parameters. If the mode propagates in ion diamagnetic direction, the radial transport decreases with increasing velocity again.

In the above calculation, care must be taken to ensure that the trigonometric theorem only applies in the way it has been applied if $|\arccos x| \leq \pi$. If this is not the case, a minus sign has to be added to Eq. 3.54, which is physically similar to radial inward transport.

3.3.3 Candidates for Edge Modes

Tab. 3.1 summarizes all the presented instabilities based on the normalized poloidal wavenumber $k_\theta \rho_\mathrm{s}$ and the phase velocity v_ph, which is normalized to the ion diamagnetic velocity $v_\mathrm{i,dia}$. Hence, a value of $v_\mathrm{ph}/v_\mathrm{i,dia} = -1$ indicates a phase velocity of $v_\mathrm{ph} = -v_\mathrm{i,dia} = v_\mathrm{e,dia}$ ($T_\mathrm{e} = T_\mathrm{i}$) in electron diamagnetic direction (EDD). Many modes are similar and almost indistinguishable, and in particular their drive is difficult to determine experimentally, but with known $k_\theta \rho_\mathrm{s}$ and v_ph it might be possible to identify the edge modes of the ELM-free regimes. For instance: if the mode propagates in ion diamagnetic direction (IDD), we can eliminate some possible candidates from the list. Then, only the three ballooning modes, i.e. ideal (IBM), resistive (RBM) and kinetic (KBM) or the ion temperature gradient mode (ITG) would remain. Other instabilities like micro-tearing modes (MTM), drift wave (DW), trapped electron mode (TEM), kinetic peeling ballooning mode (KPBM) or the electron temperature gradient mode (ETG) would remain, if the mode propagates in EDD. The latter is driven on very small scales, which means high $k_\theta \rho_\mathrm{s}$. In terms of poloidal wavenumber, the ideal peeling modes (IPM) stands out as well, since it is very small in the poloidal plane. The last

Table 3.1: Summary of Instabilities

All described plasma edge instabilities from Secs. 3.1, 3.2 and their main properties, i.e. their drive, phase velocity in the plasma frame v_{ph} and normalized poloidal wavenumber $k_\theta \rho_{\mathrm{s}}$, are summarized and references are given. Tab. adapted from Ref. [127].

Instability	Drive	$v_{\mathrm{ph}}/v_{\mathrm{i,dia}}$	$k_\theta \rho_{\mathrm{s}}$	Ref.
IPM	$J_{\|\|}$	0	$\ll 0.1$	[123, 153]
IBM	∇p	0–0.5	< 0.1	[117, 154]
RBM	∇p	0–1.0	< 0.1	[155]
KPBM	∇p	< 0	~ 0.1	[126]
KBM	$\nabla T_{\mathrm{e}}, \nabla T_{\mathrm{i}}$	0–1	0.1	[140]
MTM	∇T_{e}	$\sim$ -1	0.1	[127, 144, 156]
DW	∇n	-1	0.1-1	[131]
ITG	∇T_{i}	0–1	0.1-1	[128]
TEM	$\nabla T_{\mathrm{e}}, \nabla n$	< 0	> 0.1	[128]
ETG	∇T_{e}	-1–0	> 1	[128]

column provides references for the reader to internalize the corresponding instability.

Now that we know what quantities are required to identify the edge mode, it is discussed in the following chapter, which experimental methods can be used to determine mode properties and other relevant plasma quantities

4 Diagnostics and Methods

Having introduced the high-confinement regimes, featuring the absence of type-I edge localized modes (ELMs) and their characterizing edge fluctuation, and having laid the theoretical foundation for how edge modes can lead to the absence of ELMs, we now focus on two questions: how do we detect edge modes and, in particular, how do we obtain their characterizing quantities in order to compare them with the linear plasma edge instabilities from Sec. 3.3.3?

The fusion experiment, on which all following investigations have been carried out is the ASDEX Upgrade tokamak (AUG). Its setup and achievements are briefly described in the first part of this chapter. To answer the question of how we can detect edge modes, we will introduce the most relevant diagnostics at AUG in the second step. It is worth noting that there are a lot of diagnostic tools that are able to analyze edge modes in principle, and they all offer advantages and drawbacks. A worthwhile goal for all diagnostics is to come to the same conclusion and diagnose the edge mode in a consistent way. However, this thesis focuses on measurements of the thermal helium beam spectroscopy (THB). Therefore, a large section is dedicated to this diagnostic, in which the working principle is presented [157, 158] and, in particular, all the diagnostic effects that need to be taken into account in order to reliably investigate the edge modes are discussed. The latter part is based entirely on Ref. [159]. This is followed by a brief introduction to supporting diagnostics that will appear later. Finally, the methods of transforming the raw data from the diagnostics - especially the THB - in such a way that we can obtain useful information for analysing the edge fluctuations are presented.

4.1 ASDEX Upgrade

The 'AxialSymmetrisches Divertor-EXperiment' Upgrade or short, ASDEX Upgrade (AUG) is a fusion experiment, based on the tokamak principle (see Sec. 1.2) and is in operation since 1991 at the Max Planck Institute for Plasma Physics in Garching, Germany. AUG is a medium-sized machine whose design and maximum operating parameters are given in Tab. 4.1. In particular, the device is designed to develop scenarios that can be put into operation for the future fusion devices ITER (see Tab. 4.1) and DEMO. These scenarios are the subject of this thesis. In particular, AUG can

operate scenarios, which obey the same shaping, i.e. triangularity δ and elongation κ_{geo}, as those desired for ITER. Furthermore, AUG can generate different topologies of magnetic field lines. The X-point can be both above (upper single null, USN) or below the magnetic axis (lower single null, LSN), or even on both sides simultaneously (double null, DN). Nonetheless, the most experiments presented in this thesis are performed in the LSN configuration as shown in Fig. 4.1a. In addition, mainly deuterium plasmas are ignited, although hydrogen and helium plasmas are also possible.

Table 4.1: Design and Maximum Operation Parameters of AUG and ITER
Listed are the major R_{maj} and the minor radius a_{min}, the plasma volume V_{pl} as well as the maximum possible triangularity δ [160] and elongation κ_{geo}. Further, the maximum achievable toroidal magnetic field strength B_{t}, plasma current I_{p}, auxiliary heating powers P_{aux} and the plasma pulse length τ_{pulse} are shown. Values for ITER taken from Ref. [161].

Quantity	AUG	ITER
R_{maj} [m]	1.65	6.2
a_{min} [m]	0.5	2
V_{pl} [m^3]	13	840
δ	0.55	0.48
κ_{geo}	1.83	1.85
B_{t} [T]	3.2	5.3
I_{p} [MA]	1.6	15
P_{aux} [MW]	30	73
$P_{\mathrm{aux}}/V_{\mathrm{pl}}$ [MW/m^3]	2.3	0.08
τ_{pulse} [s]	10	400

AUG and its predecessor ASDEX have achieved several milestones in fusion research. As mentioned at the beginning of the thesis in Sec. 1.3, the high-confinement mode (H-mode) has been discovered by Wagner *et al.* in ASDEX [26]. A special feature of AUG is that it has an extremely high heating power for its machine size (see Tab. 4.1). The neutral beam injection (NBI) heating can reach values of up to $P_{\mathrm{NBI}} = 20\,\mathrm{MW}$ and the two wave heating systems peak values of up to $P_{\mathrm{ECRH}} = 6\,\mathrm{MW}$ (electron cyclotron resonance heating, ECRH) and $P_{\mathrm{ICRH}} = 4\,\mathrm{MW}$ (ion cyclotron resonance heating , ICRH). The fact that the surface of all plasma facing components (PFCs) are made of tungsten (W) is also of great importance. At AUG the divertor is made of solid tungsten tiles. Many studies in AUG have demonstrated the great advantage of W and ITER and DEMO will most likely have a divertor and the first wall made of W [162].

All these features demonstrate that AUG is a fusion experiment for conducting feasibility studies of potential plasma scenarios for operation in ITER. Moreover, the AUG experiment has a range of diagnostics to analyze the processes that take place

at the plasma edge and to measure different plasma profiles. Fig. 4.1 shows a poloidal a and toroidal b cross section of AUG, incorporating all of the diagnostics described below and their lines of sight. We start with the thermal helium beam spectroscopy (THB), which measures at the outer midplane.

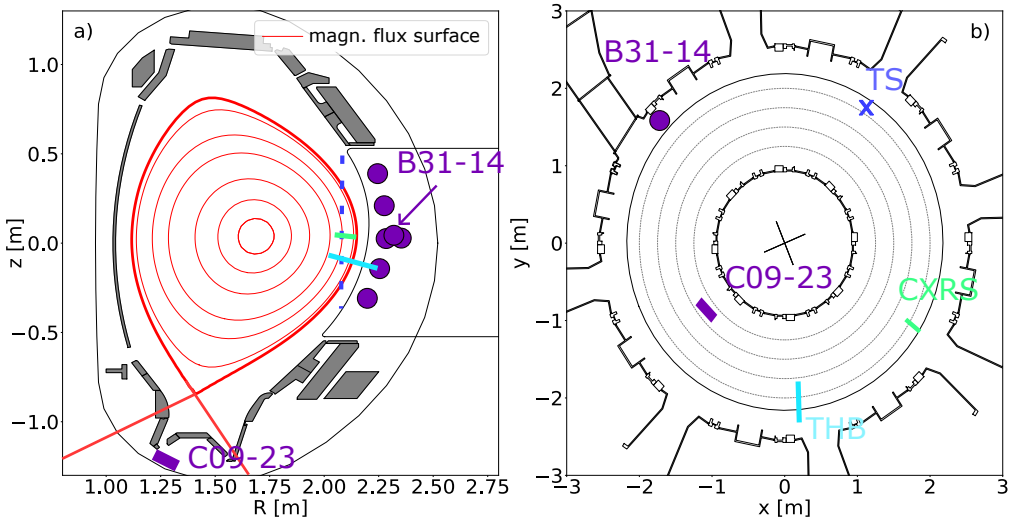

Figure 4.1: Poloidal and Toroidal Cross Section of AUG With Diagnostics *Illustration of the position and measurement points of the thermal helium beam (THB) in cyan, poloidal (square) and radial (round) magnetic coils in purple, edge Thomson scattering (TS) in blue and the charge exchange recombination spectroscopy (CXRS) in green in the poloidal a) and toroidal b) cross section of AUG. In addition, the magnetic field lines (red) for the EDA H-mode #38067 ($t = 4.0\,\mathrm{s}$) are shown in the poloidal plane.*

4.2 Thermal Helium Beam

As shown in Fig. 4.1a, the thermal helium beam diagnostic (THB) is located just below the outer midplane. The in-vessel components of the THB are shown on the left of Fig. 4.2, and the basic idea of the diagnostic is based on the principle of active spectroscopy [163], which will be explained in the following. First, a cloud of neutral helium particles is locally injected into the plasma edge via an in-vessel piezoelectric valve [164]. The flow rate is about 10^{19} He particles per second and does not affect the local electron density and temperature values of the D-plasma at the edge [165]. The He atoms have velocities of about $v_{\mathrm{He}} \sim 1760\,\mathrm{m\,s^{-1}}$ [166]. Once in the plasma, the He atoms collide mainly with the plasma electrons and get excited. Light is emitted by spontaneous emission. He is the lightest atom having two valence electrons in the innermost atomic orbital, the $s-$ orbital. Hence, He exists in the so-called singlet state,

i.e. the spins of the electrons are anti-parallel, and in the triplet state, i.e. the spins of the electrons are parallel. Therefore, when He is de-excited, photons of different energies, i.e. different wavelengths λ, are emitted from the singlet and triplet states. All the light emitted by He is collected by the optical head for up to 52 lines of sight (LOS) and transmitted through optical fibers into a polychromator system, shown on the right of Fig. 4.2. There, dichroic mirrors and interference filters separate the light intensity into four wavelengths, with $\lambda_2 = 667\,\text{nm}$ and $\lambda_4 = 728\,\text{nm}$ coming from the singlet state and $\lambda_1 = 587\,\text{nm}$ and $\lambda_3 = 706\,\text{nm}$ from the triplet state. Finally, the light path ends in photomultiplier tube (PMT) arrays, where the line emission intensity I_{λ_i} of the corresponding He line is measured for each LOS. The signal gets converted by analog-to-digital converters (ADCs), which allow a temporal resolution of 900 kHz. Although it is possible to localize the light from the injected He atoms using 3D forward modeling [157], it is superimposed with background radiation caused by Bremsstrahlung, present everywhere in the plasma. In order to be able to assign the emitted He light radially and poloidally, the He gas is not permanently blown into the tours, but chopped. Both active phases (A), in which the He gas is actively injected, and passive phases (B), in which only the background radiation is collected, last typically 50 ms. The active signal is cleaned up by subtracting the background. The chopping has been already visible in the spectrograms of Chapter 2 as vertical stripes (e.g. in Fig. 2.1e). We will see later in this section that the possibility to obtain background information is of utmost importance when analyzing edge modes.

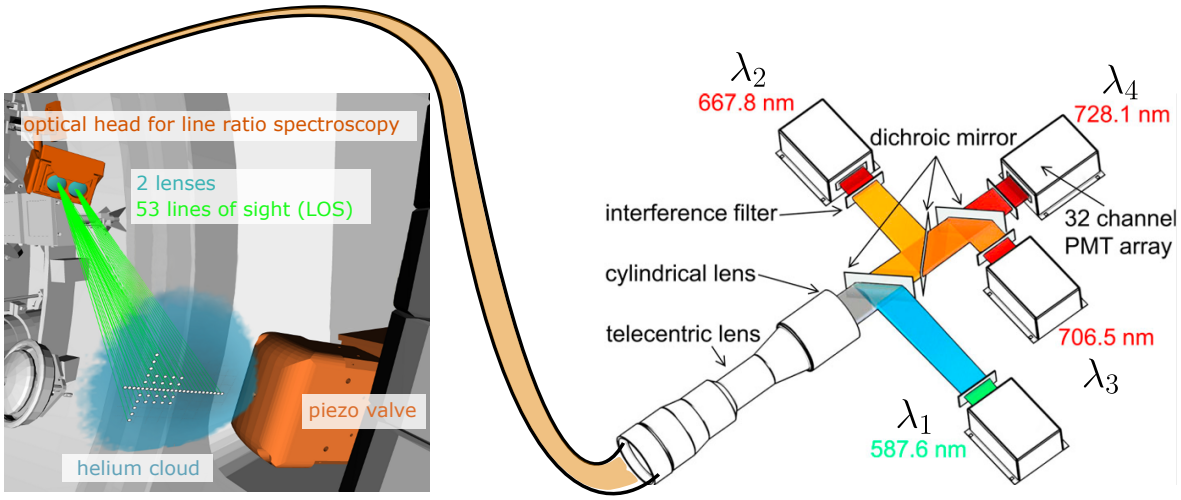

Figure 4.2: Experimental Setup of the Thermal Helium Beam Diagnostic
Left: The in-vessel components and the injected He cloud (blue) of the THB diagnostic are shown. The collected light is transmitted via optical fibres to the polychromator system on the right, which splits the light into four wavelengths. Figs. adapted from Ref. [157].

As mentioned above, it is possible to analyze several arbitrarily arranged LOS simultaneously. The THB measures 32 local channels with a spatial resolution of up to 3 mm. Typical LOS arrangements are depicted in Fig. 4.3, in which the high radial resolution grid (see Fig. 4.3a) and the 5×5 grid (Fig. 4.3b), allowing 2D intensity measurements, are shown. In general, the LOS cover the whole pedestal and extend out into the far scrape-off layer (SOL). Most important for the 5×5 grid is that the channels are located along the poloidal flux surface (red), which allows to access quantities in the poloidal direction, such as the poloidal wavenumber k_θ (cf. Sec. 4.4).

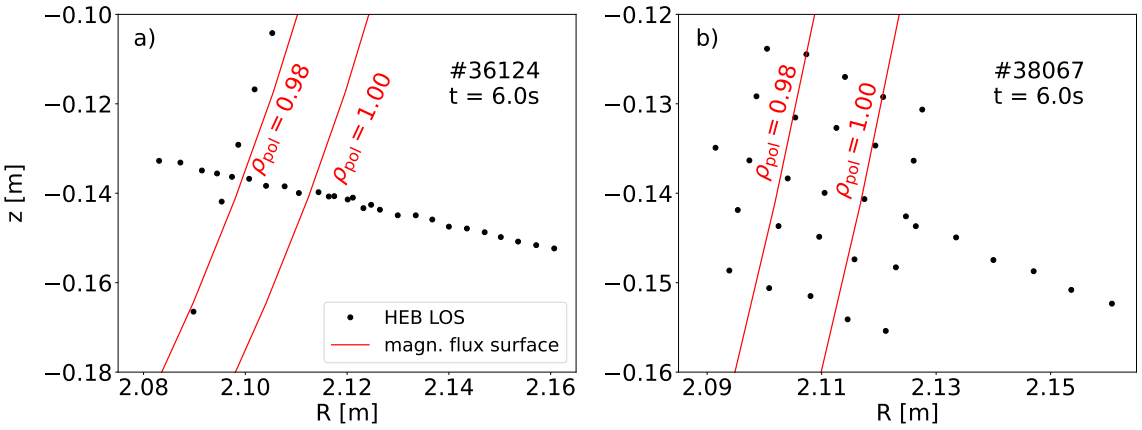

Figure 4.3: Lines of Sight Arrangement at AUG
Two thermal helium beam grid possibilities for two different discharges: either the lines of sight (LOS) are distributed radially a) or in a 5×5 grid, enabling poloidal and radial analyses b). The magnetic flux surfaces at the edge (red) are also depicted.

Interpretation of the THB Data - Challenges and Solutions

So far it has been reported that the THB diagnostic would measure the line emission intensity I_{λ_i}, but what does this quantity provide us in a physical context in terms of information about the edge modes? In fact, I_{λ_i} is related to the electron density n_e and temperature T_e as follows:

$$I_{\lambda_i} = n_\mathrm{He} n_\mathrm{e} \mathrm{PEC}_{\lambda_\mathrm{i}} (n_\mathrm{e}, T_\mathrm{e}) \,. \tag{4.1}$$

n_He is the neutral He density and $\mathrm{PEC}_{\lambda_\mathrm{i}}$ is the photo emission coefficient for the corresponding wavelength, depending on n_e and T_e, and are taken from the atomic data and analysis structure (ADAS) [167]. This means that the THB allows to derive information about the electron density n_e and temperature T_e from the measured I_{λ_i} and due to the many radial channels, the THB is a profile diagnostic. For this purpose a reconstruction algorithm that includes collisional radiative modeling is used and reliable

intensity measurements of at least three wavelengths are required. In most cases, only two wavelengths deliver reliable measurements in the confined region of the plasma, i.e. inside the LCFS. These can still be used to reliably investigate the fluctuations. Nevertheless, this means if we observe a fluctuation via the THB, i.e. a fluctuation in I_{λ_i}, we see the influence of the edge mode on n_e and/or T_e. Unfortunately, due to diagnostic effects, it is not the case that we can directly extract the needed information about the temperature or density fluctuation amplitudes from the raw data. This is because Eq. 4.1 represents a non-linear and non-monotonic relation between I_{λ_i} and n_e, T_e and n_He. It is even the case that n_He, n_e and $\mathrm{PEC}_{\lambda_\mathrm{i}}$ behave differently along the radial axis. Besides the non-linearity of Eq. 4.1, another diagnostic effect yielding misleading interpretations is the so-called shadowing effect, caused by the n_He dependence of the line emission intensities.

To demonstrate the importance of these misleading diagnostic effects, a synthetic diagnostic has been set up to compare the synthetic results with experimental data. For this purpose, we imitate an edge mode of an EDA H-mode (see Sec. 2.2.1), i.e. the quasi-coherent mode (QCM), by implementing a 40% in-phase fluctuation (compared to the background) with a frequency of 29 kHz in a restricted radial range of $\rho_\mathrm{pol} = [0.99, 1.01]$ on top of steady-state n_e and T_e background profiles. A noise signal was also added. The radial synthetic density input is shown in a space-time representation in Fig. 4.4. The same pattern is obtained for the temperature, but it is not shown here.

The colorbar reflects the intensity of the respective quantity, normalized for each radial channel individually according to $(I - min(I)) \,/\, (max(I - min(I)))$, shown in Fig. 4.4. Here, $min(\dots)$ and $max(\dots)$ describe the extreme values in the time series of the respective channel. The artificial mode is clearly visible in the region mentioned above. Further in, i.e. $\rho_\mathrm{pol} < 0.99$, the signal is dominated purely by the noise with no mode present by construction. In addition, filaments can also be seen, which we will not discuss here, but will return to in Chapter 6. Fig. 4.4b shows the neutral He density, with the red arrow representing the injection. The arrow is tilted, because the He propagates radially inwards with a finite velocity of $v_\mathrm{He} \sim 1760\,\mathrm{m\,s^{-1}}$. Immediately we see that this circumstance and the interplay of the mode and the injected He leads to a tilting of the mode structure in n_He. Even more significant is the fact that the mode activity is not only seen in the implemented restricted radial region, but also further inward. The He thus carries the mode signal inwards. Exactly this circumstance is called shadowing effect [159, 168, 169]. The multiplication of Figs. 4.4a and 4.4b and the corresponding photo emission coefficients leads to the measured signals, according to Eq. 4.1. Figs. 4.4c and 4.4d show the intensities for the triplet 587 nm and the singlet 667 nm line, respectively. These two lines are preferred, because

they achieve the highest signal-to-noise ratio (SNR). The shadowing is also present here. Furthermore, in Fig. 4.4d there is even a doubling of the frequency just outside the separatrix (horizontal white line), which is a well-documented diagnostic effect [158]. It is obvious that the experimental data taken from a single wavelength measurement can not directly be used to reconstruct mode properties, especially when it comes to inward cutoffs of reliable measurements. This means that all spectroscopic measurements based on the principle of single line measurements should be treated with caution.

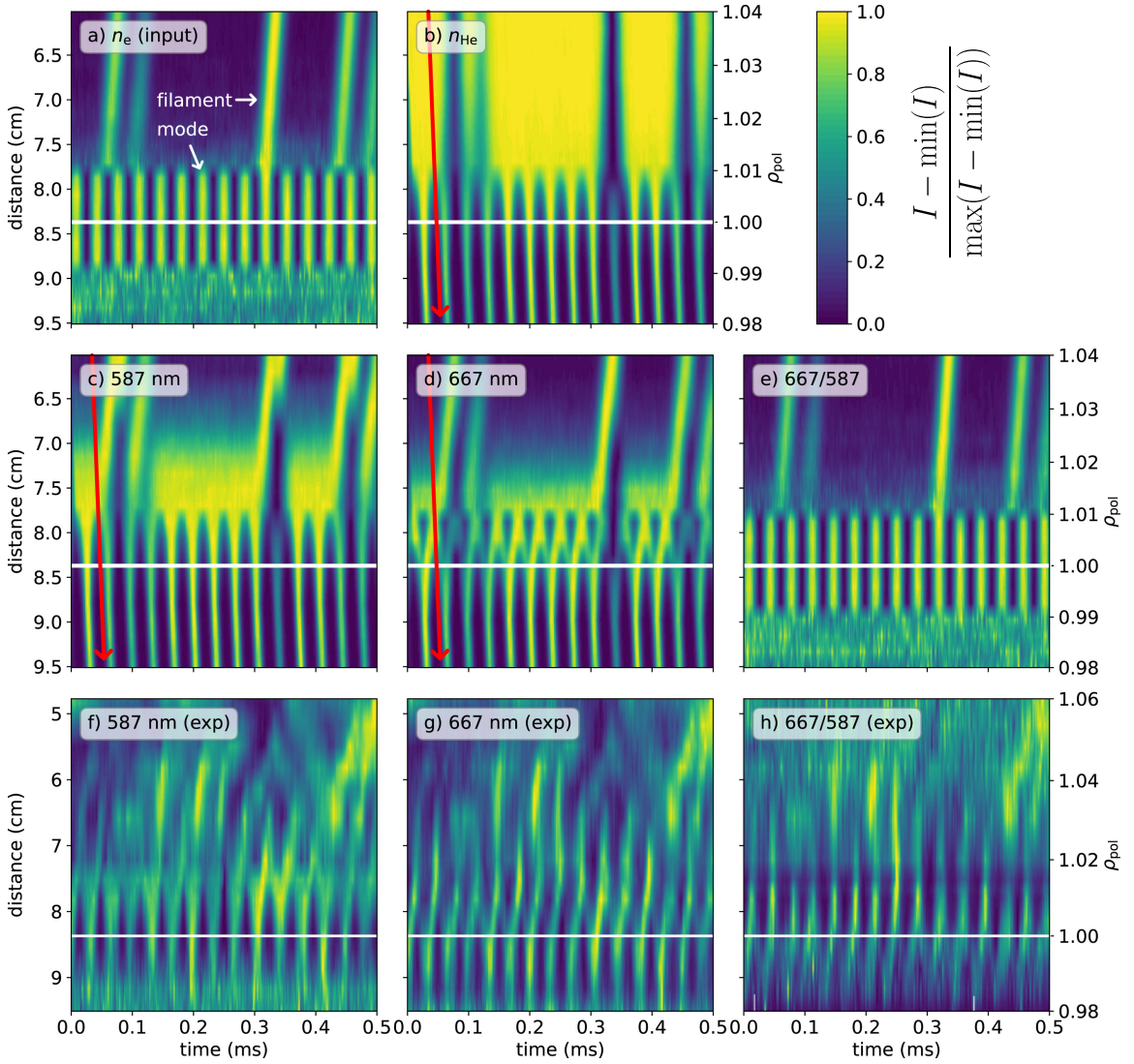

Figure 4.4: Diagnostic Effects in Forward Model and Experiment

The color code is the normalized intensity of the corresponding quantity. a) shows the electron density input n_e (T_e is given the same way, not shown) with the artificial mode around the separatrix (white horizontal line). In b) the He injection path is represented by the red arrow and the neutral He density n_{He} is shown. The line emission intensities I_{587} and I_{667} for modeled c), d) and experimental f), g) data feature a modulated behavior. In contrast, the line ratio I_{667}/I_{587} corresponds to the input e), h). Fig. adapted from Ref. [159].

However, we are in the fortunate position of being able to measure four wavelengths simultaneously, and by taking the ratio of two lines, we can get rid of the n_{He} dependence, which is the origin of the diagnostic effects, i.e.

$$\frac{I_{667}}{I_{587}} = \frac{n_{\mathrm{He}} n_{\mathrm{e}} \mathrm{PEC}_{667}\left(n_{\mathrm{e}}, T_{\mathrm{e}}\right)}{n_{\mathrm{He}} n_{\mathrm{e}} \mathrm{PEC}_{587}\left(n_{\mathrm{e}}, T_{\mathrm{e}}\right)} = \frac{\mathrm{PEC}_{667}\left(n_{\mathrm{e}}, T_{\mathrm{e}}\right)}{\mathrm{PEC}_{587}\left(n_{\mathrm{e}}, T_{\mathrm{e}}\right)}. \tag{4.2}$$

The modeled data of the line ratio I_{667}/I_{587} is depicted in Fig. 4.4e and is similar to the input from Fig. 4.4a. Since all considered diagnostic effects are eliminated, the mode can be reliably analyzed in terms of frequency, radial location and other parameters. This will be shown in the following chapters using the line ratio technique. Very similar dynamics can be observed from the experimental data in Figs. 4.4f-h.

Reliability Boundaries

In a final step, we determine to what extent we can trust the measurements of the THB signal. Usually there is no outer boundary, as the shadowing effect, for example, only shifts the inner boundary of the mode, so we only consider inner boundaries. Since the line ratio technique is the key, the measurements of both lines individually must provide sufficient signal strength towards the plasma center. The analysis of the individual lines must again take into account effects such as frequency doubling. For example, if I_{587} is dominated by noise, there is only useful information contained in signal I_{667} and hence, we are again affected by the diagnostic effects mentioned above. In particular, the strong decrease of the He density towards the inside results in low emission and therefore a weak signal. In the following two qualifying variables are presented, which should indicate the reliability of the data and base on the experimental data of the above mentioned EDA H-mode and its present QCM.

The first qualifier is the signal-to-noise ratio (SNR). To obtain the undisturbed signal level, it is important to remove the influence of the QCM from the signal. Otherwise the assessment of noise by means of the standard deviation could be contaminated by the QCM fluctuation amplitude. This is done with a band-stop filter of $\pm$ 10 kHz around the QCM frequency and $\pm$ 5 kHz around its first harmonic (due to frequency doubling). The SNR is then defined as the background subtracted signal divided by its standard deviation. The result of the calculated SNR along ρ_{pol} is shown in Fig. 4.5a. The highest values are obtained in the near scrape-off layer (SOL) and decrease outward as the standard deviation increases due to non-coherent plasma perturbations, i.e. filaments [170]. The SNR also decreases inwards as the signal becomes weaker, where a value of 1 means that the signal cannot be distinguished from the noise.

For the second qualifier, we have to keep in mind that the mode is measured not only in active phases (A), in which the He is puffed, i.e. collecting light from the He cloud,

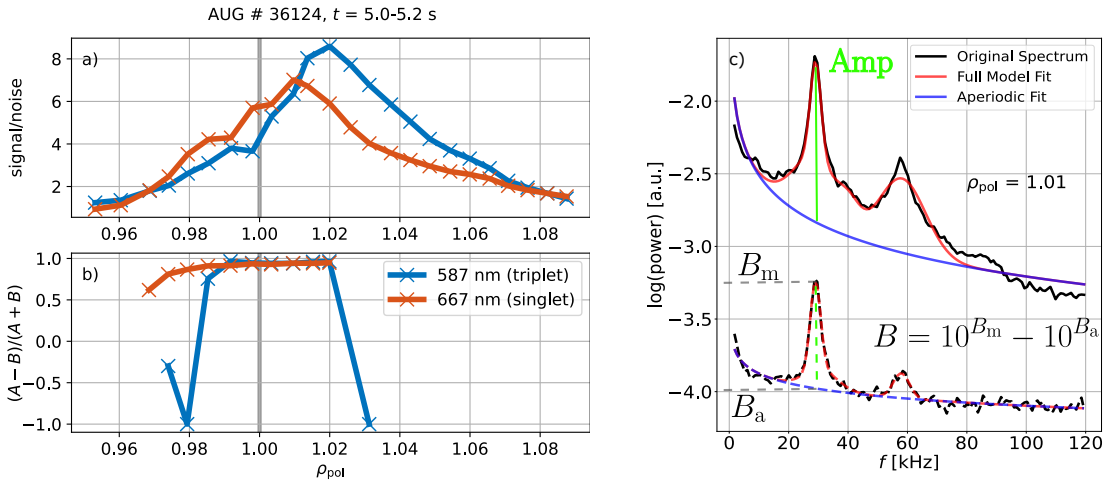

Figure 4.5: Qualifying Elements Regarding the Reliability of THB Data
a) signal-to-noise ratio for the singlet (red) and triplet (blue) He lines peaks just outside the separatrix (gray vertical). The other element represents the degree of localization of the measurement b), which can be calculated from the Fourier spectrum c). Solid lines represent the measurement in an active phase, where one can find the amplitude Amp of the mode (lime green), and dashed lines represent the background phase. Figs. a) and b) taken from Ref. [159].

but also during background phases (B), which represent the activity in the passive He signal with non-local contributions along the full length of the LOS stemming from a wide radial range of the plasma (see Fig. 2.1e). Thus, to be sure that the mode is only measured locally in the He cloud at the selected localized LOS, we need to compare the impact of the QCM, i.e. its amplitude, in both phases. To extract the mode amplitude that lies on top of the aperiodic noise, we evaluate a Fourier spectrum (see Sec. 4.4) for the signals from active phases (solid lines) and background (dashed lines) separately, as shown in Fig. 4.5c. We defined the normalized qualifier for a localized mode measurement as: $(A - B) / (A + B)$ with A as the mode amplitude in the active phase and B the mode amplitude in the background (beam-off phase). By definition, $A \geq B$, since a mode, which only appears in the background signal would have the same or a larger amplitude in the active signal, because the background signal is naturally a part of the active signal. A negative qualifier comes from the fact that no mode is visible in either signal, but a noise at the corresponding frequency is measured in the background. Fig. 4.5c shows how to calculate B, but for A it is the same way. This quantity is shown as a function of ρ_{pol} in Fig. 4.5b. A value of one means that $A \gg B$, i.e. the mode activity is well localized, and a value of zero means that $A = B$, i.e. the measurement is not localized at all since the mode amplitude in the active signal is fully given by the amplitude as it appears in the background. If the

mode is not visible in both phases, i.e. $A = B = 0$, the qualifier is not defined. We can see that the 587 nm-line is only valid for localized measurements in radial regions $\rho_{\mathrm{pol}} > 0.98$. Together with the SNR values from Fig. 4.4a we conclude that the QCM can be analyzed for the corresponding discharge and time interval reliably in radial ranges $\rho_{\mathrm{pol}} > 0.98$.

At this stage we have carefully considered various diagnostic effects and shown that it is possible to reliably analyze edge modes via the line ratio technique, i.e. I_{667}/I_{587}. Furthermore, it is even possible to decouple n_{e} and T_{e} by choosing the 'right' line ratio, but we will come back to this later in Sec. 4.4. Before we introduce the methods of processing the data provided by the THB into useful and valuable information about the different edge modes, we will present the working principle of other diagnostics in the following.

4.3 Supporting Diagnostics

Although it would be excellent, it is usually not possible to obtain all the desired edge mode properties and all the required plasma quantities with a single diagnostic. Therefore, a combination of various diagnostic tools are used.

As mentioned in Sec. 4.2, THB measurements give an indication of perturbations in the electron density and/or temperature, i.e. for electrostatic turbulence (see Sec. 3.3.2). However, modes can also drive electromagnetic turbulence, which can only be detected with magnetic coils, which will be presented first. Furthermore, it has been often assumed that the electron data is the same as the ion data, i.e. $T_{\mathrm{e}} = T_{\mathrm{i}}$. Though, we need explicit ion data for the radial electric field E_{r} from Eq. 3.49, for example. This is measured with the charge exchange recombination spectroscopy (CXRS) and can also compare our assumption in this way. Generally the integrated data analysis (IDA) tool is used to read out profile sizes at different radial positions, e.g. p_{e}. For a later separatrix analysis we need values of $n_{\mathrm{e,sep}}$ and $T_{\mathrm{e,sep}}$ that are evaluated close to the separatrix, which is done by the Thomson Scattering (TS) diagnostic.

Magnetic Pick-Up Coils

Magnetic pick-up coils [171] are the most common diagnostic used to measure deviations from the magnetic equilibrium. They directly measure a voltage that is induced by a time-varying magnetic field via Faraday's law and offer a high temporal resolution of 2 MHz. The coils can be used in any arrangement and can therefore detect deviations in the radial $\tilde{B}_{\mathrm{r}}$, poloidal $\tilde{B}_{\theta}$ and toroidal $\tilde{B}_{\mathrm{t}}$ directions. $\tilde{B}_{\mathrm{r}}$ is particularly important for the electromagnetic transport (see e.g. Fig. 2.1f), and we will see measurements of $\tilde{B}_{\theta}$-coils later (see Fig. 2.3f). The position of the coils used in the following is shown

in Fig. 4.1. However, magnetic pick-up coils do not provide radial information about the measured instability.

Charge Exchange Recombination Spectroscopy (CXRS)

Similar to the thermal helium beam diagnostic (THB), charge exchange recombination spectroscopy (CXRS) [172] is a spectroscopic diagnostic, so an emission spectrum is measured at the end. This emission spectrum then provides information about the ion temperature T_i and the poloidal and toroidal rotation speed of the plasma v_pol and v_t, respectively. Both pieces of information are needed to determine the radial electric field E_r (Eq. 3.49). In contrast to THB, neutral deuterium D^0 is usually injected into the plasma, e.g. via NBI heating beams (Sec. 2.1). The plasma ions (impurities) are excited by charge exchange with D^0 and emit a photon during de-excitation.

The injection of neutral particles via the NBI beam automatically leads to increased rotation of the plasma. If this rotation is to be avoided, only short NBI blips can be used to obtain ion data at selected times.

Integrated Data Analysis (IDA)

The integrated data analysis (IDA) [173], as its name suggests, is a computational tool that combines measurements from various diagnostics such as the lithium beam [174], interferometry [175], Thomson scattering, electron cyclotron emission [176] and thermal helium beam (Sec. 4.2) with a Bayesian probability approach to obtain reliable profiles of electron density n_e and temperature T_e, and thus pressure p_e. To achieve this unification, the measurements of the individual diagnostics are mapped to ρ_pol, for which a reliable equilibrium reconstruction is required. The profiles have a typical time resolution of 1 kHz.

Thomson Scattering (TS)

As mentioned above, the Thomson scattering (TS) diagnostic [177] is included in IDA profiles, but they are used individually for a later separatrix evaluation. The principle of the diagnostic bases on the scattering of a monochromatic electromagnetic wave, e.g a laser, on freely moving electrons. The scattered light is analyzed perpendicular to the irradiated wave, and in addition to the original laser peak, a broadening of the spectrum can be seen. From this broadening the electron density n_e and temperature T_e can be determined. The laser can obviously be aimed at the plasma core or at the edge (edge TS). We use the latter for the separatrix values, for which the edge TS data has to be averaged over a 300 ms time interval to give meaningful results [119].

4.4 Data Analysis Methods

With regard to the ultimate goal of investigating the underlying nature of the edge modes and thus generating knowledge about those, we need to transform the raw data provided by the presented diagnostics into useful information. Fortunately, there are several mathematical-statistical methods that perform exactly this processing step. With selected tools, the modes can be analyzed in terms of frequency, radial localization, coupling with other instabilities, wavenumbers, and cross-phase between electron density and temperature. The data processing procedure is presented below.

Spectral Analysis

Starting with a time series $X(t)$, such as the line emission intensity of the THB from Sec. 4.2, measured at a fixed position in space, the quantity can be transformed from time space to frequency space using the Fourier transform (FT) [178], i.e. $\hat{X}(f) \in \mathbb{C}$ with frequency f. In particular, if the original signal has a periodicity, i.e. a fluctuation, the FT provides the specific frequency at which the fluctuation oscillates. Graphically, the frequency is usually drawn against the power spectrum, which is defined as

$$S_X(f) = \left\langle \left| \hat{X}(f) \right|^2 \right\rangle = \left\langle \hat{X}(f) \hat{X}^\star(f) \right\rangle . \tag{4.3}$$

Here $\langle \dots \rangle$ represents the ensemble (time) average, which is usually done over a 20 ms time interval in this work, and $\hat{X}^\star(f)$ is the complex conjugate of the FT signal. However, the fluctuation frequency is not a single delta peak in the spectrum, but has a certain bandwidth Δf.

In addition, the entire signal is influenced by noise or background fluctuations with all possible frequencies. In general, there is an aperiodic background that scales approximately as $1/f$. To best analyze the frequency value of the fluctuation, the spectral power, the bandwidth, and also the impact of the aperiodic component, we use the approach of Donoghue *et al.* [179]. The fitting algorithm is illustrated in Fig. 4.6, but a result of it for the quasi-coherent mode has already been shown above in Fig. 4.5c.

First, the power spectrum of $X(f)$ is calculated and drawn against frequency (black line). The aperiodic part is estimated by a smart guess, e.g. $1/f$, marked in blue (a). The aperiodic signal is then subtracted from the original spectrum (b). To check if the fluctuation is present at all, a threshold (red dotted) is set as the standard deviation of the remaining signal that must be exceeded by the spectral power to declare a certain frequency as the frequency of the fluctuation. If this is the case, a Gaussian fit is performed around this peak frequency (green). The fitted Gaussian is then subtracted from the signal and the process is iterated until there are no points above the threshold

anymore (c). All the peaks found are fitted together to form a multi-Gaussian (d). The fitted multi-Gaussian is removed from the original spectrum (e) so that we get a smooth fit of the aperiodic background (f). Finally, we combine the fitted aperiodic background with the multi-Gaussian to obtain a full model fit (g), which can be compared to the original spectrum (h). We then get our desired quantities from the full model fit.

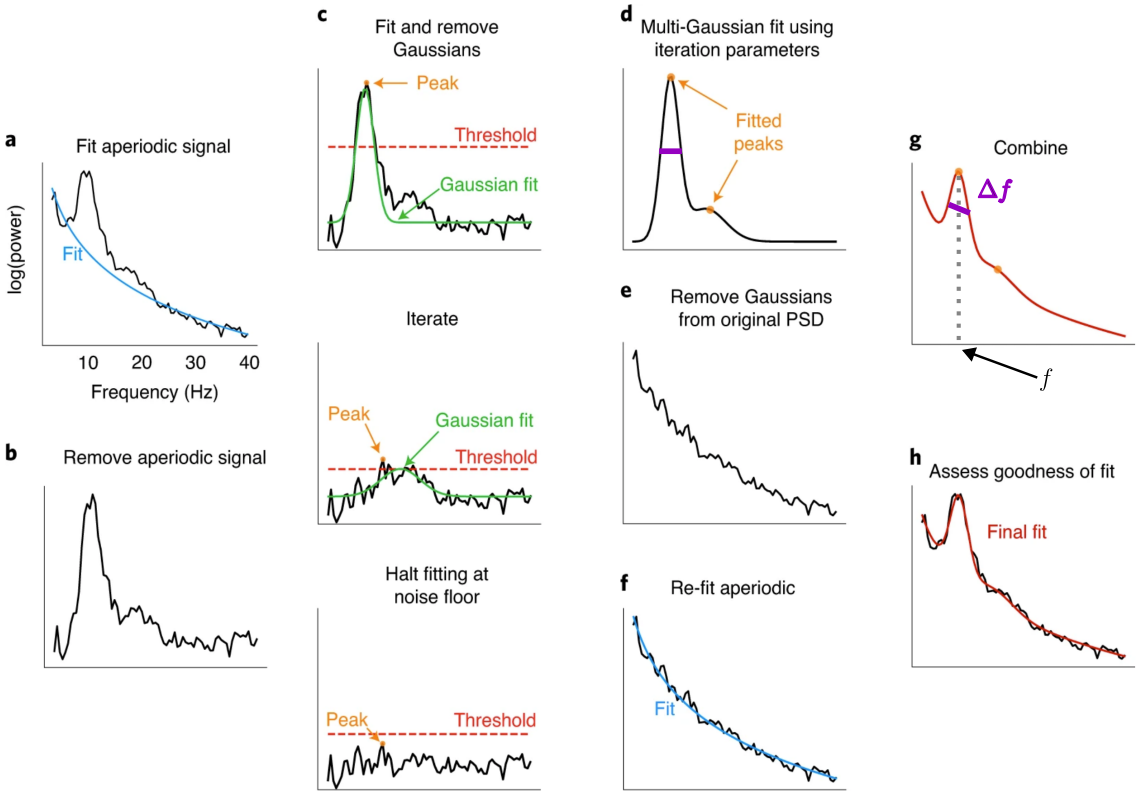

Figure 4.6: Graphical Representation of the Spectral Algorithm
A Fourier transformed signal is split into its aperiodic background component and its fluctuation component. The latter is restored using multi-Gaussian fits. It is important to note that the frequency f of the fluctuation, represented by the gray dotted line in g), and its bandwidth Δf (purple in d) and g)) can be obtained by the FWHM of the Gaussian fit. Fig. adapted from Ref. [179].

Radial Localization Method

The radial localization of an edge mode is crucial for the subsequent investigations, because we try to find scalings of mode properties that depend on local plasma properties, e.g. T_e or E_r. Since these quantities vary along the radial axis ρ_pol, we need to determine these at the mode position.

The radial mode position is defined in this work to be at the radial point where the highest normalized amplitude of the mode is found in the Fourier spectrum. This is done by comparing the mode amplitudes, i.e. their spectral power value of the full

model fit minus the aperiodic background component as shown in Fig. 4.5c. In this work we will use the line ratio technique of the THB signal as described in Sec. 4.2 and thus localize the mode radially where the highest amplitude appears in the Fourier transformed signal of I_{667}/I_{587}. However, this is only valid for an averaged time period that we choose (usually 20 ms to 40 ms), since the mode position can change within the discharge. The method therefore needs to be applied to multiple points in time. But how confident can we be that the defined position corresponds to the mode position?

To check this, we set up a new simulation of the THB signal similar to the one in Fig. 4.4. But now a Gaussian-like density $\tilde{n}_e$ (black) and temperature fluctuation $\tilde{T}_e$ (purple) is implemented to represent the impact of the radially extended mode, shown in Fig. 4.7. The mode has its maximum at $\rho_{pol} = 0.995$ and a radial width of $\Delta\rho_{pol} = 0.01$, defined as the FWHM of the given Gaussian. It can be seen that both, the line emission intensity for λ_1, i.e. $\tilde{I}_{587}$ (blue) and λ_2, i.e. $\tilde{I}_{667}$ (green) mislocalize the mode. On the other hand, the line ratio, i.e. $\tilde{I}_{667}/\tilde{I}_{587}$ (red) gives the correct localization, which is consistent with the pre-implemented $\tilde{n}_e$ and $\tilde{T}_e$ perturbation maxima. Based on these observations, we conclude that the highest amplitude of the measured I_{667}/I_{587} signal in the Fourier spectrum corresponds to the position where the mode has its maximum impact.

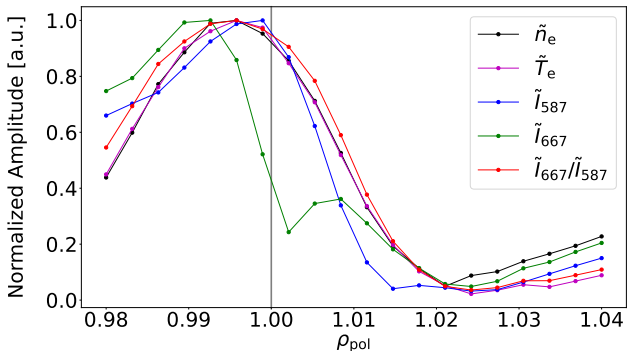

Figure 4.7: Verifying the Radial Localization Method
The implemented Gaussian-like synthetic density $\tilde{n}_e$ (black) and temperature $\tilde{T}_e$ (purple) fluctuation is correctly reproduced by the ratio of the line intensities $\tilde{I}_{667}/\tilde{I}_{587}$ (red), but not by the individual ones (blue and green). The amplitudes are normalized to their corresponding maximum, reaching it close to the separatrix (vertical gray). Fig. taken from Ref. [180].

Bicoherence Analysis

Although not yet treated, it is possible that three-wave coupling [181] between multiple instabilities can occur. However, this coupling mechanism is a result of the nonlinear quadratic treatment of the instabilities. Here, two modes with frequencies f_1 and f_2,

respectively, can couple to a third mode with $f_3 = f_1 + f_2$. A measure of the coupling is the so-called bispectrum, which is defined as follows [182]

$$B\left(f_1, f_2\right) = \left\langle \hat{X}(f_1)\hat{X}(f_2)\hat{X}^{\star}(f_3)\right\rangle, \tag{4.4}$$

where $\hat{X}(f)$ is the Fourier transformation of a data set $X(t)$. In particular, coupling of two modes to a third is possible if they obey a rigid phase difference to each other. Generally, $B\left(f_1, f_2\right)$ is complex and therefore, we need a general measure of the relation of complex quantities, which motivated the definition of the quadratic bicoherence, given as

$$b^2\left(f_1, f_2\right) = \frac{\left|B\left(f_1, f_2\right)\right|^2}{\left\langle\left|\hat{X}(f_1)\hat{X}(f_2)\right|^2\right\rangle\left\langle\left|\hat{X}^{\star}(f_3)\right|^2\right\rangle}. \tag{4.5}$$

The bicoherence $b\left(f_1, f_2\right)$ has values between zero and one, where a value of one means that the mode with $f_3 = f_1 + f_2$ has been excited by the modes with f_1 and f_2, and a value of zero portrays an independent instability. Hence, we use this measure to find out whether a mode was excited by other modes or exists independently of them.

In addition, bispectral analysis can be used to distinguish between parametric decay instability and parametric modulational instability [183]. The former appears in the bispectrum as individual aligned points at the above frequencies f_1, f_2, f_3. The latter appears as stripes in the spectrum since in this case the three waves need to interact in two separate processes.

Envelope Analysis

In addition to bicoherence, another method will be used later to find a connection between two fluctuations: the envelope modulation technique. Here, we investigate whether the signal of one mode is modulated by the other one. For example, large-scale turbulent flows such as geodesic acoustic modes (GAM) [184] can modulate small-scale structures.

The method is illustrated by an example in Fig. 4.8. Consider an artificial signal with a high frequency of $f_{\text{high}} = 40\,\text{Hz}$ that is frequency modulated by a low frequency mode $f_{\text{low}} = 4\,\text{Hz}$, shown in Fig. 4.8a. First, the low frequency component is filtered out with a high pass filter (Fig. 4.8b). We choose a cutoff frequency of $f_{\text{cut}} = 8\,\text{Hz}$. It is interesting to note that the envelope (black line in Fig. 4.8c) of the filtered signal still oscillates at the frequency of the low-frequency signal, i.e. with 4 Hz, even though this part has been filtered out. Hence, the high frequency structure is modulated.

To calculate the envelope of a signal, we use the Hilbert transform $\mathcal{H}$ [178]. The envelope of a real signal $X(t)$ is calculated in signal processing as the amplitude of the corresponding complex analytic signal. The real part of the analytic signal remains the

original signal, but the imaginary part consists of the Hilbert transform of $X(t)$. This yields

$$\mathrm{Env}(t) = \sqrt{X(t)^2 + (\mathcal{H}X(t))^2}. \tag{4.6}$$

If the high-frequency structure is modulated, the frequency of the envelope is the same as the frequency of the low-frequency structure.

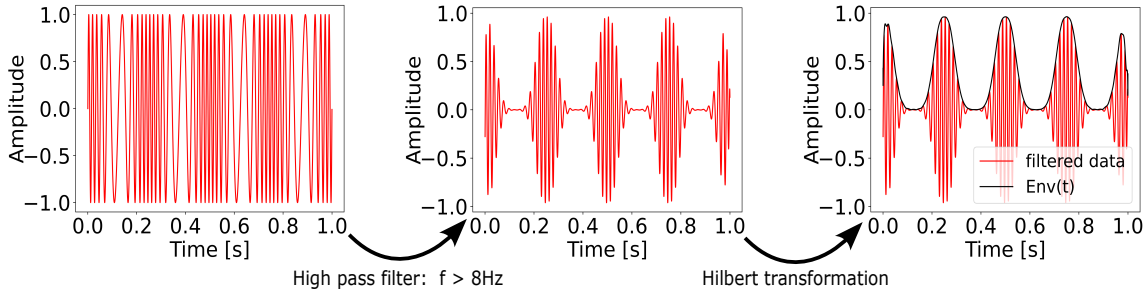

Figure 4.8: Graphical Representation of the Envelope Technique
A constructed signal (red) is superimposed by two signals with two frequencies (a). Frequencies below 8 Hz are filtered out by a high-pass filter (b). Nevertheless, the low-frequency component appears in the envelope (black), which is calculated as in Eq. 4.6 of the filtered signal (c). The high-frequency component is thus modulated by the low-frequency component.

Wavenumber Analysis

The local wavenumber of a mode can be calculated from the measured signal using the method by Beall *et al.* [185]. This requires measurements at at least two spatially separated points, i.e. $\hat{X}(\boldsymbol{r_1}, f)$ and $\hat{X}(\boldsymbol{r_2}, f)$ at positions $\boldsymbol{r_1}$ and $\boldsymbol{r_2}$. According to Ref. [185], the wavenumber can be calculated as follows

$$k_i(f) = \frac{\Theta_i(f)}{\Delta}, \tag{4.7}$$

where $\Delta = |\boldsymbol{r_1} - \boldsymbol{r_2}|$ is the distance between the two points of measurement, and $\Theta_i(f)$ is the phase of the signals, which can be calculated from the cross spectrum, i.e.

$$\Theta_i(f) = \arctan\left(\frac{\Im\left(\hat{X}_i^\star(\boldsymbol{r_1}, f)\hat{X}_i(\boldsymbol{r_2}, f)\right)}{\Re\left(\hat{X}_i^\star(\boldsymbol{r_1}, f)\hat{X}_i(\boldsymbol{r_2}, f)\right)}\right). \tag{4.8}$$

Here $\Im(\dots)$ is the imaginary and $\Re(\dots)$ is the real part of the cross spectrum. The final result of this approach is to obtain the wavenumber-frequency spectrum (also known as pseudo wavenumber spectrum or short $k - f$ spectrum), which is a kind of weighting of the various combinations of k and f, i.e. it is a kind of histogram in the 2D plane spanned by k and f indicating the most likely combinations of k and f

present in the signal. For the calculation, we must specify the step size δk in the k values. Since the wavenumber is restricted to values of $k_i \in [-\pi/\Delta, \pi/\Delta]$, we specify the step size by the number of steps M. The $k - f$ spectrum can then be calculated as a sum over each k_i as follows:

$$\mathrm{Int}(k, f) = \frac{1}{M} \sum_{i=1}^{M} I_{[0,\delta k]} \left(k - k_i(f)\right) \cdot \frac{1}{2} \left(S_{1,i}(f) + S_{2,i}(f)\right). \tag{4.9}$$

$S_{1,i}$ and $S_{2,i}$ are the auto-spectra at a fixed frequency f from Eq. 4.3 at the corresponding positions $\boldsymbol{r_1}$ and $\boldsymbol{r_2}$. Furthermore $I_{[0,\delta k]}(x)$ is the indicator function, i.e.

$$I_{[0,\delta k]}(x) = \begin{cases} 1 & x \cdot \delta k \geq 0, \\ 0 & \text{else.} \end{cases} \tag{4.10}$$

For the whole process it is necessary to average the spectra over a certain time interval, which is again chosen to be between 20 ms and 40 ms.

Depending on the choice of channels selected for this procedure, the wavenumber along different axis can be determined. For example, if the 5×5 grid of the THB is available (Fig. 4.3b), we can calculate both poloidal and radial wavenumbers, which are a central point of this work.

How to calculate $\alpha_{\mathrm{n_e,T_e}}$ with THB

Although the THB line emission intensity I_λ from Eq. 4.1 depends directly on the photo emission coefficients $\mathrm{PEC}_{\lambda_\mathrm{i}}$, which in turn depend non-linearly on electron density n_e and temperature T_e, it is possible to almost decouple n_e and T_e. The decoupling allows us to analyze the influence of the edge mode on $\tilde{n}_\mathrm{e}$ and $\tilde{T}_\mathrm{e}$ fluctuations separately and, in particular, to determine the cross-phase $\alpha_{\mathrm{n_e,T_e}}$ experimentally. Therefore, we follow the work by Nishizawa *et al.* [186].

In this paper, a variable R_I^j was constructed to have a Taylor approximated density and temperature sensitivity, i.e.

$$R_\mathrm{I}^j \approx 1 + \zeta_{\mathrm{n_e}} \frac{\tilde{n}_\mathrm{e}}{n_{\mathrm{e},0}} + \beta_{\mathrm{T_e}} \frac{\tilde{T}_\mathrm{e}}{T_{\mathrm{e},0}}, \tag{4.11}$$

where $\zeta_{\mathrm{n_e}}$ and $\beta_{\mathrm{T_e}}$ respectively control the sensitivity of R_I^j to density and temperature fluctuations. The parameters depend on I_λ of all four wavelengths (see Sec. 4.2). For given background values of $n_{\mathrm{e},0}$ and $T_{\mathrm{e},0}$, the intensities can be combined in such a way that either $\beta_{\mathrm{T_e}} \to 0$ and we have a pure density depending $R_\mathrm{I}^{\mathrm{n_e}}$, or $\zeta_{\mathrm{n_e}} \to 0$ to obtain $R_\mathrm{I}^{\mathrm{T_e}}$. Fig. 4.9 shows an example of the resulting $R_\mathrm{I}^{\mathrm{n_e}}$ (a) and $R_\mathrm{I}^{\mathrm{T_e}}$ (b) for $n_{\mathrm{e},0} = 7 \cdot 10^{18}\,\mathrm{m}^{-3}$ and $T_{\mathrm{e},0} = 50\,\mathrm{eV}$. The colored lines represent the variation of I_λ, when

n_e and T_e vary from the background values. The procedure requires that R_I^j must be recomputed for each point in the $n_e - T_e-$ space. The corresponding R_I^j will then hold for small variations in that space in the proximity of the selected pair of $n_{e,0}$ and $T_{e,0}$.

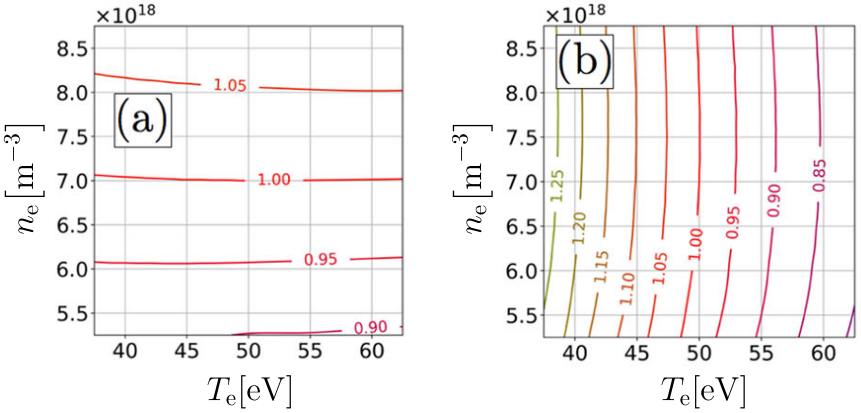

Figure 4.9: Decoupling of n_e and T_e
(a) Electron temperature insensitive quantity $R_I^{n_e}$ and (b) the density insensitive quantity $R_I^{T_e}$. The contour lines represent the deviation from the selected background values $n_{e,0} = 7 \cdot 10^{18}\,\mathrm{m}^{-3}$ and $T_{e,0} = 50\,\mathrm{eV}$. Thus, the contour line representing 1.00 crosses the point ($T_{e,0}$, $n_{e,0}$) in both cases. Fig. adapted from Ref. [186].

The corresponding power spectra of R_I^j indicate the fluctuation power in $\tilde{n}_e$ or $\tilde{T}_e$:

$$\langle (R_I^{n_e})^\star(f) R_I^{n_e}(f) \rangle \approx \zeta_{n_e}^2 \left\langle \frac{|\tilde{n}_e(f)|^2}{n_{e,0}^2} \right\rangle, \tag{4.12}$$

$$\left\langle \left(R_I^{T_e}\right)^\star(f) R_I^{T_e}(f) \right\rangle \approx \beta_{T_e}^2 \left\langle \frac{\left|\tilde{T}_e(f)\right|^2}{T_{e,0}^2} \right\rangle. \tag{4.13}$$

Of interest to us, however, is their cross spectrum, which is calculated as

$$C_{R_I}^{n_e,T_e} = \left\langle (R_I^{n_e})^\star(f) R_I^{T_e}(f) \right\rangle \approx \zeta_{n_e}\beta_{T_e} \left\langle \frac{\tilde{n}_e(f)^\star \tilde{T}_e(f)}{n_{e,0} T_{e,0}} \right\rangle, \tag{4.14}$$

since this yields the desired cross-phase

$$\alpha_{n_e,T_e} = \arctan\left(\frac{\Im\left(C_{R_I}^{n_e,T_e}\right)}{\Re\left(C_{R_I}^{n_e,T_e}\right)} \right). \tag{4.15}$$

It is important to note, that for this evaluation the measurements from all four helium lines are needed (Sec. 4.2), and that λ_3 and λ_4 are usually overshadowed by noise in H-mode-like discharges within the separatrix, i.e. their signal-to-noise ratio is too weak. Therefore, we can only apply this method to carefully selected discharges and time points.

5 Experimental Characterization of the Quasi-Coherent Mode (QCM)

Phenomenologically, we have observed that all plasma regimes that benefit from the absence of type-I edge localized modes (ELMs) seem to be accompanied by an edge mode (Chap. 2). It is believed that the latter induces sufficient radial electrostatic turbulent transport to stagnate the pressure value of the pedestal, i.e. the pedestal height according to the EPED model [148] (Sec. 3.3). Furthermore, we have seen in Chapter 4 that we are able to experimentally determine the necessary quantities of the edge modes with the thermal helium beam diagnostic (THB, Sec. 4.2) in order to compare them with the characterizing quantities of the possible underlying instabilities from Tab. 3.1. This chapter deals with edge modes of the enhanced D_α high confinement mode (EDA H-mode) and quasi-continuous exhaust scenario (QCE), which have been introduced in Secs. 2.2.1 and 2.2.2 using example discharges, respectively.

In both regimes a characteristic edge fluctuation is prominent, called the quasi-coherent mode (QCM), being a known signature of the EDA H-mode [57, 78, 79], and, as shown in this chapter, is also linked to the mode introduced by Griener *et al.* [170] and Wolfrum *et al.* [187] in the QCE regime. The QCM is believed to be responsible for a strong particle transport and thus being the key ingredient to avoid type-I ELMs. The ultimate goal of this effort would be to understand and extrapolate a possible EDA H-mode or QCE scenario to large-scale machines like ITER or DEMO, for which it is necessary as a first step to elucidate the properties of the prominent edge fluctuation. Tab. 5.1 shows an overview of the QCM properties found in previous works at various fusion experiments. Listed are the radial position where the mode was localized $\rho_{\mathrm{pol}}^{\mathrm{Loc}}$ in terms of the normalized poloidal flux coordinate, its frequency f, the poloidal wavenumber k_θ, and its velocity in the laboratory v_{lab} and plasma frame v_{ph}. These quantities are described in Chapter 3.

Special attention is paid to Alcator C-Mod, where Theiler *et al.* [80] have shown, using the gas puff imaging diagnostic that the QCM moves in ion diamagnetic direction in the plasma frame with frequency $f \approx 86\,\mathrm{kHz}$, and that it is localized near the E_{r} minimum and has a poloidal wavenumber of $k_\theta \approx 1.9\,\mathrm{cm}^{-1}$. On the other hand, LaBombard *et al.* [77] observed the QCM in Ohmic EDA-H discharges with Mirror

Table 5.1: QCM Properties from Past Analyses in Different Fusion Devices
'N/A' denotes that there is no quantified information available in the corresponding reference. A negative velocity indicates propagation in the electron diamagnetic direction.

Quantity	AUG [57]	Alcator C-Mod [77, 80]	DIII-D [74, 188]	EAST [76]
$\rho_{\mathrm{pol}}^{\mathrm{Loc}}$	N/A	0.985 (E_{r} min.)	0.95	0.98
f [kHz]	15–80	50–140	10–35	40–100
k_θ [cm^{-1}]	0.6	1.2–1.9	0.5–0.8	0.5–0.7
v_{lab} [$\mathrm{km\,s}^{-1}$]	< 0	< 0	< 0	< 0
v_{ph} [$\mathrm{km\,s}^{-1}$]	N/A	Both	~ 0	N/A

Langmuir Probes to propagate in electron diamagnetic direction in the plasma frame near the scrape-off layer with frequencies around $f \approx 130\,\mathrm{kHz}$ and a poloidal wavenumber of $k_\theta \approx 1.7\,\mathrm{cm}^{-1}$. We will also encounter and interpret these contrasting results later.

The main part of the following chapter is based on and is partly taken verbatim from the published paper: *J. Kalis, et al., "Experimental characterization of the quasi-coherent mode in EDA H-Mode and QCE scenarios at ASDEX Upgrade", Nucl. Fusion 64, 016038 (2024)* [180]. The paper reports on the properties of the QCM in EDA H-modes and QCE scenarios and outlines similarities and differences of the mode in both regimes using the THB diagnostic (Sec. 4.2) and magnetic pick-up coils (Sec. 4.3) at ASDEX Upgrade (Sec. 4.1). Tab. 5.1 indicates that some quantities are only controversial or not known experimentally, therefore the investigation presented in the following aims at closing the knowledge gaps and contributes to the understanding of previous results.

The first step is to radially locate the QCM. Based on the found position, the frequency and its dependence on global and local plasma parameters are analyzed. The bandwidth of the QCM can be used to establish a connection with the magnetic higher harmonic modes (HHMs), which are visible in the magnetic pick-up coils (see Fig. 2.1f), but the exact investigation of their coupling is then done by a bicoherence analysis. Afterwards, the poloidal and radial wavenumbers of the QCM are analyzed. Using the frequency and the poloidal wavenumber we can estimate the poloidal velocity of the QCM in the laboratory and the plasma frame. In addition, we evaluate the cross-phase between electron density n_{e} and temperature T_{e} of the QCM and categorize the discharges in an edge phase space turbulence diagram and compare EDA H-modes and QCE scenarios. Finally, the results are discussed and interpreted.

The QCM is analyzed in the following for 13 deuterium plasmas without seeding (for discharges with seeding, see e.g. Ref. [189]) at different plasma parameters. This includes variations in toroidal magnetic field strength B_{t}, plasma current I_{p}, edge safety

factor q_{95} and heating powers P for electron and ion cyclotron heating (ECRH, ICRH) and neutral beam injection (NBI). The range of plasma parameters is listed in Tab. B.1. It has to be mentioned that six discharges are classified as EDA H-modes and seven as QCE scenarios, according to the distinction criterion introduced in Sec. 5.1.

Table 5.2: Discharge Parameters for EDA H-modes and QCE
The parameters of EDA and QCE plasmas covered by the analyzed data set consisting of 13 discharges are shown.

Type	B_t [T]	I_p [MA]	q_{95}	P_{ECRH} [MW]	P_{ICRH} [MW]	P_{NBI} [MW]
EDA	2.50	0.60–0.79	5.32–6.64	1.9–3.5	0.0	0.0–2.5
QCE	1.90–2.52	0.71–1.10	3.69–5.61	0.0–4.4	0.0–3.9	0.0–5.0

In the following all profile quantities like the local electron density n_e, temperature T_e, pressure p_e and the electron pressure gradient ∇p_e are taken from integrated data analysis (Sec. 4.3), if not stated otherwise.

5.1 Appearance of QCM in Frequency Space

The temporal QCM properties of interest are the frequency f_{QCM}, the coherency Δf_{QCM}, the mode amplitude and the scaling of the frequency with given plasma parameters. These properties and the coupling of the QCM with other modes, which will be discussed in more detail in Sec. 5.2, are described below and can be used later to distinguish between EDA H-modes and QCE plasmas.

Radial Localization of the QCM

By comparing the Fourier spectra (Sec. 4.4) along the radial extent of the THB LOS, we localize the mode ρ_{pol}^{QCM} where the highest relative peak in the Fourier spectrum of the line ratio time trace (λ_2/λ_1) occurs (see Sec. 4.4). An example of radial localization for discharge #38067 at t =4.23 s and time interval of Δt = 40 ms is shown in Fig. 5.1a. The colorbar indicates the amplitude of the QCM according to Fig. 4.5c. It can be seen that the mode is present poloidally over the entire THB grid, but is relatively strongly localized radially around $\rho_{pol} = 0.99$ indicated by the green line. The amplitude decreases towards the plasma core (color changes from blue to red). Outside the separatrix (gray line), the QCM appears to be barely measurable, if at all. It is important to note that amplitudes below a certain threshold have been set as minimum values for the sake of visibility. Fig. 5.1b shows the radial position of the QCM ρ_{pol}^{QCM} for all 13 discharges, where each data point (blue) corresponds to a localization averaged over 40 ms. Hence, the QCM is generally found to be localized close to the

separatrix at $\rho_{\mathrm{pol}}^{\mathrm{QCM}} = 0.993 \pm 0.007$ in all investigated discharges. This corresponds to a distance of $\Delta R \approx 7\,\mathrm{mm}$ inside the separatrix. The results for individual discharges are shown in Tab. B.1 in Appendix B. Fig. 5.10b (purple line) shows a 1D example of the QCM amplitude profile. In addition, the radial position of the QCM is drawn against the radial position of the maximum in the electron pressure profile $\rho_{\mathrm{pol}}^{\nabla p_{\mathrm{e,max}}}$, with the black line indicating $\rho_{\mathrm{pol}}^{\mathrm{QCM}} = \rho_{\mathrm{pol}}^{\nabla p_{\mathrm{e,max}}}$. We see that the $\rho_{\mathrm{pol}}^{\nabla p_{\mathrm{e,max}}}$ values are discretely distributed, which is due to the radial resolution of the IDA profiles (Sec. 4.3). Nevertheless, the data points including the errorbars resulting from the time averaging in $\rho_{\mathrm{pol}}^{\mathrm{QCM}}$ and from the radial resolution of IDA in $\rho_{\mathrm{pol}}^{\nabla p_{\mathrm{e,max}}}$ scatter around the black line. The QCM is therefore located in the area of the steepest pressure gradient. In the following, all plasma quantities and QCM properties are determined at the radial position, at which the mode is localized by this method.

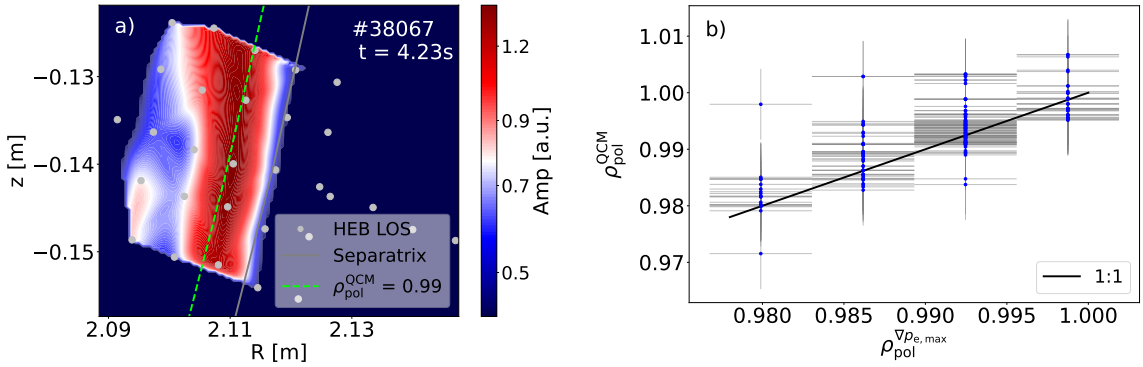

Figure 5.1: Radial Localization of the QCM in an EDA H-Mode

a) To illustrate the radial position of the mode for discharge #38067, the 5×5 grid of the THB is shown (lines of sight as black points). The colorbar shows the amplitude of the QCM as it was done in Fig. 4.5c). A high amplitude is represented by red and a low one by blue. The green line indicates the radial position of the QCM in this discharge and time interval, i.e. $t \in [3.43\,\mathrm{s}, 3.47\,\mathrm{s}]$. Outside the separatrix (gray line) the QCM amplitude is drastically reduced. Dark blue indicates that either the mode amplitude is below a selected threshold or the QCM was not measured. b) The radial position of the QCM $\rho_{\mathrm{pol}}^{\mathrm{QCM}}$ (blue) is determined for all time points and discharges from Tab. B, averaged over 40 ms time intervals and drawn against the radial position of the steepest pressure gradient $\rho_{\mathrm{pol}}^{\nabla p_{\mathrm{e,max}}}$. The black line indicates $\rho_{\mathrm{pol}}^{\mathrm{QCM}} = \rho_{\mathrm{pol}}^{\nabla p_{\mathrm{e,max}}}$.

Frequency Scaling of the QCM

The next step is to study how the QCM frequency depends on local plasma parameters. For this purpose, Fig. 5.2 shows time traces of some properties of the EDA H-mode #38067 (full discharge shown in Fig. 2.1). Since the mode is located at the edge, where strong $E \times B$ flows are present, a natural frequency dependence may occur due to the

fact that the QCM is related to the local plasma velocity $v_{\mathrm{E\times B}}$ (Eq. 3.49). According to this, f_{QCM} should be higher in plasmas with higher $E \times B$ flows at the plasma edge. Figs. 5.2a-b show that the time evolution of f_{QCM} does not follow the trend of the approximated plasma velocity, i.e.

$$v_{\mathrm{E\times B}} = E_{\mathrm{r}}/B_{\mathrm{t}} \approx -\nabla p_{\mathrm{i}}/(eB_{\mathrm{t}}n_{\mathrm{e}}) = -v_{\mathrm{i,dia}} \underbrace{\approx}_{T_{\mathrm{e}} \approx T_{\mathrm{i}}} v_{\mathrm{e,dia}}, \tag{5.1}$$

which is confirmed in Fig. 5.2e for many discharges. Here, E_{r} is the radial electric field, $v_{\mathrm{e,dia}}$ is the electron diamagnetic velocity and $v_{\mathrm{i,dia}}$ is the ion diamagnetic velocity. Setting $v_{\mathrm{E\times B}} \approx v_{\mathrm{e,dia}}$ is motivated by the observation at AUG in Ref. [190] that E_{r} is close to its neoclassical value at its minimum. In Sec. 5.4, it will be shown with data from direct measurements of E_{r} by means of charge exchange recombination spectroscopy (CXRS, Sec. 4.3) [172] that this assumption is reasonable slightly inside the separatrix.

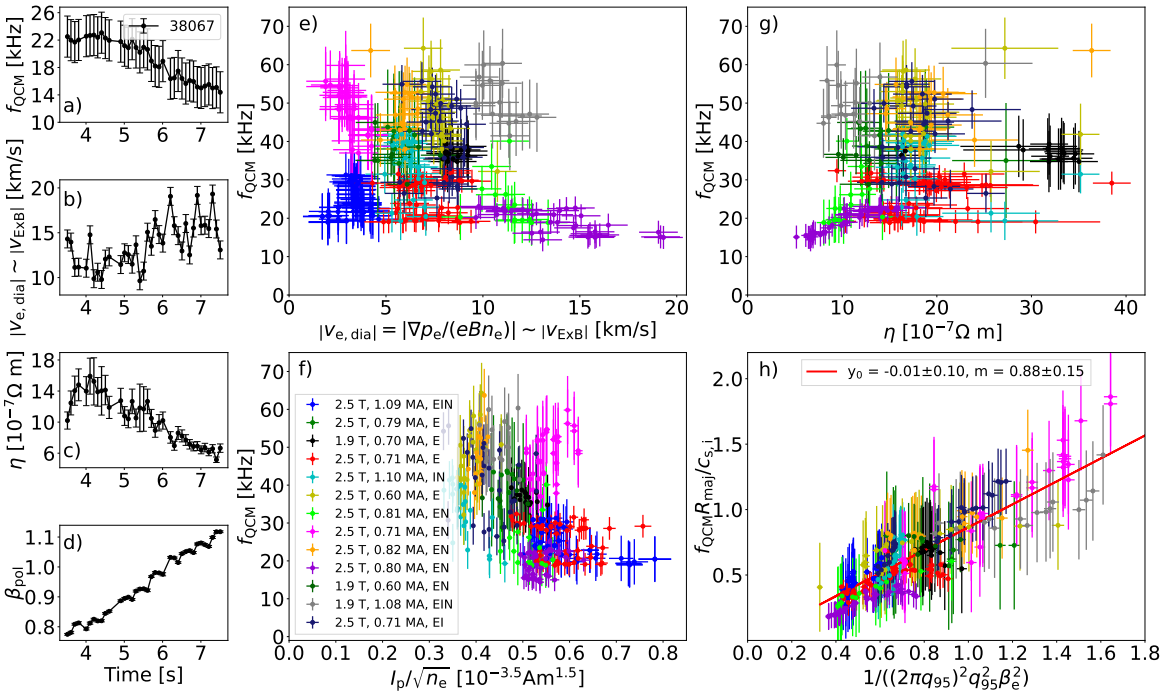

Figure 5.2: Temporal Behavior of f_{QCM} and Scaling
The Frequency of the QCM f_{QCM} a) the approximated plasma velocity $v_{\mathrm{E\times B}}$ b), resistivity η c) and the poloidal plasma beta β_{pol} d) for EDA H-mode discharge #38067. For various discharges, f_{QCM} or $f_{\mathrm{QCM}}R_{\mathrm{maj}}/c_{\mathrm{s,e}}$ is drawn against e) $v_{\mathrm{E\times B}}$, f) the poloidal Alfvén velocity approximated by $I_{\mathrm{p}}/\sqrt{n_{\mathrm{e}}}$, g) resistivity η and h) $1/\beta_{\mathrm{pol}}^2$. y_0 (offset) and m (slope) in h) are the corresponding parameters for a linear fit. The legend includes the toroidal field strength B_{t}, plasma current I_{p} and the used heating method, where E: ECRH, I: ICRH, N: NBI. Fig. taken from Ref. [180].

If the QCM would be of Alfvénic nature, a frequency dependence of $v_{\mathrm{A}} \sim B/\sqrt{n_{\mathrm{e}}}$

is expected, where B can be either the toroidal (B_t) or the poloidal (B_pol) magnetic field strength. The latter case was found for the M-mode at JET [191]. In Fig. 5.2f the poloidal Alfvén velocity is written as $v_\mathrm{A,pol} \propto I_\mathrm{p}/\sqrt{n_\mathrm{e}}$. The comparison shows that the experimental results disagree with this scaling, i.e. f_QCM does not scale with either $B_\mathrm{pol}/\sqrt{n_\mathrm{e}}$ or with $B_\mathrm{t}/\sqrt{n_\mathrm{e}}$ (not shown here).

For type-III ELMs, it has been speculated that the frequency increases with resistivity η (Fig. 5.2c) [192]. Fig. 5.2g finds such a scaling for isolated cases, but a general proportionality for all discharges is not suggested by the data.

As a best fit, a heuristic dimensionless relation for f_QCM was found as (Fig. 5.2h)

$$\frac{f_\mathrm{QCM}}{c_\mathrm{s,i}/R_\mathrm{maj}} = \frac{1}{(2\pi q_{95})^2 q_{95}^2 \beta_\mathrm{e}^2} \approx \frac{R_\mathrm{maj}^4}{(2\pi a_\mathrm{min}^2)^2 \beta_\mathrm{pol}^2}, \tag{5.2}$$

where $c_\mathrm{s,e}$ is the ion sound speed (Eq. 3.26), $\beta_\mathrm{pol} = \mu_0 n_\mathrm{e} T_\mathrm{e}/B_\mathrm{pol}^2$ is the poloidal plasma beta, and β_e is the one from Eq. 2.5. The errors of the linear fit are calculated as the standard deviation of the maximum and the minimum possible slope, including the errors of the experimental data. Eq. 5.2 is similar to the results of Birkenmeier [63] ($f_\mathrm{LCO} \sim 1/\beta_\mathrm{e}$) and Grover [96] ($f_\mathrm{LCO} \sim 1/\sqrt{\beta_\mathrm{e}}$) for limit cycle oscillations (LCO) in I-phase plasmas, which we will discuss in Sec. 6.1.

Bandwidth of the QCM and Higher Harmonic Modes

The bandwidth of the QCM, Δf_QCM, is analyzed for the discharge #40110, in which ECRH is gradually replaced by ICRH (Fig. 5.3a). Δf_QCM is calculated according to the method in Sec. 4.4. This procedure has been performed for different time intervals to gain a time evolution of Δf_QCM. The spectrogram in Fig. 5.3b, evaluated at $\rho_\mathrm{pol} = 0.996$, indicates that the QCM gets fainter and broader in frequency space when plasma heating is changed from ECRH to ICRH. Fig. 5.3c indicates that a higher QCM frequency leads to a larger bandwidth qualitatively.

Now we address signatures of the QCM [193] or of other modes in the magnetic pick-up coils by means of the magnetic spectrogram for coil $B31-14$ in Fig. 5.3d. The coil is located at the outer midplane measuring the radial magnetic field component, as shown in Fig. 4.1. We note that other modes, hereinafter referred to as higher harmonic modes (HHMs), can accompany the QCM. Both kinds of modes are highlighted in the Fourier spectrum of the magnetic coil in Fig. 5.4. The QCM with $f_\mathrm{QCM} = 22.7\,\mathrm{kHz}$ is very close to the lowest frequency HHM with $f_\mathrm{HHM,n=1} \approx 30\,\mathrm{kHz}$ and toroidal mode number of $n_\mathrm{mode} = 1$. n_mode was determined by means of the toroidal mode determination method as described in Ref. [194]. In Fig. 5.3d it is visible that the HHMs vary during the discharge. At the beginning, HHMs are clearly visible as equidistant horizontal stripes, i.e. higher harmonics of a base frequency with $f_\mathrm{HHM} \approx \ell \cdot 30\,\mathrm{kHz}$ with $\ell =$

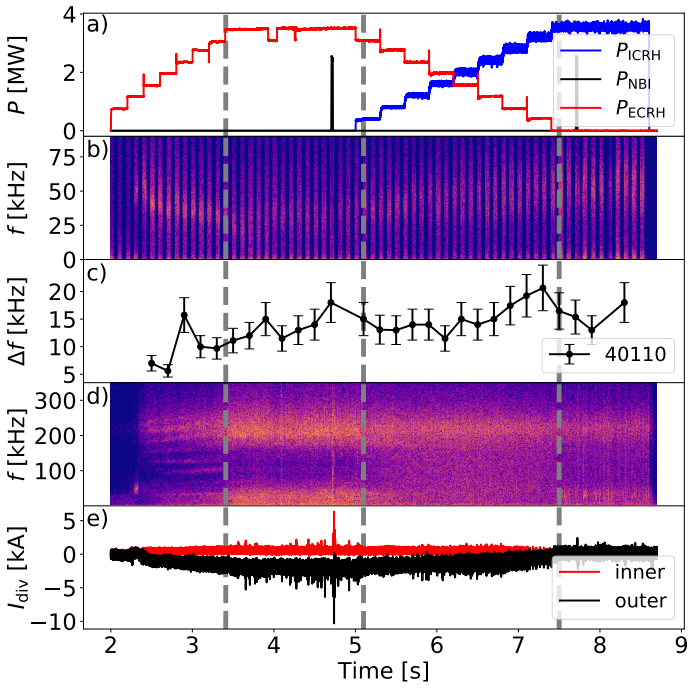

Figure 5.3: Transition from EDA H-Mode to QCE and Coherency of QCM *Heating power of different mechanisms for AUG discharge #40110 a). The QCM bandwidth Δf c) increases qualitatively during the discharge. In the spectrogram, obtained by the magnetics d), the HHMs are also changing in the different intervals (grey dotted lines). e) shows the divertor current to monitor the ELM activity. Fig. taken from Ref. [180].*

$4, \ldots, 8$. Then (between $t_0 = 3.3\,\mathrm{s}$ and $t_1 = 5.1\,\mathrm{s}$) the HHMs get less visible, but also ELMs appear in the divertor current in Fig. 5.3e, influencing the magnetic signal. Between $t_1 = 5.1\,\mathrm{s}$ and $t_2 = 7.5\,\mathrm{s}$ the HHMs seem to get broader so that they cannot be distinguished from each other and in the end, they are not observable anymore. Thus, it seems natural to consider a correlation between the presence of the HHMs and the coherency of the QCM quantified as $\Delta f_{\mathrm{QCM}}/f_{\mathrm{QCM}}$.

Therefore, we define a measure of the visibility of the HHMs as

$$\log V_{\mathrm{HHM}} = \log\left(HN\right), \tag{5.3}$$

where H is the peak height of the most dominant mode in the magnetics, and N is the number of HHMs present in the signal. The higher $\log V_{\mathrm{HHM}}$, the better is the visibility of HHMs in the signal. An example of the quantities influencing $\log V_{\mathrm{HHM}}$ is presented in Figs. 5.4a and b. For Fig. 5.4a the amplitude amounts to $H = 1.17$ and we find $N = 8$, resulting in $\log V_{\mathrm{HHM}} = 0.97$.

Fig. 5.5 compares this quantity with spectral properties of the QCM for the same set of discharges as introduced above. Although a trend between the coherency (Fig.

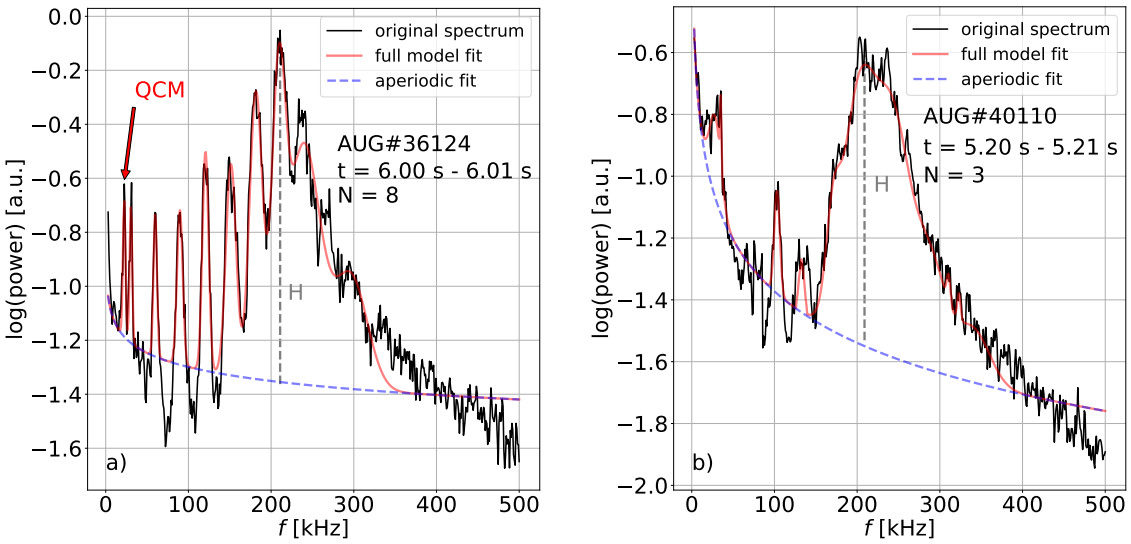

Figure 5.4: Fourier Spectra for an EDA-H Mode and QCE
Example of a Fourier spectrum for the measurements of the magnetic pick-up coil $B31-14$ for an EDA H-mode #36124 a) and QCE time points of discharge #40110 b), in which the QCM and the HHMs are visible. Fig. taken from Ref. [180].

5.5a) or the bandwidth (Fig. 5.5b) and $\log V_{\mathrm{HHM}}$ is noticeable, the most appropriate is obtained between f_{QCM} and the presence of HHMs (Fig. 5.5c). Hence, a QCM with low frequency is able to coexist with the HHMs.

Additionally, a general relationship between the applied heating mechanism and the spectral behavior of the QCM is not obtained, but the most coherent QCMs are achieved in ECRH-only plasmas (Fig. 5.5b).

As described in Sec. 2.2.2, QCE discharges are usually accompanied by ELMs or filaments with small amplitudes and EDA discharges do not feature ELMs. These filaments may transfer heat and particles into the SOL and vary n_{e} and T_{e} and hence β_{e} at the plasma edge strongly. A variation in β_{e} leads to a variation of f_{QCM}, according to Eq. 5.2. This manifests in an increase in Δf_{QCM} for QCE discharges. Therefore, the bandwidth of the QCM is used to distinguish EDA H-modes from QCE discharges. In the following analyses, an arbitrary boundary of

$$\Delta f_{\mathrm{QCM}} = 10\,\mathrm{kHz} \tag{5.4}$$

is introduced, so that discharge phases, in which a coherent mode appears, i.e. with $\Delta f_{\mathrm{QCM}} < 10\,\mathrm{kHz}$ are defined as EDA-H modes and discharge phases with $\Delta f_{\mathrm{QCM}} > 10\,\mathrm{kHz}$ as QCE regime. This boundary is chosen, because it yields two subsets of data points in Figs. 5.5a) and 5.5b) and consequently, these subsets lead to different patterns in the separatrix $\alpha_{\mathrm{d}} - \alpha_{\mathrm{MHD}}$−diagram, discussed in Sec. 5.6.

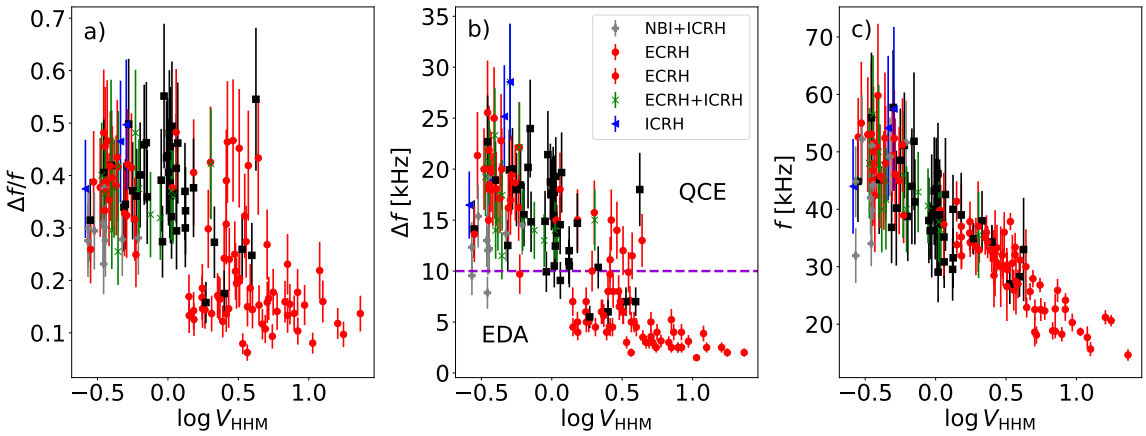

Figure 5.5: Spectral Behavior of the QCM vs. Visibility of HHMs
Correlation between the visibility of the HHMs, $\log V_{\mathrm{HHM}}$*, and the coherency* $\Delta f_{\mathrm{QCM}}/f_{\mathrm{QCM}}$ *a), the bandwidth* Δf_{QCM} *b) and the frequency* f_{QCM} *c) for different heating mechanisms applied. An arbitrary boundary to distinguish EDA H-modes from QCE scenario is set to* $\Delta f_{\mathrm{QCM}} = 10\,\mathrm{kHz}$*, indicated by the purple horizontal line. Fig. taken from Ref. [180].*

5.2 Bicoherence Analysis of QCM and HHMs

Both, the QCM and the HHMs are observed in the magnetic pick-up coils (see e.g. Figs. 5.4b) and 5.6a)). As shown in Fig. 5.5c, the modes seem to be connected since a higher visibility of HHM correlates with a lower frequency of the QCM. Generally, the most prominent HHMs have toroidal mode numbers n_{mode} in the range of $n_{\mathrm{mode}} = 5$ to $n_{\mathrm{mode}} = 8$ with frequencies of $f_{\mathrm{HHM}} = 150\,\mathrm{kHz}$ to $240\,\mathrm{kHz}$, whereas the fundamental mode ($n_{\mathrm{mode}} = 1$) has a frequency of $f_{\mathrm{HHM,n=1}} \approx 30\,\mathrm{kHz}$, which is close to the QCM frequency but usually higher than it.

Our goal is to examine whether and to what extent the QCM shows a causal relationship to the HHMs or if their simultaneous occurrence is not correlated. A natural precondition for a causality between those modes is that their phase difference must be rigid, enabling a coupling. The coupling can be analyzed by means of a bicoherence analysis, introduced in Sec. 4.4. Fig. 5.6b shows an auto-bispectrum for a 10 ms time interval of the magnetic signal from coil $B31 - 14$, implying that the HHMs couple to each other and to the QCM. Here, the data was averaged over 10 ms. Two points in the bispectrum show the interaction between the HHMs and the QCM (see enlarged window): one right below the abscissa ($f_1 = 200\,\mathrm{kHz}$, $f_2 = -18\,\mathrm{kHz}$) and one close to the diagonal for $f_2 < 0\,\mathrm{kHz}$ ($f_1 = 200\,\mathrm{kHz}$, $f_2 = -182\,\mathrm{kHz}$). To further investigate the QCM-HHM coupling, a bicoherence analysis was performed for every 40 ms. Fig. 5.6c shows the comparison of the frequency coordinates close to the diagonal (latter case) from the bicoherence analysis and the frequencies of the modes in the magnetic

spectrogram from Fig. 5.6a. The bicoherence frequencies f_1 and f_2 are marked as blue and white data points. We see that f_1 agrees with the frequency of the most prominent HHM, but f_2 is not visible, or only faintly. Contrary, their sum frequency $f = f_1 + f_2$ is equal to the frequency of the QCM. Hence, the QCM and the most prominent HHM are coupling. This can be interpreted in two ways: either the QCM at $f_{\mathrm{QCM}} = 18\,\mathrm{kHz}$ and the most prominent HHM at $f_{\mathrm{HHM,n=6}} = 200\,\mathrm{kHz}$ couple together producing a third mode at 182 kHz, or the unknown weakly visible mode at 182 kHz and the strongest HHM at $f_{\mathrm{HHM,n=6}}$ couple together producing the QCM. However, the QCM is certainly not a result of the HHMs, because the mutual coupling of the interaction of different harmonics of the HHMs yield always a mode with a frequency of a multiple of the fundamental $n_{\mathrm{mode}} = 1$ mode. In other words: if you pick a combination of f_1 and f_2 other than the ones proposed before in Fig. 5.6b, their sum frequency is equal to $\ell \cdot f_{\mathrm{HHM,n=1}}$, where $\ell \in \mathbb{N}$ and this expression is not equal to the QCM frequency.

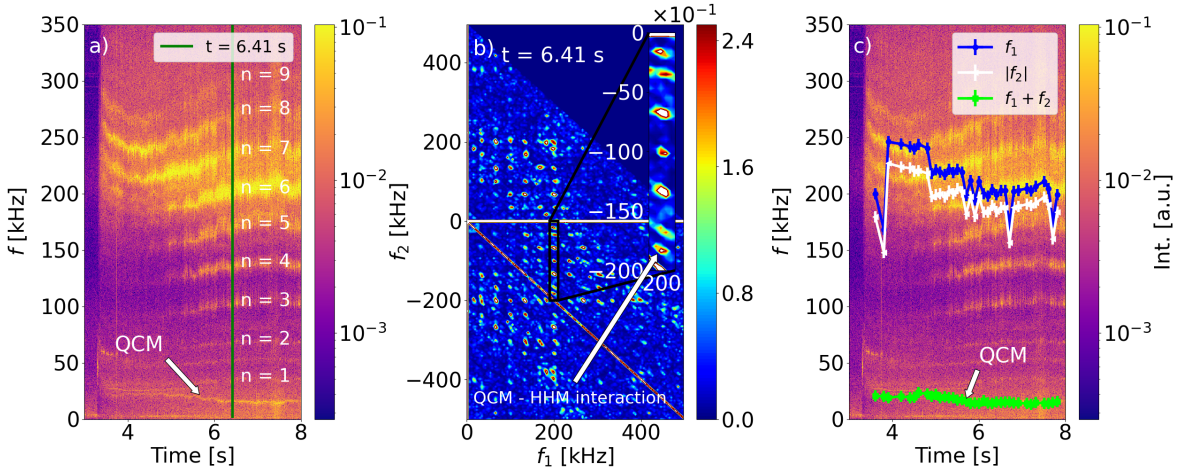

Figure 5.6: Bicoherence Analysis of QCM and HHMs

a) Spectrogram of one magnetic pick-up coil in discharge #38067 with QCM and HHM signature. HHMs are assigned with toroidal wavenumbers of up to $n_{\mathrm{mode}} = 9$. The green line $t = 6.41\,\mathrm{s}$ indicates at which a bicoherence analysis is performed in b). The temporal evolution of the combinations for (f_1, f_2) as marked in the enlarged section and their sum, $f_{\mathrm{QCM}} = f_1 + f_2$ are shown in c). Fig. taken from Ref. [180].

The fact that the HHMs do not cause the QCM is also underlined by the different time evolution of their frequencies, i.e. when f_{HHM} increases with time f_{QCM} generally decreases. Furthermore, in many QCE scenarios we observed the QCM but no HHMs or other high frequency modes, affirming the fact that the QCM can exist in absence of the HHMs or any other type of mode visible in the magnetics. This indicates that the QCM is an independent mode driven by a separate mechanism.

5.3 Wavenumber Analysis of the QCM

After analyzing the coupling of the QCM with the HHMs based on magnetic signals, we now return to the determination of properties of the QCM by means of the THB. In contrast to the frequency, which depends on the plasma background velocity, the wavenumber is not affected by this and represents therefore a more robust mode property directly accessible by local measurements in the laboratory frame. The wavenumber is calculated via the method described in Sec. 4.4.

Poloidal Wavenumber

The poloidal wavenumber k_θ quantifies the poloidal size of the QCM according to Eq. 3.1 and can be calculated by the THB if the 5×5 grid is available (Fig. 4.3b).

Fig. 5.7a shows a typical $k_\theta - f$ spectrum (see Sec. 4.4) for one time interval of 40 ms, which is of the order of an active He puffing phase for discharge #38067, in which a heating power ramp-up was implemented. The color scale indicates whether there is a mode with a specific combination of k_θ and f. In this example, the mode activity concentrates around $k_\theta = -0.64\,\mathrm{cm}^{-1}$ and $f \approx 17.1\,\mathrm{kHz}$. The found frequency is equal to the one of the QCM as determined in the standard Fourier spectrum, yielding the corresponding poloidal wavenumber of the QCM of about $k_\theta^{\mathrm{QCM}} = -0.64\,\mathrm{cm}^{-1}$. The negative sign of k_θ indicates that the mode propagates in electron diamagnetic direction in the laboratory frame, but in the following only the absolute value of k_θ is used. By evaluating the $k_\theta - f$ spectra for small and consecutive time intervals of 20 ms, it is possible to analyze the temporal evolution of k_θ and the influence of local or global plasma parameters on k_θ during the whole discharge. Fig. 5.7b presents the time series of k_θ at a radial position right inside the separatrix at $\rho_{\mathrm{pol}} = 0.995$. The error bars σ_{k_θ} correspond to the FWHM of the peak of the $k_\theta - f$ spectrum along the k_θ-axis at the frequency of maximum amplitude (the QCM frequency). Furthermore, we compare k_θ for different discharges and thus, different plasma parameters. k_θ and f are connected via the phase velocity in the laboratory frame as $v_{\mathrm{lab}} = 2\pi f / k_\theta$, which will be discussed in Sec. 5.4. The values of k_θ deviate for ASDEX Upgrade [57] and Alcator C-Mod [77, 80]. In order to make comparisons to other tokamaks and to theoretical approaches, the poloidal wavenumber normalized to the hybrid gyroradius $k_\theta \rho_{\mathrm{s}}$ is used, where ρ_{s} is defined in Eq. 3.2. This is depicted in Fig. 5.7c. k_θ varies by less than a factor of two in this discharge, however, $k_\theta \rho_{\mathrm{s}}$ changes from 0.038 to 0.075. The reason for this difference is the change of the electron temperature T_{e}, which enters the definition of ρ_{s}. n_{e} is nearly constant during the discharge and a comparison between k_θ, $k_\theta \rho_{\mathrm{s}}$ and the profile quantities T_{e} and p_{e}, shown in Figs. 5.7d)-f), respectively, leads to the observation that a scaling law between those exists, which will be shown quantitatively

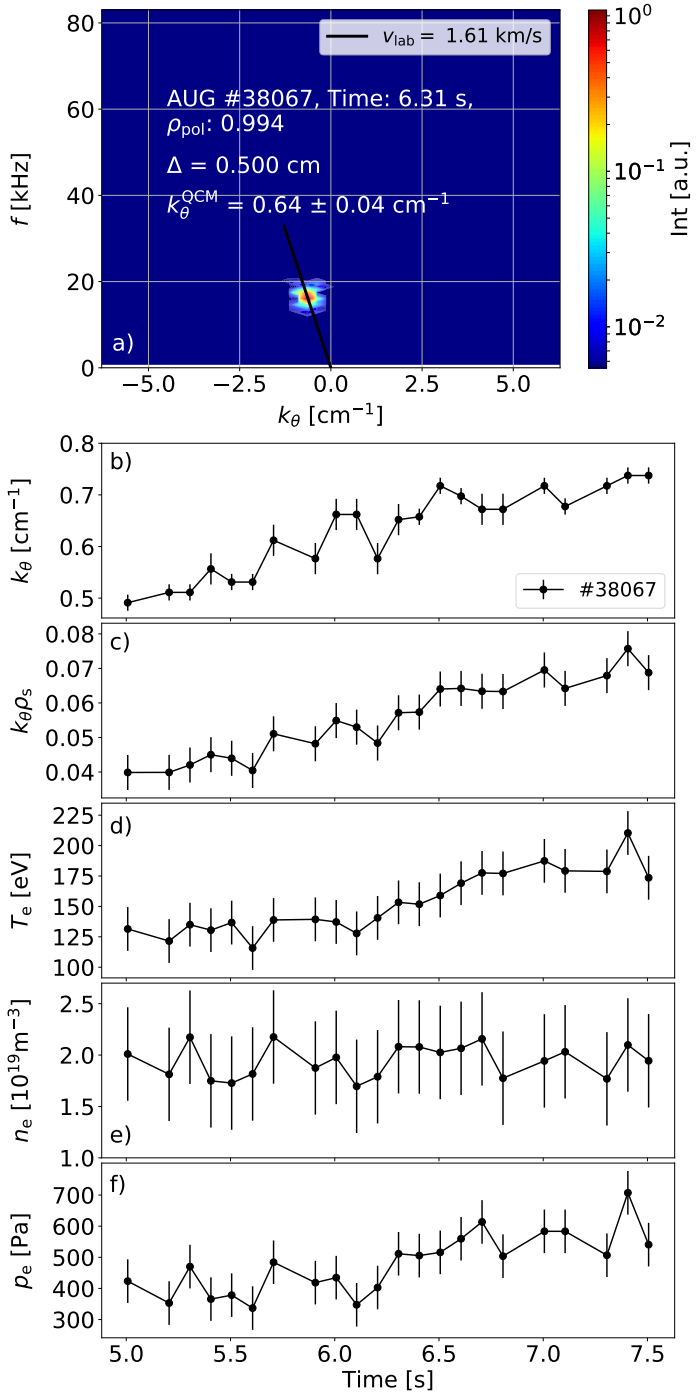

Figure 5.7: Time Series of the Poloidal Wavenumber of the QCM

Example of a $k_\theta - f$ spectrum in discharge #38067 for the time interval $t = [6.30\,\mathrm{s}, 6.34\,\mathrm{s}]$ a), where the spot of high intensity marks the QCM. The slope of the black line displays the phase velocity in the laboratory frame v_{lab}. k_θ b) and the normalized wavenumber $k_\theta\rho_s$ c) vary during the discharge. Local electron temperature d), density e) and pressure f) are measured at $\rho_{\mathrm{pol}} \approx 0.995$ for the same discharge. Fig. taken from Ref. [180].

in the following.

After a promising relation for the frequency of the QCM f_{QCM} has been found (see Eq. 5.2 above), we now try to find a correlation of $k_\theta \rho_\mathrm{s}$ with plasma parameters guided by theoretical considerations. The Drift-Alfvén (DALF) model [116] is a system of plasma fluid equations and describes turbulence at the plasma edge in toroidal geometry. Based on the DALF model it is possible, to differentiate between three regimes: the electromagnetic (EM), the resistive ballooning mode (RBM) and the ideal ballooning mode (IBM) regime. This discrimination was proposed in a similar way by Drake *et al.* [120]. All three regimes are characterized by a specific scaling of the poloidal mode number, which are derived in Ref. [119]:

$$k_{\mathrm{EM}}\rho_\mathrm{s} = \sqrt{\frac{\mu_0 m_\mathrm{i} p_\mathrm{e}}{B_\mathrm{t}^2 m_\mathrm{e}}}, \tag{5.5}$$

$$k_{\mathrm{RBM}}\rho_\mathrm{s} = K\frac{\sqrt{\alpha_\mathrm{c}} T_\mathrm{e} \lambda_{\mathrm{p_e}}^{1/4}}{q_{95}^2 \sqrt{n_\mathrm{e}}}, \tag{5.6}$$

$$k_{\mathrm{ideal}}\rho_\mathrm{s} = C\frac{T_\mathrm{e}^{3/2}}{\lambda_{\mathrm{p_e}}^{1/4} B_\mathrm{t}}. \tag{5.7}$$

μ_0 is the magnetic permeability, α_c is the critical α_{MHD} (see Eqs. 3.19, 3.20), $\lambda_{\mathrm{p_e}}$ is the typical perpendicular gradient length, and $K = 792 \cdot 10^6$ eV^{-1}m$^{-7/4}$ and $C = 688 \cdot 10^{-6}$ m$^{1/4}$eV$^{-3/2}$T are the corresponding constants for AUG.

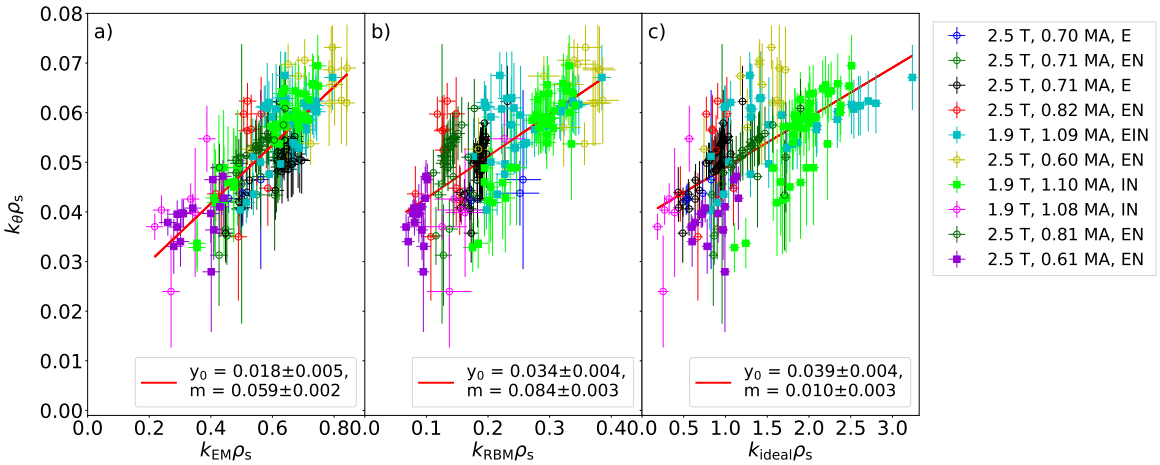

Figure 5.8: Scaling of $k_\theta \rho_\mathrm{s}$ of the QCM

For numerous discharges the normalized poloidal wavenumber is compared to characteristic wavenumbers like the electromagnetic $k_{\mathrm{EM}}\rho_\mathrm{s}$ a), the resistive ballooning mode $k_{\mathrm{RBM}}\rho_\mathrm{s}$ b) and the ideal ballooning instability $k_{\mathrm{ideal}}\rho_\mathrm{s}$ c). y_0 (offset) and m (slope) are the corresponding parameters for the linear fits. The legend includes the toroidal field strength B_t, plasma current I_p and the used heating mechanism, where E: ECRH, I: ICRH, N: NBI. Fig. taken from Ref. [180].

k_{EM} describes the transition between the electromagnetic ($k_\theta < k_{\mathrm{EM}}$) and the electrostatic regime ($k_\theta > k_{\mathrm{EM}}$) in wavenumber space at low collisionality (Eq. 2.10). k_{RBM} is the typical wavenumber of the electrostatic RBM and k_{ideal} describes the transition between the ideal ($k_\theta < k_{\mathrm{ideal}}$) and resistive MHD-like ($k_\theta > k_{\mathrm{ideal}}$) regime in wavenumber space. These are typical wavenumbers, for which one does not expect an exact match with the maximum growth rates. However, these are well-defined quantities whose scaling can be well studied analytically and in numerical investigations. If a scaling with the quantities is found experimentally, this would be helpful for further theoretical investigations.

In Fig. 5.8, the experimental values of $k_\theta \rho_{\mathrm{s}}$ are compared to all three quantities. The electromagnetic wavenumber $k_{\mathrm{EM}}\rho_{\mathrm{s}}$ reproduces the experimental trend the best. An increase in $\sqrt{\beta}$ leads to a higher wavenumber. That the experimental values scale well with $k_{\mathrm{EM}}\rho_{\mathrm{s}}$ is further supported by a small offset (y_0), indicating that the poloidal wavenumber depends on the normalized energy content of the plasma. In the case of the characteristic RBM wavenumber $k_{\mathrm{RBM}}\rho_{\mathrm{s}}$ in Fig. 5.8b and the IBM wavenumber $k_{\mathrm{ideal}}\rho_{\mathrm{s}}$ in Fig. 5.8c, the offset of the linear fit is larger and the data points are more scattered. In all cases, the absolute values are not reproduced since the slope is $m \ll 1$, which has been explained above.

Overall, the measured values of the poloidal wavenumber of $0.025 < k_\theta \rho_{\mathrm{s}} < 0.075$ are in a range between micro-instabilities with $k_\theta \rho_{\mathrm{s}} > 0.01$ (Sec. 3.2) and typical MHD modes with $k_\theta \rho_{\mathrm{s}} < 0.01$ (Sec. 3.1), and in a range, where EM effects are expected to become important.

Radial Wavenumber

In Fig. 5.9a the radial structure of the mode, i.e. its radial wavenumber k_{r} is determined by cross-correlating radially aligned THB LOS according to the method from Sec. 4.4. As shown in Fig. 5.9b, the radial wavenumber is approximately zero for a radial region between $\rho_{\mathrm{pol}} = 0.994$ and $\rho_{\mathrm{pol}} = 1.002$. In addition, the measured laboratory velocity of $v_{\mathrm{lab}} \gg 1\,\mathrm{km\,s^{-1}}$ might indicate the occurrence of streamers [137]. Streamers are radially elongated flows, transporting heat and particles into the far SOL. Additionally, Fig. 5.9b shows that $k_{\mathrm{r}} > 0\,\mathrm{cm^{-1}}$ inside the pedestal and that it shrinks to a small value at the position of the QCM close to the separatrix. $k_{\mathrm{r}} > 0\,\mathrm{cm^{-1}}$ means that the QCM signal was first measured further in and then further out, indicating a radial movement towards the highest QCM amplitude, i.e. radial outwards.

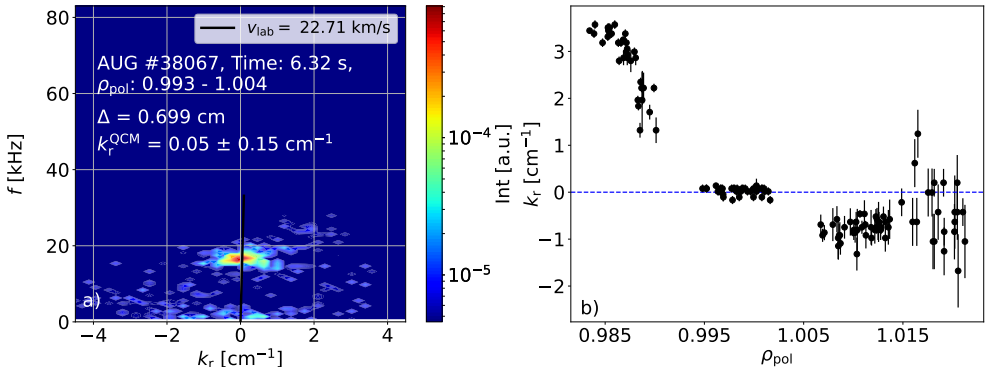

Figure 5.9: Radial Wavenumber

Example of a $k_r - f$ spectrum from discharge #38067 a), where the bright point marks the QCM. The radial profile of the radial wavenumber k_r is shown in b) and is approximately zero for a wide radial range. Fig. taken from Ref. [180].

5.4 Phase Velocity of the QCM in the Plasma Frame

The phase velocity in the co-moving plasma frame v_{ph}, is an important quantity of a mode due to the fact that the direction of motion excludes potential underlying instabilities. As explained in Sec. 3.3.2 v_{ph} is given as the difference of the mode velocity in the laboratory frame v_{lab}, obtained from the $k_\theta - f$ spectrum (cf. Fig. 5.7a), and the $E \times B$ background plasma velocity $v_{E\times B}$ (see Eq. 3.49), i.e. $v_{ph} = v_{lab} - v_{E\times B}$. According to Eq. 3.49, the calculation of $v_{E\times B}$ requires the measurement of ion data, like the ion pressure p_i. On AUG $v_{E\times B}$ is routinely measured by edge CXRS (Sec. 4.3). This implies that NBI heating is a necessity to determine $v_{E\times B}$ by means of CXRS. Though, on AUG $v_{E\times B}$ is close to the negative ion diamagnetic velocity $v_{i,dia}$, which can be approximated by the electron diamagnetic velocity [190] (as it has been done in Sec. 5.1) for discharges lacking NBI heating as in Eq. 5.1.

This is verified in Fig. 5.10a, where $v_{e,dia} \approx v_{E\times B}$ within the errorbars (blue pluses and red triangles). It should be noted that this agreement is only valid at the radial position of the QCM, but not further inside. For discharge #39605, the plasma $E \times B$ velocity is between $-10\,\mathrm{km\,s^{-1}}$ and $-5\,\mathrm{km\,s^{-1}}$ during the whole discharge. The negative sign implies that the plasma rotates in electron diamagnetic direction. In addition to the $E \times B$ background velocity, the velocity of the QCM in the laboratory frame is marked as black dots in Fig. 5.10a and is approximately constant over time at a value of $v_{lab} \approx -3.5\,\mathrm{km\,s^{-1}}$. The green squares are the sum of the ion diamagnetic velocity $v_{i,dia}$ and $v_{E\times B}$, obtained by CXRS. Here, a value slightly above zero is achieved. The phase velocity of the QCM in the plasma frame is calculated by the difference of v_{lab} and $v_{E\times B}$. Remarkably, v_{lab} (black dots) is constantly above the background velocity, indicating that $v_{ph} = v_{lab} - v_{E\times B} > 0\,\mathrm{km\,s^{-1}}$, so that the QCM phase velocity is in

ion diamagnetic direction in the plasma frame at the position, at which the QCM is located. Though, the phase velocity in the plasma frame is smaller than the ion diamagnetic velocity, $v_{\mathrm{i,dia}}$ (black dots below green squares), which was determined according to Eq. 5.1 but with ion data instead of electron data.

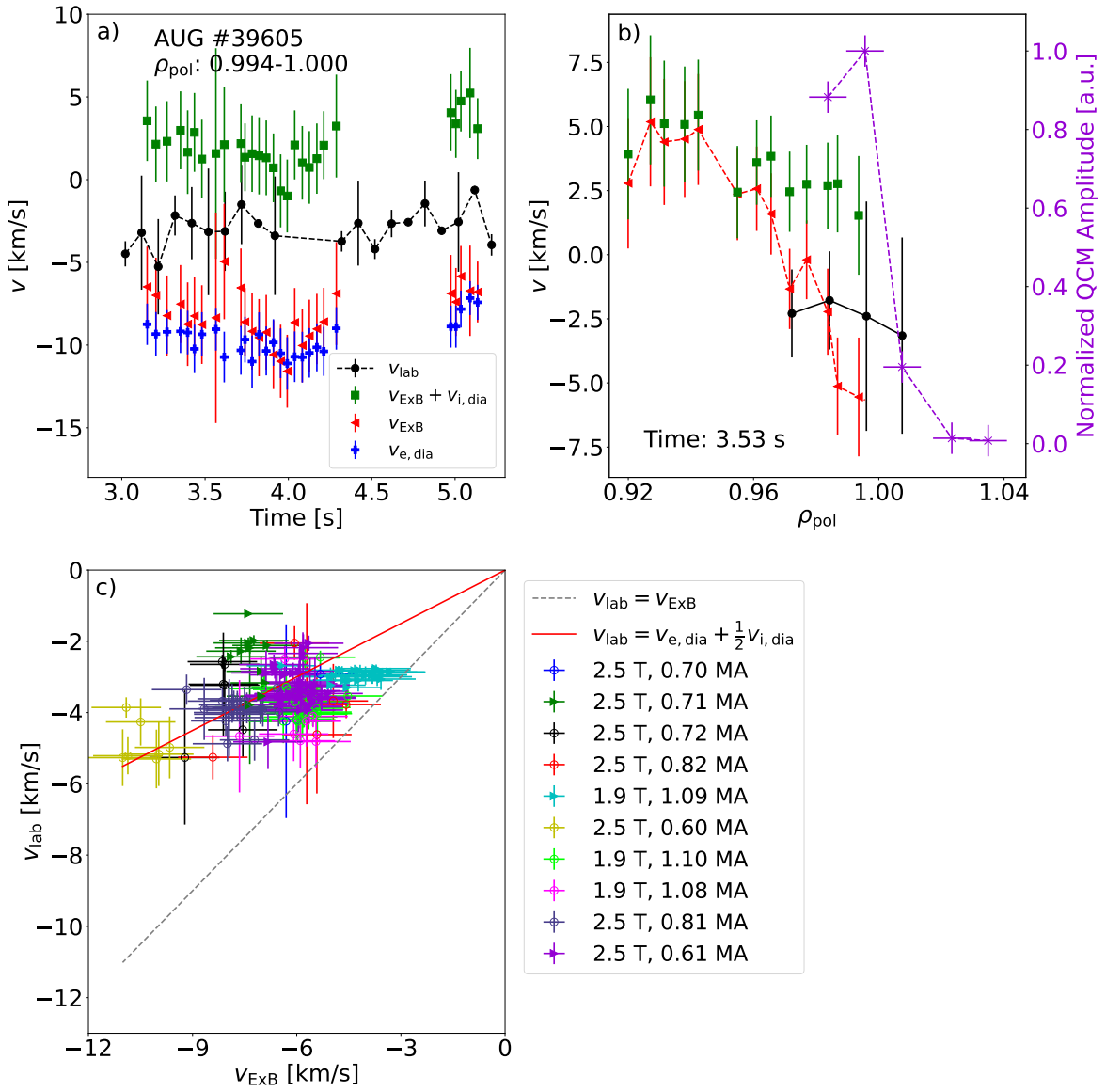

Figure 5.10: Phase Velocity of the QCM

Comparison of $v_{\mathrm{E\times B}}$ from CXRS, the approximated plasma velocity $v_{\mathrm{e,dia}}$ and v_{lab}, obtained from the $k_\theta - f$ spectra a) in discharge #39605. One radial profile of the velocities is shown together with the amplitudes of the QCM along the radial axis (purple crosses) as described in Sec. 5.1 in b). c) Overview of all discharges analyzed with the approximation $v_{\mathrm{e,dia}} \approx v_{\mathrm{E\times B}}$. The legend includes the toroidal field strength B_{t} and plasma current I_{p}. Fig. taken from Ref. [180].

Fig. 5.10b present radial profiles of the different velocities. f_{QCM} as well as k_θ do not change drastically along the radial positions, leading to a nearly constant v_{lab}

over a certain radial range. On the contrary, $v_{\mathrm{E\times B}}$ varies radially, where its highest absolute value is reached inside the E_r well. Combining $v_{\mathrm{E\times B}}$ and v_lab, it seems that the direction of motion of the QCM in the plasma frame changes with ρ_pol, i.e. the determination of v_ph seems to depend on the considered radial position, illustrated in Fig. 5.12b. This fact might explain the contradicting results from Theiler *et al.* [80], claiming that the QCM moves in ion diamagnetic direction and localized near the E_r minimum, and LaBombard *et al.* [77], observing the QCM in Ohmic EDA H-modes in the near SOL with a movement in electron diamagnetic direction. In order to obtain a unique value of the plasma velocity for the QCM in our case, we assume that the relevant radial position of the QCM is located where the maximum mode amplitude is found, as described in Sec. 5.1. We determine v_lab and $v_{\mathrm{E\times B}}$ at this location, e.g. at $\rho_\mathrm{pol} = 0.995$ in Fig. 5.10b to calculate v_ph.

By using the approximation $|v_\mathrm{i,dia}| \approx v_\mathrm{e,dia} \approx v_{\mathrm{E\times B}}$, it is possible to compare v_lab with $v_{\mathrm{E\times B}}$ for all discharges analyzed in Fig. 5.10c, including plasmas, for which no CXRS measurements was available. As shown in Fig. 5.10c, all data points are above the $E \times B$ velocity (grey dotted line), i.e. for all cases the phase velocity in the plasma frame is in the ion diamagnetic direction. The data points are symmetrically scattered around the line indicating $v_\mathrm{ph} \approx 1/2 v_\mathrm{i,dia}$ (red). Therefore, the data is consistent with the predictions for ballooning modes where finite Larmor radius effects are taken into account [117], which is discussed in Sec. 3.1.1 and 3.1.2.

Based on the consideration in Sec. 3.3.2, it is possible to estimate from the phase velocity in the plasma frame determined whether the mode causes radial transport Γ_r. Inserting v_ph into Eq. 3.54, we obtain

$$\Gamma_\mathrm{r} = \frac{|k_\theta|}{B_\mathrm{t}} |\tilde{n}_\mathrm{e}| \left|\tilde{\phi}\right| \sqrt{1 - \left| \frac{0.5 v_\mathrm{i,dia}}{\left|\tilde{\phi}\right| \nabla n_0 / (|\tilde{n}_\mathrm{e}|\, B_\mathrm{t})} \right|^2} > 0. \tag{5.8}$$

Unfortunately, the density $\tilde{n}_\mathrm{e}$ and potential fluctuations $\tilde{\phi}$ cannot be calculated with the THB diagnostic, but we see that $\Gamma_\mathrm{r} > 0$ and thus the QCM causes radial outward transport and can indeed play its assigned role.

5.5 Cross-Phase between Electron Temperature and Density

In Sec. 3.3.2 it is shown that the cross-phase between density $\tilde{n}_\mathrm{e}$ and potential fluctuations $\tilde{\phi}$, i.e. $\alpha_{\mathrm{n_e},\phi}$, plays an important role in the radial transport (Eq. 3.47) and also in the characterization of an edge instability. As explained above, it is not possible to study $\tilde{\phi}$ with the THB diagnostic which is why $\alpha_{\mathrm{n_e},\phi}$ is not accessible. However, we

are able to calculate the cross-phase between $\tilde{n}_e$ and temperature fluctuations $\tilde{T}_e$ of the QCM, i.e. $\alpha^{QCM}_{n_e,T_e}$ using the method developed by Nishizawa *et al.* [186]. Although this quantity is rarely used in theoretical considerations, it provides another indication of the underlying instability of the QCM, as this quantity can potentially be validated by simulation results. As mentioned Sec. 4.4, it requires measurements of all four spectral lines of the THB to get α_{n_e,T_e}. Since the measurements are only reliable for all four lines outside the separatrix, we can only analyze the cross-phase for certain discharges, e.g. EDA H-mode #36124, shown in Fig. 5.11a.

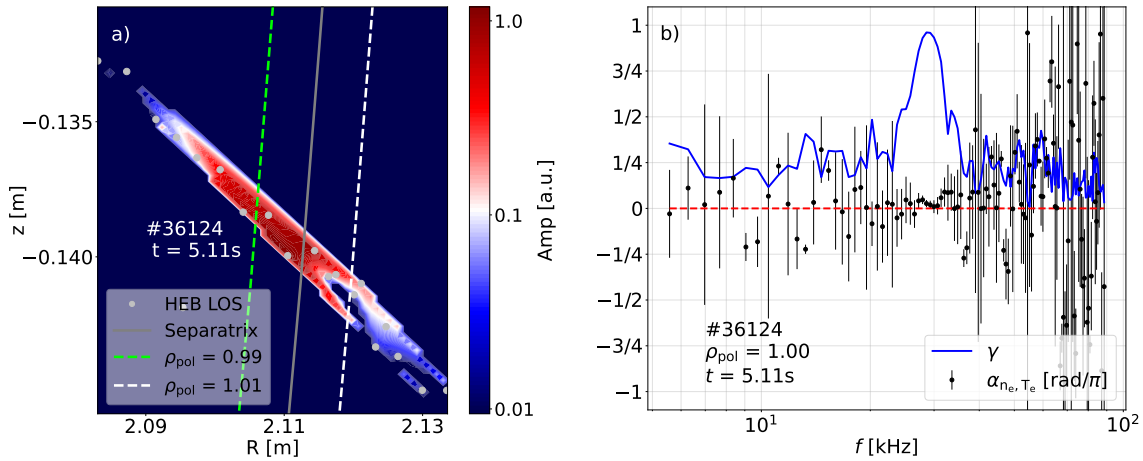

Figure 5.11: Cross-Phase Between n_e and T_e of the QCM
a) to determine the cross-phase α_{n_e,T_e} of the QCM, it is necessary that the QCM is also visible outside the separatrix (gray line). The colorbar shows that an amplitude can also be measured in the SOL. Lines for various ρ_{pol} are drawn for clarity. b) this allows the coherence (blue) of the density and temperature sensitive signal to be calculated, which in turn leads to a reliable estimate of α_{n_e,T_e} (black points).

Note that only the radial grid is available in this plasma pulse. Nevertheless, the QCM with a frequency of about 29 kHz seems to be active exceptionally far out. To determine α_{n_e,T_e} (black dots in Fig. 5.11b), it is necessary that the coherence γ (blue) of the density sensitive $R_I^{n_e}$ and temperature sensitive signal $R_I^{T_e}$ (defined in Sec. 4.4), is sufficiently large. The coherence is defined as

$$\gamma = \frac{\left|\left\langle R_I^{n_e}(f)\left(R_I^{T_e}\right)^{\star}(f)\right\rangle\right|^2}{\sqrt{\left\langle\left(R_I^{n_e}(f)\right)^2\right\rangle\left\langle\left(R_I^{T_e}(f)\right)^2\right\rangle}}. \tag{5.9}$$

A value of one indicates a strong correlation and a value of zero indicates that they are completely uncorrelated. We see in Fig. 5.11b that γ is clearly larger than 50% and with a maximum of more than 90% and thus is sufficiently large at the QCM frequency. This means that we can trust the cross-phase measurements in this frequency range around the QCM. As it can be seen, $\tilde{n}_e$ and $\tilde{T}_e$ are in phase, i.e. $\alpha^{QCM}_{n_e,T_e} \approx 0$. Hence, the

density and temperature fluctuations are in-phase indicating that the QCM amplitude is a pressure perturbation without separate dynamics for n_{e} and T_{e}. This result confirms also the assumption of the synthetic signal presented in Sec. 4.2, where density and temperature perturbations were assumed to be in-phase for the diagnostic sensitivity study.

5.6 EDA H-mode and QCE in an $\alpha_{\mathrm{d}} - \alpha_{\mathrm{MHD}}-$ diagram

A concept of a phase space for tokamak edge turbulence was introduced first by Rogers, Drake and Zeiler (RDZ) [120] in 1998 and serves to categorize operational points of the plasma based on simulations. The underlying physics addresses the existence of some regime boundaries observed in tokamaks, namely a density limit, changes in confinement and the ideal ballooning limit. In 2021, Eich and Manz compared the theory of RDZ to separatrix values of AUG [119] using the originally proposed normalized variables α_{MHD} and α_{d}. With a number of modifications this work then led to the concept of the separatrix operational space, which is characterized by a turbulence parameter [122] (Eq. 3.23)

$$\alpha_{\mathrm{T}} = 3.13 \cdot 10^{-18} R_{\mathrm{maj}} q_{95}^2 n_{\mathrm{e}} Z_{\mathrm{eff}} / T_{\mathrm{e}}^2, \tag{5.10}$$

where $\ln \Lambda = 13.7$ is used, and three typical wavenumbers k_{EM}, k_{RBM} and k_{ideal}, introduced in Sec. 5.3. Myra *et al.* associated the EDA H-mode with a characteristic regime in an $\alpha_{\mathrm{d}} - \alpha_{\mathrm{MHD}}-$diagram [195] at the separatrix, based on the theory of RDZ. We compare this theory with the experimental data at AUG, using the dimensionless MHD ballooning parameter from Sec. 3.1.1

$$\alpha_{\mathrm{MHD}} = c_{\mathrm{MHD}} \frac{q_{95}^2 n_{\mathrm{e,sep}} T_{\mathrm{e,sep}}}{B_{\mathrm{t}}^2 \lambda_{\mathrm{p_e}}}, \tag{5.11}$$

and the diamagnetic parameter from Sec. 3.1.2

$$\alpha_{\mathrm{d}} = c_{\mathrm{d}} \frac{T_{\mathrm{e,sep}}}{q_{95} \lambda_{\mathrm{p_e}}^{1/4} \sqrt{n_{\mathrm{e,sep}}}}. \tag{5.12}$$

The local values of $n_{\mathrm{e,sep}}$ and $T_{\mathrm{e,sep}}$ are taken at 1 mm inside the separatrix from the Thomson scattering diagnostic [177] (Sec. 4.3) and $c_{\mathrm{MHD}} \approx 332 \cdot 10^{-22} \mathrm{eV}^{-1}\mathrm{m}^4\mathrm{T}^2$ and $c_{\mathrm{d}} \approx 128 \cdot 10^6 \mathrm{eV}^{-1}\mathrm{m}^{-5/4}$ are constants from Eqs. 3.19 and 3.22, when inserting AUG specific parameters.

These two parameters control the transport in the edge of the tokamak. In general, a region for large $\alpha_{\mathrm{MHD}} > \alpha_{\mathrm{c}}$ indicates the ideal MHD limit, at which the plasma gets unstable to ideal ballooning modes (IB). For our discharges analyzed it holds that

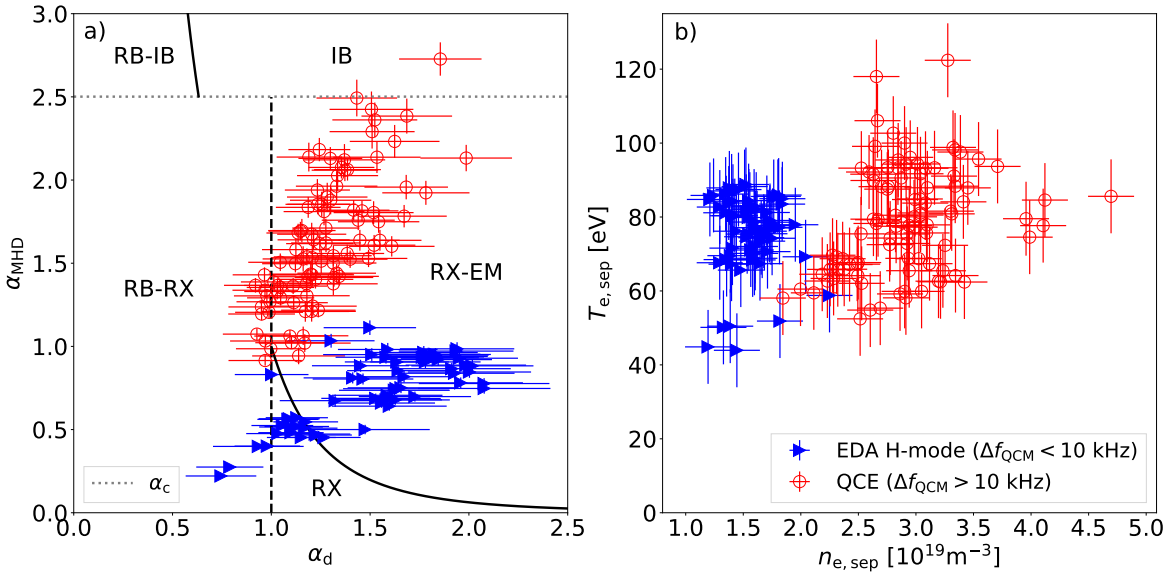

Figure 5.12: Separatrix Evaluation of EDA H-Mode and QCE
Classification of various discharges into an edge phase space turbulence diagram in terms of α_{MHD} and α_d, where $\alpha_{MHD} > \alpha_c \approx 2.51$ implies that the plasma is ideal ballooning (IB) unstable, $\alpha_d < 1$ indicates a resistive ballooning (RB) unstable regime and $\alpha_d > 1$ lead to resistive X-point modes (RX and RX-EM) a). Blue triangles are identified as EDA H-modes, whereas red hollow circles are QCE discharges. The two regimes are also well separated in the separatrix $n_{e,sep} - T_{e,sep}$ graphic b). Fig. taken from Ref. [180].

$\alpha_c > 2.51$. On the other hand, if $\alpha_{MHD} < \alpha_c$ and $\alpha_d < 1$, the stability conditions in the plasma edge give rise to a resistive ballooning mode (RB). This condition is typically fulfilled in AUG H-mode operation [119]. By including X-Point physics, it is possible to derive regimes for IB stable plasmas and values of $\alpha_d > 1$, that are unstable to resistive X-point modes (RX and RX-EM). These regimes have been derived by Myra *et al.* in Ref. [195]. All operational points of the considered discharges are characterized as unstable to resistive X-point modes with an electromagnetic fingerprint (RX-EM) in Fig. 5.12a as also proposed in Ref. [195].

Two branches are found: one following the blue triangles (EDA H-modes) and one the red spheres (QCE). The differentiation between EDA H-mode discharges and QCE plasmas was done by means of the boundary of bandwidth according to Eq. 5.4. The different slopes of the two branches can be explained by the variety of $n_{e,sep}$ and $T_{e,sep}$ as shown in Fig. 5.12b. EDA H-modes are characterized by smaller $n_{e,sep}$ and in general by a relatively small variation of densities, explaining the larger values of α_d at smaller values of α_{MHD}. QCE plasmas extend over a wider range of densities and temperatures, and the way this type of discharges are operated, e.g. by applying higher plasma currents and heating power for higher fuelling rates, lead to a simultaneous increase in density and temperature at the separatrix. Consequently, the α_{MHD} parameter rises

faster relative to α_d resulting in a steeper slope of the QCE data points (red) compared to the EDA H-mode data (blue) in Fig. 5.12a. It has to be mentioned that only a subset of data points are presented here and a general overview, containing more data is work in progress. The fact that the QCE discharges (characterized by $\Delta f_{QCM} > 10\,\text{kHz}$) appear at higher densities as shown in Fig. 5.12b implies that the coherence of the QCM decreases with density possibly related to an increased ballooning instability producing more frequent and larger filaments at higher densities [196].

5.7 Discussion and Interpretation

After presenting the properties of the QCM, we discuss and classify the obtained results and compare those with preceding and ongoing analyses.

For the physical interpretation of the measurements we introduced necessary assumptions. First, the most crucial point is the radial localization of the QCM. We decided to define the QCM position at the radial location, where density and temperature fluctuation peaks. This corresponds to the maximum amplitude of the line ratio time trace I_{667}/I_{587} along the radius. In order to support this approach, we have already shown in Sec. 4.4 that the ratio of two emission intensities shows a maximum, where the highest density or temperature fluctuation is present. Second, the background velocity $v_{E\times B}$ was approximated by the diamagnetic velocity of the electrons. Where available this was compared to the more precise CXRS data, justifying the approximation. Third, all profile data are subject to inaccuracies inherent to the equilibrium reconstruction, which was needed to map the radial profiles of the different diagnostic onto each other. Only on the basis of these assumptions and the involved inaccuracies the following statements hold.

The QCM propagates in ion diamagnetic direction (IDD) in the plasma frame for each discharge (Sec. 5.4), explaining the counter-intuitive relation between f_{QCM} and $v_{E\times B}$, i.e. the QCM propagates against the direction of the background plasma (Sec. 5.1). This conclusion relies on the precision of the radial localization of the mode and the accuracy of the radial profiles, since already a small radial shift by 3 mm would lead to a propagation in electron diamagnetic direction (EDD) (cf. Fig. 5.10b). Based on the measured velocity, which is determined to be in IDD by means of our approach, a whole group of modes, i.e. modes which are typically propagating in EDD, can be excluded (see Tab. 3.1). Qualitatively, IDD propagation applies to ideal (IBM), resistive (RBM), kinetic ballooning modes (KBM) or ion temperature gradient modes (ITG), which remain as candidates for the QCM. Furthermore, IBMs and RBMs propagate with $v_{ph} \geq 1/2 v_{i,dia}$ [117], which is in agreement with the experimentally observed results from Fig. 5.10c.

All remaining candidate instabilities, i.e. IBMs (Sec. 3.1.1), RBMs (Sec. 3.1.2), KBMs (Sec. 3.2.5) and ITGs (Sec. 3.2.2) possess typical perpendicular wavenumbers lying within the range of the experimentally measured, normalized poloidal wavenumbers $0.025 < k_\theta \rho_\mathrm{s} < 0.075$. However, the absolute values of the experimental $k_\theta \rho_\mathrm{s}$ are significantly lower than the ones delivered theoretically by the DALF system (see Fig. 5.8). For the electromagnetic wavenumber, i.e. $k_\theta \rho_\mathrm{s} \ll k_\mathrm{EM} \rho_\mathrm{s}$ it means that the performed discharges are deep in the electromagnetic regime and for $k_\mathrm{EM} \rho_\mathrm{s} \gtrsim 0.5$ the QCM gives rise to very strong electromagnetic turbulent transport [119], which is in agreement with the properties of KBMs. The postulated electromagnetic nature inferred from the wavenumber measurement matches the observation of the QCM in the magnetic signal (e.g. in Fig. 5.4). Generally, ITG turbulence is strongly reduced in the electromagnetic regime (Fig. 3.6), so that ITGs can be ruled out as a candidate.

The separatrix analysis (Sec. 5.6) indicates that EDA H-modes and QCE discharges are neither unstable regarding IBMs ($\alpha_\mathrm{MHD} < \alpha_\mathrm{c}$) nor RBMs ($\alpha_\mathrm{d} > 1$). However, IBMs and RBMs still can exist in H-modes, i.e. the regimes shown in Fig. 5.12a are not exclusive for their existence. According to the $\alpha_\mathrm{d} - \alpha_\mathrm{MHD}-$diagram at the separatrix, EDA and QCE discharges should give rise to an X-point mode with electromagnetic fingerprint (RX-EM), which cannot be confirmed yet disproved in experiments so far, but this result is in agreement with the simulations in Refs. [195] and [197].

To compare the results with those of Alcator C-Mod, DIII-D and EAST, summarized in Tab. 5.1, it is important to note where the QCM was localized radially. The poloidal wavenumber k_θ and especially $k_\theta \rho_\mathrm{s}$ - since we have to include B_t - is in very good agreement in all devices. The only exception are the results of DIII-D of Ref. [188], but this is because they localize the mode much further inside and thus ρ_s is much larger. All devices see the QCM propagate in EDD in the laboratory frame. The identification of v_ph in the plasma frame depends on the localization as described in Sec. 5.4, which is why it differs for the different machines.

Tab. 5.3 summarizes the experimental results of this work and compares them to two simulations that will be discussed in more detail below.

Simulations with the JOREK code [198] of an EDA H-mode can reproduce resistive peeling-ballooning modes with $n_\mathrm{mode} = 6$ to $n_\mathrm{mode} = 9$, resembling higher harmonic modes, similar to those being visible in the magnetic coils. Though, the poloidal wavenumber and frequency in the simulation is close to the one of the QCM, but no harmonics of the QCM are visible in the experiment. As shown in Sec. 5.2 the QCM is not a result of the HHMs or vice versa. Additionally, the HHMs are not well visible in QCE discharges (either the HHMs do not exist there, or we do not detect those), but QCE scenarios also do not exhibit major type-I ELMs generally, so that the HHMs do not seem to be the relevant characteristic for ELM avoidance.

Harrer *et al.* [82] (HELENA) showed that a common feature of QCE discharges is that they are very close to the ideal $n_{\mathrm{mode}} \to \infty$ ballooning stability limit at $\rho_{\mathrm{pol}} = 0.99$, i.e. inside the separatrix. This unstable region is overlapping with the radial range at which the QCM has its highest amplitude in our experiments. Fig. 5.12a shows that QCE discharges are closer to the ideal MHD stability limit at the separatrix than EDA H-modes. Initial investigations of the ideal ballooning stability threshold in EDA H-mode discharges indicate that the pedestal is ballooning unstable over a wider region.

The characterization of the QCM and the measured QCM properties presented here leave three instability candidates for the QCM: IBM, RBM or KBM, which are nearly impossible to distinguish on an experimental level.

Table 5.3: QCM Properties from our Analyses Compared to Simulation Results

'N/A' denotes that there is no quantified information available in the corresponding reference. A positive velocity indicates propagation in the ion diamagnetic direction.

Quantity	HELENA [82]	JOREK [198]	Experiment [180]
$\rho_{\mathrm{pol}}^{\mathrm{QCM}}$	0.99	0.99	0.993±0.007
f [kHz]	N/A	8–40	15–80
$k_\theta \rho_{\mathrm{s}}$	N/A	0.01–0.05	0.025–0.075
v_{ph}	N/A	> 0	$1/2\ v_{\mathrm{i,dia}}$
Instability	IBM, RBM or KBM	Resistive P-B Mode	EM Ballooning Mode

Moreover, for the purpose of the previous analyses, a distinction between EDA H- and QCE discharges has been achieved explicitly by solely considering the QCM frequency bandwidth. In addition, the existence or visibility of the HHMs in the magnetic coils support the differentiation of the two regimes. The arbitrary boundary of Eq. 5.4 shows good agreement with the behaviors of the two scenarios in the $\alpha_{\mathrm{d}} - \alpha_{\mathrm{MHD}}-$diagram from Fig. 5.12a. QCE scenarios are characterized by a higher $n_{\mathrm{e,sep}}$ (Fig. 5.12b), but similar $T_{\mathrm{e,sep}}$ are achieved. At this higher $n_{\mathrm{e,sep}}$, type-II ELMs appear, as already mentioned in Sec. 2.2.2, which cause radial transport and thus an increase of the density in the scrape-off layer, i.e. a so-called density shoulder is formed. The following list enumerates the differences found between EDA H-mode and QCE:

i) QCE scenarios feature a broader QCM , i.e. $\Delta f_{\mathrm{QCM}} > 10\,\mathrm{kHz}$ (Eq. 5.4),

ii) $\log V_{\mathrm{HHM}}$ is generally higher in EDA H-modes, i.e. HHMs are more visible,

iii) QCE has a higher $n_{\mathrm{e,sep}}$,

iv) EDA H-modes and QCE scenarios obey different slopes in the $\alpha_{\mathrm{d}}-\alpha_{\mathrm{MHD}}-$diagram,

v) EDA H-modes do not feature any ELMs, but QCE has small type-II ELMs,

vi) QCE is often characterized by a density shoulder in the SOL, which is missing in EDA H-mode.

6 The I-Phase Precursor Mode

Now that we have intensively analyzed the edge mode of the EDA H-mode (Sec. 2.2.1) and the QCE regime (Sec. 2.2.2), i.e. the quasi-coherent mode (QCM) in Chapter 5, and have determined from our analysis that a ballooning mode with an electromagnetic fingerprint is present, we turn to the intermediate phase, abbreviated as the I-phase[1]. As introduced in Sec. 2.2.3, the I-phase is a scenario that occurs at the transition from the L-mode to the fully developed H-mode and is therefore important for future fusion devices if they are going to operate H-mode scenarios close to the L-H power threshold. The I-phase is characterized by the absence of type-I edge localized modes (ELMs), and is accompanied by the appearance of one or more edge instabilities. As can be seen in Fig. 2.3, there is not just one fluctuation in the I-phase, but two. On the one hand, there is a low-frequency fluctuation, which we will refer to as the limit cycle oscillation (LCO)[2], and a high-frequency mode, which we will refer to as the precursor mode[3].

In the first section, we will review the previous results in the literature on the I-phase edge properties. We will see that the precursor mode in particular has not received much attention. As the name of this chapter suggests, we will propose to interpret the high frequency oscillation as precursors of the LCO bursts by means of experiments on the ASDEX Upgrade tokamak (AUG, Sec. 4.1). Accordingly, an attempt will be made to assign an underlying linear instability from Tab. 3.1 to the precursor mode using data from the thermal helium beam diagnostic (THB, Sec. 4.2) and other supporting diagnostics like magnetic coils and integrated data analysis (Sec. 4.3).

The procedure is similar to the analysis of the QCM, and after the review we start with the radial localization of the precursor and its frequency behavior. The wavenumbers (poloidal and radial) are then analyzed and compared with local plasma parameters. This allows us to determine parametric dependencies of the precursor phase velocity in the plasma frame and we will see that it seems to change with varying α_T (see Eq. 6.6). The last property investigated is the lifetime of the mode, i.e. how long the precursor exists and what the lifetime depends on. Based on the physical quantities obtained, the possible nature of the mode will be discussed in the concluding part of this chapter.

[1] In JET this regime is called M-mode [191], and in DIII-D it is called IM-mode [92].
[2] The name 'low-frequency oscillation' (LFO) can also be found in literature [95].
[3] The name 'high-frequency oscillation' (HFO) can also be found in literature [95].

6.1 Edge Fluctuations in the I-Phase

In this section, the previous results concerning the edge modes of the I-phase are presented. Fig. 6.1 shows Fourier spectra of a 20 ms time interval during an I-phase according to the method described in Sec. 4.4. For better visibility, the frequency axis is plotted logarithmically. Fig. 6.1a shows THB data at $\rho_{\mathrm{pol}} = 0.98.$, Fig. 6.1b depicts data from magnetic coil $C09-23$, which measures deviations of the poloidal magnetic field, and Fig. 6.1c represents data from coil $B31-14$, which detects radial $B-$field perturbations. It is interesting to note that the THB and $\tilde{B}_{\mathrm{r}}$-coil detect the low-frequent limit cycle oscillations (LCOs) and the high-frequent precursor mode while the $\tilde{B}_{\mathrm{pol}}$ detects only the LCOs. To characterize the I-phase as such, the presence of LCOs is usually used as a criterion. The LCOs, and in particular their frequency scaling, are described in more detail below.

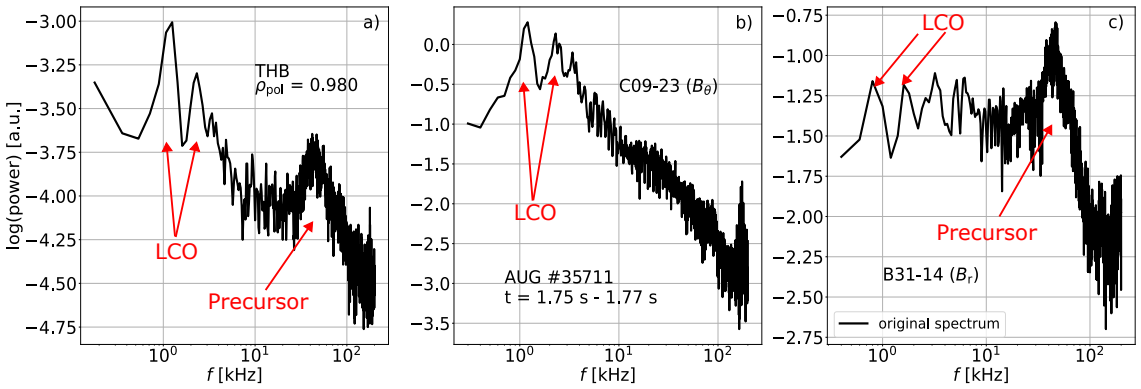

Figure 6.1: I-Phase Fourier Spectra from THB and Magnetic Coils
Fourier spectra of THB line ratio measurements a), poloidal magnetic coil $C09-23$ b) and radial magnetic coil $B31-14$ for the I-phase #35711 and the time interval $t \in [1.75\,\mathrm{s}, 1.77\,\mathrm{s}]$ show that the LCOs are present in a), b) and c) and the precursor is present only in a) and c). The spectra are calculated according to Sec. 4.4.

LCOs are always found in the low frequency range of a few kilohertz at different fusion devices compared to other coherent edge modes in ELM-free regimes. In JET, the frequency of LCOs was found to be related to the poloidal Alfvén velocity [191], i.e.

$$v_{\mathrm{A,pol}} \propto I_{\mathrm{p}}/\sqrt{n_{\mathrm{e}}}, \tag{6.1}$$

where I_{p} is the plasma current and n_{e} is the local electron density. This fact is thought to be due to a possible Alfvénic coupling of the LCOs (see Sec. 3.2.5). Experiments at AUG have shown that this scaling also holds for single discharges, but does not take into account the behavior of LCOs in discharges with different toroidal field strengths

B_t. An empirical approach resulted in a dependence of the LCO frequency as [63]

$$f_\mathrm{LCO}^\mathrm{AUG} \sim \frac{1}{\beta_\mathrm{e,ped} q_{95}^{1.5}}, \tag{6.2}$$

where $\beta_\mathrm{e,ped}$ is the pedestal plasma β (Eq. 2.5) evaluated at $\rho_\mathrm{pol} = 0.95$ and q_{95} is the safety factor from Sec. 2.1. Furthermore, it was found that LCOs have both regular and intermittent phases, i.e. an alternation of periodic and chaotic phases. In the following we will mainly deal with the I-phases that feature regular LCOs. With a theoretically based justification and a multi-machine database, Grover *et al.* have found a frequency scaling of LCOs that includes these two discoveries with slight deviations [96], i.e.

$$f_\mathrm{LCO}^\mathrm{Grover} = \frac{\sqrt{1+\tau_\mathrm{i}} c_\mathrm{s,i}}{2\pi q_{95} R_\mathrm{maj} \sqrt{1 + (1+\tau_\mathrm{i}) \left(k_\mathrm{EM}\rho_\mathrm{s}\right)^2}}, \tag{6.3}$$

where $\tau_\mathrm{i} = p_\mathrm{i}/p_\mathrm{e}$ (≈ 1 for us), $c_\mathrm{s,i}$ is the ion sound speed (Eq. 3.26) and $k_\mathrm{EM}\rho_\mathrm{s}$ is the electromagnetic wavenumber, derived from the DALF model (see Eq. 5.5 and Sec. 5.3). This formula interprets LCOs as the result of an interplay of the attempt of the ions to balance the asymmetry from the Stringer spin-up mechanism (SSU) [199, 200] with $c_\mathrm{s,i}$ over the connection length $2\pi q_{95} R_\mathrm{maj}$ and the restraint of this by the Alfvénic coupling. The latter is represented by the term $\sqrt{1 + (1+\tau_\mathrm{i}) \left(k_\mathrm{EM}\rho_\mathrm{s}\right)^2}$ in Eq. 6.3. The SSU is a phenomenon where an in-out asymmetry in the pressure, e.g. caused by a large transport event (ballooning, Sec. 3.1.1) at the outer midplane, leads to an asymmetric (ion) flow perturbation that attempts to correct the pressure asymmetry [201].

Furthermore, single excursion events during an LCO are often described as bursts, since they cause a strong density perturbation and thus a particle transport similar to an ELM crash (Sec. 3.3.1). Since the LCOs are additionally accompanied by some kind of magnetic precursor, they are referred to as type-III ELMs [63, 202] (Sec. 2.1).

The name 'precursor' can be easily understood from the representation of the modes in the time frame on a small time scale, as shown in Fig. 6.2. Fig. 6.2a shows a 6 ms time interval and a total of six LCO bursts visible in the THB (red), the $\tilde{B}_\mathrm{r}$-coil (green) and the $\tilde{B}_\mathrm{pol}$-coil (blue). If we zoom in further and investigate a single LCO burst, shown in Fig. 6.2b, we see that there is a high-frequency fluctuation in the THB and $\tilde{B}_\mathrm{r}$-coil (precursor mode) that peaks just before the LCO burst appears. The high frequency mode disappears, so it precedes the LCO burst, hence the name precursor. It has been therefore reasonable to assume that the precursor mode triggers the LCO burst [63].

The precursor mode should not be confused with the mode that appears in the near H-mode region, which can also be seen in the H-mode phases in Figs. 2.3f, g. This

mode is called modulating pedestal mode (MPM) [203] or the 'fork' mode, which is believed to be a micro-tearing mode (MTM, Sec. 3.2.6) [204].

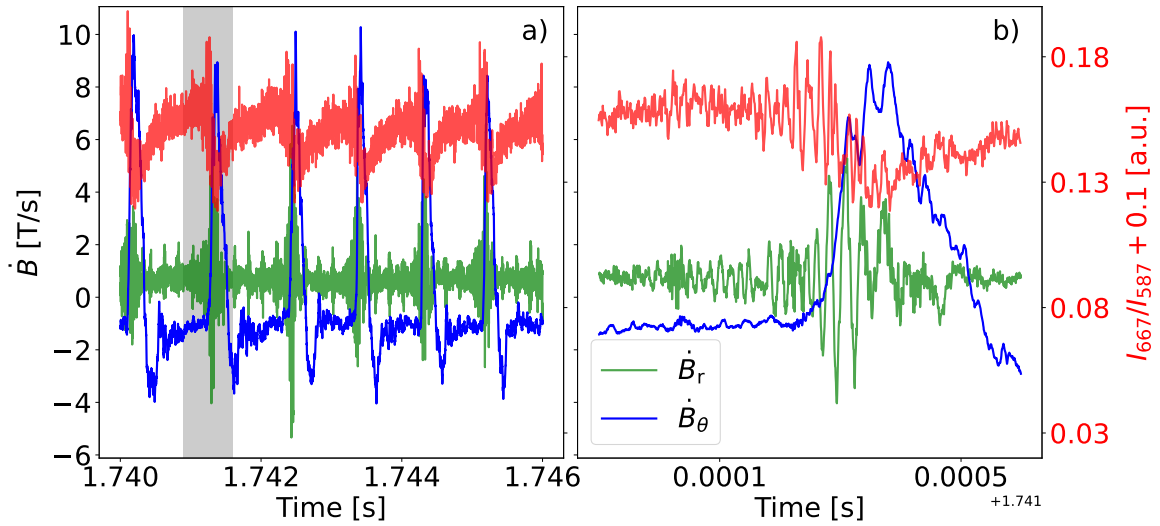

Figure 6.2: Precursor Behaviour of High Frequency Mode for LCOs
The raw data of the THB line ratio measurements are shown in red (offset by 0.1 *for visibility), the raw signal of the* $\tilde{B}_r-$*coil is shown in green and the raw signal of the* $\tilde{B}_{pol}-$*coil is shown in blue for six LCO cycles a). A zoom into the gray area of a) reveals the precursor-like behavior in the THB and* $\tilde{B}_r-$*coil data for one LCO burst b).*

Grover *et al.* attempted to identify the precursor as a kinetic Alfvén wave in terms of its frequency behaviour [96]. The kinetic Alfvén wave is a result of the ideal MHD theory (Sec. 3.1) when finite Larmor radius (FLR) effects and finite electron parallel conductivity effects are added [205].

In the EAST experiment, precursor frequencies between $f_{pre} \sim 100\,\text{kHz}$ and $f_{pre} \sim 150\,\text{kHz}$ are observed [94], and a down-chirping of the frequency is detected just before the onset of a low-frequency mode (type-III ELM in the paper). The precursor is localized within the confined region.

In AUG, the precursor features frequencies between $f_{pre} \sim 40\,\text{kHz}$ and $f_{pre} \sim 100\,\text{kHz}$, and a rapid drop in f_{pre} is also observed. Moreover, the mode is also localized inside the separatrix and is thought to be close to the radial electric field E_r minimum. The poloidal wavenumber is of the order of $k_\theta \approx 0.28\,\text{cm}^{-1}$ and the mode appears to propagate in the electron diamagnetic direction (EDD) in the laboratory frame at a speed of about $v_{lab} \approx 12\,\text{km}\,\text{s}^{-1}$ [63].

All these observations about the LCOs and precursor mode lead to the following idea: the precursor is partially driven by steep edge gradients, its amplitude increases due to some unknown circumstance and the induced transport by the precursor continues to increase, giving rise to a flattening of the edge profiles. When the profiles are maximally

flat, the precursor disappears and the profiles rise again. We then measure a (type-III) ELM-like transport in the signal, i.e. the LCO burst. Following this line of thought, the LCOs are not a mode by themselves, but the result of the precursor mode. The questions that naturally arise are: what causes the precursor mode and, in particular, what causes the increase in particle transport of the precursor mode? And it are these questions that we can only answer if we can identify the underlying instability of the precursor. In a similar approach as in Sec. 5.1 for the QCM, the precursor mode is first analyzed in frequency space.

6.2 Spectral Analysis - Precursor and LCOs

Before we can compare properties of the precursor mode, e.g. its frequency, with the plasma properties, we need to identify the radial position, where the mode has its maximum impact on the transport, i.e. we need to localize the precursor mode radially. After that the frequency of the precursor is investigated.

Radial Localization of the I-Phase Edge Fluctuations

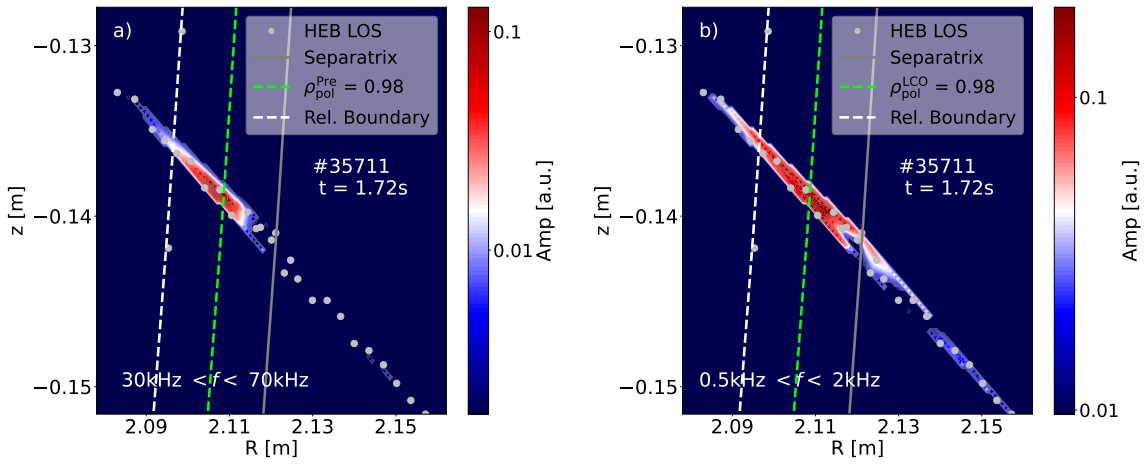

Figure 6.3: Radial Localization of the Precursor Mode and LCO
An example localization of the precursor mode is shown in a) for the discharge #35711 in the time interval $t \in [1.72\,\mathrm{s}, 1.74\,\mathrm{s}]$. To localize the precursor radially, the amplitudes from the Fourier spectra of the different THB lines of sight (black dots) are compared along the radial axis. The colorbar reflects the amplitude of the mode (see Fig. 4.5c), which was calculated for mode frequencies of 30 kHz−70 kHz, with red representing a high mode activity and blue a low one. It can be seen that the precursor in this case is localized at about $\rho_{\mathrm{pol}} = 0.98$, indicated by the lime-green dashed line. The separatrix is given by the gray line and the inner reliability limit, calculated according to the methodology of Sec. 4.2, is given by the white dashed line. This was done analogously for the LCO for frequencies between 0.5 kHz and 2 kHz in b).

As described in the methodology part in Sec. 4.4, the mode is localized at the point where the highest amplitude of the line ratio intensities from the THB data can be seen in the Fourier space. Fig. 6.3a shows such a localization of the precursor mode as an example for a 20 ms time interval of an I-phase of discharge #35711. For this purpose, all Fourier amplitudes peaking in a frequency range between 30 kHz and 70 kHz are radially compared with each other and are reflected in the colorbar. This frequency range results from the frequency of the precursor and its broad appearance in Fourier space. Furthermore, we can trust the THB data in terms of mode analysis up to a $\rho_{\mathrm{pol}} = 0.96$. This limit is shown as a white dashed line in Fig. 6.3 and is determined using the qualifiers established in Sec. 4.2. In this example, the highest amplitude value appears around $\rho_{\mathrm{pol}} = 0.98$, represented by the lime green dashed line. This methodology has been applied to all the discharges considered below for 40 ms time intervals and the result for each discharge is listed in App. B. In summary, the precursor mode can be located around $\rho_{\mathrm{pol}}^{\mathrm{Pre}} = 0.985 \pm 0.007$.

It is important to note that in this example (as in many others) only the radial THB grid is available (see Fig. 4.3). Therefore, Fig. 6.3a does not show the poloidal extension of the precursor. This will be discussed in more detail in Sec. 6.3.

For comparison, the radial localization of the LCO using the same THB data and methodology as for the precursor is shown in Fig. 6.3b. Here, all maxima in Fourier space are compared, peaking at a frequency between 0.5 kHz and 2 kHz, i.e. around the LCO frequency. We see that the LCO is localized at a similar position, but a little further out, averaged over all discharges, i.e. at $\rho_{\mathrm{pol}} = 0.989 \pm 0.005$. Furthermore, the LCO seems to be present in a larger radial range up to the near SOL.

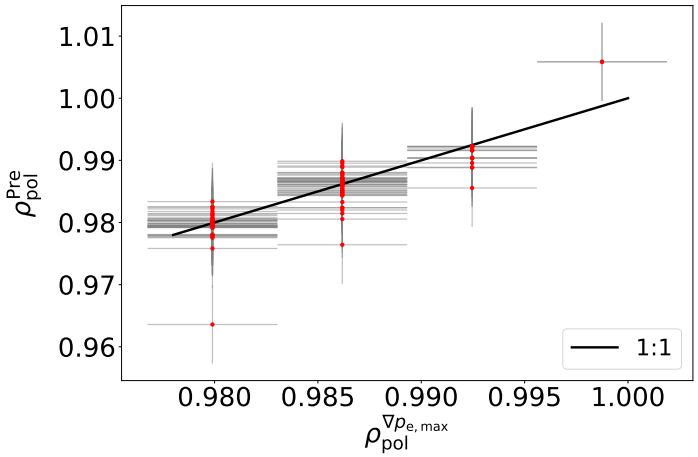

Figure 6.4: Localization of Precursor and Pressure Gradient Maximum
The radial position of the precursor mode $\rho_{\mathrm{pol}}^{\mathrm{Pre}}$ (red) is determined for all time points and discharges from Tab. B, averaged over 40 ms time intervals and drawn against the radial position of the steepest pressure gradient $\rho_{\mathrm{pol}}^{\nabla p_{\mathrm{e,max}}}$. The black line indicates $\rho_{\mathrm{pol}}^{\mathrm{Pre}} = \rho_{\mathrm{pol}}^{\nabla p_{\mathrm{e,max}}}$.

Similar to the radial localization of the QCM in Fig. 5.1b, the radial position of the precursor mode $\rho_{\mathrm{pol}}^{\mathrm{Pre}}$ for all seven discharges (see Tab. B.1), where each data point (red) corresponds to a localization averaged over 40 ms, is drawn against the radial position of the steepest electron pressure gradient $\rho_{\mathrm{pol}}^{\nabla p_{\mathrm{e,max}}}$ in Fig. 6.4. The $\rho_{\mathrm{pol}}^{\nabla p_{\mathrm{e,max}}}$ values are again discrete due to the radial resolution of IDA (Sec. 4.3). Nevertheless, we see an accumulation of data points along the equivalence line $\rho_{\mathrm{pol}}^{\mathrm{Pre}} = \rho_{\mathrm{pol}}^{\nabla p_{\mathrm{e,max}}}$ (black line in Fig. 6.4), which leads us to conclude that the precursor is localized in the region of steepest pressure gradient.

In the following all local plasma parameters are taken at the position where the precursor is localized, if not stated otherwise.

Frequency Scaling of the Precursor Mode

The first step is to examine the precursor frequency f_{pre}, first as an example for a single discharge (#35711) and then in a larger picture for seven discharges. The comparison of local plasma parameters with f_{pre} for discharge #35711 is shown in Fig. 6.5. Analogous to the QCM (Chapter 5), the precursor is also an edge mode, where strong $E \times B$ flows are present, which is why the $E \times B$ velocity $v_{\mathrm{E\times B}} = E_{\mathrm{r}}/B_{\mathrm{t}}$ is compared with f_{pre}. Fortunately, the complete evaluation of the radial electric field E_{r} as in Eq. 3.49 is not necessary, since the measured E_{r} values agree very well with the values predicted by the neoclassical theory in the I-phase and especially at the transition from L-mode to I-phase [91]. Therefore, in the following, the approximated $E \times B$ velocity as in Eq. 5.1 is assumed, i.e. an agreement with the electron diamagnetic velocity

$$v_{\mathrm{e,dia}} = \nabla p_{\mathrm{e}}/(e n_{\mathrm{e}} B_{\mathrm{t}}). \tag{6.4}$$

If we compare the time evolution of f_{pre} and $v_{\mathrm{E\times B}}$ in Fig. 6.5, we see that there tends to be a negative correlation. This can be illustrated near the H-mode transition: f_{pre} decreases significantly, but $v_{\mathrm{e,dia}}$ increases as expected. In addition, f_{pre} is nearly constant before (at $t \approx 1.51\,\mathrm{s}$) and just after the H-mode (at $t \approx 1.67\,\mathrm{s}$), whereby $v_{\mathrm{e,dia}}$ is higher directly after the H-mode. This contradicts the $E \times B$ shear stabilization of the precursor mode.

Furthermore, it was mentioned above that the LCOs are often classified as type-III ELMs, for which a frequency dependence on the Spitzer resistivity η, i.e.

$$\eta = 1.67 \cdot 10^{-3} \frac{1}{T_{\mathrm{e}}^{3/2}} \tag{6.5}$$

was speculated. The comparison of η and f_{pre} shows that there could be a correct trend, even if η seems to underestimate the values close to the H-mode.

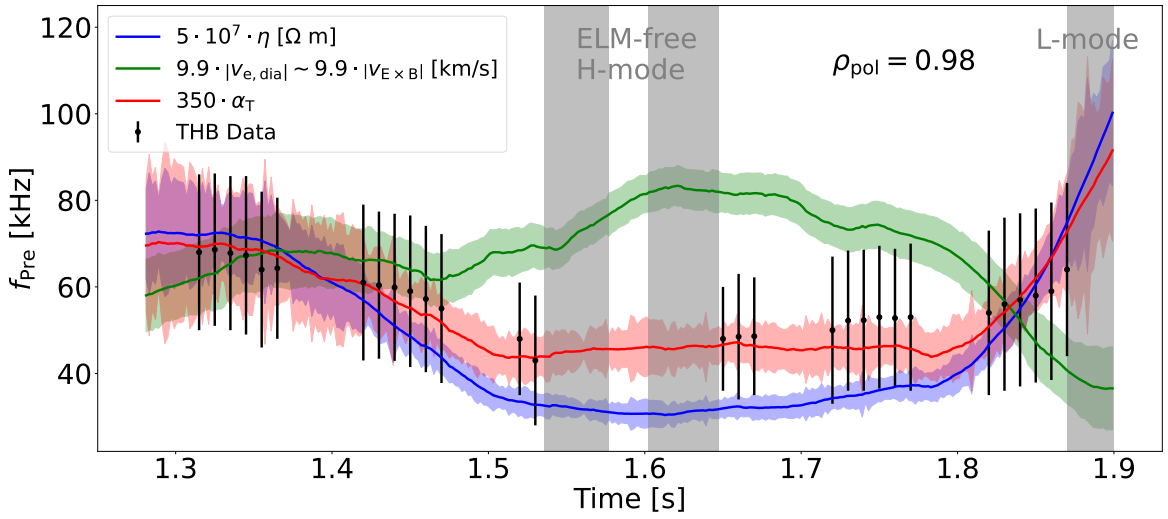

Figure 6.5: Temporal Precursor Frequency Evolution for Discharge #35711

Shown in black is the time evolution of the precursor frequency for discharge #35711, determined with the THB diagnostic and averaged over 10 ms at $\rho_{pol} = 0.98$. This is compared with the resistivity η (blue), the $E \times B$ velocity $v_{E\times B}$ (green) and the turbulence parameter α_T (red). The gray areas represent the ELM-free H-mode, in which we do not observe the precursor mode and therefore have no data available.

The last parameter in the time comparison is the dimensionless turbulence parameter α_T, already introduced in Sec. 3.2.1 and closely related to the collisionality $\nu^\star_{ped}$ from Eq. 2.10, i.e.

$$\alpha_T = 3.13 \cdot 10^{-18} R_{maj} q_{95}^2 n_e Z_{eff} / T_e^2. \tag{6.6}$$

As a reminder, α_T indicates which turbulence process, i.e. interchange (IC, Sec. 3.1.1) or drift-wave (DW, Sec. 3.2.1), dominates the plasma. A value of $\alpha_T \ll 1$ means that the plasma is DW unstable and a value of $\alpha_T \to 1$ indicates IC dominance. Usually the value of α_T was mainly determined at the separatrix, but here we evaluate it locally at the mode position according to Eq. 6.6. We see that α_T has the best qualitative agreement with f_{pre}. It should be noted that the collisionality from Eq. 2.10 could have been used, but it turned out that $\alpha_T \propto q_{95}\nu^\star_{ped}$ is the better choice when comparing many discharges. For a possible 1:1 comparison, $v_{E\times B}$, η and α_T have been multiplied by a specific factor for better visibility in Fig. 6.5.

We will now present the trends found for several discharges and under different plasma parameters, shown in Fig. 6.6. In general, all discharges are operated with a toroidal magnetic field of $B_t = -2.5\,T$ and a plasma current of $I_p = 0.8\,MA$, unless otherwise stated. First of all, it can be seen that in the investigated discharges precursor frequencies in the range of $50\,kHz < f_{pre} < 75\,kHz$ are observed. Moreover, there is a relatively high error of about $\sigma_{f_{pre}} = 16\,kHz$ on average, which is due to fast decrease

of the mode frequency within each cycle, which we will discuss later (cf. Fig. 6.14). In addition to the quantities from above, the relationship between the frequencies of the LCOs f_{LCO} and the precursor frequency f_{pre} is shown in Fig. 6.6a. We find a clear positive correlation but given the large scattering of the data, we cannot deduce a clear linear trend.

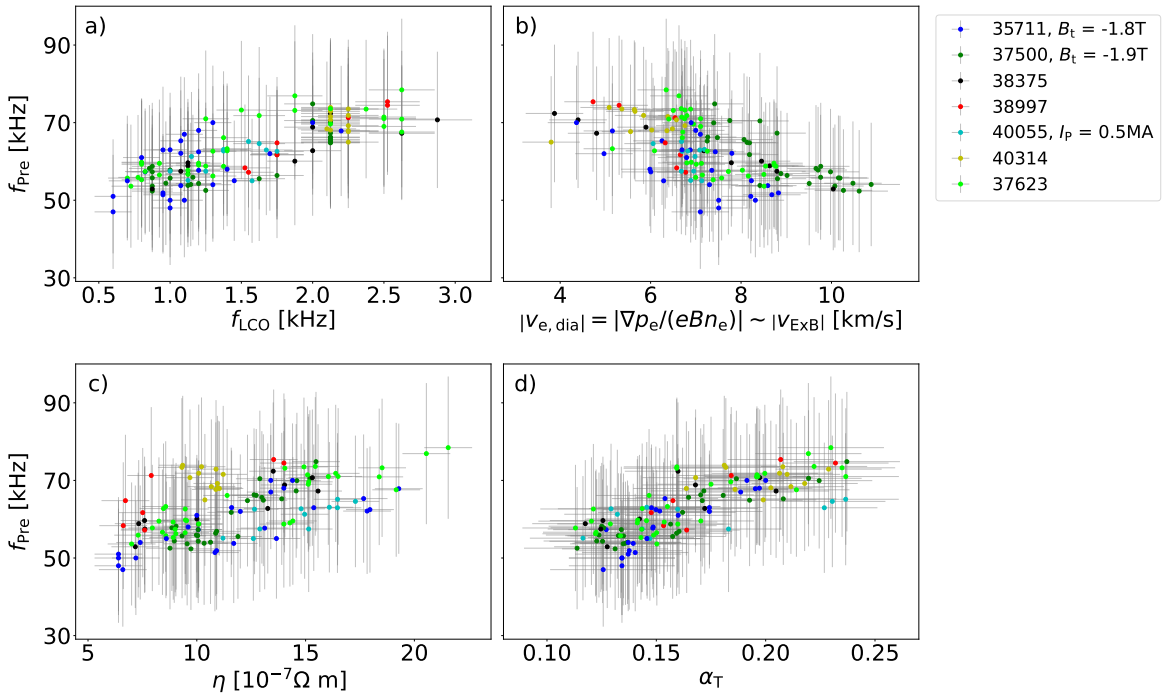

Figure 6.6: Precursor vs. LCO Frequency and Local Plasma Parameters
The frequency of the precursor f_{pre} is plotted against the frequency of the LCOs f_{LCO}, the approximated $E \times B$ velocity of the plasma $v_{\mathrm{E\times B}} \sim v_{\mathrm{e,dia}}$, the resistivity η and the turbulence parameter α_{T} for various discharges, which by default have a toroidal field of $B_{\mathrm{t}} = -2.5\,\mathrm{T}$ and a plasma current $I_{\mathrm{p}} = 0.8\,\mathrm{MA}$, unless otherwise indicated. All variables are evaluated at the respective position of the precursor.

The trend observed in Fig. 6.5 can be confirmed for $v_{\mathrm{E\times B}}$ for many discharges in Fig. 6.6b. Qualitatively, f_{pre} decreases with increasing plasma rotation. Similarly, for the resistivity η in Fig. 6.6c, a well-consistent relation can be found for individual discharges. However, drawing α_{T} against f_{pre}, i.e. adding the safety factor q_{95} and local electron density n_{e}, leads to an even better merging of the data points, shown in Fig. 6.6d.

6.3 Poloidal and Radial Wavenumber of the Precursor

Using the THB (Sec. 4.2) and the method from Beall *et al.* [185], described in Sec. 4.4, we will investigate the poloidal wavenumber k_θ (see Fig. 3.1) of the precursor and

its dependence on the local plasma parameters, and then we will analyze the radial wavenumber k_r.

Poloidal Wavenumber

As described in Sec. 4.4, it is necessary that the mode is measurable in at least two poloidally aligned THB lines of sight to determine its poloidal wavenumber k_θ. Furthermore, as described in Sec. 5.3, it is useful if the 5×5 grid of the THB (Fig. 4.3) is available, because then we are able to evaluate k_θ at different radial positions and especially at the precursor position, as described in Sec. 6.2. However, this is not possible in most cases of the considered discharges, since only the radial grid is available, featuring only one poloidal array. This is mostly found between $\rho_\mathrm{pol} = 0.963$ and $\rho_\mathrm{pol} = 0.975$ (varying in the discharges), which is deeper in the confined region than the mode position, but still within the reliability limits on average (see Fig. 6.3). This implies that all local plasma quantities such as the background $E \times B$ velocity $v_\mathrm{E\times B}$, resistivity η and α_T are evaluated at the position where it is possible to evaluate k_θ, which is approximately at $\rho_\mathrm{pol} = 0.97$.

Fig. 6.7 shows four $k_\theta - f$ spectra of different times of discharge #35711, averaged over 30 ms. The brightest (reddish) region in each figure marks the precursor mode, and the respective k_θ^pre values are indicated in each figure. It is evident that the determined k_θ values are negative, indicating a propagation of the precursor in the electron diamagnetic direction (EDD), but we will analyze this in more detail in Sec. 6.4 and consider the absolute value of k_θ in the following. For the sake of clarity, and because we only want to capture the precursor, we have bandpass filtered the signal around $30\,\mathrm{kHz} < f < 110\,\mathrm{kHz}$. The different time points mark the following evolutionary stages of the I-phase already presented in Fig. 6.5:

a) deep in the (regular) I-phase, which is similar to the case in Ref. [63], hence featuring similar k_θ^pre,

b) directly at the transition from I-phase to ELM-free H-mode, featuring a lower precursor frequency f_pre and very low k_θ, i.e. it becomes a poloidally large structure,

c) after the H-I transition with similar, slightly higher k_θ values, and

d) near the L-mode, where the precursor has a higher k_θ, i.e. it becomes smaller.

The overall behavior is qualitatively similar to that of f_pre. A comparison with Fig. 6.5 shows that the precursor has a low value of f_pre and k_θ^pre near the fully developed H-mode and a higher value near the L-mode. It is therefore reasonable to make the

same comparisons, i.e. with the same parameters, for the same discharges as in Fig. 6.6. These comparisons between k_θ and $v_{\mathrm{E\times B}}$ (a)), η (b)) and α_{T} (c)) are shown in the top row of Fig. 6.8. Indeed, similar parametric dependencies can be found as for f_{pre}, which are connected via the lab velocity as $v_{\mathrm{lab}} = 2\pi f_{\mathrm{pre}}/k_\theta^{\mathrm{pre}}$. The anti-correlation of k_θ and $v_{\mathrm{E\times B}}$ is even stronger than for the frequency, and the positive correlation between k_θ and α_{T} is also evident. In general, values of $0.1\,\mathrm{cm}^{-1} < k_\theta^{\mathrm{pre}} < 0.7\,\mathrm{cm}^{-1}$ are observed, indicating a strong variation (up to a factor of seven).

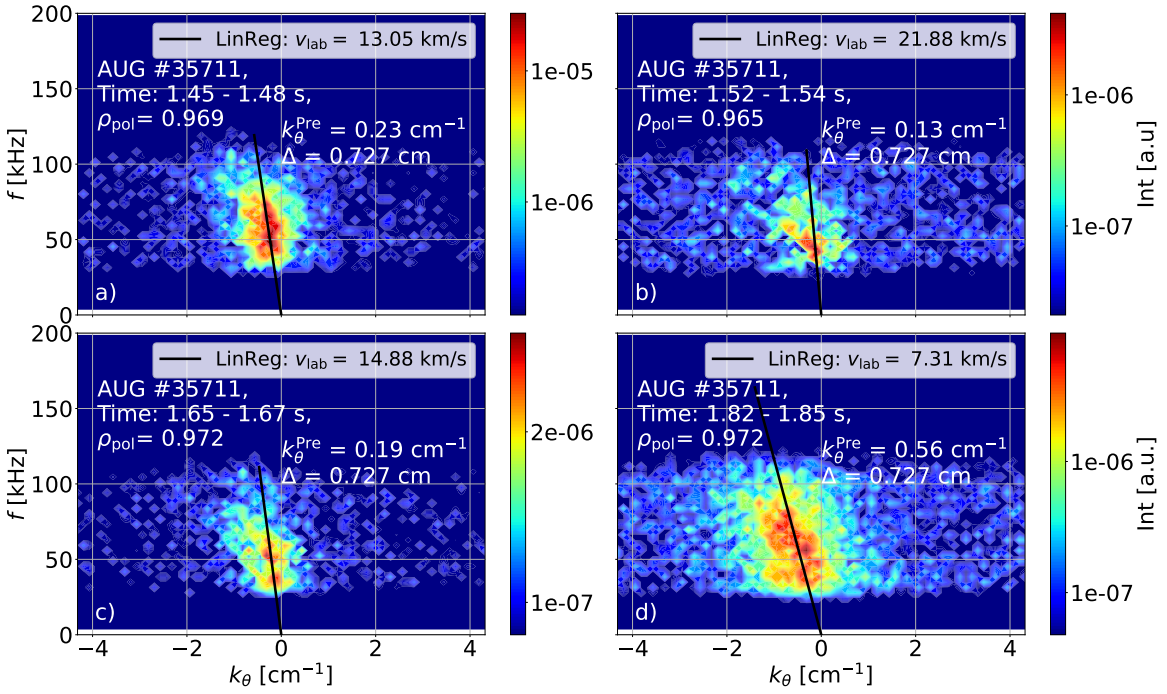

Figure 6.7: Temporal Evolution of k_θ for Discharge #35711
Shown are the $k_\theta - f$ spectra of discharge #35711, evaluated in chronological order from a) to d). All spectra are analyzed at the radial position, where the poloidal array is available, according to the methodology described in Sec. 4.4. The bright reddish maxima mark the precursor. The velocity of the mode in the laboratory frame v_{lab} is calculated from the slope of the black line.

Due to the possibility of comparing our experimental data with those of other machines, simulations and also the criterion of Eq. 3.2, the poloidal wavenumber normalized to the hybrid gyroradius $k_\theta\rho_{\mathrm{s}}$ is used. This quantity is also plotted against $v_{\mathrm{E\times B}}$ (d)), η (e)) and α_{T} (f)) in the lower row of Fig. 6.8 and shows a similar behavior to the non-normalized quantity. This is mainly due to the fact that $\rho_{\mathrm{s}} \sim 1\,\mathrm{mm}$ for all discharges and deviates little, which simply reduces the value of k_θ by a factor of ten. The trends are still good, but the scaling gets worse. The values of $k_\theta\rho_{\mathrm{s}}$ lie between $0.01 < k_\theta\rho_{\mathrm{s}} < 0.06$, implying that the poloidal size of the precursor mode lies in a range between MHD instabilities (Sec. 3.1), for which $k_\theta\rho_{\mathrm{s}} \lesssim 0.01$ roughly holds, and microinstabilities (Sec. 3.2), for which $k_\theta\rho_{\mathrm{s}} \gtrsim 0.1$ is usually assumed.

The typical electromagnetic wavenumber $k_{\mathrm{EM}}\rho_{\mathrm{s}}$, defined in Eq. 5.5 and explained in Sec. 5.3, is here on average $k_{\mathrm{EM}}\rho_{\mathrm{s}} \sim 0.77 \pm 0.13 > 0.5$, but no possible scaling can be achieved. Though, we can say that the I-phase discharges are at the corresponding radial position deep in the electromagnetic regime.

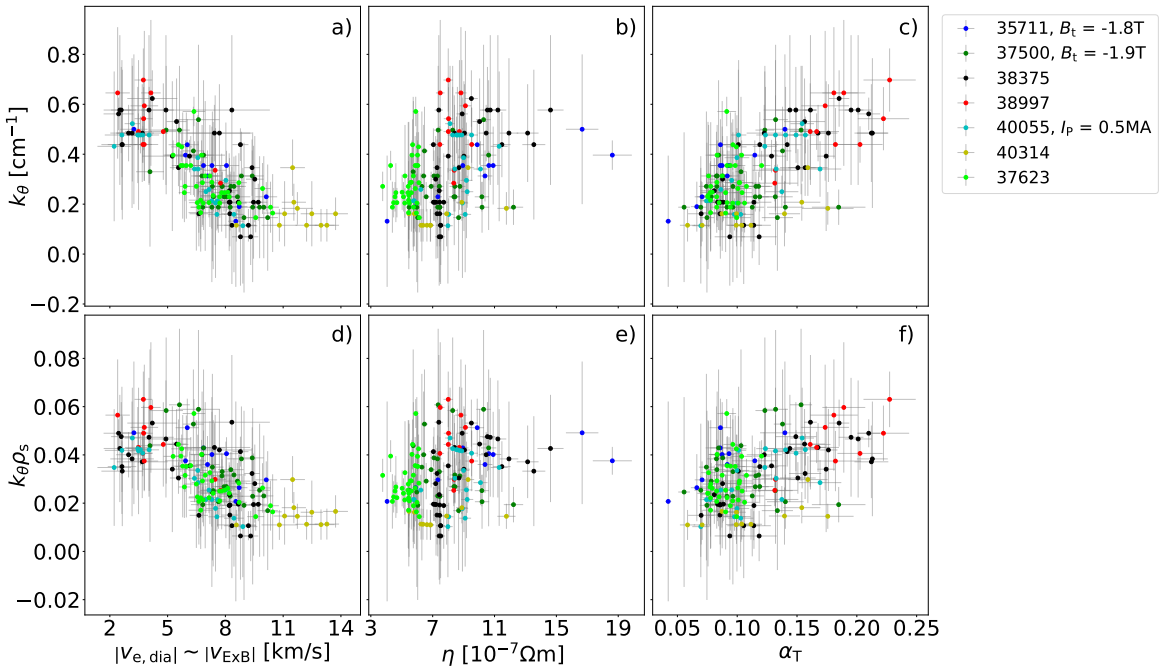

Figure 6.8: Poloidal Wavenumber of the Precursor Depending on Local Parameters

For numerous discharges, the poloidal wavenumber k_θ a)-c) and the normalized poloidal wavenumber $k_\theta\rho_{\mathrm{s}}$ d)-f) of the precursor mode are plotted against the approximated background velocity $v_{\mathrm{E\times B}} \sim v_{\mathrm{e,dia}}$, the resistivity η and the turbulence parameter α_{T}. All discharges are operated with a toroidal field $B_{\mathrm{t}} = -2.5\,\mathrm{T}$ and plasma current $I_{\mathrm{p}} = 0.8\,\mathrm{MA}$, unless not stated otherwise.

Radial Wavenumber

The radial wavenumber $k_{\mathrm{r}}^{\mathrm{pre}}$ represents the radial structure of the precursor. Again, k_{r} is calculated using the method in Sec. 4.4, but this time we take two radially aligned LOS of the THB. It is important to note that although $k_{\mathrm{r}} = 2\pi/\lambda_{\mathrm{r}}$, the value of k_{r} does not necessarily indicate the full radial extent of the mode. Rather, a positive value of k_{r} implies that the mode is first detected further out radially and vice versa, e.g. due to a tilting of the mode structure. A value of $k_{\mathrm{r}} \sim 0\,\mathrm{cm}^{-1}$ means that the precursor mode is observed in both radial channels simultaneously.

Fig. 6.9a shows an exemplary $k_{\mathrm{r}} - f$ spectrum at the precursor position, i.e. at $\rho_{\mathrm{pol}} = 0.98$, for a 30 ms time interval in the middle of the stable I-phase in discharge #35711. At this point, $k_{\mathrm{r}}^{\mathrm{pre}}$ seems to vanish within the errorbars, i.e. $k_{\mathrm{r}}^{\mathrm{pre}} \sim 0\,\mathrm{cm}^{-1}$,

which on the one hand might indicate a simultaneous measurement of the mode in both channels and on the other hand is an indicator for the generation of streamers [137] (see Sec. 5.3). If we analyze the radial behavior for the aforementioned time interval in Fig. 6.9b, we see that the value of k_r gradually changes from $k_\mathrm{r}^\mathrm{pre} \sim 1\,\mathrm{cm}^{-1}$ in the inner part of the plasma to $k_\mathrm{r}^\mathrm{pre} \sim -1\,\mathrm{cm}^{-1}$ in the outer part at the separatrix. $k_\mathrm{r}^\mathrm{pre} > 0\,\mathrm{cm}^{-1}$ indicates that the mode is measured first in the radial channel, which is further in, and vice versa. From the radial behavior of k_r, we can see that the precursor mode is first measured at the position, where we localized it, i.e. at $\rho_\mathrm{pol} \approx 0.984$ (green line in Fig. 6.9b). The gradual change of k_r suggests that the precursor structure propagates mainly poloidally and that it is not tilted (in which case k_r would be positive/negative everywhere).

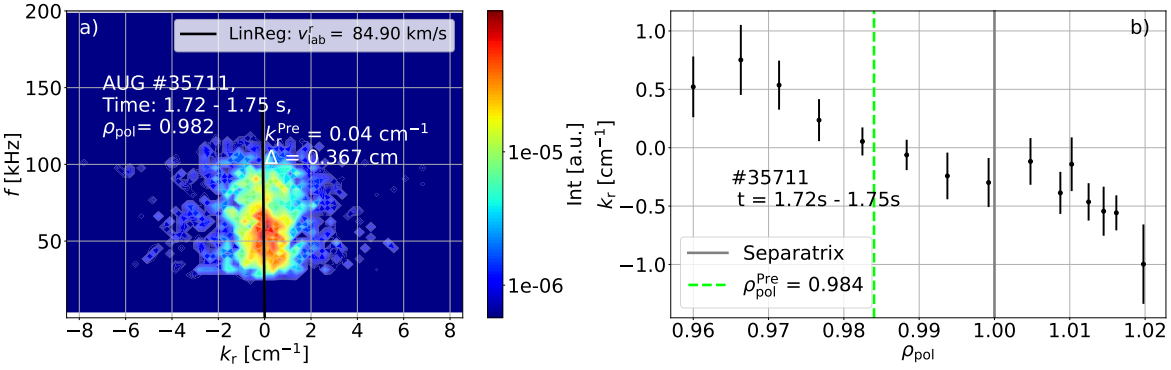

Figure 6.9: Radial Wavenumber of the Precursor for Discharge #35711
Example of a $k_\mathrm{r} - f$ spectrum at the position where we locate the precursor mode a). The bright red dot represents the precursor and the radial wavenumber k_r almost disappears at this position. In the radial profile of k_r, shown in the colorbar, it can be seen that k_r is positive further inward (blue) and becomes negative outward toward the separatrix (red).

6.4 Phase Velocity of the Precursor Mode

After a brief excursion into the radial properties of the precursor mode, we return to the poloidal properties, i.e. the phase velocity in the co-moving plasma frame. As described in Sec. 3.3.2, this is composed of the mode velocity, which is measured from the 'outside', i.e. in the laboratory frame, subtracted by the rotation velocity of the plasma, reflected by the $E \times B$ velocity, which we further approximate with $v_\mathrm{e,dia}$ (Eq. 6.4), as shown in Eq. 3.50. Furthermore, we have seen in Secs. 3.3.2 and 3.3.3 that v_ph is a crucial property, since it leads to the exclusion of about half of the linear instabilities from Tab. 3.1.

From the $k_\theta - f$ spectra in Fig. 6.7, the propagation velocity of the precursor in the laboratory frame is calculated from the coordinates $(k_\theta^\mathrm{pre}, f_\mathrm{pre})$ where the brightest

(reddish) point appears. Using Eq. 3.48, we then obtain values between $-7\,\mathrm{km\,s^{-1}}$ and $-22\,\mathrm{km\,s^{-1}}$ in these four cases. Due to the negative k_θ value, v_{lab} is also negative, indicating a motion of the mode in electron diamagnetic direction (EDD), shown e.g. Fig. 3.1. In the time evolution of Fig. 6.7 it can be seen that v_{lab} is the highest near the H-mode (Fig. 6.7b), becomes lower in the I-phase (Figs. 6.7a, c) and reaches the lowest value just before the L-mode (Fig. 6.7d).

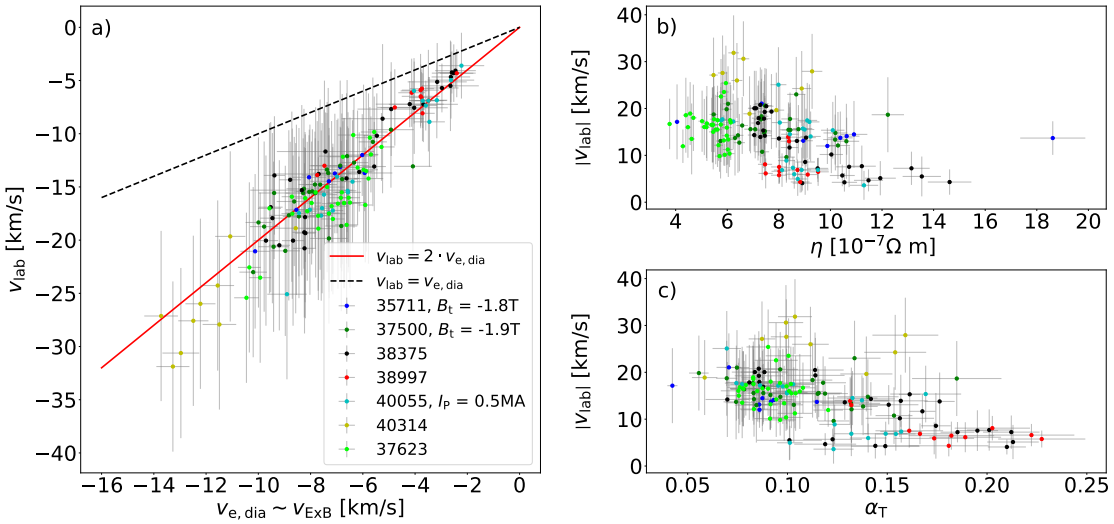

Figure 6.10: Phase Velocity of the Precursor Mode

The poloidal velocity in the laboratory frame v_{lab} of the precursor can be determined from the $k_\theta - f$ spectra and is plotted against the approximated background velocity $v_{\mathrm{E\times B}} \sim v_{\mathrm{e,dia}}$ a), the resistivity η b) and the turbulence parameter α_{T} c) for different discharges. The discharges are operated by default at $B_{\mathrm{t}} = -2.5\,\mathrm{T}$ and plasma current $I_{\mathrm{p}} = 0.8\,\mathrm{MA}$, unless otherwise noted. The red line in a) indicates a lab velocity twice that of the electron diamagnetic velocity $v_{\mathrm{e,dia}}$ and the black dashed line indicates equivalence of $v_{\mathrm{lab}} = v_{\mathrm{e,dia}}$.

Since the mode velocity is defined as $v_{\mathrm{lab}}^{\mathrm{pre}} = 2\pi f_{\mathrm{pre}}/k_\theta^{\mathrm{pre}}$ (see Eq. 3.48) and is thus composed of the frequency f_{pre}, which decreases with increasing $v_{\mathrm{E\times B}}$ (Fig. 6.6b) and the poloidal wavenumber k_θ^{pre}, which has the same $v_{\mathrm{E\times B}}$ tendency (Fig. 6.8a), it is not trivial to assess how v_{lab} will behave with respect to $v_{\mathrm{E\times B}}$. However, as already mentioned in Sec. 6.3, the k_θ variation is significantly stronger than the frequency variation, so one could expect an increase of v_{lab} with increasing $v_{\mathrm{E\times B}}$. And indeed, such a tendency can be seen in Fig. 6.10a for all the discharges considered above. The black dashed line shows a 1:1 correspondence, i.e. we would measure the mode exactly with the $E \times B$ velocity from the outside. So, if all data points would be along this line, the precursor would have no intrinsic phase velocity, since $v_{\mathrm{lab}} = v_{\mathrm{E\times B}} + v_{\mathrm{ph}}$. But all data points are below this line, so a negative phase velocity is necessary to explain the measured values of v_{lab}. Furthermore, the red line represents $v_{\mathrm{lab}} = 2v_{\mathrm{e,dia}}$, i.e.

$v_{\mathrm{lab}} \approx v_{\mathrm{E\times B}} + v_{\mathrm{e,dia}}$, which means that the precursor would have a phase velocity of $v_{\mathrm{ph}} = v_{\mathrm{e,dia}}$. The measured values of v_{lab} range from $-5\,\mathrm{km\,s^{-1}}$ to $-32\,\mathrm{km\,s^{-1}}$, but the errors are correspondingly large because both the error in the frequencies (see Fig. 6.6) and the error in the poloidal wavenumber (see Fig. 6.8) must be integrated via Gaussian error propagation. Although, the resulting errorbars are large, we can confidently say that the data points cluster around the red line in Fig. 6.10a, i.e. the precursor has a phase velocity in the plasma frame of about $v_{\mathrm{ph}} = v_{\mathrm{e,dia}}$.

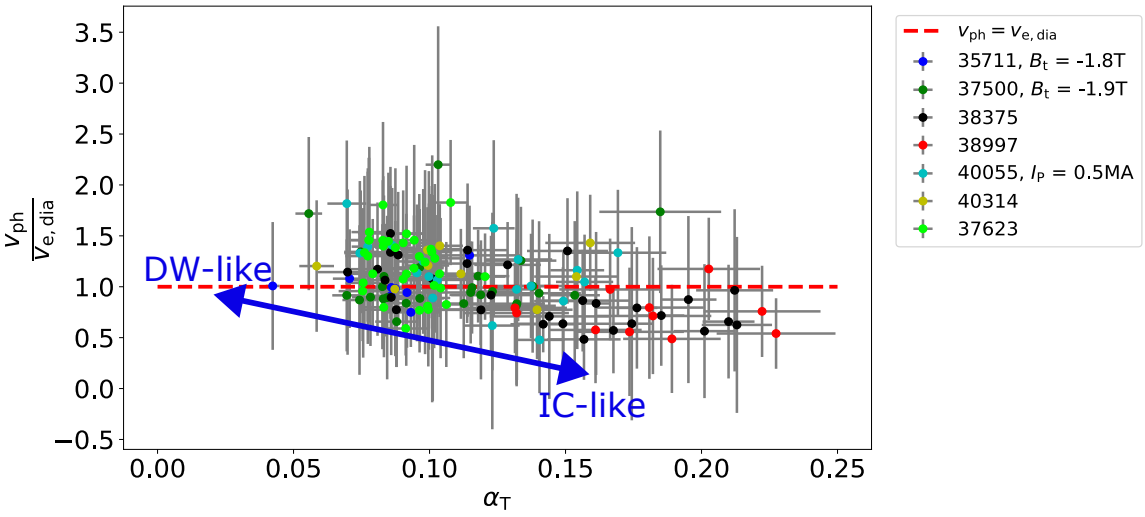

Figure 6.11: Precursor Phase Velocity vs. Turbulence Parameter
The phase velocity of the mode in the plasma frame v_{ph} is calculated from the lab velocity minus the background velocity, i.e. $v_{\mathrm{ph}} = v_{\mathrm{lab}} - v_{\mathrm{E\times B}}$. If we normalize this to the electron diamagnetic velocity $v_{\mathrm{e,dia}}$, we can see if v_{ph} changes with increasing turbulence parameter α_{T}, as in the case for a drift-wave instability according to the theory in Sec. 3.2.1. A phase velocity of $v_{\mathrm{ph}} = v_{\mathrm{e,dia}}$ and $\alpha_{\mathrm{T}} \ll 1$ corresponds to the drift-wave case and $v_{\mathrm{ph}} \to 0$ and $\alpha_{\mathrm{T}} \to 1$ corresponds to the interchange case (Sec. 3.1.1), indicated by the blue arrow.

This phase velocity is consistent with the properties of drift-wave-like instabilities (DW) as described in Sec. 3.2.1. According to Sec. 3.3.2, the precursor mode would therefore not cause any electrostatic radial transport, i.e. $\Gamma_{\mathrm{r}} = 0$. Figs. 6.10b and c show the relationship between v_{lab} and resistivity η and turbulence parameter α_{T}. It can be seen that higher resistivities roughly correlate with lower mode velocities. However, since the data are highly scattered, η does not seem to be a good parameter for describing the velocity of the precursor. The rough tendency comes from the fact that H-mode pedestals generally feature lower resistivities and thus show the opposite behavior to the electron diamagnetic velocity $v_{\mathrm{e,dia}}$. Although a perfect relationship cannot be found, it can be seen that lower α_{T} values correlate qualitatively with higher precursor velocities in the lab frame. This is particularly interesting if we recall the unstable DW case due to increasing collisionality $\nu^{\star}_{\mathrm{ped}}$ (Eq. 2.10), i.e. increasing α_{T},

which was also discussed in Sec. 3.2.1. There it has been derived that increasing α_T hampers the electron mobility and leads to a transition from DW-like turbulence to interchange-like turbulence (IC, see Eq. 3.40). We have already seen in Sec. 3.3.2 that the phase velocity v_{ph} is related to the underlying turbulence, so according to the theory we should be able to show a deviation of v_{ph} from $v_{e,dia}$ at higher α_T. The comparison between v_{ph} normalized to $v_{e,dia}$ and α_T is shown in Fig. 6.11. According to the theory, a value of $\alpha_T \ll 1$ would correspond to DW turbulence, i.e. $v_{ph} = v_{e,dia}$, and a value of $\alpha_T \to 1$ would correspond to IC, i.e. $v_{ph} = 0\,\mathrm{km\,s^{-1}}$. Unfortunately, we do not achieve high α_T values in the observed discharges at the corresponding radial positions, but a slight trend of decreasing v_{ph} with increasing α_T is recognizable from the data. This reflects the correct trend according to the theory.

6.5 Lifetime Scaling of the Precursor Mode

As discussed in Sec. 6.1, and as can be seen in Fig. 6.2, the precursor mode seems to exist for only a certain amount of time, because at some point the LCO appears and the precursor disappears. To find the circumstance or mechanism that causes the precursor mode to disappear, it is advisable to investigate the time scale on which the precursor exists and what happens during that time. The time in which the precursor can be measured by the THB is called its lifetime τ_L. In the first part of this section we will discuss the method of obtaining the lifetime of the precursor and in the second part we will try to relate the lifetime to plasma quantities and point out the limitations of the methodology.

Method - How to Obtain the Precursor Lifetime τ_L

The determination of the precursor mode lifetime τ_L is illustrated in Fig. 6.12. In Fig. 6.12a the raw data of the line ratio measurements of the THB are shown, which measure both the precursor and the LCO. The impact of the LCO burst can be seen directly as a rapid drop in the value of the measured line ratio. The precursor can be seen by zooming in closer or by using the envelope modulation technique, introduced in Sec. 4.4. The raw data is band-pass filtered ($\pm 25\,\mathrm{kHz}$) around the precursor frequency, i.e. between $30\,\mathrm{kHz}$ and $80\,\mathrm{kHz}$, as shown in Fig. 6.12b (red). Signal traces that fluctuate with other frequencies are thus cut out. Although low frequencies have been filtered out, the remaining precursor signal is modulated. This can be seen more clearly after the next step: the calculation of the envelope using the Hilbert transform $\mathcal{H}$ and Eq. 4.6, shown in black in Fig. 6.12b. The envelope of the filtered signal is well achieved, but we can see that the directly calculated envelope features a lot of fluctuations. Especially the dips towards zero make the determination of the precursor

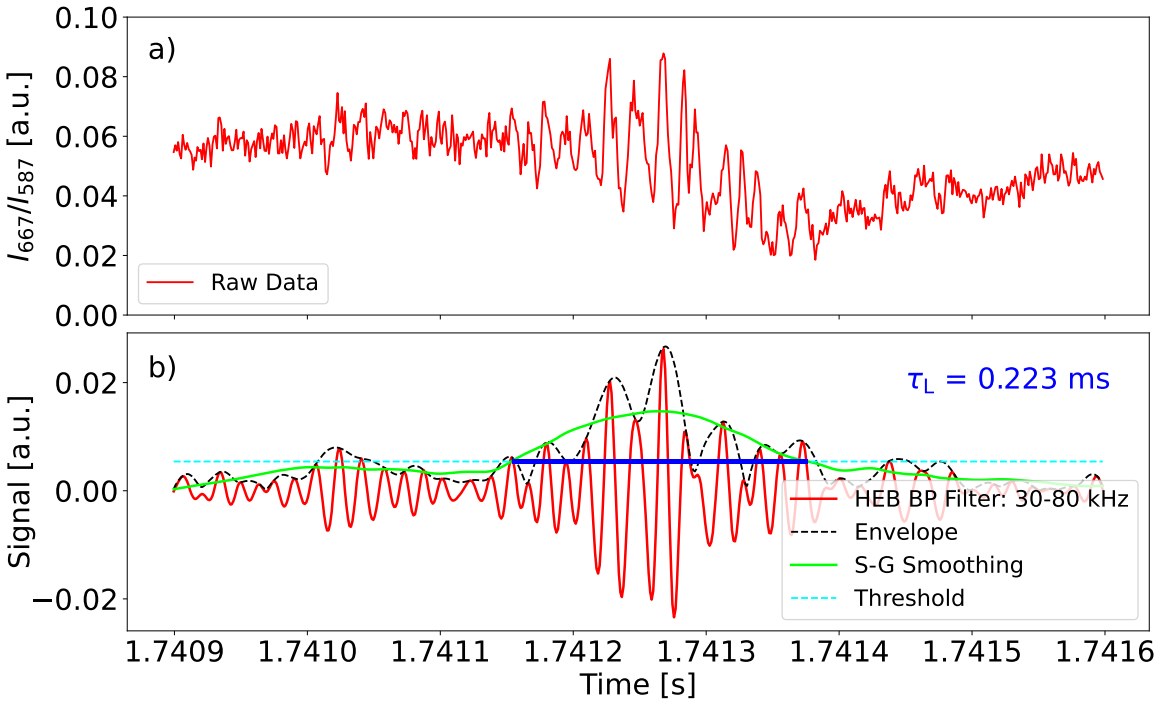

Figure 6.12: Graphical Representation of Precursor Lifetime Acquisition *a) The raw data from the line ratio measurements of the THB shows a clear drop in the signal, which corresponds to the appearance of the LCO burst. b) Band-pass filtered THB signal around the precursor frequency, here around* 30 kHz− 70 kHz. *Computed envelope (black) of the filtered THB signal using the Hilbert transform (see Sec. 4.4), smoothed with the Savitzky-Golay filter, shown in lime green (S-G smoothing). Threshold of* $1/e$ *of the lime green signal maximum (cyan) to obtain the lifetime of the precursor* τ_L *(dark blue) as the time the lime green signal is above this threshold.*

lifetime difficult. Therefore, the envelope is smoothed using the Savitzky-Golay filter (S-G), represented by the lime green curve. The S-G filter is a digital filter that cleverly performs polynomial regression via convolution processes [206]. The strong amplitude modulations in the signal now roughly disappear and a single peak is visible. Obviously, the height of the envelope is not correctly represented in the smoothed signal, but this is not important for the determination of τ_L, since we only need the width. We can see this in Fig. 6.12b. Here, we set an appropriate threshold, chosen to be $1/e$ of the maximum of the lime green signal, where e is Euler's number. The threshold is shown in cyan. Thus, we set the Gaussian width of the smoothed envelope of the precursor signal as the lifetime of the precursor τ_L, i.e. the time that the lime green signal is above the threshold, shown in dark blue. In this particular case, the precursor lifetime is $\tau_L = 0.223$ ms. We can summarize the approach as follows: the lifetime of the precursor mode is the time, for which the Savitzky-Golay smoothed envelope of the band-pass filtered signal of the line ratio of the THB is above $1/e$ of its maximum

amplitude.

Scaling of τ_L

Now that we know how the lifetime of the precursor mode τ_L is calculated, we can begin to extract physical output from it.

From the example in Fig. 6.12, it is clear that the precursor exists only for a comparably small duration of a few ten microseconds, making it difficult to compare local plasma quantities with τ_L. It should be noted that the IDA profiles (see Sec. 4.3), which are typically used in the analyses, have a time resolution of about 1 ms. This means that the IDA time scale is a factor five to ten larger than the precursor lifetime. Consequently, it is impossible to compare a single time window of precursor existence with the profile sizes from IDA, so a microscopic analysis of the precursor is at this point not possible. For a possible correlation study we therefore combine 6 ms time windows, i.e. about six precursors, and average their lifetimes $\overline{\tau}_L$. The number of precursors within this 6 ms period depends on the LCO frequency (see Fig. 6.2b).

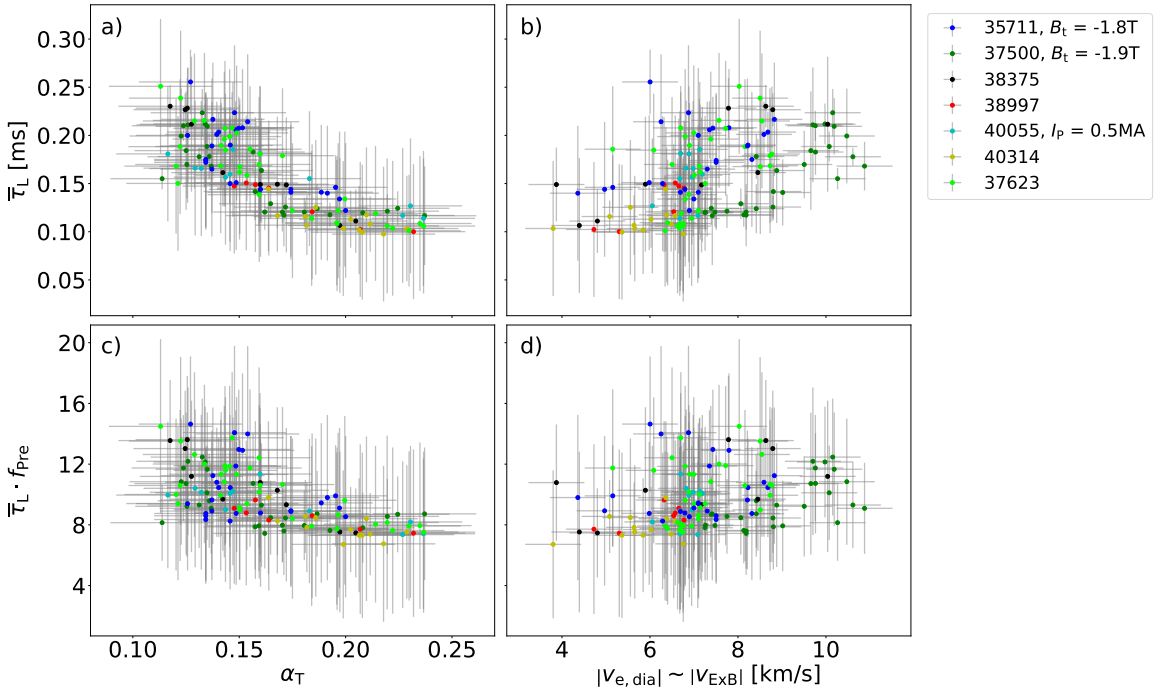

Figure 6.13: Scaling of the Precursor Lifetime

The averaged precursor lifetime $\overline{\tau}_L$ is plotted for multiple discharges operated at toroidal magnetic field $B_t = 2.5\,T$ and plasma current $I_p = 0.8\,MA$, unless otherwise stated, against the turbulence parameter α_T a) and the approximated background velocity $v_{E\times B} \sim v_{e,dia}$ b). The precursor lifetime can also be represented dimensionless by multiplying τ_L with the precursor frequency f_{pre}. This quantity corresponds to the number of oscillations the precursor makes before it disappears and is also plotted against α_T c) and $v_{E\times B} \sim v_{e,dia}$ d).

The averaged lifetimes $\overline{\tau}_{\mathrm{L}}$ for all discharges considered above are plotted against the turbulence parameter α_{T} and the approximated $E \times B$ velocity in the upper row of Fig. 6.13. The large errors for $\overline{\tau}_{\mathrm{L}}$ result from averaging. Nevertheless, we obtain a negative correlation between $\overline{\tau}_{\mathrm{L}}$ and α_{T} (Fig. 6.13a), i.e. $\overline{\tau}_{\mathrm{L}}$ seems to decrease with increasing α_{T}. For the $E \times B$ velocity in Fig. 6.13b, no perfect but a rather positive correlation can be estimated. The relationship between the resistivity η (Eq. 6.5) and $\overline{\tau}_{\mathrm{L}}$ is not shown here, but it also shows a negative correlation - similar to α_{T} - but much more scattered.

One can go one step further and calculate the number of oscillations a precursor makes before it disappears (Sec. 6.2). This can be estimated as the inverse of the time interval between the precursor peaks, and its lifetime $\overline{\tau}_{\mathrm{L}}$. The result is shown in the lower row of Fig. 6.13. The number of oscillations is between 7 and 15 and shows approximately the same trend with respect to α_{T} (Fig. 6.13c) as $\overline{\tau}_{\mathrm{L}}$ itself, but a little worse since f_{pre} correlates positively with α_{T} (see Fig. 6.6d). No relationship with $v_{\mathrm{E\times B}}$ or η (not shown) could be obtained for the data set examined. A limitation of this approach is the assumption that the precursor frequency is constant over the lifetime of the precursor, which is not the case (see Fig. 6.14). Therefore, the obtained results might be unreliable or increase the scatter in Fig. 6.13c and d, since the precursor frequency might vary during the precursor lifetime and between different LCO bursts.

From Figs. 6.13a and c we come to the conclusion that the higher α_{T}, i.e. the more interchange dominated the plasma is, the shorter the precursor exists.

6.6 Discussion and Interpretation

Now that the properties of the precursor mode have been presented, we can interpret the results obtained, categorize them in terms of the linear instabilities from Tab. 3.1, and discuss the results.

First of all, the following statements apply only to the same assumptions that we have made for the interpretation of the QCM in Sec. 5.7. These assumptions are that the mode is localized where we have identified them with our method (Sec. 4.4), that equilibrium reconstruction has arbitrarily small errors and the assumption that the underlying $E \times B$ velocity can be approximated by the electron diamagnetic velocity $v_{\mathrm{e,dia}}$ [91].

The precursor mode propagates in the electron diamagnetic direction (EDD) in the plasma frame for each discharge considered and has a phase velocity that matches with $v_{\mathrm{ph}} = v_{\mathrm{e,dia}}$ within the errorbars (Sec. 6.4). What is important here, in contrast to the derivation of $v_{\mathrm{e,dia}}$ for the drift wave (DW) in Sec. 3.2.1, is the inclusion of the temperature gradient when compared to our measurements. According to Tab. 3.1, this

result rules out some instabilities, leaving only drift waves (DW, Sec. 3.2.1), electron temperature gradient modes (ETG, Sec. 3.2.3), trapped electron modes (TEM, Sec 3.2.4), micro-tearing modes (MTM, Sec. 3.2.6) and kinetic peeling-ballooning modes (KPBM, Sec. 3.1.3) as potential candidates.

As we have already seen in Fig. 6.1, the precursor is clearly visible in the signal of the $\tilde{B}_\mathrm{r}$-coil. According to Sec. 3.3.2, this implies that the precursor also possesses an electromagnetic (EM) component. The fact that the Fourier amplitude in the $\tilde{B}_\mathrm{r}$-coil is as large as that in the THB indicates that the EM component is not negligible. The role of the EM nature is further confirmed by the fact that $k_\mathrm{EM}\rho_\mathrm{s} \sim 0.77 > 0.5$, which is well above the experimentally measured values $0.01 < k_\theta\rho_\mathrm{s} < 0.06$. Since EM effects have a stabilizing influence on TEMs, TEMs might be rather suppressed [134].

Furthermore, the measured $k_\theta\rho_\mathrm{s}$ values indicate that the precursor mode is in the intermediate range between MHD instabilities (Sec. 3.1) and micro-instabilities (Sec. 3.2). Thus, according to Tab. 3.1, the precursor is too large for ETGs to be the underlying instability.

Another reason that TEMs may not play a major role here is the high pedestal top collisionality (Eq. 2.10) in the observed discharges, which is between $0.8 \leq \nu^\star_\mathrm{ped} \leq 14$. If we average the collisionality over all discharges and times, we obtain a mean value of $\nu^\star_\mathrm{ped} \sim 3.5$. We therefore exclude TEMs from the list of possible instabilities.

Another way to express the collisionality is the turbulence parameter α_T, which seems to play an important role in describing the precursor, as shown in all analyses. In fact, it has been suggested that α_T may contribute to a change in the underlying instability of the precursor mode. Although the data points should be treated with caution due to the large errorbars, a higher α_T seems to change the precursor phase velocity v_ph in the plasma frame so that it deviates from $v_\mathrm{e,dia}$ (Sec. 6.4), making the mode more interchange-like (IC, Sec. 3.1.1). The precursor thus seems to change its underlying nature. In general, however, based on our current state of knowledge, we conclude that the precursor has DW-like properties and is most compatible with MTMs or KPBMs. Due to the poloidal size of the precursor, a classical MHD-like tearing mode (TM, Sec. 3.2.6) is also a potential candidate instability. As shown in Ref. [24], tearing modes also propagate in EDD with electron diamagnetic velocity. However, it is not generally known to observe classical TMs at the edge, so this would have to be verified quantitatively with an MHD simulation code at first. However, we do not rule it out of the candidate list of possible instabilities.

The data at hand suggests the following mechanism at play giving rise to LCO bursts as well as type-III ELMs: a (M-)TM or KPBM is triggered due to the elevated gradients at the edge in the I-phase. This is the observed precursor mode. The amplitude of this instability grows over time, and while it is growing, the edge transport is increased

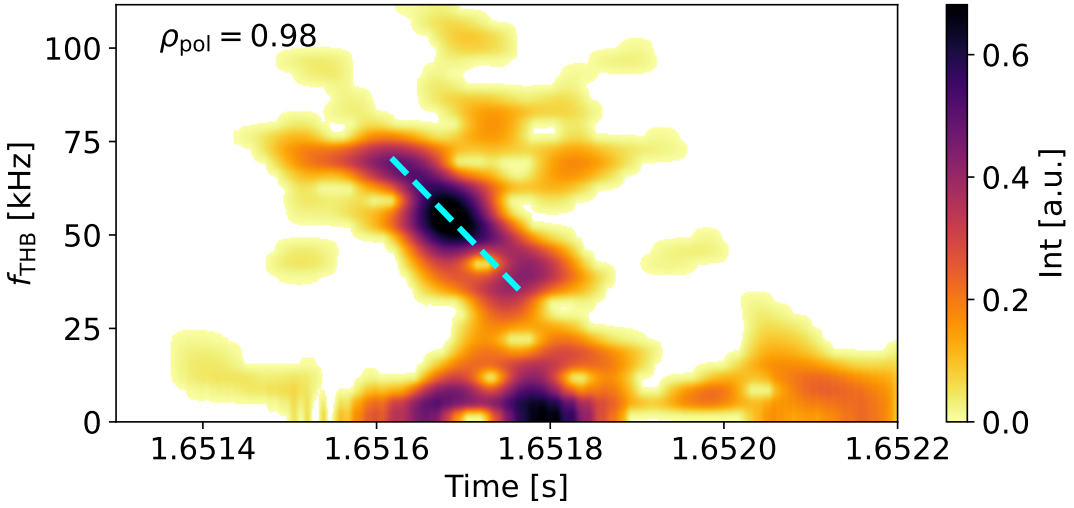

Figure 6.14: Precursor Frequency on Small Timescale
Spectrogram of a single I-phase precursor on a small time scale. We can see that the precursor frequency drops rapidly in a few microseconds (cyan). This emphasizes that the precursor mode may change its underlying nature during its lifetime.

in parallel. At a certain point, the transport is so large, that particles and energy are expelled to a large amount manifesting as a burst, i.e. the LCO burst. During this strong transport event, the gradients at the edge flatten, extinguishing the drive of the (M-)TM or KPBM. At higher edge α_T, the interchange nature of the mode is more pronounced resulting in velocities deviating from the electron diamagnetic velocity and in shorter precursor lifetimes since the transport levels required to generate a burst are more easily achieved. Elevated levels of α_T and thus transport lead likewise to a higher repetition rate of LCOs/type-III ELMs. In the opposite case, when α_T becomes very small, the drift wave nature of the precursor mode dominates and the transport caused by the mode becomes smaller. Accordingly, the mode becomes so stable that it exists on longer time scales (cf. Fig. 6.13a) and no longer triggers a burst. This might be the observed modulating pedestal mode (MPM)/fork mode mentioned in Sec. 6.1, which is present in the H-mode without type-I ELMs. However, the transition between the precursor and the MPM has to be investigated in detail to check this theory.

However, it must be pointed out again that the entire study is based on averaged quantities. Since we mostly average over time intervals of 10 ms to 30 ms in the analyses, and the precursor exists on time scales of the order of 100 µs (Sec. 6.5), we will examine this short time scale in Fig. 6.14 as a kind of outlook for further studies. It is visible that the frequency of the precursor (dark in the colorbar) decreases rapidly on this time scale, which is illustrated by the cyan line. This behavior also explains the large errorbars in the frequency from Sec. 6.2, since we average over at least one precursor lifetime.

From this finding we hypothesize that the key to the underlying instability lies in the microscopic analysis of the precursor. If we could show that on this time scale of about $\sim 150\,\mu s$ the turbulence parameter α_T increases and the precursor phase velocity in the plasma frame v_{ph} deviates so far from the $E \times B$ background velocity, i.e. that the mode becomes completely interchange dominated shortly before its disappearance, we could confirm the theory presented above. For the cross-phase between electron temperature and potential perturbations (see Sec. 3.2.1) of the weakly coherent mode (Chapter 7) exactly this change in the underlying mechanism has already been shown numerically and has been called the "sudden jump in cross-phase" [207]. Hence, the fully IC-like precursor would thus trigger a major transport event, which are the LCO bursts. This would be consistent with the fact that the precursor exists for a shorter time at a higher averaged α_T, since the mode reaches its 'IC-threshold', i.e. the corresponding α_T threshold, more quickly.

Furthermore, the large observed particle transport of the precursor argues against the (M-)TM, since (M-)TMs mainly affect the electron temperature profiles. KPBMs, on the other hand, cause enhanced particle and heat transport, which is consistent with the observed phenomena. Since the LCO bursts are identified as type-III ELMs [202], the smoothest transition from the precursors to the LCOs may be given by the KPBM, so we want to underline again this underlying instability for the precursor mode.

7 Weakly Coherent Mode (WCM)

As a last example of edge phenomena in a plasma regime without type-I edge localized modes (ELMs, Sec. 3.3.1), in this chapter we will focus on the edge mode of the improved energy confinement mode (I-mode) [64, 97]: the weakly coherent mode (WCM). In many cases, in addition to the WCM, the geodesic acoustic mode (GAM) can also be measured in I-modes, which is not discussed further in this work. For more information on the GAM, see e.g. the review by Conway *et al.* [184].

As explained in Sec. 2.2.4, the I-mode usually appears in unfavorable ∇B-drift configurations. This and the special property of L-mode-like electron densities n_e and H-mode-like electron temperatures T_e make the I-mode unique. This special confinement is often attributed to the WCM. However, the WCM is detected not only in the I-mode, but also in L-mode plasmas before the transition to the I-mode [103, 208], so the necessity of the WCM to obtain the I-mode needs to be investigated.

I-modes are followed with great interest both experimentally and by simulations [65, 152, 209–211]. The experimental results from ASDEX Upgrade (AUG, Sec. 4.1), Alcator C-Mod and EAST are summarized in Tab. 7.1. All experiments localize the mode radially within the separatrix, close to the radial electric field minimum E_r ($\rho_\mathrm{pol}^\mathrm{Loc}$). AUG and Alcator C-mod experiments have shown that the WCM propagates in the electron diamagnetic direction (EDD) in the laboratory frame. On Alcator C-mod, Theiler *et al.* [80] show that the WCM has a small phase velocity v_ph in EDD, but Hubbard *et al.* [212] claim a larger phase velocity in the plasma frame, i.e. $v_\mathrm{ph} = v_\mathrm{e,dia}$. The results in AUG plasmas are discussed in more detail below and are largely based on the work by Herschel *et al.* [213]. The study presented there includes I-modes in upper single null (USN) and lower single null configurations (see Sec. 4.1) with reversed plasma current I_p and toroidal magnetic field B_t (LSNrev).

For AUG, the characteristics of the WCM are obtained using a combination of the THB (Sec. 4.2) and the Doppler back-scattering diagnostic (DBS) [215]. DBS is a microwave diagnostic that can provide information about the frequency of the WCM f_WCM, its amplitude and the background $E \times B$ velocity $v_\mathrm{E\times B}$ (see Eq. 3.49) by analyzing the back-scattered fraction of an obliquely irradiated microwave. There, the frequency of the incident wave undergoes a Doppler shift. In principle, both the frequency and the wavenumber at the reflection point ($k_\mathrm{DBS} \sim 10\,\mathrm{cm}^{-1}$) of the incident

Table 7.1: WCM Properties from Analyses in Different Fusion Devices
'N/A' denotes that there is no quantified information in the corresponding reference. A negative velocity indicates propagation in the electron diamagnetic direction.

Quantity	AUG [213]	Alcator C-Mod [80, 212]	EAST [214]
$\rho_{\mathrm{pol}}^{\mathrm{Loc}}$	E_{r} min.	E_{r} min.	E_{r} min.
f [kHz]	50–150	100–300	25–150
k_θ [cm^{-1}]	0.5–0.69	1.3–1.8	< 2
v_{lab} [$\mathrm{km\,s}^{-1}$]	< 0	< 0	N/A
v_{ph} [$\mathrm{km\,s}^{-1}$]	< 0	< 0	N/A

microwave are chosen so that it is reflected at a specific radial position, i.e. at a specific electron density n_{e}[1] - the so-called density cutoff layer [12]. If the density fluctuation, in our case the WCM, is close to the cutoff layer, the reflected wave is modulated and we can obtain information about the WCM. Assuming that the phase velocity on the wavenumber scale of structures probed at the cutoff layer is negligible, $v_{\mathrm{E\times B}}$ can be determined directly from the Doppler shift. Usually, we can neglect the phase velocity on the probed DBS scale [101, 151, 216].

7.1 Spectral Analysis of the WCM

As mentioned above, the following analyses have already been published in Ref. [213], but are described here in detail and placed in the context of other edge modes.

As a first step, we localize the WCM at the radial position where the intensity line ratio I_{667}/I_{587} of the THB (see Sec. 4.2) has a maximum in Fourier space, as described in Sec. 4.4. The position of the WCM is shown in green in Fig. 7.1 and drawn against the radial position of the maximum of the electron pressure gradient $\rho_{\mathrm{pol}}^{\nabla p_{\mathrm{e,max}}}$. In addition, the localization data of the quasi-coherent mode (QCM) from Fig. 5.1b (blue) and the I-phase precursor mode from Fig. 6.4 (red) are included for a direct comparison. We can also see that the WCM data points are arranged along the black line, which represents the equality of the corresponding mode position $\rho_{\mathrm{pol}}^{\mathrm{Loc}}$ and $\rho_{\mathrm{pol}}^{\nabla p_{\mathrm{e,max}}}$. Ref. [213] localizes the WCM radially using the DBS system. In this paper the WCM is located close to the minimum of the radial electric field E_{r}, i.e. approximately at $\rho_{\mathrm{pol}} = 0.991 \pm 0.006$, using the same approach as described in Sec. 4.4 but with DBS. Assuming that E_{r} can be approximated by $E_{\mathrm{r}} = \nabla p_{\mathrm{e}} / (e n_{\mathrm{e}})$ (Eq. 5.1) with the elementary charge e and electron density n_{e}, the observations are in agreement.

Similar to Chapter 6, for many I-mode discharges only the radial THB grid (Fig.

[1] Only valid in the so-called O-mode. In X-mode this position also depends on the magnetic field strength B.

4.3) is available, so the poloidal wavenumber k_θ from the THB data and the resulting velocity in the laboratory frame are not necessarily measured at the WCM position. However, the corresponding electron density n_e, temperature T_e and $v_{E\times B}$ are always measured at the radial position, where the WCM is localized.

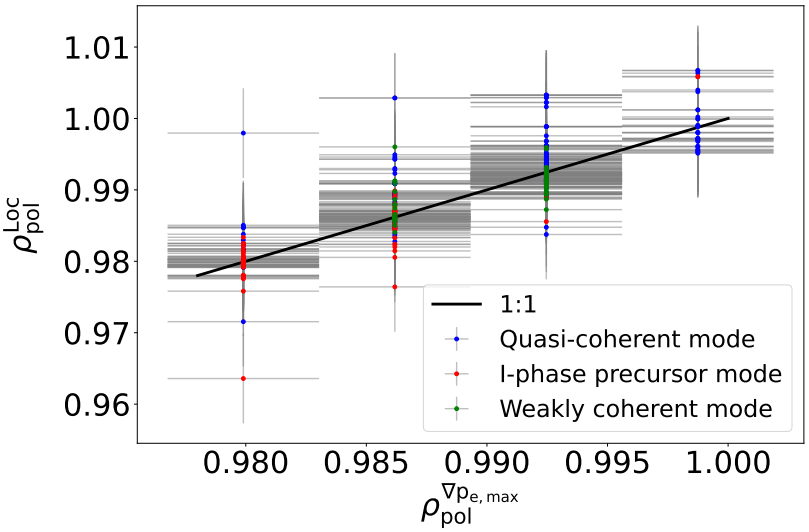

Figure 7.1: Localization of WCM, QCM and Precursor vs. Pressure Gradient Maximum
The radial position of the weakly coherent mode ρ_{pol}^{WCM} (green) is determined for all time points and discharges from Tab. B, averaged over 40 ms time intervals and drawn against the radial position of the steepest pressure gradient $\rho_{pol}^{\nabla p_{e,max}}$. In addition, the radial positions, where we localized the quasi-coherent mode (blue) and the I-phase precursor mode (red) are included. The black line indicates $\rho_{pol}^{Loc} = \rho_{pol}^{\nabla p_{e,max}}$.

If we visualize the WCM in frequency space, we see that it has a broad or more incoherent appearance, which is why the mode is called 'weakly' coherent. This can be clearly seen in Fig. 7.2a. The Fourier representation of the THB line ratio signal for the 30 ms time interval at the radial position $\rho_{pol} = 0.987$ follows the methodology of Sec. 4.4. In addition to the broad WCM at a central frequency of $f_{WCM} \sim 72$ kHz, the fitting routine finds another coherent peak at about $f_{GAM} \sim 10$ kHz. This is the geodesic acoustic mode (GAM) often observed in I-modes as described above. The frequency of the WCM is radially constant.

The WCM also appears broad in the poloidal wavenumber space, as shown in the $k_\theta - f$ spectrum in Fig. 7.2b generated via the method from Sec. 4.4. Further, the central poloidal wavenumber for the same discharge and time interval as above is around $k_\theta \sim 0.5\,\mathrm{cm}^{-1}$. Generally, it has been shown that the WCM has poloidal wavenumbers in the range of $0.5\,\mathrm{cm}^{-1} < k_\theta < 0.69\,\mathrm{cm}^{-1}$ at AUG and barely varies in different discharges. Though, the higher k_θ are found in USN discharges and the lower ones in LSNrev. k_θ also remains constant along the radial axis. In particular, the normalized

poloidal wavenumber $k_\theta \rho_s$ normalized to the hybrid gyroradius ρ_s from Eq. 3.2 is almost completely constant at around $k_\theta \rho_s \sim 0.05$. This quantity is particularly interesting to analyze the difference between the WCM in L-modes and I-modes. However, it has been shown that $k_\theta \rho_s$ remains the same in both modes [213]. This is due to the fact that the L-mode WCM has a higher poloidal wavenumber but a lower T_e. Therefore, the measured frequency plays an important role for the upcoming velocity analysis of the WCM.

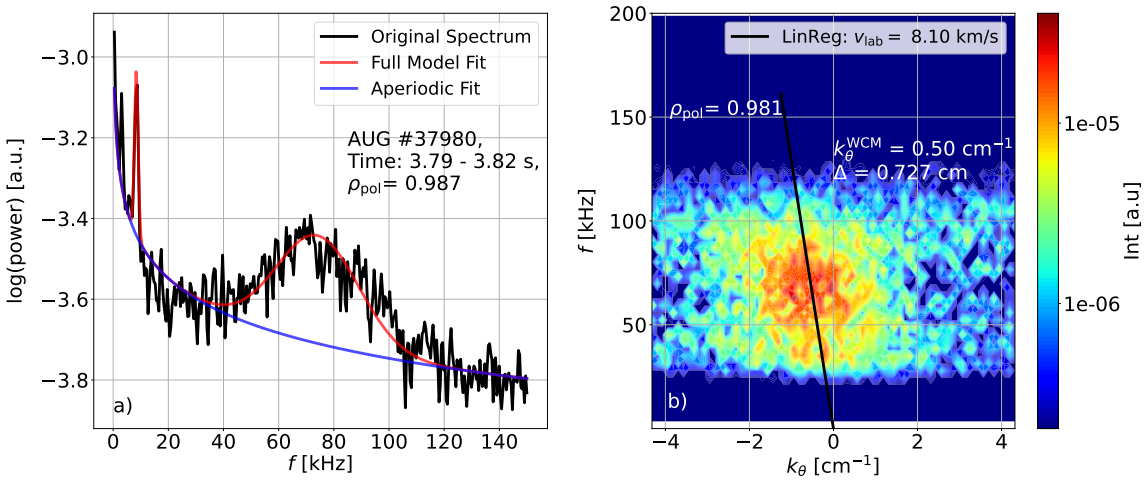

Figure 7.2: Spectral Analysis of the WCM for Discharge #37980
a) Example of a THB line ratio (Sec. 4.2) Fourier spectrum for a 30 ms time interval at $\rho_{pol} = 0.987$ for discharge #37980. The geodesic acoustic mode can be seen around 10 kHz and the broad peak around 70 kHz represents the weakly coherent mode (WCM). b) The WCM is also visible in the $k_\theta - f$ spectrum (Sec. 4.4) for the same time interval, but the spectrum is evaluated at a different radial position, i.e. $\rho_{pol} = 0.981$. Here we can see that the WCM is not only broad in frequency but also in the poloidal wavenumber k_θ. Nevertheless, the WCM is assigned a central poloidal wavenumber of $k_\theta = -0.5\,\mathrm{cm}^{-1}$. The minus sign implies that the WCM propagates in electron diamagnetic direction. The velocity of the mode in the laboratory frame can be determined from the slope of the black line.

7.2 Phase Velocity of the WCM

From the $k_\theta - f$ spectra of the THB we can now compare the phase velocity of the WCM in the laboratory frame v_{lab} with the background $E \times B$ velocity $v_{E\times B}$ from the DBS measurements. The first property we notice is that v_{lab} is negative from Fig. 7.2b, indicating a propagation of the WCM in the electron diamagnetic direction (EDD). This is shown in a radial comparison in Fig. 7.3a. As described above, we localize the WCM with the DBS diagnostic in the E_r minimum (highlighted in gray in Fig. 7.3a) within the radial uncertainties of the DBS. However, we determine the

laboratory velocity v_{lab} with the THB (Sec. 4.2) from Fig. 7.2b. Unfortunately, we do not have a poloidal array at the radial position of the E_{r} minimum, so we use the next one and v_{lab} is measured further inward. Furthermore, the poloidal wavenumber k_θ and the frequency of the WCM are radially constant, which allows us to assume a nearly radially constant v_{lab}. Hence, we can state that $|v_{\mathrm{lab}}|$ is larger than $|v_{\mathrm{E\times B}}|$, so an intrinsic phase velocity of the mode in the plasma frame (v_{ph}) in EDD is obvious (see Eq. 3.50).

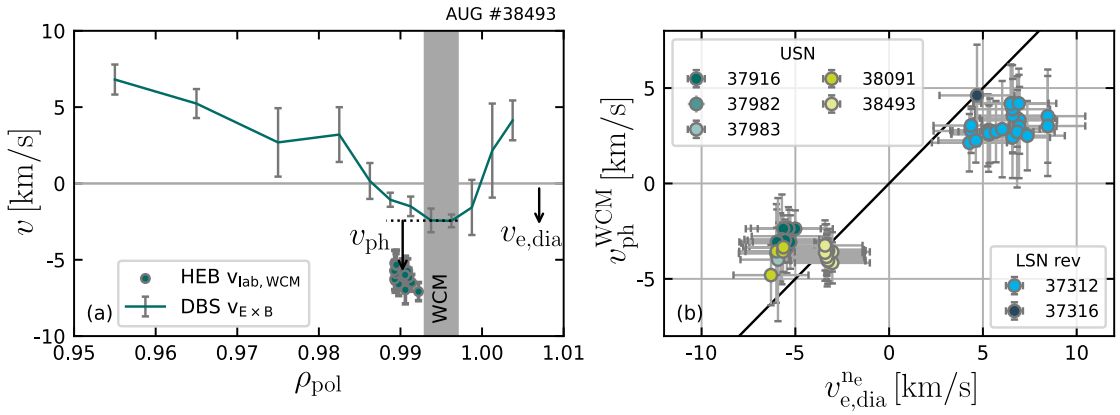

Figure 7.3: Velocities of the Weakly Coherent Mode

a) The radial $E \times B$ velocity profile and the WCM velocity in the laboratory frame are shown. The radial position of the WCM, which corresponds to the position of the E_{r} minimum, is highlighted in gray. Due to the poloidal THB grid (see Fig. 4.3b), however, it is possible to determine the laboratory velocity at a radial position close to the WCM position. This velocity is larger than the maximum $E \times B$ velocity (in absolute values), indicating that the WCM has an intrinsic phase velocity $v_{\mathrm{ph}}^{\mathrm{WCM}}$ in the electron-diamagnetic direction (EDD). b) A comparison of the theoretical phase velocity of the drift wave, i.e. $v_{\mathrm{e,dia}}^{\mathrm{n_e}}$, and the determined $v_{\mathrm{ph}}^{\mathrm{WCM}}$ shows that the WCM propagates at a similar velocity as the drift wave in the EDD. Positive velocities are obtained for the lower single null with reversed plasma current and toroidal field configuration (LSNrev) and negative velocities for the upper single null configuration (USN). Fig. adapted from Ref. [213].

Fig. 7.3b shows the comparison of $v_{\mathrm{ph}}^{\mathrm{WCM}} = v_{\mathrm{lab,WCM}} - v_{\mathrm{E\times B}}$ of the WCM with the calculated electron diamagnetic velocities $v_{\mathrm{e,dia}}^{\mathrm{n_e}}$. It is important to note that in Fig. 7.3b only the density gradient as in the theoretical derivation of the drift wave velocity (DW) from Sec. 3.2.1, i.e.

$$v_{\mathrm{e,dia}}^{\mathrm{n_e}} = \frac{T_{\mathrm{e}}}{e\lambda_{\mathrm{n_e}} B_{\mathrm{t}}} \tag{7.1}$$

is considered. Here, e is the elementary charge, B_{t} is the toroidal magnetic field strength and $\lambda_{\mathrm{n_e}} = -n_{\mathrm{e}}/\nabla n_{\mathrm{e}}$ is the density gradient length. It can be shown that considering

the entire pressure gradient ∇p_e in the electron diamagnetic velocity, i.e.

$$v_{\mathrm{e,dia}}^{\mathrm{p_e}} = \frac{\nabla p_\mathrm{e}}{e n_\mathrm{e} B_\mathrm{t}}, \tag{7.2}$$

the phase velocities of the WCM no longer fit to theory, and thus the temperature gradient must be neglected. However, most data points are such that the phase velocity of the WCM is slightly lower than the electron diamagnetic velocity from Eq. 7.1.

7.3 Discussion and Interpretation

For the analysis of the WCM, the same assumptions regarding radial localization and equilibrium reconstruction are made as in Secs. 5.7 and 6.6.

The weakly coherent mode (WCM) has a phase velocity in the plasma frame in electron diamagnetic direction and reaches values around $v_\mathrm{ph}^\mathrm{WCM} \sim v_{\mathrm{e,dia}}^{\mathrm{n_e}}$, but without taking the temperature gradient into account. From this fact alone, Tab. 3.1 leaves only the general drift-wave (DW, Sec. 3.2.1), trapped electron modes (TEM, Sec. 3.2.4), micro-tearing modes (MTM, Sec. 3.2.6), kinetic-peeling ballooning modes (KPBM, Sec. 3.1.3) and electron temperature gradient modes (ETG, Sec. 3.2.3) as candidates for the underlying instability of the WCM. But why do the temperature fluctuations not play a role in the description of the WCM? For this we refer to the attempt of explanation by Manz *et al.* [201]. The I-mode has as a basic requirement in the operation in the unfavourable ∇B configuration. In this configuration, due to the much higher L-H power threshold (see Sec. 2.3), it is possible to induce significantly more heating power into the system without entering the H-mode. This leads to higher electron temperatures T_e and thus to lower electron-ion collisionality (Eq. 2.10), i.e. a reduced electron-ion coupling. This leads to higher ion temperatures in the scrape-off layer [217] and thus to a steeper gradient is created in ∇T_e than in the ion temperature ∇T_i. This suppresses the ITG turbulence [201] (Sec. 3.2.2), which is dominant for the L-mode interchange-like turbulence (IC, Sec. 3.1.1), and allows the DW-like turbulence to develop. In addition, higher T_e leads to higher parallel thermal conductivity, which means that $\tilde{T}_\mathrm{e}$ can be compensated quickly and are therefore generally suppressed. Nevertheless, temperature fluctuations in the range of $\tilde{T}_\mathrm{e}/T_\mathrm{e} \sim 2-4\%$ are present, but they are rather small compared to the density fluctuations of $\tilde{n}_\mathrm{e}/n_\mathrm{e} \sim 10\%$ [213] and the cross-phase between electron density and temperature fluctuations $\alpha_{\mathrm{n_e,T_e}}$ is inconclusive [103, 208].

Furthermore, we can see from the poloidal size of the WCM that ETGs can be eliminated from the list of candidate modes (see Tab. 3.1).

On AUG, the WCM is not observed in the magnetic coil signal, so one could conclude

that electromagnetic (EM) transport does not play a major role for the WCM (cf. Sec. 3.3.2). The electromagnetic wavenumber (Eq. 5.5) for the analyzed I-modes is in the range of $k_{\mathrm{EM}}\rho_{\mathrm{s}} \sim 0.5$, which indicates that we are exactly at the transition to the EM regime, for which $k_{\mathrm{EM}}\rho_{\mathrm{s}} = 0.5$ applies. From Sec. 3.2.6 we know that MTMs tend to be excited in the high EM regime, which is not obtained here. However, the WCM was observed at Alcator C-mod experiments in magnetic probes [212], so the AUG results do not suggest MTMs, but due to the results at Alcator C-mod, we cannot completely exclude them from the list. The same is true for KPBMs, which also induce a high EM transport and should be clearly visible in the magnetic coils (Sec. 3.1.3).

The low collisionality of $0.3 < \nu^{\star}_{\mathrm{ped}} < 1.6$ found in the analyzed I-modes (cf. Tab. 2.2) also may allow the development of TEMs (Sec. 3.2.4).

We therefore maintain that the WCM is DW-like, i.e. either a general DW, TEM, MTM or KPBM are candidates for the WCM.

As mentioned in Sec. 6.6, it is observed in Ref. [207], using a gyrofluid simulation code, that the WCM can change its underlying instability from DW-like to IC-like. There, a jump of the cross-phase between electron temperature $\tilde{T}_{\mathrm{e}}$ and potential fluctuations $\tilde{\phi}$ from $\alpha_{\mathrm{T_e},\phi} = 0$ (DW) to $\alpha_{\mathrm{T_e},\phi} = \pi/2$ (IC) is observed within about 20 µs. In the simulation, however, it is not the collisionality that is responsible for the instability change (see Sec. 3.2.1), but the induction. Induction, like collisionality, can prevent the parallel dynamics necessary for the DW mechanism and thus lead to a change in the behavior. Experimentally, however, it is difficult to detect a change on such a time scale. Nevertheless, according to this result, the WCM would be able to cause radial transport (Sec. 3.3.2). In this context, so-called pedestal relaxation events [218] are observed, which will not be discussed further here.

Therefore, it is advisable in the future to compare the variation of the WCM properties on a small time scale and in general with the variation of the turbulence parameter α_{T} (Eq. 3.23) and the plasma beta β (Eq. 2.5). In particular, these two parameters reflect the influence of two effects on DW-like instabilities. Both the Alfvénic coupling and the magnetic flutter effect (Sec. 3.2.5) due to β as well as the change of the underlying instability due to α_{T} could be studied experimentally.

8 Conclusion and Outlook

After the detailed presentation of the results and the discussion and interpretation of the experimental achievements, the thesis will be reviewed by answering the key questions postulated in Sec. 1.4. This is followed by a brief outlook on possible future research and questions that should be considered.

8.1 Summary and Answers to Key Questions

Since the discovery of the high-confinement mode (H-mode) [26], fusion physicists have been searching for a way to avoid type-I edge localized modes (ELMs), which are detrimental for future fusion reactors such as ITER or DEMO, and still achieve H-mode-like plasma confinement. Fortunately, there are several natural type-I ELM-free regimes that should make this goal possible. However, it is not clear to what extent these regimes can really be operated in future fusion devices, and whether the corresponding characteristic, i.e. the associated edge mode, is responsible for the type-I ELM absence. The key questions regarding type-I ELM-free regimes will be answered in the following with the help of experiments performed on ASDEX Upgrade (Sec. 4.1) and the detailed textualization of the results.

Which plasma scenarios without type-I edge localized modes are promising for the operation of a future fusion reactor?

We have seen in Chapter 2 that all natural type-I ELM-free scenarios need further development to reach the desired values of the dimensionless parameters for the DEMO baseline scenario from Tab. 2.2. Almost all scenarios have their raison d'être and all scenarios (with the exception of the X-point radiator, in which no edge mode is observed so far and the negative delta regime, which is L-mode-like) are accompanied by an edge mode during the ELM-free period, which might be responsible for the absence of ELMs. In this work, the plasma edge properties of the enhanced D_α high confinement mode (EDA H-mode), quasi-continuous exhaust regime (QCE), the intermediate phase (I-phase) and the improved energy confinement mode (I-mode) has been investigated in detail. After extensive analysis, these regimes do not exhibit any properties that

would preclude operation in a future fusion reactor. The characterizations presented in this thesis, together with simulation codes, will contribute greatly to determine which regime will ultimately be the most suitable.

How can edge modes be responsible for the absence of type-I edge localized modes?

Using the EPED model [148], it is shown in Sec. 3.3.1 that the ELM crash is induced exactly when the pedestal height, defined by the electron pressure at the pedestal top, and the pedestal width can evolve along the instability limit for kinetic ballooning modes (KBMs, Sec. 3.2.5) until they reach the ideal peeling-ballooning limit [147]. At this limit, the current-driven (peeling modes, Sec. 3.1.3) and pressure-driven instabilities (ideal ballooning modes, Sec. 3.1.1) couple to produce a large transport event: an ELM. Along the KBM constraint, therefore, the plasma edge instability of the corresponding ELM-free regime must prevent the pedestal from building up, i.e. it must cause sufficient electrostatic radial transport Γ_r to let the pressure profile stagnate below the peeling-ballooning limit.

What properties of edge modes do we need to identify their underlying nature?

The poloidal phase velocity of the mode v_ph and its poloidal structure size or poloidal wavenumber k_θ are essential to assign an underlying instability to it (cf. Tab. 3.1). As already mentioned, radial electrostatic transport Γ_r plays the most important role and this is different for the different linear instabilities, presented in Secs. 3.1 and 3.2. For example, interchange modes (Sec. 3.1.1) cause maximum transport and regular drift waves (DW, Sec. 3.2.1) cause none. Radial transport depends directly on the cross-phase between electron density and potential fluctuations $\alpha_{\mathrm{n_e},\phi}$. However, in this work it is shown that a qualitative statement as to whether the edge mode causes radial transport at all can be made solely from its poloidal phase velocity in the plasma frame.

How can we obtain the properties of the edge modes, and can this be done reliably?

The main diagnostic we used to study the edge modes from the aforementioned type-I ELM-free regimes is the thermal helium beam diagnostic (THB, Sec. 4.2), which is based on the principle of active spectroscopy [163]. In particular, light intensity measurements of the THB at different excitation wavelengths enabled to study the influence of the edge mode on the electron density and temperature. All the edge modes

we have studied are visible in the THB signal. To avoid undesired diagnostic effects and to obtain reliable and localized mode measurements, it is necessary to measure the mode in signals of at least two spectral lines and to analyze their intensity ratio. Because of the best signal-to-noise ratio, we chose the wavelengths $\lambda_1 = 587\,\mathrm{nm}$ and $\lambda_2 = 667\,\mathrm{nm}$ and their ratio for the investigations. In addition, this work introduced quantifiers that provide reliable information about which THB channels are trustworthy and which are not (see Fig. 4.5).

What are the instabilities of the edge modes in the different regimes and can they really cause the absence of type-I ELMs?

The results on the quasi-coherent mode (QCM) from Chapter 5, the I-phase precursor mode from Chapter 6 and the weakly coherent mode (WCM) from Chapter 7 are summarized in Tab. 8.1 and will be placed in the context of their importance in their respective regimes.

Table 8.1: Properties of Edge Modes, Measured at AUG in the Corresponding Type-I ELM-free Regime
The modes are localized at the radial position $\rho_{\mathrm{pol}}^{\mathrm{Loc}}$, with associated frequencies f, poloidal wavenumbers k_θ, normalized poloidal wavenumbers $k_\theta\rho_\mathrm{s}$, poloidal velocities in the laboratory frame v_{lab}, and phase velocities in the plasma frame v_{ph}. Using Eq. 3.54, we can assess whether the modes cause radial electrostatic transport Γ_r. The table also presents whether the modes are electromagnetic (EM). Finally, candidate instabilities are assigned to the modes based on Tab. 3.1.

	Quasi-Coherent Mode	Precursor Mode	Weakly Coherent Mode
Regime	EDA H-Mode, QCE	I-Phase	I-Mode
$\rho_{\mathrm{pol}}^{\mathrm{Loc}}$	0.993±0.007	0.985±0.007	0.991±0.006
f [kHz]	15–80	40–80	50–150
k_θ [cm^{-1}]	0.3–0.8	0.05–0.7	0.5–0.7
$k_\theta\rho_\mathrm{s}$	0.025–0.075	0.007–0.065	~ 0.06
$\lvert v_{\mathrm{lab}}\rvert$ [$\mathrm{km\,s}^{-1}$]	1–6	5–34	6–10
v_{ph}	$1/2\ v_{\mathrm{i,dia}}$	$v_{\mathrm{e,dia}}^{\mathrm{p_e}}$	$v_{\mathrm{e,dia}}^{\mathrm{n_e}}$
Γ_r	large	small	small
EM	Yes	Yes	No
Instability	EM Ballooning Mode	(M-)TM or KPBM	DW, TEM, MTM or KPBM

From the radial positions of the modes $\rho_{\mathrm{pol}}^{\mathrm{Loc}}$ we see that the QCM and WCM seem to have its maximum impact further out than the precursor mode, which follows from the fact that the gradients of the kinetic profile (n_e, T_e, p_e) in EDA H-mode, QCE and I-mode peak further out than in the I-phase, displayed in Fig. 7.1. Thus, all modes are finally localized in the region of the strongest gradients.

The measured frequencies f from the laboratory frame differ in that only the QCM is present at low frequencies, but the high frequency QCMs (in QCE) are in the same range as the precursor and the low frequency WCMs. In addition, the normalized frequency of the QCM shows a positive correlation with $1/\beta_{\mathrm{pol}}^2$, where β_{pol} is the poloidal plasma beta (Eq. 2.5), and a negative correlation with the background $E \times B$ velocity $v_{\mathrm{E\times B}}$. The precursor frequency also shows a negative correlation with $v_{\mathrm{E\times B}}$, but it increases with increasing turbulence parameter α_{T} (Eq. 3.23). The WCM reaches the highest frequency values, but shows no clear dependence on a local plasma parameter.

The poloidal wavenumber $k_\theta = 2\pi/\lambda_\theta$, representing the poloidal size of the mode λ_θ, and the poloidal wavenumber $k_\theta \rho_{\mathrm{s}}$ normalized to the hybrid gyroradius (Eq. 3.2) are in an intermediate range between typical MHD instabilities (Sec. 3.1) and micro-instabilities (Sec. 3.2). The $k_\theta \rho_{\mathrm{s}}$ values of the QCM scale strongly with the electromagnetic wavenumber $k_{\mathrm{EM}}\rho_{\mathrm{s}} \sim \sqrt{\beta}$ (Eq. 5.5), which can be derived theoretically from the DALF system. This emphasizes the electromagnetic character of the QCM. The values of the precursor $k_\theta \rho_{\mathrm{s}}$ show a negative correlation with $v_{\mathrm{E\times B}}$ and a positive one with α_{T} - similar to its frequency behavior. No clear scaling is obtained for the WCM, which could be due to the fact that the range of values of $k_\theta \rho_{\mathrm{s}}$ of the WCM is significantly smaller than that of the other two edge modes.

Tab. 8.1 shows the absolute value of the poloidal velocity of the mode in the laboratory frame v_{lab}, but in fact only negative values are measured, corresponding to a propagation in electron diamagnetic direction (EDD). The precursor mode reaches the highest laboratory velocities just before the transition to the H-mode.

As described above, the phase velocity of the mode in the plasma frame v_{ph} is decisive for the identification of the underlying instability. Therefore we have to compare the measured laboratory velocity with the background $E \times B$ background velocity in order to obtain the phase velocity (Eq. 3.50). Taking this into account, results in a QCM propagating in the opposite direction, i.e. in the ion diamagnetic direction (IDD), at about $1/2 v_{\mathrm{i,dia}}$. In contrast, the precursor mode and the WCM propagate in EDD in the plasma frame. However, the precursor seems to move faster, since v_{ph} of the precursor is the electron diamagnetic velocity $v_{\mathrm{e,dia}}^{\mathrm{p_e}}$, including the pressure gradient (Eq. 7.2), while v_{ph} of the WCM is $v_{\mathrm{e,dia}}^{\mathrm{n_e}}$ (Eq. 7.1), which according to the drift wave theory (Sec. 3.2.1) includes only the density gradient.

As mentioned above, we can estimate the radial electrostatic transport Γ_{r} of the modes using the phase velocities v_{ph}. To do this, we consider the last factor of Eq. 3.54 that contains v_{ph}, i.e. $\sqrt{1 - \left| v_{\mathrm{ph}} / \left(\left| \tilde{\phi} \right| \nabla n_0 / \left(|\tilde{n}_{\mathrm{e}}| B_{\mathrm{t}} \right) \right) \right|^2}$. This factor is close to zero if the phase velocity approaches the electron diamagnetic velocity $v_{\mathrm{e,dia}}$. According to this, we argue that the QCM causes a significant amount of transport since the phase velocity sufficiently deviates enough from $v_{\mathrm{e,dia}}$. Moreover, the I-phase precursor does

not seem to cause any transport, although it should be noted that we have seen clear evidence that the precursor might change its underlying instability and thus induce sufficient transport, which we then measure as the LCO bursts (see Sec. 6.6). The WCM seems to give rise to only little radial transport, as the phase velocity seems to deviate slightly from $v_{\mathrm{e,dia}}$.

Moreover, both the QCM and the I-phase precursor are found to be deep in the electromagnetic (EM) regime and they consistently exhibit EM signatures in magnetic probes, which the WCM does not feature, at least not in AUG plasmas.

In conclusion, from all the observations we can state that the quasi-coherent mode as it appears in EDA H-mode and the QCE regime is an electromagnetic ballooning mode. Whether it is an ideal (Sec. 3.1.1), resistive (Sec. 3.1.2) or kinetic ballooning mode (Sec. 3.2.5) is difficult to clarify experimentally. Consistently, the ballooning mode property can play its intended role with respect to the necessary radial transport, thus leading to the absence of ELMs. The precursor mode observed in the I-phase seems to be an electromagnetic drift wave-like instability, which is either a kinetic peeling-ballooning mode (Sec. 3.1.3) or a (micro-)tearing mode (Sec. 3.2.6), neither of which should cause high levels of electrostatic radial transport according to theory. However, we have found evidence that the precursor may change its underlying nature, in particular shown as the limit cycle oscillations (Sec. 6.1), i.e. the low frequency type-III ELM-like mode of the I-phase, which causes ELM-like transport and correlates with elevated values of the turbulence parameter α_{T} pointing to an interchange-like contribution. The role of the WCM is ambiguous, as it appears to be a drift-wave, trapped electron mode (Sec. 3.2.4), micro-tearing mode, or kinetic peeling-ballooning mode, thus causing little transport according to theory and no other edge phenomenon consistently appears during the I-mode.

8.2 Outlook

As stated in Chapter 2, resonant magnetic perturbation coils (RMPs) will be used in ITER to suppress type-I ELMs, which is an alternative approach to avoid type-I ELMs by means of an external actuator. Like in natural type-I ELM-free scenarios, the RMP plasmas likewise exhibit a characteristic edge mode [219, 220]. Therefore, it would be interesting to dedicate a series of experiments to the combination of RMPs and natural type-I ELM-free regimes, as this could possibly protect the machine even more reliably against type-I ELMs. Moreover, we have seen in Sec. 2.3 that the X-point radiator regime is also of high importance, since it naturally combines excellent detachment control and avoidance of ELMs at decent confinement. In this regime, no edge mode has yet been observed. The question that arises from the lack of observation of an edge

mode is whether there really is no edge mode, and what else might cause the absence of type-I edge localized modes then. A series of experiments focusing on the plasma edge of the X-point radiator regime is recommended.

Furthermore, more plasma parameter dependent analyses of the mode properties are especially needed for the weakly-coherent mode and the I-phase precursor mode. In the case of the weakly-coherent mode, in particular, the dependence of its phase velocity on different values of collisionality or turbulence parameter α_{T} needs to be investigated, as the underlying instability could also change here, similar to the precursor mode. To definitively reveal the change in the nature of the I-phase precursor mode, we need to study the plasma properties and the properties of the mode within its lifetime, i.e. $\tau_{\mathrm{L}} \sim \mathcal{O}\,(100\,\mu\mathrm{s})$. This investigation might be possible with the thermal helium beam alone, as it measures all required quantities on a sufficiently small time scale.

An analysis of the modulating pedestal mode or 'fork' mode (Sec. 6.1) in the H-mode that follows the I-phase is also advisable in order to assess if this mode is coupled to the emergence of the I-phase precursor.

In general, the ultimate goal has always been to be able to predict the ELM-free regimes in future fusion reactors. For this purpose, the reason for the absence of type-I ELMs, i.e. the edge modes, have to be extrapolated to the larger future fusion reactors ITER and DEMO. This extrapolation is only possible with the help of simulation codes which, in a first step, must reflect the many dependencies of the various edge mode properties presented in this work. Only when these properties have been verified by simulation, it is possible to predict the achievability of the respective regime in future reactors. A potential quantitative comparison of the found experimental results with magnetohydrodynamic codes like CASTOR3D [221] and gyro kinetic codes like GENE [128], GENE-X [222] and GRILLIX [223] are envisaged. However, any comparison of advanced edge turbulence or MHD models with the experimental results of this work will improve the predictability of fusion reactor plasmas and thus provide a more reliable path to fusion energy on Earth.

Appendix

A Mathematical Description of Ideal Ballooning Modes

In the following we assume that ideal ballooning modes are driven by the interchange mechanism and therefore the interchange instability will be discussed in the following.

The first part describes the propagation of ideal ballooning modes without kinetic effects. The second part includes finite Larmor radius (FLR) effects, which changes the propagation velocity of ideal ballooning modes in the plasma frame.

Propagation of Ideal Ballooning Modes

The following derivation bases on Ref. [224], but with modifications, since in the reference the velocity of blobs is derived.

In magnetohydrodynamics one typically assumes the conservation of the electrical current $\boldsymbol{j}$, or in other words: the divergence of the orthogonal currents balance that of the parallel currents, i.e.

$$-\nabla_\perp \cdot \boldsymbol{j}_\perp = \nabla_\parallel j_\parallel. \tag{A.1}$$

The orthogonal current consists of the generalized polarization drift and the diamagnetic currents. In the following, we assume cold ions, i.e. $p_\mathrm{i} = 0$ and concentrate only on the electrons. We obtain [225]

$$\nabla_\perp \cdot \left(\frac{\partial}{\partial t} \frac{\rho_\mathrm{m}}{B^2} \nabla_\perp \phi + \frac{\nabla p_\mathrm{e} \times \boldsymbol{B}}{B^2} \right) = \nabla_\parallel j_\parallel, \tag{A.2}$$

where $\rho_\mathrm{m} = m_\mathrm{i} n_0$ is the mass density. It can be shown that the divergence of the diamagnetic current (second term on the LHS) is related to the magnetic curvature, i.e.

$$\nabla_\perp \cdot \boldsymbol{j}_\mathrm{dia} = \nabla_\perp \cdot \left(\frac{\boldsymbol{B} \times \nabla p_\mathrm{e}}{B^2} \right) = -\frac{2}{B \lambda_\mathrm{B}} \nabla_\perp p_\mathrm{e}, \tag{A.3}$$

where $\lambda_\mathrm{B} = -B/\partial_\mathrm{x} B$. Substituting this relation into Eq. A.2, we get

$$\frac{\partial}{\partial t} \frac{\rho}{B^2} \nabla_\perp^2 \phi + \frac{2}{B \lambda_\mathrm{B}} \nabla_\perp p_\mathrm{e} = \nabla_\parallel j_\parallel. \tag{A.4}$$

From the relation $\boldsymbol{E} = -\nabla\phi$ and by means of Fig. 3.3b we see that the relevant electric field points in $y-$direction, i.e. we only have to consider the derivative in the $y-$direction. The $E \times B$ velocity in the $x-$direction is given by $v_\mathrm{x} = -\partial_\mathrm{y}\phi/B$, leading to

$$-\frac{\partial}{\partial t}\frac{\rho}{B}\frac{\partial}{\partial y}v_\mathrm{x} + \frac{2}{B\lambda_\mathrm{B}}\nabla_\perp p_\mathrm{e} = \nabla_\parallel j_\parallel. \tag{A.5}$$

Now we linearize the equation using the wave ansatz of the form $p_\mathrm{e} = p_\mathrm{e0} + \tilde{p}_\mathrm{e} = p_\mathrm{e0} + p_\mathrm{e1}\exp\left(i\left(\boldsymbol{kr} - \omega t\right)\right)$. The index 0 indicates equilibrium quantities and $\tilde{p_\mathrm{e}}$ the perturbed one, and the wavenumber $\boldsymbol{k} = \left(k_\mathrm{x}, k_\mathrm{y}, k_\parallel\right)^T$. We set the velocity in the equilibrium to zero. We assume that the pressure fluctuation corresponds to the density fluctuation, i.e. $\tilde{p}_\mathrm{e} = T_\mathrm{e}\tilde{n}_\mathrm{e}$. Furthermore, we consider in the first-order only derivatives in the $y-$direction, since we assume that the wavenumbers $k_\mathrm{x} \ll 1$ and $k_\parallel \ll 1$ are very small. So we get

$$i\omega\frac{\rho}{B}ik_\mathrm{y}v_\mathrm{x} + \frac{2}{B\lambda_\mathrm{B}}ik_\mathrm{y}T_\mathrm{e}\tilde{n}_\mathrm{e} = 0. \tag{A.6}$$

The last step is to clarify how we can describe the density fluctuation. For this we use the first order continuity equation and get

$$\frac{\partial\tilde{n}_\mathrm{e}}{\partial t} + v_\mathrm{x}\frac{\partial n_\mathrm{e0}}{\partial x} = 0 \Longleftrightarrow \tilde{n}_\mathrm{e} = i\frac{n_\mathrm{e0}v_\mathrm{x}}{\omega\lambda_{\mathrm{n_e}}}, \tag{A.7}$$

where $\lambda_{\mathrm{n_e}} = -n_\mathrm{e0}/\partial_\mathrm{x}n_\mathrm{e0}$. Inserting the density fluctuation into Eq. A.6 leads to the following expression

$$\omega\frac{\rho}{B}k_\mathrm{y}v_\mathrm{x} + \frac{2}{B\lambda_\mathrm{B}}k_\mathrm{y}T_\mathrm{e}\frac{n_\mathrm{e0}v_\mathrm{x}}{\omega\lambda_{\mathrm{n_e}}} = 0. \tag{A.8}$$

Finally, we can rearrange according to the frequency of the instability and obtain

$$\omega = i\sqrt{\frac{2T_\mathrm{e}}{\lambda_\mathrm{B}\lambda_{\mathrm{n_e}}m_\mathrm{i}}}, \tag{A.9}$$

where we have used that $\rho = m_\mathrm{i}n_\mathrm{e0}$. We see that the frequency is pure imaginary and hence, ideal ballooning modes do not propagate in the plasma frame and are just a purely growing mode.

Finite Larmor Radius Effects on Ideal MHD

As already explained in Sec. 3.1.1, ideal ballooning modes (IBMs) propagate in the plasma frame at exactly $v_\mathrm{ph} = 1/2v_\mathrm{i,dia}$, where $v_\mathrm{i,dia}$ is the diamagnetic velocity of the ions. This relationship is derived mathematically below and is based entirely on Ref. [226]. To obtain the desired result, we start with an extensive treatment of the resistive magnetohydrodynamics (MHD) and end with the limit for the ideal MHD. Therefore, we assume that all non-MHD effects and ion inertia are important within a 'singular'

layer around r_0. Outside this layer the plasma is described by ideal MHD.

The MHD equations from Sec. 3.1 form the basis of the calculation, i.e.

$$\frac{\partial n_\alpha}{\partial t} + \nabla \cdot (n_\alpha \boldsymbol{v}_\alpha) = 0, \tag{A.10}$$

$$m_\alpha n_\alpha \left(\frac{\partial \boldsymbol{v}_\alpha}{\partial t} + (\boldsymbol{v}_\alpha \cdot \nabla)\, \boldsymbol{v}_\alpha \right) = -\nabla p_\alpha - \nabla \cdot \overleftrightarrow{\pi} + q_\alpha n_\alpha \left(\boldsymbol{E} + \boldsymbol{v} \times \boldsymbol{B} \right) + \overleftrightarrow{R}_\alpha. \tag{A.11}$$

We also need the energy balance equation, i.e.

$$\frac{3}{2} n_\alpha \left(\frac{\partial T_\alpha}{\partial t} + (\boldsymbol{v}_\alpha \cdot \nabla)\, T_\alpha \right) + p_\alpha \nabla \cdot \boldsymbol{v}_\alpha = 0, \tag{A.12}$$

and the two Maxwell equations

$$\nabla \times \boldsymbol{E} = -\frac{\partial \boldsymbol{B}}{\partial t}, \tag{A.13}$$

$$\nabla \times \boldsymbol{B} = \mu_0 \boldsymbol{j}. \tag{A.14}$$

Here $\alpha = e, i$ denotes the particle species (electrons, ions), n_α is the particle density, v_α is the fluid density, m_α is the mass, p_α is the scalar pressure, q_α is the electric charge, T_α is the temperature, $\boldsymbol{j} = en(\boldsymbol{v}_\mathrm{i} - \boldsymbol{v}_\mathrm{e})$ is the total current density, $\overleftrightarrow{\pi}$ is the stress tensor and $\overleftrightarrow{R}_\alpha$ represents the collisional momentum transfer. $\boldsymbol{E}$ and $\boldsymbol{B}$ represent the electric and magnetic field and μ_0 is the magnetic permeability. We see that the force balance in Eq. A.11 also includes the ion stress and collisional momentum tensor, compared to Eq. 3.5, which are crucial for the next calculations.

Combining the equations of motions for electrons and ions and neglecting the electron inertia and electron stress tensor (which is usually valid when electron-ion collisions are sufficiently frequent), we get equation of motion of the plasma as follows

$$\rho \left(\frac{\partial \boldsymbol{v}_\mathbf{i}}{\partial t} + (\boldsymbol{v}_\mathbf{i} \cdot \nabla)\, \boldsymbol{v}_\mathbf{i} \right) = -\nabla p - \nabla \overleftrightarrow{\pi}_\mathrm{i} + (\boldsymbol{j} \times \boldsymbol{B}). \tag{A.15}$$

$\rho = m_\mathrm{i} n$ is the plasma mass density and $p = p_\mathrm{e} + p_\mathrm{i}$ is the total pressure. Moreover, it is important to know that $\overleftrightarrow{R}_\mathrm{i} = -\overleftrightarrow{R}_\mathrm{e}$ and only the ion stress tensor $\overleftrightarrow{\pi}_\mathrm{i}$ is included now, which can be looked up in Ref. [227] for instance.

Analogously, one can calculate the electron equation of motion, using $\overleftrightarrow{R}_\mathrm{e} = en\left(\eta_\parallel \boldsymbol{j}_\parallel + \eta_\perp \boldsymbol{j}_\perp\right) - 0.71 n \nabla_\parallel T_\mathrm{e}$, yielding the generalized Ohm's law

$$\eta_\parallel \boldsymbol{j}_\parallel + \eta_\perp \boldsymbol{j}_\perp = \boldsymbol{E} + \boldsymbol{v}_\mathrm{e} \times \boldsymbol{B} + \frac{\nabla p_\mathrm{e}}{en} + 0.71/e \nabla_\parallel T_\mathrm{e}. \tag{A.16}$$

η is the electrical resistivity and $\parallel$ and $\perp$ denote the parallel and perpendicular com-

ponents with respect to the magnetic field.

Now we assume a perturbation in all quantities of the form $\boldsymbol{B} = \boldsymbol{B}_0 + \boldsymbol{B}_1 \exp(i\boldsymbol{kr} - i\omega t)$, where $\boldsymbol{B}_1$ represents the perturbed quantity, $\boldsymbol{B}_0$ the background value, $\boldsymbol{k} = (k_\mathrm{r}, k_\theta, k_\mathrm{z})^T$ is the wavenumber and ω is the frequency of the perturbation in the plasma frame. The first-order of the plasma equation of motion (Eq. A.15) in radial direction yields then

$$-i\omega\rho v_{\mathrm{i1r}} = -\frac{d}{dr}\left(p_1 + (\boldsymbol{B_0 B_1})/\mu_0\right) + iF(r)B_{1\mathrm{r}} - \frac{2B_\theta B_{1\theta}}{\mu_0 r} + \mu_\perp \frac{d^2 v_{i1r}}{dr^2}. \tag{A.17}$$

In particular, Maxwell's equation A.14 has to be evaluated in cylindrical coordinates and $\boldsymbol{B_0 B_1} = B_z B_{1z} + B_\theta B_{1\theta}$ ($B_\mathrm{r} = 0$). In addition, we introduced $F(r) = \boldsymbol{kB_0}/\mu_0 = (mB_\theta/r + k_\mathrm{z} B_\mathrm{z})/\mu_0$ (we used $k_\theta = m/r$) to combine contributions in B_z and B_θ, and $\mu_\perp = 0.3 n T_\mathrm{i}/\Omega_\mathrm{i}^2 \tau_\mathrm{i}$ is the transverse collisional viscosity coefficient, coming from the ion stress tensor. Ω_i is the ion gyrofrequency and τ_i is the ion-ion collision time.

Taking two times the radial derivative of the Eq. A.17 leads to the vanishing of the first, second and fourth term on the right hand side. We obtain

$$\rho\left(\omega - i\frac{\mu_\perp}{\rho}\frac{d^2}{dr^2}\right)\frac{d^2}{dr^2} v_{\mathrm{i1r}} = -F(r)\frac{d^2}{dr^2} B_{1\mathrm{r}}. \tag{A.18}$$

Now we introduce the radial displacement via $v_{\mathrm{i1r}} = -i(\omega - \omega_{\mathrm{i}\star})\xi$, where $\omega_{\mathrm{i}\star} = -k_\theta dp_{\mathrm{i0}}/dr/(eB_0)$ evaluated at $r = r_0$ ('singular' layer) is the ion diamagnetic frequency and we obtain the first important equation:

$$\boxed{i\rho(\omega - \omega_{\mathrm{i}\star})\left(\omega - i\frac{\mu_\perp}{\rho}\frac{d^2}{dr^2}\right)\frac{d^2\xi}{dr^2} = F(r)\frac{d^2}{dr^2} B_{1\mathrm{r}}.} \tag{A.19}$$

For the second important equation, we need to investigate the equation of motion for the electrons, i.e. Eq. A.16 and need to linearize the radial component of Eqs. A.13 and A.14. We obtain

$$i(\omega - \hat{\omega}_{\mathrm{e}\star}) B_{1\mathrm{r}} = -iF(r) v_{\mathrm{e1r}} - \frac{0.71}{eB_0 r} F(r) T_{\mathrm{e1}} - \eta_\parallel \frac{d^2}{dr^2} B_{1\mathrm{r}}. \tag{A.20}$$

Here, the electron diamagnetic frequency $\omega_{\mathrm{e}\star} = k_\theta dp_{\mathrm{e0}}/dr/(enB_0)$ is included in $\hat{\omega}_{\mathrm{e}\star} = \omega_{\mathrm{e}\star} + 0.71 k_\theta dT_{\mathrm{e0}}/dr/(enB_0)$, evaluated at $r = r_0$. Using the electron energy balance equation (Eq. A.12), we get

$$T_{\mathrm{e1}} = -i\frac{dT_{\mathrm{e0}}/dr}{\omega - \omega_{e\star}} v_{\mathrm{e1r}}. \tag{A.21}$$

We once again introduce the radial displacement, which is similar to the one above

due to quasi-neutrality, i.e. $v_{\mathrm{e1r}} = -i\left(\omega - \omega_{\mathrm{e}^\star}\right)\xi$. Combining Eqs. A.20 and A.21 we further get

$$B_{1\mathrm{r}} = iF(r)\xi + i\eta_{\parallel}\frac{1}{\omega - \hat{\omega}_{\mathrm{e}^\star}}\frac{d^2}{dr^2}B_{1\mathrm{r}}, \tag{A.22}$$

which is the second important equation to describe our physical system.

To get the physics out of the 'singular' layer, in which the non-MHD effects and ion inertia are included, we introduce the dimensionless variable $x = (r - r_0)/r_0$ and define further $\lambda = -i\omega\tau_{\mathrm{H}}$, $\lambda_{\mathrm{i}} = -\omega_{\mathrm{i}^\star}\tau_{\mathrm{H}}$, $\lambda_{\mathrm{e}} = -\hat{\omega}_{\mathrm{e}^\star}\tau_{\mathrm{H}}$ and $\psi = iB_{1\mathrm{r}}/\left(rdF/dr\right)|_{r=r_0}$. Here, $\tau_{\mathrm{H}} = r_0/v_{\mathrm{A}\theta}$ is the typical Alfvén time, featuring the Alfvén velocity $v_{\mathrm{A}\theta} = B/\left(\mu_0\rho\right)$, evaluated at $r = r_0$. Expanding $F(r)$ around r_0, using $F(r_0) = 0$ ($k_{\mathrm{z}} = B_\theta/\left(B_{\mathrm{z}}r_0\right)$ is valid there) and inserting the dimensionless variables into Eq. A.19 and A.22, we obtain the following set of equations:

$$\left(\lambda - i\lambda_{\mathrm{i}}\right)\left(\lambda\xi'' - D\xi''''\right) = x\psi'', \tag{A.23}$$

$$\psi = -x\xi + \frac{\varepsilon}{\lambda - i\lambda_{\mathrm{e}}}\psi''. \tag{A.24}$$

These are the 'singular' layer equations. Here $'$ denotes the derivative with respect to x and $D = \mu_\perp\tau_{\mathrm{H}}/\left(\rho r_0^2\right)$ represents the diffusion coefficient for the transverse ion momentum due to ion-ion collisions. Moreover, $\varepsilon = \tau_{\mathrm{H}}/\tau_{\mathrm{r}}$ is the resistivity coefficient, where $\tau_{\mathrm{r}} = \mu_0 r_0^2/\eta$ is the resistive diffusion time. If one had done the whole calculation without keeping the ion stress tensor $\overleftrightarrow{\pi}_{\mathrm{i}}$ and the collisional momentum transfer tensor $\overleftrightarrow{R}_{\mathrm{e}}$, one would have obtained equations similar to those above, but with one crucial difference: there $\lambda_{\mathrm{i}} = \lambda_{\mathrm{e}} = D = 0$ is valid.

However, we will set $D = 0$ in the following as a limiting case for the sake of simplification. Now we introduce the generating function

$$\chi(x) = x\psi' - \psi = \lambda\left(\lambda - i\lambda_{\mathrm{i}}\right)\xi' + \chi_\infty, \tag{A.25}$$

to solve the derived set of equations. Using this ansatz, Eq. A.23 is fulfilled instantaneously, but Eq. A.24 changes to [226]

$$\chi'' - 2\frac{\chi'}{x} - \left(\frac{\lambda - i\lambda_{\mathrm{e}}}{\varepsilon} + \frac{\lambda - i\lambda_{\mathrm{e}}}{\varepsilon\lambda\left(\lambda - i\lambda_{\mathrm{i}}\right)}x^2\right)\chi + \frac{\lambda - i\lambda_{\mathrm{e}}}{\varepsilon\lambda\left(\lambda - i\lambda_{\mathrm{i}}\right)}\chi_\infty x^2 = 0. \tag{A.26}$$

Obviously, the solutions in the 'singular' layer have to match the MHD solutions, which are valid outside the 'singular' layer. Ref. [226] shows that the condition to match these MHD solutions is

$$\chi_\infty = \frac{2}{\pi}\lambda_{\mathrm{H}}\int_0^\infty dx\frac{\chi'}{x}, \tag{A.27}$$

which is not straightforward to solve. Here $\lambda_{\mathrm{H}} \sim r_0^2/R_{\mathrm{maj}}^2$ is a parameter that describes the growth rate of an ideal MHD instability. If $\lambda_{\mathrm{H}} = 0$, the plasma is stable against ideal MHD modes. Transforming the coordinates from $x \to \hat{x} = x/\delta$, where

$$\delta = \left(\varepsilon\lambda \frac{\lambda - i\lambda_{\mathrm{i}}}{\lambda - i\lambda_{\mathrm{e}}}\right)^{1/4}, \tag{A.28}$$

yields the following differential equation

$$\frac{d^2\chi}{d\hat{x}^2} - \frac{2}{\hat{x}}\frac{d\chi}{d\hat{x}} - \left(\hat{x}^2 + \Lambda^{3/2}\right)\chi = -\hat{x}^2\chi_\infty. \tag{A.29}$$

Here we introduced

$$\Lambda = \left(\hat{\lambda}\left(\hat{\lambda} - i\hat{\lambda}_{\mathrm{e}}\right)\left(\hat{\lambda} - i\hat{\lambda}_{\mathrm{i}}\right)\right)^{1/3}, \tag{A.30}$$

where $\hat{\lambda} = \lambda/\varepsilon^{1/3}$ and $\hat{\lambda}_{\mathrm{e,i}} = \lambda_{\mathrm{e,i}}/\varepsilon^{1/3}$ are connected to the resistivity parameter from above. Via the usage of Laguerre Polynomials we can show that the following expression is a solution of Eq. A.29 [226]:

$$\frac{\chi}{\chi_\infty} = 1 - \frac{\Lambda^{3/2}}{2}\int_0^1 dt\,(1-t)^{\left(\Lambda^{3/2}-5\right)/4}(1+t)^{-\left(\Lambda^{3/2}+5\right)/4}e^{-0.5t\hat{x}^2}. \tag{A.31}$$

Now we have to solve the integral from Eq. A.27 using the solution from Eq. A.31 to get an eigenvalue equation. First we can use the Feynman trick to differentiate under the integral and obtain the double integral, which can be solved via a smart application like WOLFRAM ALPHA[1], i.e.

$$\int_0^1\int_0^\infty t\,(1-t)^{\left(\Lambda^{3/2}-5\right)/4}(1+t)^{-\left(\Lambda^{3/2}+5\right)/4}e^{-0.5t\hat{x}^2}d\hat{x}dt = \frac{\pi\Gamma\left(\left[\Lambda^{3/2}-1\right]/4\right)}{8\Gamma\left(\left[\Lambda^{3/2}+5\right]/4\right)}, \tag{A.32}$$

provided that $\Re\left(\Lambda^{3/2}\right) > 1$. Another factor in the equation reduces to

$$\frac{\Lambda^{3/2}}{\delta} = \frac{\left(\hat{\lambda}\left(\hat{\lambda} - i\hat{\lambda}_{\mathrm{e}}\right)\left(\hat{\lambda} - i\hat{\lambda}_{\mathrm{i}}\right)\right)^{1/2}}{\left(\varepsilon^{4/3}\hat{\lambda}\left(\hat{\lambda} - i\hat{\lambda}_{\mathrm{i}}\right)/\left(\hat{\lambda} - i\hat{\lambda}_{\mathrm{e}}\right)\right)^{1/4}} = \frac{\Lambda^{9/4}}{\sqrt{\hat{\lambda}\left(\hat{\lambda} - i\hat{\lambda}_{\mathrm{i}}\right)}}\frac{1}{\varepsilon^{1/3}}. \tag{A.33}$$

With this we get the following dispersion relation

$$\boxed{\sqrt{\hat{\lambda}\left(\hat{\lambda} - i\hat{\lambda}_{\mathrm{i}}\right)} = \frac{\hat{\lambda}_{\mathrm{H}}}{8}\Lambda^{9/4}\frac{\Gamma\left(\left[\Lambda^{3/2}-1\right]/4\right)}{\Gamma\left(\left[\Lambda^{3/2}+5\right]/4\right)}.} \tag{A.34}$$

Although we have included resistivity the whole time, we will now look at the ideal

[1] `https://www.wolframalpha.com`, accessed: 04.06.24

MHD case, i.e. $\varepsilon \to 0$. This leads to really large values of $\hat{\lambda}$, $\hat{\lambda}_\mathrm{i}$ and Λ, i.e. $\Lambda \gg 1$. With this we can approximate the gamma function in the following way

$$\frac{\Gamma\left(\Lambda^{3/2}/4 - 1/4\right)}{\Gamma\left(\Lambda^{3/2}/4 + 5/4\right)} \overbrace{=}^{z=\Lambda^{3/2}/4-1/4} \frac{\Gamma(z)}{\Gamma(z+3/2)} \to z^{-3/2} \approx \frac{8}{\Lambda^{9/4}}. \tag{A.35}$$

This reduces Eq. A.34 to a simple expression, i.e.

$$\lambda\left(\lambda - i\lambda_\mathrm{i}\right) = \lambda_\mathrm{H}^2. \tag{A.36}$$

Now we can solve the quadratic equation in λ and obtain the following positive solution

$$\lambda = \lambda_\mathrm{H}\sqrt{1 - \frac{\lambda_\mathrm{i}^2}{4\lambda_\mathrm{H}^2}} + i\frac{\lambda_\mathrm{i}}{2} \approx \lambda_\mathrm{H}\left(1 - \frac{\lambda_\mathrm{i}^2}{8\lambda_\mathrm{H}^2}\right) + i\frac{\lambda_\mathrm{i}}{2}. \tag{A.37}$$

With the definition for $\lambda = -i\omega\tau_\mathrm{H}$ and $\lambda_\mathrm{i} = -\omega_{\mathrm{i}^\star}\tau_\mathrm{H}$, we see that the imaginary part in Eq. A.37 corresponds to the real part for the frequency of the mode and hence its propagation, we get:

$$\boxed{\omega = \frac{\omega_{\mathrm{i}^\star}}{2}.} \tag{A.38}$$

This corresponds to a propagation of the mode in ion diamagnetic direction, with a phase velocity of $v_\mathrm{ph} = 1/2 v_\mathrm{i,dia}$, where we used $\omega = k_\theta v_\mathrm{ph}$ and $\omega_{\mathrm{i}^\star} = k_\theta v_\mathrm{i,dia}$.

B Discharges

In Tab. B.1 all single discharges analysed are displayed with various quantities like toroidal magnetic field strength B_t, plasma current I_p, edge safety factor q_{95} and heating powers P for electron and ion cyclotron heating (ECRH, ICRH) and neutral beam injection (NBI). Additionally, the regime of the corresponding discharge, i.e. EDA H-mode (Sec. 2.2.1, QCE (Sec. 2.2.2)[2], I-phase (Sec. 2.2.3) or I-mode (2.2.4), the number of the corresponding edge mode data points acquired from each shot and the radial position of the mode, $\rho_\mathrm{pol}^\mathrm{LOC}$, are shown. The discharge #40110 is shown in Fig. 5.3 as a transition discharge, starting in EDA H-mode and ending in QCE.

[2]EDA H-mode and QCE are separated according to Eq. 5.4.

Table B.1: Analyzed Discharges and Corresponding Parameters

The discharge number, the corresponding regime, the number collected data points, the availability of the 5×5 THB grid, the toroidal magnetic field strength B_t, the plasma current I_p, the edge safety factor q_{95}, the input ECRH (P_{ECRH}), ICRH (P_{ICRH}) and NBI (P_{NBI}) heating powers and the radial position, where we localize the corresponding mode ρ_{pol}^{Loc} according to the method described in Sec. 4.4 are shown.

Discharge	Regime	#data points	5×5 Grid	B_t [T]	I_p [MA]	q_{95}	P_{ECRH} [MW]	P_{ICRH} [MW]	P_{NBI} [MW]	ρ_{pol}^{Loc}
#36124	EDA	52	No	2.50	0.79	5.30	3.0	0.0	0.0	0.998±0.007
#38067	EDA	37	Yes	2.50	0.70	5.61	3.5	0.0	0.0	0.990±0.006
#39400	QCE	22	Yes	2.50	0.71	5.66	3.5	0.0	2.5	0.995±0.007
#39404	EDA	15	Yes	2.50	0.71	5.61	2.4	0.0	Blip	0.989±0.009
#39541	QCE	16	Yes	2.45	0.82	4.87	2.4	0.0	2.5	0.995±0.008
#39605	QCE	16	Yes	1.90	1.09	3.20	0.2	3.7	5.0	0.995±0.009
#39666	EDA	23	Yes	2.50	0.60	6.48	1.4	0.0	2.5	0.988±0.006
#40110	EDA/QCE	28	No	2.51	0.71	5.61	3.5	3.7	Blip	0.992±0.010
#40226	QCE	17	Yes	1.90	1.10	3.21	0.0	3.8	4.1	0.995±0.006
#40227	QCE	7	Yes	1.90	1.08	3.21	0.0	3.9	4.1	0.994±0.007
#40613	QCE	11	Yes	2.50	0.81	5.49	4.4	0.0	5.0	0.995±0.006
#40637	QCE	35	No	2.50	0.80	5.52	4.4	0.0	5.0	0.993±0.008
#40647	EDA	65	Yes	2.52	0.60	6.63	1.9	0.0	0.0	0.989±0.007
#35711	I-Phase	24	No	1.8	0.81	3.80	0.0	0.0	1.86	0.982±0.005
#37500	I-Phase	30	No	1.9	0.79	4.08	0.7	0.0	0.0	0.986±0.006
#37623	I-Phase	33	No	2.5	0.82	5.12	2.8	0.0	0.0	0.985±0.007
#38375	I-Phase	32	Yes	2.5	0.80	5.09	0.8	0.0	0.0	0.984±0.005
#38997	I-Phase	11	Yes	2.5	0.79	4.74	0.4	0.0	0.0	0.982±0.006
#40055	I-Phase	19	No	2.5	0.50	7.82	0.8	0.0	2.6	0.980±0.005
#40314	I-Phase	13	Yes	2.4	0.80	4.65	1.7	0.0	5.7	0.981±0.006
#37916	I-Mode	N/A	No	2.5	1.01	3.49	1.6	0.0	4.1	0.990±0.004
#37980	I-Mode	N/A	No	2.5	1.01	3.92	3.4	0.0	2.2	0.992±0.004
#37982	I-Mode	N/A	No	2.5	1.00	3.62	1.4	0.0	3.1	0.991±0.004
#37983	I-Mode	N/A	No	2.5	1.00	4.05	2.2	0.0	2.6	0.995±0.006
#38091	I-Mode	N/A	Yes	2.5	0.99	3.94	1.5	0.0	2.6	0.989±0.006
#38493	I-Mode	N/A	Yes	2.5	1.00	3.93	1.5	0.0	3.0	0.994±0.004

List of Figures

Bibliography

1. *1950: What the scientists are saying about the H-bomb* https://thebulletin.org/premium/2020-12/1950-what-the-scientists-are-saying-about-the-h-bomb/. Accessed: 20.04.2024. 2020.
2. Rhodes, R. *Dark sun: the making of the hydrogen bomb* en. ISBN: 0-684-80400-2 (Simon & Schuster Paperbacks, 1996).
3. Rhodes, R. *The making of the atomic bomb* en. ISBN: 0-671-44133-7 (Simon & Schuster Paperbacks, 2012).
4. Edenhofer, O. *et al. Renewable Energy Sources and Climate Change Mitigation Special Report of the Intergovernmental Panel on Climate Change* en. ISBN: 978-1-107-02340-6 (Cambridge University Press, 2012).
5. IEA. *World Energy Outlook 2022* https://www.iea.org/reports/world-energy-outlook-2022. Accessed: 23.04.2024. 2022.
6. (Spektrum), A. K.-S. *Fusionsforschung: Der Reaktionsparameter oder "Warum eigentlich Deuterium + Tritium ?"* https://scilogs.spektrum.de/formbar/fusionsforschung-der-reaktionsparameter-oder-warum-eigentlich-deuterium-tritium/. Accessed: 23.04.2024. 2016.
7. Harwit, M. *Astrophysical Concepts: Fourth Edition* en. ISBN: 0-387-32943-9 (Springer, 2006).
8. Hund, F. Zur Deutung der Molekelspektren. III. Bemerkungen über das Schwingungs- und Rotationsspektrum bei Molekeln mit mehr als zwei Kernen. *Zeitschrift für Physik* **43,** 805–826. doi:10.1007/BF01397249 (1927).
9. Adelberger, E. G. *et al.* Solar fusion cross sections. II. The *pp* chain and CNO cycles. *Rev. Mod. Phys.* **83,** 195–245. doi:10.1103/RevModPhys.83.195 (1 2011).
10. Dux, R. *Vorlesungsskript: Plasmaphysik und Fusionsforschung, Teil II: Fusionsforschung* (Augsburg (Sommersemester 2010)).
11. Kaufmann, M. *Plasmaphysik und Fusionsforschung* (Springer Spektrum, 2013).
12. Stroth, U. *Plasmaphysik: Phänomene, Grundlagen und Anwendungen* de. ISBN: 978-3-662-55235-3 (Springer Spektrum, 2018).

13. Zohm, H. On the Use of High Magnetic Field in Reactor Grade Tokamaks. *Journal of Fusion Energy* **38.** doi:10.1007/s10894-018-0177-y (Feb. 2019).

14. Giancarli, L. *et al.* Overview of the ITER TBM program. *Fusion Engineering and Design* **87,** 395–402. doi:10.1016/j.fusengdes.2011.11.005 (May 2012).

15. Miyamoto, K. *Plasma Physics for Controlled Fusion* en. ISBN: 978-3-662-49780-4 (Springer-Verlag Berlin Heidelberg, 2016).

16. Einstein, A. *The Meaning of Relativity* en (Princeton Univ. Press, 1954, 1921).

17. Zylstra, A. *et al.* Burning plasma achieved in inertial fusion. *Nature* **601,** 542–548. doi:10.1038/s41586-021-04281-w (Jan. 2022).

18. Spitzer Lyman, J. The Stellarator Concept. *The Physics of Fluids* **1,** 253–264. ISSN: 0031-9171. doi:10.1063/1.1705883 (July 1958).

19. Lobner, P. *Return of the Stellarator* https://lynceans.org/tag/stellarator/. Accessed: 16 May 2024. 2020.

20. Shimada, M. *et al.* Overview and summary - ITER. *Nuclear Fusion* **47,** 01–17. doi:10.1088/0029-5515/47/6/S01 (2007).

21. Siccinio, M. *et al.* DEMO physics challenges beyond ITER. *Fusion Engineering and Design* **156,** 111603. doi:10.1016/j.fusengdes.2020.111603 (July 2020).

22. Kadomtsev, B. B. From MTR to ITER. *Physics-Uspekhi* **39,** 419. doi:10.1070/PU1996v039n05ABEH000143 (1996).

23. Shafranov, V. D. Equilibrium of a toroidal plasma in a magnetic field. *Journal of Nuclear Energy. Part C, Plasma Physics, Accelerators, Thermonuclear Research* **5,** 251. doi:10.1088/0368-3281/5/4/307 (1963).

24. Zohm, H. *Magnetohydrodynamic Stability of Tokamaks* en. ISBN: 978-3-527-41232-7 (Wiley-VCH Verlag GmbH Co. KGaA, 2015).

25. Wiki, F. *Triangularity* https://wiki.fusion.ciemat.es/wiki/Triangularity. Accessed: 16 May 2024.

26. Wagner, F. *et al.* Regime of Improved Confinement and High Beta in Neutral-Beam-Heated Divertor Discharges of the ASDEX Tokamak. *Phys. Rev. Lett.* **49,** 1408–1412. doi:10.1103/PhysRevLett.49.1408 (19 1982).

27. Mlynek, A. *et al.* Design of a digital multiradian phase detector and its application in fusion plasma interferometry. *Review of Scientific Instruments* **81,** 033507. ISSN: 0034-6748. doi:10.1063/1.3340944 (Mar. 2010).

28. Manz, P. The Microscopic Picture of Plasma Edge Turbulence. *Habilitation Thesis* (2018).

29. Eich, T. *et al.* ELM divertor peak energy fluence scaling to ITER with data from JET, MAST and ASDEX upgrade. *Nuclear Materials and Energy* **12.** Proceedings of the 22nd International Conference on Plasma Surface Interactions 2016, 22nd PSI, 84–90. ISSN: 2352-1791. doi:https://doi.org/10.1016/j.nme.2017.04.014 (2017).

30. Lawson, J. D. Some Criteria for a Power Producing Thermonuclear Reactor. *Proceedings of the Physical Society. Section B* **70,** 6. doi:10.1088/0370-1301/70/1/303 (1957).

31. Wenninger, R. *et al.* The physics and technology basis entering European system code studies for DEMO. *Nuclear Fusion* **57,** 016011. doi:10.1088/0029-5515/57/1/016011 (2016).

32. Koch, R. Plasma Heating by Neutral Beam Injection. *Fusion Science and Technology* **45,** 183–192. doi:10.13182/FST04-A482 (2004).

33. Ongena, J *et al.* Recent advances in physics and technology of ion cyclotron resonance heating in view of future fusion reactors. *Plasma Physics and Controlled Fusion* **59,** 054002. doi:10.1088/1361-6587/aa5a62 (2017).

34. Ott, E., Hui, B. & Chu, K. R. Theory of electron cyclotron resonance heating of tokamak plasmas. *The Physics of Fluids* **23,** 1031–1045. ISSN: 0031-9171. doi:10.1063/1.863085 (May 1980).

35. McCracken, G. & Stott, P. *Fusion: The Energy of the Universe* en. ISBN: 978-0123846563 (Academic Press, 2012).

36. Keilhacker, M. *et al.* High fusion performance from deuterium-tritium plasmas in JET. *Nuclear Fusion* **39,** 209. doi:10.1088/0029-5515/39/2/306 (1999).

37. Ikeda, K. Progress in the ITER Physics Basis. *Nuclear Fusion* **47,** E01. doi:10.1088/0029-5515/47/6/E01 (2007).

38. Siccinio, M. *et al.* Development of the plasma scenario for EU-DEMO: Status and plans. *Fusion Engineering and Design* **176,** 113047. ISSN: 0920-3796. doi:https://doi.org/10.1016/j.fusengdes.2022.113047 (2022).

39. Database, I. C. & (presented by J G Cordey), M. W. G. Energy confinement scaling and the extrapolation to ITER. *Plasma Physics and Controlled Fusion* **39,** B115. doi:10.1088/0741-3335/39/12B/009 (1997).

40. Verdoolaege, G. *et al.* The updated ITPA global H-mode confinement database: description and analysis. *Nuclear Fusion* **61,** 076006. doi:10.1088/1741-4326/abdb91 (2021).

41. Troyon, F., Gruber, R., Saurenmann, H., Semenzato, S. & Succi, S. MHD-Limits to Plasma Confinement. *Plasma Physics and Controlled Fusion* **26.** doi:10.1088/0741-3335/26/1A/319 (Jan. 1984).

42. Team, J. H., Team, E. H., of the IFERC Project Team, D. U., *et al. Second Intermediate Report of BA DEMO Design Activity* https://www.iferc.org/wp-content/uploads/2021/03/news-2017-12.pdf. Accessed: 15 May 2024. 2017.

43. Kruskal, M., Tuck, J. L. & Chandrasekhar, S. The instability of a pinched fluid with a longitudinal magnetic field. *Proceedings of the Royal Society of London. Series A. Mathematical and Physical Sciences* **245,** 222–237. doi:10.1098/rspa.1958.0079 (1958).

44. Rosenbluth, M. & Longmire, C. Stability of plasmas confined by magnetic fields. *Annals of Physics* **1,** 120–140. ISSN: 0003-4916. doi:https://doi.org/10.1016/0003-4916(57)90055-6 (1957).

45. Greenwald, M. *et al.* A new look at density limits in tokamaks. *Nuclear Fusion* **28,** 2199. doi:10.1088/0029-5515/28/12/009 (1988).

46. Hirshman, S. & Sigmar, D. Neoclassical transport of impurities in tokamak plasmas. *Nuclear Fusion* **21,** 1079. doi:10.1088/0029-5515/21/9/003 (1981).

47. Sauter, O., Angioni, C. & Lin-Liu, Y. Neoclassical conductivity and bootstrap current formulas for general axisymmetric equilibria and arbitrary collisionality regime. *Physics of Plasmas* **6,** 2834–2839. doi:10.1063/1.873240 (1999).

48. Viezzer, E. *et al.* Prospects of core-edge integrated no-ELM and small-ELM scenarios for future fusion devices. *Nuclear Materials and Energy* **34,** 101308. ISSN: 2352-1791. doi:https://doi.org/10.1016/j.nme.2022.101308 (2023).

49. Pitcher, C. S. & Stangeby, P. C. Experimental divertor physics. *Plasma Physics and Controlled Fusion* **39,** 779. doi:10.1088/0741-3335/39/6/001 (1997).

50. Leonard, A. W. Plasma detachment in divertor tokamaks. *Plasma Physics and Controlled Fusion* **60,** 044001. doi:10.1088/1361-6587/aaa7a9 (2018).

51. Martin, Y. R., Takizuka, T & the ITPA CDBM H-mode Threshold Database Working Group. Power requirement for accessing the H-mode in ITER. *Journal of Physics: Conference Series* **123,** 012033. doi:10.1088/1742-6596/123/1/012033 (2008).

52. Loarte, A *et al.* High confinement/high radiated power H-mode experiments in Alcator C-Mod and consequences for International Thermonuclear Experimental Reactor (ITER) QDT= 10 operation. *Physics of Plasmas* **18.** doi:10.1063/1.3567547 (2011).

53. Goldston, R. J. & Rutherford, P. H. *Introduction to Plasma Physics* en. ISBN: 0-7503-0325-5 (Institute of Physics Publishing, 1995).

54. Evans, T., Moyer, R., Watkins, J., Osborne, T. & P.R. Thomas4 M. Becoulet4, J. B. E. D. M. F. K. F. Suppression of large edge localized modes with edge resonant magnetic fields in high confinement DIII-D plasmas. *Nuclear Fusion* **45,** 595. doi:10.1088/0029-5515/45/7/007 (2005).

55. Kirk, A *et al.* Understanding the effect resonant magnetic perturbations have on ELMs. *Plasma Physics and Controlled Fusion* **55,** 124003. doi:10.1088/0741-3335/55/12/124003 (2013).

56. Greenwald, M. *et al.* Characterization of enhanced D_α high-confinement modes in Alcator C-Mod. *Physics of Plasmas* **6,** 1943–1949. ISSN: 10897674. doi:10.1063/1.873451 (1999).

57. Gil, L. *et al.* Stationary ELM-free H-mode in ASDEX Upgrade. *Nuclear Fusion* **60,** 054003. ISSN: 17414326. doi:10.1088/1741-4326/ab7d1b (2020).

58. Saibene, G. *et al.* Characterization of small ELM experiments in highly shaped single null and quasi-double-null plasmas in JET. *Nuclear Fusion* **45,** 297. doi:https://doi.org/10.1088/0029-5515/45/5/001 (2005).

59. Kirk, A. *et al.* Comparison of small edge-localized modes on MAST and ASDEX Upgrade. *Plasma Physics and Controlled Fusion* **53,** 095008. ISSN: 07413335. doi:10.1088/0741-3335/53/9/095008 (2011).

60. Faitsch, M. *et al.* Broadening of the power fall-off length in a high density, high confinement H-mode regime in ASDEX Upgrade. *Nuclear Materials and Energy* **26,** 100890. ISSN: 23521791. doi:10.1016/j.nme.2020.100890 (2021).

61. Conway, G. D., Angioni, C., Ryter, F., Sauter, P. & Vicente, J. Mean and Oscillating Plasma Flows and Turbulence Interactions across the $L-H$ Confinement Transition. *Phys. Rev. Lett.* **106,** 065001. doi:10.1103/PhysRevLett.106.065001 (6 2011).

62. Solano, E. R. *et al.* Axisymmetric oscillations at L–H transitions in JET: M-mode. *Nuclear Fusion* **57,** 022021. doi:10.1088/0029-5515/57/2/022021 (2016).

63. Birkenmeier, G. *et al.* Magnetic structure and frequency scaling of limit-cycle oscillations close to L- to H-mode transitions. *Nuclear Fusion* **56,** 086009. doi:10.1088/0029-5515/56/8/086009 (2016).

64. Whyte, D. *et al.* I-mode: an H-mode energy confinement regime with L-mode particle transport in Alcator C-Mod. *Nuclear Fusion* **50,** 105005. doi:10.1088/0029-5515/50/10/105005 (2010).

65. Manz, P. *et al.* Physical mechanism behind and access to the I-mode confinement regime in tokamaks. *Nuclear Fusion* **60,** 096011. doi:10.1088/1741-4326/ab9e17 (2020).

66. Bernert, M. *et al.* The X-Point radiating regime at ASDEX Upgrade and TCV. *Nuclear Materials and Energy* **34,** 101376. ISSN: 2352-1791. doi:https://doi.org/10.1016/j.nme.2023.101376 (2023).

67. Lunt, T. *et al.* Compact Radiative Divertor Experiments at ASDEX Upgrade and Their Consequences for a Reactor. *Phys. Rev. Lett.* **130,** 145102. doi:10.1103/PhysRevLett.130.145102 (14 2023).

68. Burrell, K. *et al.* Quiescent double barrier high-confinement mode plasmas in the DIII-D tokamak. *Physics of Plasmas* **8,** 2153–2162. doi:10.1063/1.1355981 (2001).

69. Suttrop, W *et al.* ELM-free stationary H-mode plasmas in the ASDEX Upgrade tokamak. *Plasma Physics and Controlled Fusion* **45,** 1399. doi:10.1088/0741-3335/45/8/302 (2003).

70. Pochelon, A. *et al.* Recent TCV Results - Innovative Plasma Shaping to Improve Plasma Properties and Insight. *Plasma and Fusion Research* **7,** 2502148–2502148. doi:10.1585/pfr.7.2502148 (2012).

71. Bécoulet, M. *et al.* Mechanism of Edge Localized Mode Mitigation by Resonant Magnetic Perturbations. *Phys. Rev. Lett.* **113,** 115001. doi:10.1103/PhysRevLett.113.115001 (11 2014).

72. Hughes, J. *et al.* Access to pedestal pressure relevant to burning plasmas on the high magnetic field tokamak Alcator C-Mod. *Nuclear Fusion* **58,** 112003. doi:10.1088/1741-4326/aabc8a (2018).

73. Paz-Soldan, C. & the DIII-D Team. Plasma performance and operational space without ELMs in DIII-D. *Plasma Physics and Controlled Fusion* **63,** 083001 (2021).

74. Mossessian, D. *et al.* Edge dimensionless identity experiment on DIII-D and Alcator C-Mod. *Physics of Plasmas* **10,** 689â€“698. doi:https://doi.org/10.1063/1.1538252 (2003).

75. Sun, P. *et al.* Experimental study of quasi-coherent mode using EAST tangential CO2 laser collective scattering diagnostic in far-forward mode. *Physics of Plasmas* **26,** 012304. doi:https://doi.org/10.1063/1.5049209 (2019).

76. Gao, X. *et al.* Experimental study of pedestal turbulence on EAST tokamak. *Nuclear Fusion* **55,** 083015. doi:10.1088/0029-5515/55/8/083015 (2015).

77. LaBombard, B. *et al.* New insights on boundary plasma turbulence and the quasi-coherent mode in Alcator C-Mod using a Mirror Langmuir Probe. *Physics of Plasmas* **21,** 056108. doi:10.1063/1.4873918 (May 2014).

78. Griener, M. *et al.* Qualification and implementation of line ratio spectroscopy on helium as plasma edge diagnostic at ASDEX Upgrade. *Plasma Physics and Controlled Fusion* **60,** 025008. ISSN: 13616587. doi:10.1088/1361-6587/aa97e8 (2018).

79. Vanovac, B., Stober, J., Wolfrum, E. & Willensdorfer, W. Electron temperature fluctuation levels of the quasi-coherent mode across the plasma radius. *EPJ Web of Conferences* **277,** 03003. doi:https://doi.org/10.1051/epjconf/202327703003 (2023).

80. Theiler, C *et al.* Radial localization of edge modes in Alcator C-Mod pedestals using optical diagnostics. *Plasma Physics and Controlled Fusion* **59,** 025016. ISSN: 0741-3335. doi:10.1088/1361-6587/aa52e5 (2017).

81. Snipes, J. A. *et al.* ELMs and fast edge fluctuations in Alcator C-Mod. *Plasma Physics and Controlled Fusion* **40,** 765. doi:10.1088/0741-3335/40/5/039 (1998).

82. Harrer, G. F. *et al.* Quasicontinuous Exhaust Scenario for a Fusion Reactor: The Renaissance of Small Edge Localized Modes. *Phys. Rev. Lett.* **129,** 165001. doi:https://doi.org/10.1103/PhysRevLett.129.165001 (Oct. 2022).

83. Labit, B. *et al.* Dependence on plasma shape and plasma fueling for small edge-localized mode regimes in TCV and ASDEX Upgrade. *Nuclear Fusion* **59,** 086020. ISSN: 17414326. doi:10.1088/1741-4326/ab2211 (2019).

84. Ozeki, T. *et al.* Plasma shaping, edge ballooning stability and ELM behaviour in DIII-D. *Nuclear Fusion* **30,** 1425. doi:10.1088/0029-5515/30/8/003 (1990).

85. Xu, G. S. *et al.* Promising High-Confinement Regime for Steady-State Fusion. *Phys. Rev. Lett.* **122,** 255001. doi:10.1103/PhysRevLett.122.255001 (25 2019).

86. Kamada, Y *et al.* Disappearance of giant ELMs and appearance of minute grassy ELMs in JT-60U high-triangularity discharges. *Plasma Physics and Controlled Fusion* **42,** A247. doi:10.1088/0741-3335/42/5A/329 (2000).

87. Harrer, G. *et al.* Parameter dependences of small edge localized modes (ELMs). *Nuclear Fusion* **58,** 112001. doi:10.1088/1741-4326/aad757 (2018).

88. Faitsch, M. *et al.* Analysis and expansion of the quasi-continuous exhaust (QCE) regime in ASDEX Upgrade. *Nuclear Fusion* **63,** 076013. doi:10.1088/1741-4326/acd464 (2023).

89. Eich, T. *et al.* Scaling of the tokamak near the scrape-off layer H-mode power width and implications for ITER. *Nuclear Fusion* **53,** 093031. doi:10.1088/0029-5515/53/9/093031 (2013).

90. Manz, P. *et al.* Origin and turbulence spreading of plasma blobs. *Physics of Plasmas* **22,** 022308. ISSN: 1070-664X. doi:10.1063/1.4908272 (Feb. 2015).

91. Cavedon, M. *et al.* Interplay between turbulence, neoclassical and zonal flows during the transition from low to high confinement mode at ASDEX Upgrade. *Nuclear Fusion* **57,** 014002. doi:10.1088/0029-5515/57/1/014002 (2016).

92. Colchin, R. *et al.* Physics of slow L-H transitions in the DIII-D tokamak. *Nuclear Fusion* **42,** 1134. doi:10.1088/0029-5515/42/9/312 (2002).

93. Grover, O. *et al.* Limit cycle oscillations measurements with Langmuir and ball-pen probes on COMPASS. *Nuclear Fusion* **58,** 112010. doi:10.1088/1741-4326/aabb19 (2018).

94. Xu, G. *et al.* Dynamics of L-H transition and I-phase in EAST. *Nuclear Fusion* **54,** 103002. doi:10.1088/0029-5515/54/10/103002 (2014).

95. Rèfy, D. *et al.* Identity of the JET M-mode and the ASDEX Upgrade I-phase phenomena. *Nuclear Fusion* **60,** 056004. doi:10.1088/1741-4326/ab7594 (2020).

96. Grover, O *et al.* Experimentally corroborated model of pressure relaxation limit cycle oscillations in the vicinity of the transition to high confinement in tokamaks. *Nuclear Fusion* **64,** 026001. doi:10.1088/1741-4326/ad0eae (2023).

97. Ryter, F *et al.* H-mode power threshold and transition in ASDEX Upgrade. *Plasma Physics and Controlled Fusion* **40,** 725. doi:10.1088/0741-3335/40/5/032 (1998).

98. Greenwald, M *et al.* Transport phenomena in Alcator C-Mod H-modes. *Plasma Physics and Controlled Fusion* **40,** 789. doi:10.1088/0741-3335/40/5/044 (1998).

99. Marinoni, A. *et al.* Characterization of density fluctuations during the search for an I-mode regime on the DIII-D tokamak. *Nuclear Fusion* **55,** 093019. doi:10.1088/0029-5515/55/9/093019 (2015).

100. Liu, Y. *et al.* Power threshold and confinement of the I-mode in the EAST tokamak. *Nuclear Fusion* **60,** 082003. doi:10.1088/1741-4326/ab88e0 (2020).

101. Happel, T. *et al.* Approaching detachment in I-mode-response of core confinement and the edge pedestal in the ASDEX Upgrade tokamak. *Nuclear Fusion* **61,** 036026. doi:10.1088/1741-4326/abd7b7 (2021).

102. Ryter, F. *et al.* I-mode studies at ASDEX Upgrade: L-I and I-H transitions, pedestal and confinement properties. *Nuclear Fusion* **57,** 016004. doi:10.1088/0029-5515/57/1/016004 (2016).

103. Bielajew, R *et al.* Edge turbulence measurements in L-mode and I-mode at ASDEX Upgrade. *Physics of Plasmas* **29.** doi:10.1063/5.0088062 (2022).

104. Asakura, N. *et al.* A simulation study of large power handling in the divertor for a Demo reactor. *Nuclear Fusion* **53,** 123013. doi:10.1088/0029-5515/53/12/123013 (2013).

105. Huber, A *et al.* Peculiarity of highly radiating multi-impurity seeded H-mode plasmas on JET with ITER-like wall. *Physica Scripta* **2020,** 014055. doi:10.1088/1402-4896/ab5753 (2020).

106. Glöggler, S. *et al.* Characterisation of highly radiating neon seeded plasmas in JET-ILW. *Nuclear Fusion* **59,** 126031. doi:10.1088/1741-4326/ab3f7a (2019).

107. Hubbard, A. *et al.* Multi-device studies of pedestal physics and confinement in the I-mode regime. *Nuclear Fusion* **56,** 086003. doi:10.1088/0029-5515/56/8/086003 (2016).

108. Castelvecchi, D. *Strömungsphysik: Der Turbulenz auf der Spur* https://www.spektrum.de/news/der-turbulenz-auf-der-spur/1513527. Accessed: 04.02.2024. 2017.

109. Scott, B. D. Energetics of the interaction between electromagnetic ExB turbulence and zonal flows. *New Journal of Physics* **7,** 92. doi:10.1088/1367-2630/7/1/092 (2005).

110. Kadomtsev, B. B. *Plasma Turbulence* en (Academic Press, Inc., 1965).

111. Tsinober, A. *An Informal Introduction to Turbulence* en. ISBN: 0-306-48384-X (Kluwer Academic Publishers, 2001).

112. Atanasiu, C., Günter, S, Lackner, K & Miron, I. Analytical solutions to the Grad–Shafranov equation. *Physics of plasmas* **11,** 3510–3518. doi:10.1063/1.1756167 (2004).

113. Kull, H. Theory of the Rayleigh-Taylor instability. *Physics Reports* **206,** 197–325. ISSN: 0370-1573. doi:https://doi.org/10.1016/0370-1573(91)90153-D (1991).

114. Bernard, L., Helton, F., Moore, R. & Todd, T. MHD beta limits: scaling laws and comparison with Doublet III data. *Nuclear Fusion* **23,** 1475. doi:10.1088/0029-5515/23/11/005 (1983).

115. Eich, T. *et al.* Correlation of the tokamak H-mode density limit with ballooning stability at the separatrix. *Nuclear Fusion* **58,** 034001. doi:10.1088/1741-4326/aaa340 (2018).

116. Scott, B. D. Drift wave versus interchange turbulence in tokamak geometry: Linear versus nonlinear mode structure. *Physics of Plasmas* **12.** doi:10.1063/1.1917866 (2005).

117. Aiba, N. Impact of ion diamagnetic drift on ideal ballooning mode stability in rotating tokamak plasmas. *Plasma Physics and Controlled Fusion* **58,** 045020. doi:10.1088/0741-3335/58/4/045020 (2016).

118. Brunetti, D, Graves, J. P., Cooper, W. A. & Wahlberg, C. Fast growing resistive two fluid instabilities in hybrid-like tokamak configuration. *Plasma Physics and Controlled Fusion* **56,** 075025. doi:10.1088/0741-3335/56/7/075025 (2014).

119. Eich, T., Manz, P. & the ASDEX Upgrade team. The separatrix operational space of ASDEX Upgrade due to interchange-drift-Alfvén turbulence. *Nuclear Fusion* **61,** 086017. doi:10.1088/1741-4326/ac0412 (2021).

120. Rogers, B. N., Drake, J. F. & Zeiler, A. Phase Space of Tokamak Edge Turbulence, the $L-H$ Transition, and the Formation of the Edge Pedestal. *Phys. Rev. Lett.* **81,** 4396–4399. doi:10.1103/PhysRevLett.81.4396 (20 1998).

121. Zeiler, A, Biskamp, D, Drake, J. & Guzdar, P. Three-dimensional fluid simulations of tokamak edge turbulence. *Physics of Plasmas* **3,** 2951–2960. doi:10.1063/1.871630 (1996).

122. Eich, T. *et al.* Turbulence driven widening of the near-SOL power width in ASDEX Upgrade H-Mode discharges. *Nuclear Fusion* **60,** 056016. doi:10.1088/1741-4326/ab7a66 (2020).

123. Lortz, D. The general "peeling" instability. *Nuclear Fusion* **15,** 49. doi:10.1088/0029-5515/15/1/007 (1975).

124. Mercier, C. A necessary condition for hydromagnetic stability of plasma with axial symmetry. *Nuclear Fusion* **1,** 47. doi:10.1088/0029-5515/1/1/004 (1960).

125. Wilson, H. Edge localized modes in tokamaks. *Fusion science and technology* **57,** 174–182. doi:10.13182/FST10-A9408 (2010).

126. Wan, W. *et al.* Global Gyrokinetic Simulation of Tokamak Edge Pedestal Instabilities. *Phys. Rev. Lett.* **109,** 185004. doi:10.1103/PhysRevLett.109.185004 (18 2012).

127. Manz, P *et al.* Velocimetry analysis of type-I edge localized mode precursors in ASDEX Upgrade. *Plasma Physics and Controlled Fusion* **56,** 035010. doi:10.1088/0741-3335/56/3/035010 (2014).

128. Told, D. *et al.* Gyrokinetic microinstabilities in ASDEX Upgrade edge plasmas. *Physics of Plasmas* **15.** doi:10.1063/1.3000132 (2008).

129. Garbet, X., Idomura, Y., Villard, L. & Watanabe, T. Gyrokinetic simulations of turbulent transport. *Nuclear Fusion* **50,** 043002. doi:10.1088/0741-3335/52/12/124038 (2010).

130. Liewer, P. C. Measurements of microturbulence in tokamaks and comparisons with theories of turbulence and anomalous transport. *Nuclear Fusion* **25,** 543. doi:10.1088/0029-5515/25/5/004 (1985).

131. Horton, W. Drift waves and transport. *Rev. Mod. Phys.* **71,** 735–778. doi:10.1103/RevModPhys.71.735 (3 1999).

132. Scott, B. D. The nonlinear drift wave instability and its role in tokamak edge turbulence. *New Journal of Physics* **4,** 52. doi:10.1088/1367-2630/4/1/352 (2002).

133. Nunami, M., Watanabe, T.-H., Sugama, H. & Tanaka, K. Linear gyrokinetic analyses of ITG modes and zonal flows in LHD with high ion temperature. *Plasma and Fusion Research* **6,** 1403001–1403001. doi:10.1585/pfr.6.1403001 (2011).

134. Pueschel, M. & Jenko, F. Transport properties of finite-β microturbulence. *Physics of Plasmas* **17.** doi:10.1063/1.3435280 (2010).

135. Garbet, X *et al.* Physics of transport in tokamaks. *Plasma Physics and Controlled Fusion* **46,** B557. doi:10.1088/0741-3335/46/12B/045 (2004).

136. Maeyama, S. *et al.* Cross-Scale Interactions between Electron and Ion Scale Turbulence in a Tokamak Plasma. *Phys. Rev. Lett.* **114,** 255002. doi:10.1103/PhysRevLett.114.255002 (25 2015).

137. Cheng, J. *et al.* Formation of radially elongated flow leading to onset of type-III edge localized modes in toroidal plasmas. *Nuclear Fusion* **60,** 046021. doi:10.1088/1741-4326/ab742a (Feb. 2020).

138. Jenko, F., Dorland, W, Kotschenreuther, M & Rogers, B. Electron temperature gradient driven turbulence. *Physics of plasmas* **7,** 1904–1910. doi:10.1063/1.874014 (2000).

139. Groebner, R. *et al.* Limits to the H-mode pedestal pressure gradient in DIII-D. *Nuclear Fusion* **50,** 064002. doi:10.1088/0029-5515/50/6/064002 (2010).

140. Aleynikova, K. & Zocco, A. Quantitative study of kinetic ballooning mode theory in simple geometry. *Physics of Plasmas* **24.** doi:10.1063/1.5000052 (2017).

141. Terry, P. *et al.* Overview of gyrokinetic studies of finite-β microturbulence. *Nuclear Fusion* **55,** 104011. doi:10.1088/0029-5515/55/10/104011 (2015).

142. Belli, E. & Candy, J. Fully electromagnetic gyrokinetic eigenmode analysis of high-beta shaped plasmas. *Physics of Plasmas* **17.** doi:10.1063/1.3495976 (2010).

143. Kaufmann, M. *Plasmaphysik und Fusionsforschung* de. ISBN: 978-3-658-03238-8 (Springer Spektrum, 2003).

144. Dickinson, D. *et al.* Microtearing modes at the top of the pedestal. *Plasma Physics and Controlled Fusion* **55,** 074006. doi:10.1088/0741-3335/55/7/074006 (2013).

145. Dickinson, D. *et al.* Kinetic Instabilities that Limit β in the Edge of a Tokamak Plasma: A Picture of an H-Mode Pedestal. *Phys. Rev. Lett.* **108,** 135002. doi:10.1103/PhysRevLett.108.135002 (13 2012).

146. Gladd, N., Drake, J., Chang, C. & Liu, C. Electron temperature gradient driven microtearing mode. *The Physics of Fluids* **23,** 1182–1192. doi:10.1063/1.863119 (1980).

147. Snyder, P. *et al.* Edge localized modes and the pedestal: A model based on coupled peeling–ballooning modes. *Physics of Plasmas* **9,** 2037–2043. doi:10.1063/1.1449463 (2002).

148. Snyder, P. *et al.* A first-principles predictive model of the pedestal height and width: development, testing and ITER optimization with the EPED model. *Nuclear Fusion* **51,** 103016. doi:10.1088/0029-5515/51/10/103016 (2011).

149. Snyder, P. *et al.* The EPED pedestal model and edge localized mode-suppressed regimes: Studies of quiescent H-mode and development of a model for edge localized mode suppression via resonant magnetic perturbations. *Physics of plasmas* **19.** doi:10.1063/1.3699623 (2012).

150. Auciello, O. & Flamm, D. L. *Plasma Diagnostics* en. ISBN: 0-12-067635-4 (Academic Press, Inc., 1989).

151. Viezzer, E. *et al.* High-accuracy characterization of the edge radial electric field at ASDEX Upgrade. *Nuclear Fusion* **53,** 053005. doi:10.1088/0029-5515/53/5/053005 (2013).

152. Lang, Y. *et al.* Simulation study of particle transport by weakly coherent mode in the Alcator C-Mod tokamak. *Nuclear Fusion* **62,** 086018. doi:10.1088/1741-4326/ac7245 (2022).

153. Bongard, M. *et al.* Characterization of peeling modes in a low aspect ratio tokamak. *Nuclear Fusion* **54,** 114008. doi:10.1088/0029-5515/54/11/114008 (2014).

154. Halpern, F. D., Jolliet, S., Loizu, J., Mosetto, A. & Ricci, P. Ideal ballooning modes in the tokamak scrape-off layer. *Physics of Plasmas* **20,** 052306. doi:10.1063/1.4807333 (May 2013).

155. Bourdelle, C., Garbet, X., Singh, R. & Schmitz, L. New glance at resistive ballooning modes at the edge of tokamak plasmas. *Plasma Physics and Controlled Fusion* **54,** 115003. doi:10.1088/0741-3335/54/11/115003 (Nov. 2012).

156. Hassan, E. *et al.* Identifying the microtearing modes in the pedestal of DIII-D H-modes using gyrokinetic simulations. *Nuclear Fusion* **62,** 026008. doi:10.1088/1741-4326/ac3be5 (2021).

157. Griener, M. *et al.* Helium line ratio spectroscopy for high spatiotemporal resolution plasma edge profile measurements at ASDEX Upgrade. *Review of Scientific Instruments* **89.** doi:10.1063/1.5034446 (2018).

158. Griener, M. Active Line Ratio Spectroscopy on Thermal Helium at ASDEX Upgrade. *PhD Thesis* (2018).

159. Griener, M *et al.* Compensation of plasma fluctuation induced shadowing effects in gas puff imaging data. *Nuclear Materials and Energy* **34,** 101346. doi:https://doi.org/10.1016/j.nme.2022.101346 (2023).

160. Gruber, O. *ASDEX Upgrade* https://www.ipp.mpg.de/2810242/05_aug_letter_4_03.pdf. Accessed: 04.06.2024. 2007.

161. Green, B. J., Team, I. I. & Teams, P. ITER: burning plasma physics experiment. *Plasma Physics and Controlled Fusion* **45,** 687. doi:10.1088/0741-3335/45/5/312 (2003).

162. International, N. E. *ITER reviews plans* https://www.neimagazine.com/news/newsiter-reviews-plans-11199208. Accessed: 07.02.2024. 2023.

163. Zweben, S., Terry, J., Stotler, D. & Maqueda, R. Invited Review Article: Gas puff imaging diagnostics of edge plasma turbulence in magnetic fusion devices. *Review of Scientific Instruments* **88.** doi:10.1063/1.4981873 (2017).

164. Griener, M *et al.* Fast piezoelectric valve offering controlled gas injection in magnetically confined fusion plasmas for diagnostic and fuelling purposes. *Review of scientific instruments* **88.** doi:10.1063/1.4978629 (2017).

165. Griener, M *et al.* Qualification and implementation of line ratio spectroscopy on helium as plasma edge diagnostic at ASDEX Upgrade. *Plasma Physics and Controlled Fusion* **60,** 025008. doi:10.1088/1361-6587/aa97e8 (2017).

166. Wendler, D *et al.* Collisional radiative model for the evaluation of the thermal helium beam diagnostic at ASDEX upgrade. *Plasma Physics and Controlled Fusion* **64,** 045004. doi:10.1088/1361-6587/ac49f8 (2022).

167. Summers, H. *The ADAS User Manual* https://www.adas.ac.uk. Accessed: 07.02.2024. 2004.

168. Stotler, D. *et al.* Shadowing effects in simulated Alcator C-Mod gas puff imaging data. *Nuclear Materials and Energy* **19,** 113–119. ISSN: 2352-1791. doi:https://doi.org/10.1016/j.nme.2019.02.008 (2019).

169. Coroado, A & Ricci, P. Numerical simulations of gas puff imaging using a multi-component model of the neutral–plasma interaction in the tokamak boundary. *Physics of Plasmas* **29.** doi:10.1063/5.0077336 (2022).

170. Griener, M. *et al.* Continuous observation of filaments from the confined region to the far scrape-off layer. *Nuclear Materials and Energy* **25,** 100854. ISSN: 2352-1791. doi:https://doi.org/10.1016/j.nme.2020.100854 (2020).

171. Strait, E., Fredrickson, E., Moret, J.-M. & Takechi, M. Chapter 2: magnetic diagnostics. *Fusion Science and technology* **53,** 304–334. doi:https://doi.org/10.13182/FST08-A1674 (2008).

172. Cavedon, M *et al.* A fast edge charge exchange recombination spectroscopy system at the ASDEX Upgrade tokamak. *Review of Scientific Instruments* **88** (2017).

173. Fischer, R *et al.* Integrated data analysis of profile diagnostics at ASDEX Upgrade. *Fusion science and technology* **58,** 675–684. doi:https://doi.org/10.13182/FST10-110 (2010).

174. Willensdorfer, M *et al.* Characterization of the Li-BES at ASDEX Upgrade. *Plasma Physics and Controlled Fusion* **56,** 025008. doi:10.1088/0741-3335/56/2/025008 (2014).

175. Silva, A *et al.* Ultrafast broadband frequency modulation of a continuous wave reflectometry system to measure density profiles on ASDEX Upgrade. *Review of Scientific Instruments* **67,** 4138–4145. doi:10.1063/1.1147517 (1996).

176. Rathgeber, S. K. *et al.* Estimation of edge electron temperature profiles via forward modelling of the electron cyclotron radiation transport at ASDEX Upgrade. *Plasma Physics and Controlled Fusion* **55,** 025004. doi:10.1088/0741-3335/55/2/025004 (2012).

177. Kurzan, B & Murmann, H. Edge and core Thomson scattering systems and their calibration on the ASDEX Upgrade tokamak. *Review of scientific instruments* **82.** doi:10.1063/1.3643771 (2011).

178. Fritzsche, K. *Grundkurs Funktionentheorie: Eine Einführung in die komplexe Analysis und ihre Anwendungen* de. ISBN: 978-3-8274-1949-1 (Spektrum Akademischer Verlag, 2009).

179. Donoghue, T. *et al.* Parameterizing neural power spectra into periodic and aperiodic components. *Nature neuroscience* **23,** 1655–1665. doi:https://doi.org/10.1038/s41593-020-00744-x (2020).

180. Kalis, J. *et al.* Experimental characterization of the quasi-coherent mode in EDA H-Mode and QCE scenarios at ASDEX Upgrade. *Nuclear Fusion* **64,** 016038. doi:10.1088/1741-4326/ad0d32 (2023).

181. Hidalgo, C. *et al.* Experimental evidence of three-wave coupling on plasma turbulence. *Phys. Rev. Lett.* **71,** 3127–3130. doi:10.1103/PhysRevLett.71.3127 (19 1993).

182. Kim, Y. & Powers, E. Digital bispectral analysis of self-excited fluctuation spectra. *The Physics of Fluids* **21,** 1452–1453. doi:10.1063/1.862365 (1978).

183. Galeev, A. & Sagdeev, R. Parametric phenomena in a plasma. *Nuclear Fusion* **13,** 603. doi:10.1088/0029-5515/13/4/013 (1973).

184. Conway, G., Smolyakov, A. & Ido, T. Geodesic acoustic modes in magnetic confinement devices. *Nuclear Fusion* **62,** 013001. doi:10.1088/1741-4326/ac0dd1 (2021).

185. Beall, J., Kim, Y. & Powers, E. Estimation of wavenumber and frequency spectra using fixed probe pairs. *Journal of Applied Physics* **53,** 3933–3940. doi:10.1063/1.331279 (1982).

186. Nishizawa, T *et al.* Linearized spectrum correlation analysis for thermal helium beam diagnostics. *Review of Scientific Instruments* **92.** doi:10.1063/5.0062436 (2021).

187. Wolfrum, E. *et al.* Characterization of edge profiles and fluctuations in discharges with type-II and nitrogen-mitigated edge localized modes in ASDEX Upgrade. *Plasma Physics and Controlled Fusion* **53,** 085026. ISSN: 07413335. doi:10.1088/0741-3335/53/8/085026 (2011).

188. Macwan, T. *et al.* ELM-free Enhanced D_α H-mode with Near Zero NBI Torque Injection in DIII-D Tokamak. doi:https://doi.org/10.48550/arXiv.2402.06789 (2024).

189. Kallenbach, A. *et al.* Developments towards an ELM-free pedestal radiative cooling scenario using noble gas seeding in ASDEX Upgrade. *Nuclear Fusion,* 016002. ISSN: 0029-5515. doi:10.1088/1741-4326/abbba0 (2020).

190. Viezzer, E. *et al.* Evidence for the neoclassical nature of the radial electric field in the edge transport barrier of ASDEX Upgrade. *Nuclear Fusion* **54,** 012003. doi:10.1088/0029-5515/54/012003 (Feb. 2014).

191. Solano, E. R. *et al.* Axisymmetric oscillations at L-H transitions in JET: M-mode. *Nuclear Fusion* **57,** 022021. ISSN: 17414326. doi:10.1088/0029-5515/57/2/022021 (2017).

192. Zohm, H. Edge localized modes (ELMs). *Plasma Physics and Controlled Fusion* **38,** 105–128. ISSN: 07413335. doi:10.1088/0741-3335/38/2/001 (1996).

193. Snipes, J. *et al.* The quasi-coherent signature of enhanced D_α H-mode in Alcator C-Mod. *Plasma Physics and Controlled Fusion* **43,** L23. doi:10.1088/0741-3335/43/4/101 (2001).

194. Mink, F. *et al.* Toroidal mode number determination of ELM associated phenomena on ASDEX Upgrade. *Plasma Physics and Controlled Fusion* **58,** 125013. ISSN: 13616587. doi:10.1088/0741-3335/58/12/125013 (2016).

195. Myra, J. & D'Ippolito, D. Edge instability regimes with applications to blob transport and the quasicoherent mode. *Physics of Plasmas* **12.** doi:10.1063/1.2048847 (2005).

196. Radovanovic, L. *et al.* Developing a physics understanding of the quasi-continuous exhaust regime: pedestal profile and ballooning stability analysis. *Nuclear Fusion* **62,** 086004. doi:10.1088/1741-4326/ac6d6a (2022).

197. Mazurenko, A. *et al.* Experimental and Theoretical Study of Quasicoherent Fluctuations in Enhanced Dα Plasmas in the Alcator C-Mod Tokamak. *Phys. Rev. Lett.* **89,** 225004. doi:https://doi.org/10.1103/PhysRevLett.89.225004 (2001).

198. Cathey, A *et al.* Probing non-linear MHD stability of the EDA H-mode in ASDEX Upgrade. *Nuclear Fusion* **63,** 062001. doi:10.1088/1741-4326/acc818 (Apr. 2023).

199. Stringer, T. E. Diffusion in Toroidal Plasmas with Radial Electric Field. *Phys. Rev. Lett.* **22,** 770–774. doi:10.1103/PhysRevLett.22.770 (15 1969).

200. Hassam, A. B. & Drake, J. F. Spontaneous poloidal spin-up of tokamak plasmas: Reduced equations, physical mechanism, and sonic regimes. *Physics of Fluids B: Plasma Physics* **5,** 4022–4029. ISSN: 0899-8221. doi:10.1063/1.860622 (Nov. 1993).

201. Manz, P. *et al.* Poloidal asymmetric flow and current relaxation of ballooned transport during I-phase in ASDEX Upgrade. *Physics of Plasmas* **23,** 052302. ISSN: 10897674. doi:10.1063/1.4948787 (2016).

202. Griener, M. *et al.* Characteristics of I-phase bursts and their identity to type-III ELMs. *Paper submitted to Nucl. Fusion* (2024).

203. Eldon, D. *et al.* Evolution of $E \times B$ shear and coherent fluctuations prior to H-L transitions in DIII-D and control strategies for H-L transitions. *Physics of Plasmas* **22,** 112506. ISSN: 1070-664X. doi:10.1063/1.4935919 (Nov. 2015).

204. Qu, C. M. *et al.* Experimental observation of micro-tearing modes in the tokamak pedestal. *Radiation Effects and Defects in Solids* **0,** 1–11. doi:10.1080/10420150.2023.2294033 (2024).

205. Sharapov, S. E. *et al.* Alfvén wave cascades in a tokamak. *Physics of Plasmas* **9,** 2027–2036. ISSN: 1070-664X. doi:10.1063/1.1448346 (May 2002).

206. Savitzky, A. & Golay, M. J. Smoothing and differentiation of data by simplified least squares procedures. *Analytical chemistry* **36,** 1627–1639 (1964).

207. Manz, P. *et al.* Gyrofluid simulation of an I-mode pedestal relaxation event. *Physics of Plasmas* **28,** 102502. ISSN: 1070-664X. doi:10.1063/5.0059295 (Oct. 2021).

208. Happel, T. *et al.* Stationarity of I-mode operation and I-mode divertor heat fluxes on the ASDEX Upgrade tokamak. *Nuclear Materials and Energy* **18,** 159–165. ISSN: 2352-1791. doi:https://doi.org/10.1016/j.nme.2018.12.022 (2019).

209. Liu, Z. X. *et al.* The physics mechanisms of the weakly coherent mode in the Alcator C-Mod Tokamak. *Physics of Plasmas* **23,** 120703. ISSN: 1070-664X. doi:10.1063/1.4972088 (Dec. 2016).

210. Liu, Z. *et al.* Experimental and theoretical study of weakly coherent mode in I-mode edge plasmas in the EAST tokamak. *Nuclear Fusion* **62,** 086029. doi:10.1088/1741-4326/ac7537 (2022).

211. Yang, H., Zhou, T. & Xiao, Y. Gyrokinetic simulation of turbulent transport for I-mode edge plasmas. *Nuclear Fusion* **61,** 056006. doi:10.1088/1741-4326/abebcd (2021).

212. Hubbard, A. E. *et al.* Edge energy transport barrier and turbulence in the I-mode regime on Alcator C-Moda). *Physics of Plasmas* **18,** 056115. ISSN: 1070-664X. doi:10.1063/1.3582135 (May 2011).

213. Herschel, M. *et al.* Experimental evidence for the drift wave nature of the weakly coherent mode in ASDEX Upgrade I-mode plasmas. *Nuclear Fusion* **64,** 076052. doi:10.1088/1741-4326/ad4b3b (2024).

214. Feng, X. *et al.* I-mode investigation on the Experimental Advanced Superconducting Tokamak. *Nuclear Fusion* **59,** 096025. doi:10.1088/1741-4326/ab28a7 (2019).

215. Happel, T *et al. The optimized steerable W-band Doppler reflectometer on ASDEX Upgrade: possibilities and issues* in *11th International Reflectometry Workshop (IRW11)* (2013).

216. Plank, U. The Effect of the Radial Electric Field around the Separatrix on the Access to the High Confinement Mode at ASDEX Upgrade. *PhD Thesis* (2021).

217. Carralero, D. *et al.* Recent progress towards a quantitative description of filamentary SOL transport. *Nuclear Fusion* **57,** 056044. doi:10.1088/1741-4326/aa64b3 (2017).

218. Silvagni, D. *et al.* I-mode pedestal relaxation events at ASDEX Upgrade. English. *Nuclear Fusion* **60.** Publisher Copyright: © EURATOM 2020. ISSN: 0029-5515. doi:10.1088/1741-4326/abb423 (Dec. 2020).

219. Leuthold, N. Experimental investigation of enhanced particle transport due to magnetic perturbations on ASDEX upgrade. *PhD Thesis* (2020).

220. Willensdorfer, M. *et al.* Field-Line Localized Destabilization of Ballooning Modes in Three-Dimensional Tokamaks. *Phys. Rev. Lett.* **119,** 085002. doi:10.1103/PhysRevLett.119.085002 (8 2017).

221. Strumberger, E. & Günther, S. CASTOR3D: linear stability studies for 2D and 3D tokamak equilibria. *Nuclear Fusion* **57,** 016032. doi:10.1088/0029-5515/57/1/016032 (Jan. 2017).

222. Michels, D., Stegmeir, A., Ulbl, P., Jarema, D. & Jenko, F. GENE-X: A full-f gyrokinetic turbulence code based on the flux-coordinate independent approach. *Computer Physics Communications* **264,** 107986. ISSN: 0010-4655. doi:https://doi.org/10.1016/j.cpc.2021.107986 (2021).

223. Stegmeir, A. *et al.* GRILLIX: a 3D turbulence code based on the flux-coordinate independent approach. *Plasma Physics and Controlled Fusion* **60,** 035005. doi:10.1088/1361-6587/aaa373 (2018).

224. Birkenmeier, G. Structure formation at the edge of high temperature plasmas. *Habilitation Thesis* (2022).

225. Krasheninnikov, S. I., D'Ippolito, D. A. & Myra, J. R. Recent theoretical progress in understanding coherent structures in edge and SOL turbulence. *Journal of Plasma Physics* **74,** 679â€“717. doi:10.1017/S0022377807006940 (2008).

226. Ara, G. *et al.* Magnetic reconnection and m = 1 oscillations in current carrying plasmas. *Annals of Physics* **112,** 443–476. ISSN: 0003-4916. doi:https://doi.org/10.1016/S0003-4916(78)80007-4 (1978).

227. Braginskii, S. I. *Reviews of Plasma Physics (Vol. 1)* en (Consultants Bureau, New York, 1965).

Acknowledgments

Who would have thought that I would be writing these words at the end of a dissertation? Well, certainly not my 18-year-old self of 2015, when I ventured out into the "big wide world" from a village of just under 450 inhabitants. It wasn't an easy road to get here. After my excursions into particle physics in my bachelor's degree and into laser-plasma physics in my master's degree, it was plasma physics (and especially fusion physics) that fascinated me. I would like to take this opportunity to thank *Hartmut Zohm*, *Thomas Pütterich* and *Jörg Stober* for the great lectures at the LMU that paved the way for me. There are many people who have been invaluable to this work over the last 3 years and 4 months, and now is the time to thank them.

In general, I would like to thank the ASDEX Upgrade team with their incredibly competent technicians and experts in their field. Especially during the experimental phase of this thesis - the operation of the i-HIBP - I was able to convince myself of this. Although the time and effort invested in the i-HIBP is not reflected in this thesis, it was an enlightening and exciting time that also allowed me to stand inside the ASDEX Upgrade reactor. For the operation of the i-HIBP I would like to thank *Balázs Tál*, *Hannah Lindl* and *Gregor Birkenmeier*, who operated the beam with me in shifts.

Thanks to the 11:30 PhD lunch group, even though I wasn't always there - because honestly, who eats lunch at 11:30? - for the distraction from the day and the interesting topics of conversation. I would like to thank *Felix Klossek*, *Benedikt Zimmermann*, *Magdalena Bauer*, *David Kulla*, *Raphael Schramm*, *Tabea Gleiter*, *Sebastian Hörmann*, *Michael Bergmann*, *Michael Sieben*, *Fabian Solfronk*, *Michaela Mayer*, *Vanessa Harnisch*, *Paul Heinrich*, *Roxána Takács* and *Jonas Puchmayr*.

Special thanks go to *Robert Lürbke*, *Markus Weiland* and *Manuel Herschel*, with whom I was able to drink a beer or two from time to time. I also found working with Manuel on the WCM pleasant, especially his proofreading of the WCM chapter helped me a lot.

I would like to thank *Matthias Bernert*, *Tilmann Lunt*, *Matthias Willensdorfer*, *Rainer Fischer*, *Lidija Radovanovic* and *Marco Cavedon* for their contributions to this work.

As part of my first author paper, there were frequent meetings in the EDA H-mode and QCE group, without which I would never have gained so many insights and

approaches. Although the official difference between EDA H-mode and QCE is still a point of contention, the meetings were fruitful and hotly debated. I would especially like to thank *Luis Gil*, *Michael Faitsch*, *Mike Dune*, *Branka Vanovac*, *Thomas Eich*, *Elisabeth Wolfrum* and *Gustavo Grenfell*. I had particularly intense discussions with the latter about the nature of QCM.

I would like to thank *Ridhesh Goti*, who assisted me with the data analysis and took some of the work off my shoulders.

Thanks to *Daniel Wendler* for being my savior in times of Python problems and organizational outrages. Especially during the IT changeover, which overlapped with the submission of my paper, you helped me out of a tight spot - thank you very much!

Moreover, I thank *Thomas Eich*, who acted as a kind of mentor to me during the first two years. Our common Westphalian origin, your soccer knowledge and your cool concerts come immediately to mind.

A big thank you goes to *Elisabeth Wolfrum* for allowing me to participate in her PEP working group, for always coming up with new ideas, and even for having a 'Lisl widerlegen' group in the meantime, which kept the flow of physical ideas going. But often it was the other way around and we were taught better. I'm already looking forward to my time as a postdoc and am excited about it. Let's see if I can take off my turbulence goggles a bit for the edge phenomena.

On the other hand, I would like to thank *Peter Manz*, whom I only met in real life during my first weeks at the IPP and at the DPG 2023 in Dresden. You introduced me to turbulence theory, and your way of developing an exciting theory from the most unintuitive data fascinated me beyond belief. It was also exciting to look at the data from the GEMR code together, even though it has not been published yet. Thank you very much for being part of my thesis advisory committee.

Another big thank you goes to *Ulrich Stroth*. Due to our quarterly meetings, you kept me on track, so that from time to time I had to pack up my results and see what I had already achieved in the past. The many suggestions you gave me and your way of translating complicated physical phenomena into simple pictures were of great value to me.

Michael Griener was a major contributor to this work. His help in understanding and interpreting the helium beam data was fundamental, and our efforts resulted also in a paper. Your proofreading of most of the chapters here also added an incredible amount of value. Our next paper is already in the pipeline and I look forward to our future collaboration. Thank you for everything!

Let's come to the most important person for this work: a big thank you goes to *Gregor Birkenmeier*! I can only say that you are truly an ideal supervisor, both personally and in terms of content, and that I am lucky to be able to write this

thesis with you. Your supportive attitude in every situation, your wealth of ideas, your understanding of physics, and also your manner and professionalism in explaining highly complex phenomena as simply as possible have helped me a lot in my career. Even though I sometimes got on your nerves with all my questions, you were always able to help me in a calm and balanced way. I hope we will sit together again sometime in the future. Hopefully again outside of work. All in all, thank you for everything.

In addition, I would like to thank the Helmholtz Association for funding my work under grant No. VH-NG-1350.

Not in terms of content, but personally, all my friends helped me - we always laughed and had fun in good times and bad. I would especially like to thank my boys from Brilon-Wald, who have been with me since my childhood. I may have left Brilon-Wald, but I've never forgotten you and I'm very grateful for your support. In this context I would like to mention our Stammtisch 'Boni-Boys' and the 'Schützenverein Brilon-Wald'. A big thank you goes to the guys from our Discord channel, who were online until the early morning hours to distract me. Luckily there are a few unemployed among us.

Finally, I would like to thank my family, who have had my back since 2015 and have always supported me emotionally and financially without ever asking for anything in return. That's what family is all about. Thanks to my parents *Manuela Kalis* and *Ingo Kalis*, as well as my brother *Robin Kalis*, his wife *Aiperi* and their son *Oskar*.